

中国气象科学研究院年报

ANNUAL REPORT OF CAMS



2014



中国气象科学研究院
Chinese Academy of Meteorological Sciences



中国气象科学研究院年报 2014

主办单位：中国气象科学研究院
编辑出版：《中国气象科学研究院年报》编辑部
主 编：端义宏
执行主编：袁凤杰
制作印刷：北京永峰印刷有限责任公司
地 址：北京中关村南大街 46 号，邮编 100081
[http: //qk.cams.cma.gov.cn](http://qk.cams.cma.gov.cn)
Email: kjdt@cams.cma.gov.cn

ANNUAL REPORT OF CAMS 2014

Sponsor: Chinese Academy of Meteorological Sciences
Publication: Annual Report of CAMS Editorial Division
Chief Editor: Duan Yihong
Executive Chief Editor: Yuan Fengjie
Design and Printing: Beijing Yongzheng Printing Ltd. Co.
Address: 46 Zhongguancun Nandajie, Beijing, 100081, China
[http: //qk.cams.cma.gov.cn](http://qk.cams.cma.gov.cn)
Email: kjdt@cams.cma.gov.cn

中国气象科学研究院年报
ANNUAL REPORT OF CAMS

2014

中国气象科学研究院
Chinese Academy of Meteorological Sciences

目 次

科研成果与进展

灾害天气	4
气候系统与气候变化	19
大气探测与雷电防护	29
大气物理与人工影响天气	42
生态环境与农业气象	60
大气成分和大气化学	78
消息与动态	112
2014 年新项目	124
人才培养	127
合作与交流	130
2014 年出版物	137

Scientific Achievements and Advances

Severe Weather	4
Climate System and Climate Change	19
Atmospheric Sounding and Lightning Protection	29
Atmospheric Physics and Weather Modification	42
Ecological Environment and Agrometeorology	60
Atmospheric Composition and Atmospheric Chemistry	78
News and Notes	112
New Projects in 2014	124
Education and Training	127
Cooperation and Communication	130
Publications in 2014.....	137

灾害天气 Severe Weather

灾害天气研究进展

1 灾害天气监测与资料应用

1.1 雨滴谱数据在双线偏振雷达雨滴谱反演及降水估测中的应用

利用双线偏振雷达在广东鹤山（2014年5月1日至6月15日）参加华南前汛期暴雨外场观测试验，获得大量的暴雨、大暴雨野外观测资料，对资料进行了质量控制。利用雨滴谱观测数据分析了华南前汛期滴谱结构，重新拟合偏振参量进行降水估测，提高了偏振雷达定量降水估测精度；利用双线偏振雷达在西藏那曲（7月1日至8月31日）开展的第3次青藏高原科学考察野外观测试验数据，研究了高原对流云的宏、微观特征。（胡志群）

1.2 C波段调频连续波雷达降水云结构研究及降水参数反演

C-FMCW雷达可以描述降水云的精细垂直结构和快速演变特征。利用C-FMCW雷达参加江淮梅雨锋降水观测试验、华南季风强降水外场试验和青藏高原那曲局地对流云的高原观测试验所获得的资料，开展了降水云垂直结构分析和降水参数反演研究。回波谱参数和谱分布的协同分析，有助于深入认识云中的水汽与动力过程，上升和下降运动的强烈变化在回波强度谱分布中的表现更加清晰，在弱回波强度区中发现了高空强的大气下沉速度；反演的广东阳江降水云中雨滴谱分布与地面雨滴谱仪观测数据一致性较好（图1~2）。（阮征）

1.3 联合多种观测设备在多个科研项目上开展外场试验

完成行业专项“第3次青藏高原科学试验——边界层和对流层观测”中的青藏高原云降水预观测试验、华南季风强降水外场试验和973项目“高原东移降水系统观测”等外场试验，获取了云降水微物理结构和动力结构数据。主要创新点：在国内首次利用云雷达、微降水雷达和水汽云探测激光雷达等云观测设备，以及X波段相控阵天气雷达和C波段双线偏振雷达的强对流观测设备，在青藏高原和高原东坡实现了云垂直结构和对流系统中尺度结构的观测。以此为基础，初步形成了多种遥感手段反演高原对流系统空气上升速度和云水/云冰/雨水/雪水的垂直廓线的反演方法，验证了国产新型探测设备在高原工作的能力，为青藏高原云和降水的研究提供了数据（图3）。（刘黎平）

1.4 我国持续性强降水的动力预报理论与方法和可预报性研究

构建了基于集合预报、全球海陆气耦合模式和高分辨率区域模式嵌套的持续性强降水动力预报原型系统；开展了全球海陆气耦合模式和同化系统研究，形成了全球海陆气耦合预报与同化一体化系统，并进行了初步的数值试验。结果显示，对于20天内预报，相对于使用FNL直接插值作为初值的确定性预报，使用CESM-DART预报同化系统的输出作为初值的集合预报在北半球5天后的预报效果较好。开展了现有业务模式对持续性强降水预报能力的评估；研究了高分辨率区域模式的持续性强降水预报方法与技术，表明谱逼近方法对降水的量级、落区以及连续性都有较好的预报，2波及其以上波段的逼近效果更好，其中对降水TS评分的提高尤其体现在中雨及其以上量级的预报。（王东海）

1.5 东亚云水特征及其在参数化中的应用

利用1980—1982年北方5省（新疆，内蒙古，陕西，宁夏，吉林）外场飞机观测资料，探讨了云中云水含量与云滴浓度的关系，并将该统计关系用于云微物理参数化方案中云滴数浓度的约束。利用2006—2011年CloudSat卫星观测数据统计分析了东亚地区云垂直结构特征，并基于统计结果改进了

Kessler型云雨自动转换过程参数化的表达。利用CALIPSO-GOCCP数据统计分析了东亚地区3D云垂直结构特征。(尹金方, 王东海)

2 灾害天气结构与形成机理

2.1 第3次青藏高原大气科学试验

全面开展了2014年度观测任务,进行了加密探空、边界层和雷达观测试验数据的质量控制。初步完成了雷达径向风和反射率、卫星产品、风廓线雷达资料、GPS/MET水汽资料的同化。研究了高原地区不同下垫面地气能量交换特征、辐射收支和水热交换变化特征,以及感热、潜热通量变化特征。研究了青藏高原地区云的时空变化特征,完善了混合相态的云微物理过程,改进了目前双参数云物理方案中的气溶胶活化方案;研究了青藏高原及周边地区对流系统的变化特征,对比了青藏高原低涡的东移机制。分析了高原影响下中尺度气旋在向淮河流域移动过程中引发暴雨过程的机制;揭示了青藏高原大气加热场异常变化对我国旱涝的影响,分析了年际尺度高原异常与我国西南地区5、6月降水的相关关系。(徐祥德)

2.2 青藏高原对梅雨区水分循环及降水变异的影响

进行了梅雨系统上游关键区青藏高原及东缘数据再分析与同化试验研究;开展了青藏高原热力特征变化及其对季风梅雨区环流系统影响的诊断分析、青藏高原热力特征变化对中低纬水汽交换及梅雨区大气水分循环过程的影响研究、青藏高原热力特征变化对梅雨带异常及其旱涝灾害分布影响机理研究,以及青藏高原热力特征变化对梅雨区大气水分循环及降水异常影响的模拟试验研究。(徐祥德)

2.3 不同天气系统特征和变化规律及其对气候变化的响应

基于重污染天气(重点霾天气)时空变化特征,采用历史相关各类气象资料,剖析我国重污染天气大范围时空变化及其对气候变化的年代际响应,探讨大地形对我国重污染天气季节特征及其时空分布变化规律的影响,归纳出重污染天气过程预警业务应用的天气背景各类模型。(徐祥德)

2.4 WMO/WWRP RDP“华南季风降水试验”(SCMREX)

2014年4月3—6日,进行了WMO/WWRP RDP“华南季风降水试验”(SCMREX)外场试验仪器设备的选址工作。5月1日至6月15日,在业务观测网基础上开展了加密观测,暴雨发生期间对移动观测设备进行24 h监控。探空加密观测从2014年5月1日08:00开始,2014年6月15日08:00结束,华南3省的7个高空观测站每站每日增加了14:00和02:00的观测。观测试验之后,收集了移动设备观测数据和华南地区业务数据,并进行了质量控制,完成了项目网站与数据库建设与维护,观测资料已经初步整理并在项目网站上进行共享。针对SCMREX 2014和2013年观测试验期间的暴雨过程,开展了多尺度机理研究以及资料同化影响、模式物理过程参数化方案等相关数值天气预报试验和研究,取得了初步的成果。2014年2次向WMO汇报SCMREX项目进展,得到肯定。(罗亚丽)

2.5 华南暖区暴雨发生发展机制及关键预报技术研究

把具有一定区域意义的暖区暴雨的天气形势分为锋面类、暖湿急流北上类和低涡东移动类3种类型。给出3种类型暖区暴雨的统计特征及其差异。基于综合分析几个华南暖区暴雨个例,给出暖区对流触发与组织过程与冷池传播、地形等的可能关系。推导出适合于华南暖区暴雨的不稳定判据,修正了Richardson数和Brunt-Vaisala频率。个例研究表明,修正后的Richardson数和Brunt-Vaisala频率表征的不稳定区较之以前的不稳定参数与未来雨区有较好的对应。(姜智娜)

2.6 基于EnKF资料同化方法的华南前汛期暖区暴雨集合数值模拟研究

华南前汛期暖区暴雨的定量降水预报(QPF)水平很低,应用集合卡尔曼滤波(EnKF)资料同化技术可以改善模式初始条件,从而提高定量降水预报水平。利用WRF-EnKF系统开展集合预报的模拟试验,研究同化地面资料、探空资料和多普勒雷达径向风资料对模式初值和模拟结果的影响;将集合

模拟与实际观测分析相结合, 研究对流系统的结构和生消演变机制, 重点关注对流触发和维持机制、对流系统的组织模态、热力和动力特征及其与中尺度环境大气的相互作用。个例研究表明, 利用WRF-EnKF系统同化常规探空资料, 显著改善了数值预报的初始场, 减小了各物理量的预报偏差和预报均方根误差, 进而提高了暴雨过程的降水落区和强度的预报准确率。(宝兴华)

2.7 高污染区大气冰核活化参数化方法及对强降水的影响

利用华北(北京及周边)地区1960—2013年的外场冰核观测资料, 分析冰核浓度和活化谱特征, 结合当前已有的多种冰核活化参数化方法, 提出高浓度冰核背景条件下冰核的活化新方法。将新方法耦合到WRF-SBM分档模式中, 利用改进后的模式, 以华北地区常规观测、地基雷达观测、A-Train系列卫星探测、风云(FY)卫星观测等资料的实例作为研究对象, 进行精细模拟, 定量分析强降水过程中不同相态水物质之间相互转换, 揭示冰核对强降水粒子群的影响途径和量级, 以便改进数值模式中冰核活化的参数化描述方法, 提高数值模式对高污染区强降水的预报能力。(尹金方, 王东海)

2.8 我国陆面水体对台风残涡维持及其降水的影响

内陆水体与陆面其他种类特征差异显著, 其热量通量分布不均性更加明显, 导致台风中尺度对流系统活动以及降水强度和落区差异。富含水汽的台风下垫面(鄱阳湖及其周围湿地)具有较高的感热和潜热通量, 可为台风维持提供水汽供应, 从而也有利于降水。敏感性试验发现, 陆面水体移除(扩大)时可产生正(负)气压扰动, 升高(降低)台风海平面气压, 即陆面水体对陆上台风残涡维持有积极作用。宽广水面表层摩擦较小, 低层风加大, 从而改变低层风场辐合的强度和位置, 影响降水强度及其落区。水体在夜间作为一个热源, 比陆地土壤释放更多的表层水热通量, 从而加热加湿低层大气, 是降水的一个能量源。(李英)

2.9 孟加拉湾热带气旋活动及其对我国天气的影响

对中国降水与孟加拉湾风暴活动的相关性进行了分析, 并对风暴活动期间的降水进行EOF分解。发现二者有较好的相关性, 其通过0.01的相关显著性检验的高相关系数区位于中国西南地区、西藏东南部、西北地区东南部和山西南部, 长江下游地区和台湾部分地区也有较小范围的高相关系数区。降水量多少与风暴活动日数有较好的对应。风暴活动主要并同时影响中国西南地区和长江下游地区降水, 且对秋季降水的影响比春季更显著。(李英)

2.10 西北太平洋高空冷涡对台风路径突变影响的机理研究

统计分析发现, 当台风与冷涡中心距离小于5经(纬)距时, 其未来12 h移向转角明显大于气候平均值, 而且台风在冷涡影响下平均移速有所减缓, 尤其是移向突变的台风。台风“莫兰蒂”(2010年)即为在冷涡影响下发生突然北折现象的典型个例。诊断分析表明, 高空冷涡自台风中心东侧向西北方向移动过程中改变了“莫兰蒂”的高空引导气流的方向, 是其路径突变的一个重要原因(图4)。(李英)

2.11 超强台风“丹娜丝”对2013年第23号强台风“菲特”极端降水的作用

利用地面观测资料、台风定位资料、ECMWF全球再分析资料等, 采用热带气旋(TC)降水天气图客观识别法(OSAT)、TC路径相似面积指数(TSAI)和气流轨迹模式HYSPLIT等方法, 从2013年第23号强台风“菲特”在我国东南沿海引发台风暴雨的极端性分析及其成因诊断入手, 揭示了双台风作用对极端暴雨的增强作用。结果表明: 首先, 强台风“菲特”给浙江带来了1958年以来单站日降水排名第2的极端降水, 余姚和奉化日降水量均为395.6 mm; “菲特”降水过程有2个明显的强降水阶段; 其次, 秋季强台风“菲特”登陆后之所以出现如此强度且持续的台风暴雨, 与超强台风“丹娜丝”的存在密不可分。在强降水第1阶段, 双台风作用增强了降水的极端性, 台风“丹娜丝”向降水区域输送了约79%的水汽, 对杭州湾南侧的强降水过程有重要贡献; 在台风“菲特”强降水第2阶段, “菲特”的环流已经基本消散, 超强台风“丹娜丝”与冷空气的共同作用主导了这一阶段强降水的发生。(任福民)

2.12 孟加拉湾和阿拉伯海热带气旋活动双峰型差异及可能成因

针对北印度洋热带气旋（TC）研究中存在的TC资料对比不足和TC活动双峰型特征的区域性差异分析不足的现状，采用联合台风警报中心（JTWC）TC资料和印度气象局（IMD）TC资料开展了针对性的研究。结果如下：IMD资料的时段（1990—2012年）较短且资料记录时刻规律性差；而JTWC资料自1977年突变之后时段仍明显长于IMD资料且资料记录时刻稳定，故采用1977—2012年JTWC资料进行TC气候特征分析。1977—2012年，孟加拉湾TC频数呈下降趋势，而阿拉伯海TC频数呈显著增多趋势；二者多年平均TC频数分别为3.6个和1.5个；两海区TC频数的季节变化都表现为双峰型，但在双峰型的峰值时间、强度以及双峰的强弱配置上存在较大差异。研究表明，纬向风垂直切变和相对涡度的季节变化可能分别是影响孟加拉湾和阿拉伯海TC活动双峰型的关键因子；就整个北印度洋而言，南亚夏季风开始前和结束后，风垂直切变维持在10 m/s及以下、正的相对涡度、较高的海表温度、较大的相对湿度都是TC生成的有利条件。（任福民）

2.13 热带气旋初始结构对快速加强速率的影响

利用多层嵌套、可压缩、非静力热带气旋数值模式研究了不同的涡旋初始结构对热带气旋的快速加强过程的影响，涡旋的初始结构主要包括通过设置不同大风半径来描述的涡旋的大小以及用不同初始最大风速径向衰减曲率来表示的涡旋的不同的眼墙宽度。试验结果表明，当初始涡旋切向风自最大大风半径沿径向迅速衰减，同时向台风中心平缓衰减时，热带气旋快速加强明显。反之，当初始涡旋切向风自最大大风半径沿径向衰减缓慢时，同时向台风中心衰减迅速时，热带气旋快速加强受到抑制。另外，初始涡旋尺度的敏感性试验表明，初始涡旋尺度大不利于热带气旋快速加强，而小的初始涡旋有利于热带气旋的快速加强。（徐晶）

2.14 海南岛海陆风演变特征及其引发的中尺度对流天气预报技术研究

统计分析了2013年海南岛海陆风演变规律的年变化、月变化和日变化特征及其与温度场和降水场的关系。分析显示海南岛各个月份的海陆风特征明显，海风一般发生在上午11:00至晚上20:00之间，11:00附近和20:00附近为海风与陆风的转换阶段，20:00以后至次日11:00前为陆风明显的阶段。海陆风演变造成的辐散关系与降水分布关系密切，海陆温差分布特征是造成海陆风演变的主要原因。海陆风的辐合为降水提供了很好的抬升机制，但需要水汽配合方能发生明显的降水过程，地面相对湿度很好地反映了水汽条件的状况。（梁钊明，王东海）

2.15 我国东部小时降水的特征分析

利用中国区域1951—2013年6月1日至8月31日2420个站点逐小时降水资料，经过质量控制、无资料剔除等处理，建立了我国105°E以东区域内1980—2012年6—8月无缺测记录的1489个站点的逐小时降水资料序列。分析了夏季年平均小时降水频次、雨强和小时极端强降水频次、雨强的分布特征；夏季降水频次的变化趋势；夏季和夏季分月雨强的趋势变化；夏季和各月极端强降水频次的趋势变化；夏季和各月极端强降水雨强的趋势变化。结果表明，我国东部夏季小时降水频次整体以减少趋势为主，小时降水平均雨强以增加趋势为主，小时极端强降水频次整体呈减少趋势，极端强降水雨强整体呈增加趋势（图5）。（赵琳娜）

3 数值天气预报和模式关键技术

3.1 高分辨模式物理过程研发

分析检验了CAMS云微物理方案在青藏高原地区雨滴谱截距偏小导致雨滴偏大和雷达反射率偏大的问题；利用飞机观测资料总结了云水物质含量与云滴浓度的关系，并采用卫星遥感资料分析了东亚地区云垂直结构，改进了云雨自动转化参数化过程，从而有效改进了CAMS云微物理方案对我国高原和华南地区降水的模拟效果。利用观测资料，对半干旱区地表交换系数检验修正，改善了交换系数和地表冠层阻尼参数化，改善了地表热通量计算（图6）。（高文华，尹金方，张果）

3.2 GRAPES模式准均匀网格技术研究

采用Schwarz方法在阴阳网格第1类边界条件强迫条件下首次成功实施了对阴阳网格非静力大气动力模式的半隐式半拉格朗日求解, 实现了GRAPES阴阳网格模式动力框架的稳定积分; 采用ILU预条件处理提高了阴阳网格GCR法求解Helmholtz方程的效率, 加速了数值解的收敛速度。成功确认了准均匀网格GRAPES模式的二阶精度算法改进和长期积分试验, 3D动力框架在2个月时间积分中保持很好的稳定性和计算精度, 为下一代高分辨率GRAPES模式发展提供了一个解决方案(图7)。(彭新东)

3.3 降水短期预报的客观订正

利用高分辨率降水分析资料和距平积分数值订正(ANO)方法, 对2013年7月四川暴雨中尺度模式环流预报场和高分辨降水模拟进行了订正试验。结果表明, 订正对高分辨大气环流场有明显的改进, 明显改善了近地层大气的日周期环流特征预报, 位势高度、温度和比湿分别在对流层中层550 hPa和底层750 hPa改进尤为显著, 同时确认了高分辨WRF中尺度模式的短期降水预报的改善(图8)。(彭新东)

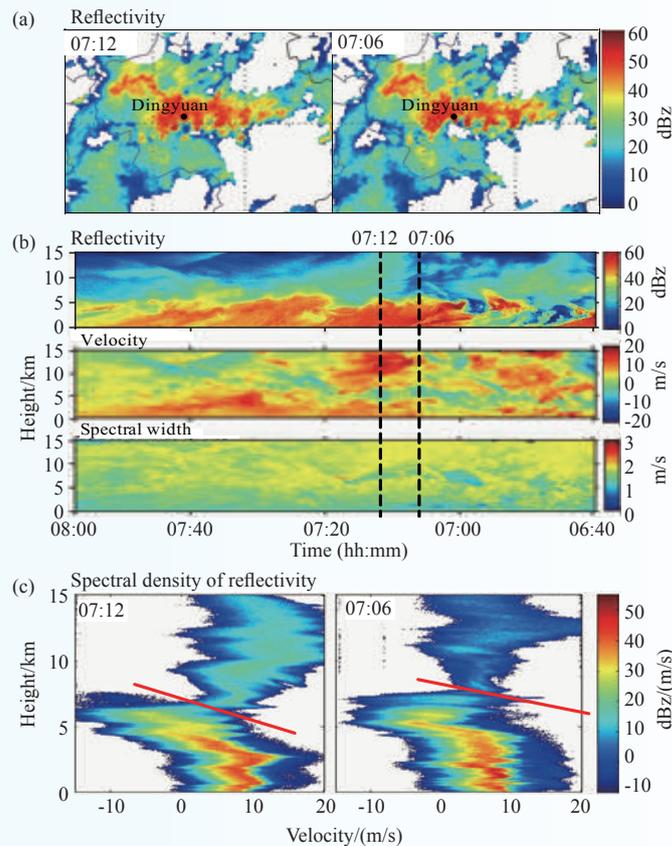


图1 2013年8月24日安徽蚌埠SA雷达和定远C-FMCW雷达探测产品(a: SA雷达回波强度; b: C-FMCW雷达谱参数时序图; c: C-FMCW回波强度谱密度分布)

Fig. 1 Images of SA radar in Bengbu and C-FMCW radar in Dingyuan on August 24, 2013 (a: reflectivity of SA Radar; b: time-height section of C-FMCW radar; c: spectral density of reflectivity of C-FMCW radar)

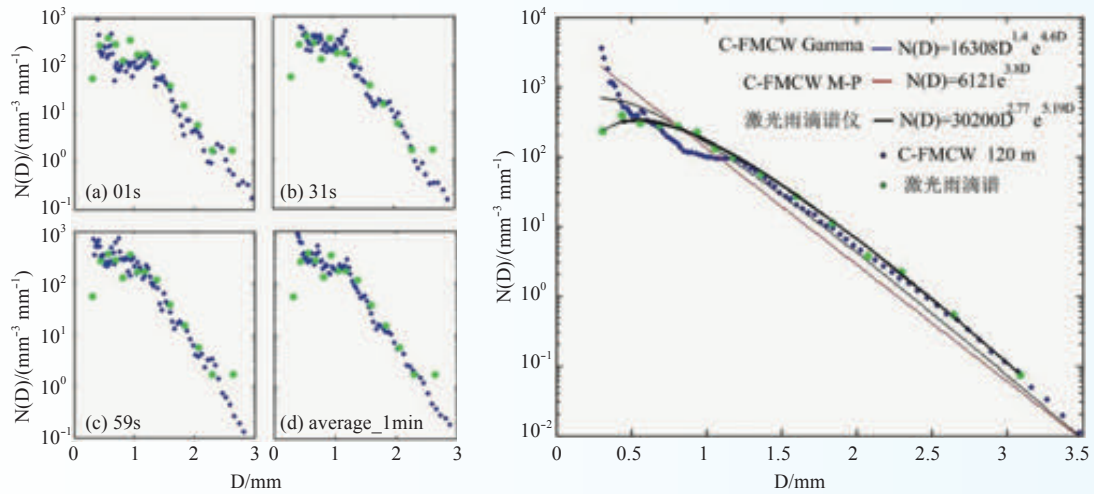


图2 广东阳江C-FMCW雷达反演(120 m)雨滴谱与地面雨滴谱分布比对(左图: 1 min平均; 右图: 10 min平均)
Fig. 2 Raindrop size distributions at 120 m retrieved from C-FMCW radar in comparison with Parsivel disdrometer on surface (Yangjiang, Guangdong Province, May 8, 2014. left: average_1 min; right: average_10 min)



图3 青藏高原云降水外场试验观测主要设备
Fig. 3 The main equipment used in the experiment in the Tibetan Plateau

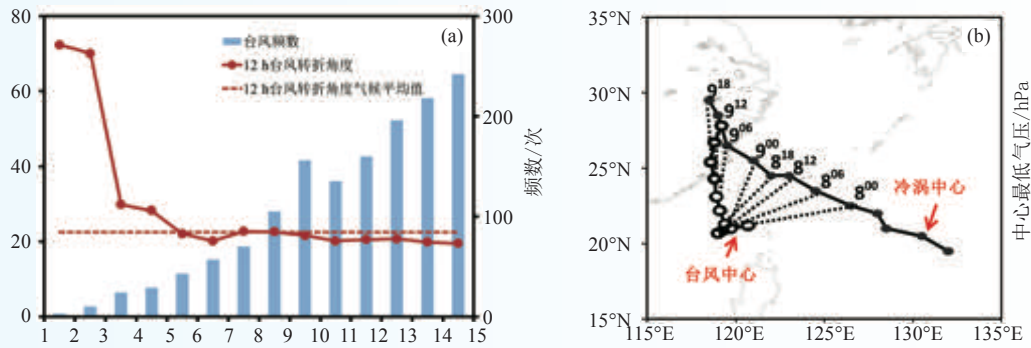


图4 台风移向12 h转折角度(曲线)及台风频数(柱状)随台风与冷涡中心相对距离的变化(a)、台风“莫兰蒂”地面中心(空心圆)和高空冷涡(实心圆)的路径(b)

Fig. 4 (a) Variation of average 12 h directional change of TC movement (red solid line) and accumulative frequency (blue bar) with the relative distance between TC and UTCL (The red dash line indicates the western North Pacific climatology). (b) The tracks of typhoon Meranti (empty circle) and UTCL (dot)

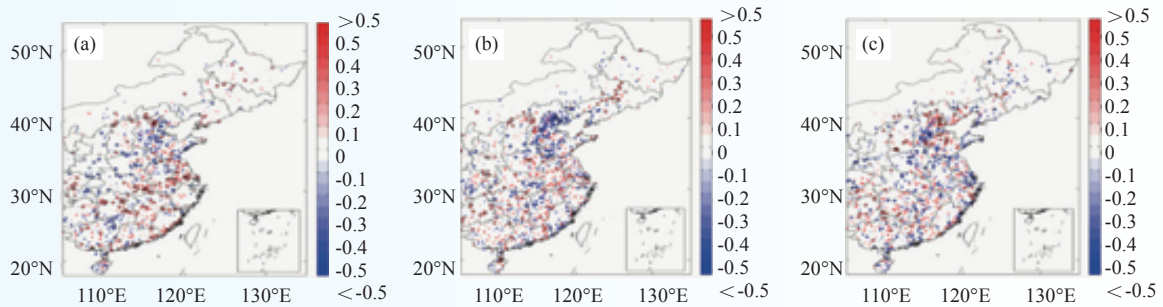


图5 我国东部夏季及夏季各月极端强降水雨强的变化趋势空间分布(单位: %/10a): (a)6月; (b)7月; (c)8月

Fig. 5 The spatial distribution features of the extreme precipitation intensity in summer over the east of China (Unit: %/10a): (a) June; (b) July; (c) August

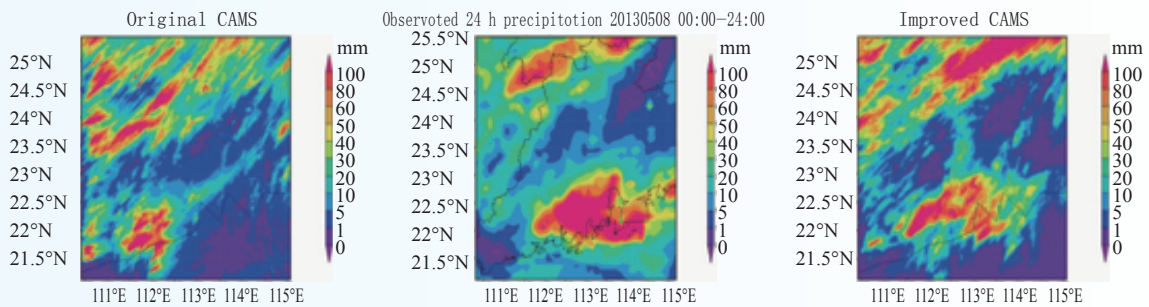


图6 2013年5月8日TRMM/TMI观测降水(中)和CAMS云微物理方案改进前(左)后(右)模拟降水

Fig. 6 The observed (middle) and WRF-CAMS microphysics simulated (left, original; right, improved) 24 h accumulated precipitation during 00:00 to 24:00 (UTC) on 8 May 2013

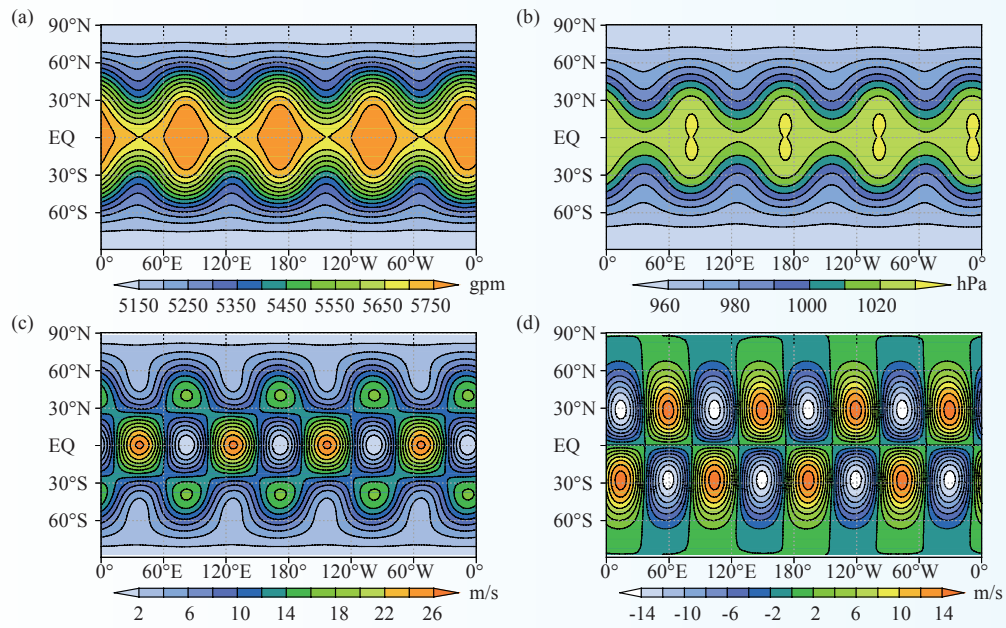


图7 Haurwitz-Rossby波传播第14天位势高度(a)、地面气压(b)、 u 风分量(c)和 v 风分量(d)

Fig. 7 The Haurwitz-Rossby wave propagation on day 14: (a) geopotential height; (b) surface pressure; (c) u component; (d) v component

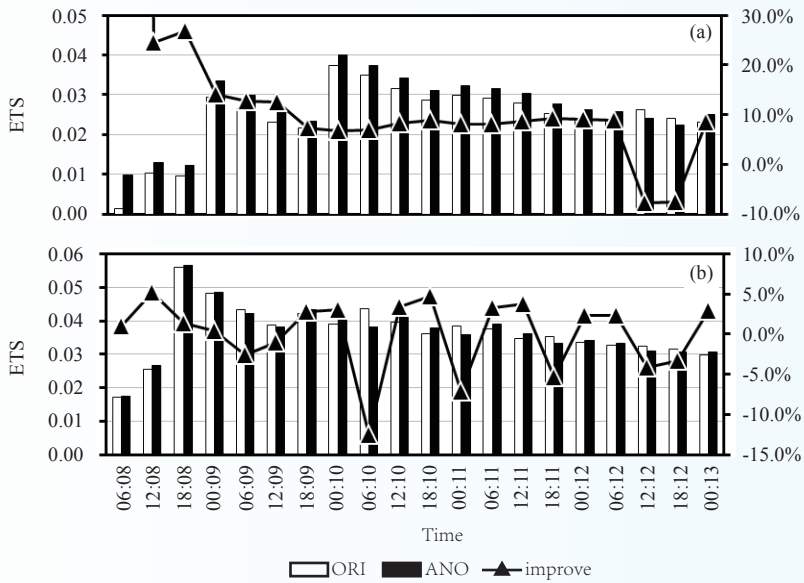


图8 WRF模式预报(ORI)和ANO订正后的暴雨(a)和大雨(b)预报的ETS评分

Fig. 8 Torrential (a) and heavy (b) rainfall forecasting of the original WRF model prediction (ORI) and ANO correction

Advances in Research on Severe Weather

1 Severe weather monitoring technology and data application

1.1 Application of rain drop size distribution (DSD) data to DSD retrieval and precipitation estimation with a dual polarization radar

Heavy rain data were observed with the dual linear polarization radar and disdrometer from May 1 to June 15, 2014 in Heshan, Guangdong Province during pre-rainy season in South China. The dual polarization radar data were controlled in quality before usage. By using the data observed with the disdrometers, the drop size distribution (DSD) of the pre-rainy season in South China was analyzed, and the algorithm of radar quantitative precipitation estimation (QPE) by polarimetric parameters was refitted to improve the accuracy of QPE. The DSD was also retrieved by a dual linear polarization radar in Naqu Tibet during the third Tibetan Plateau Atmospheric Science Experiment (from July 1 to August 31, 2014), which was compared with distrometers. (Hu Zhiqun)

1.2 Micro-physics parameters retrieving vertical structure in the precipitation cloud using a C-FMCW radar

The C-FMCW radar data were used in such experiments as the Meiyu seasonal precipitation in Changjiang-Huaihe River valley, the South China sea monsoon onset and the precipitation cloud structure at the main region of Tibetan Plateau. Data from other active and passive remote sensing systems were used to research the microphysical parameters. The rain parameters were used to retrieve detailed vertical structures and raindrop size distributions in precipitation cloud (Fig.1–2). (Ruan Zheng)

1.3 Various kinds of equipment were employed in field observation experiments for many scientific projects

The Third Tibetan Plateau Atmospheric Science Experiment, heavy rainfall experiment in Huanan for RDP project and precipitation system observation from Tibetan Plateau in 973 Project were carried out and comprehensive measurements of water vapor, clouds, and precipitation were conducted. The most advanced radars in China, such as Ka-Band millimeter-wave cloud, Ku-Band micro-rain, C-Band continuous-wave and lidar, and microwave radiometer and disdrometer were deployed to observe high spatial-temporal resolution vertical structures of clouds and precipitation. Based on the radar measurements in this experiment, the air vertical draft and content profiles for water cloud, ice cloud, rain and snow were retrieved. The observation capabilities of equipment made in China were verified. The above measurements and preliminary analyses provide a basis for further in-depth study of cloud physics and precipitation processes in the Tibetan Plateau (Fig.3). (Liu Liping)

1.4 Forecasting theory and method and predictability of persistent extreme precipitation events in China

A dynamic prototype forecast system for persistent extreme precipitation is constructed based on the ensemble forecast technique, globally coupled oceanic-land-atmospheric model and nested high-resolution regional model. An integrated system composed of globally coupled forecast and global assimilation is developed and used to perform preliminary numerical experiments. The results show that for 20-day forecast,

compared with deterministic forecasts, which use the interpolated FNL analysis as initial conditions, the ensemble forecasts, which use the output of the CESM-DART forecast-assimilation system as initial conditions, exhibit better forecast skills after 5 days for Northern Hemisphere. The prediction ability of the operational model for persistent extreme precipitation is verified. The forecasting theory and method of persistent extreme precipitation events by using the high-resolution regional model are studied. The results show that the numerical simulations by using the spectral nudging and filtering methods have improved obviously precipitation forecasting for magnitude, rain band and continuity, the better nudging effect reflects above 2-wave bands, and, the TS scores also display an improvement in the precipitation rate categories above light rain. (Wang Donghai)

1.5 The cloud-precipitation characteristics and their application in cloud microphysical parameterization

A statistical analysis of cloud microphysical properties was performed based on the in-situ observations from the North China Cloud Physics Detection Project (NCCPDP) during the period from 1980 to 1982. From the statistical results, the relationship between liquid water content (LWC) and cloud number concentration (NC) was investigated. The vertical distributions of LWC in precipitating and non-precipitating clouds were analyzed based on a large number of CloudSat observations over Asian land areas between June 2006 and April 2011. The results of this analysis were used to propose a new definition of the threshold value for Kessler-type parameterization of warm cloud autoconversion. The spatial distribution of clouds and their seasonal variations, and the three-dimensional (3D) cloud structures over East Asia were analyzed with the CALIPSO-GOCCP data during the period from 2007 to 2012. (Yin Jinfang, Wang Donghai)

2 Structures and mechanisms of severe weather

2.1 The 3rd Tibetan Plateau Atmospheric Science Experiment (TIPEX III)

During the period of TIPEX III in 2014, all the following actions were conducted: (1) the observation was executed comprehensively, in which the quality control for intensive sounding, boundary layer and radar observation data was carried out, and the assimilation of observations from radar radial velocity and reflectivity, satellite products, wind profiler radar data, GPS/MET water vapor was completed initially; (2) the exchange characteristics between the ground and the atmosphere, the change in radiation budget and water-heat exchange, and flux change in sensible and latent heats underlying surface on the plateau were researched; (3) the spatial and temporal variation of the cloud in the Tibetan Plateau was investigated, in which the cloud's microphysical processes in mixed phases were refined, and the aerosol activation scheme in existing dual-parameter cloud's physical processes was improved; (4) the change characteristics of a convective system over the Tibetan Plateau and its neighboring areas were studied, in which the mechanism of eastward movement of low vortex in Tibetan Plateau was detected, and the mechanism of storms triggered by the mesoscale cyclones when moving eastward to Huaihe River Basin was analyzed; (5) the influence of abnormal atmospheric heating field in Tibetan Plateau on flood and drought in China was revealed, in which the relationship between the interannual-scale anomalies in plateau and precipitation in May and June in Southwest China was analyzed. (Xu Xiangde)

2.2 The effect of Qinghai-Xizang Plateau on water cycle and precipitation variation in Plum Rain region

We have made a reanalysis and assimilation experiment for the data of the Qinghai-Xizang Plateau and its

eastern margin, the key upstream areas for the Plum Rain system, a diagnostic analysis of the thermodynamic variation characteristics in the Qinghai-Xizang Plateau region and a study of its impact on the circulation system in the monsoon and Plum Rain region, a study of the influence of the thermodynamic variation in the Qinghai-Xizang Plateau on the water vapor exchange between low and middle latitude areas, as well as atmospheric water circulation processes in the Plum Rain area, a study of the mechanism on the influence of the thermodynamic variation in the Qinghai-Xizang Plateau on the anomalies of the Plum Rain zone and the distribution of flood and drought disasters, and a simulated experimental study of the influence of the thermodynamic variation in the Qinghai-Xizang Plateau on the anomalies of atmospheric water cycle and precipitation in the Plum Rain area. (Xu Xiangde)

2.3 Characteristics and evolution of different weather systems and their response to climate change

Building on the spatial and temporal characteristics of the seriously-polluted weather (particularly the haze) derived from all kinds of historical meteorological data associated, we described the large-scale temporal and spatial variation of seriously-polluted weather and its decadal response to the climate change in China, and explored the effects of large scale topography on the seasonal evolution of seriously-polluted weather and its spatial and temporal distribution. At last, we established diverse synoptic background models for warning application during the formation of seriously-polluted events. (Xu Xiangde)

2.4 WMO/WWRP RDP South China Monsoon Rainfall Experiment (SCMREX)

During 3–6 April 2014, the site selection of the field experiment instruments and equipment was completed. Based on the conventional observation network, intensive observations were made during May 1–June 15. The mobile observation equipment was under the 24-hour monitoring during periods of heavy rainfall. Intensive sounding observations started at 8 BST on May 1, 2014 and ended at 8 BST on June 15, 2014. 7 upper-air stations in the three South China provinces made additional observations at 14 BST and 02 BST per day. After the observation experiment, not only the conventional observation data but also the mobile equipment observation data were collected and controlled in quality. Also, the development and maintenance of the project website and database were achieved. After being primarily processed, the observation data were shared on the project website. Focusing on these heavy rainfall cases during 2013–2014 SCMREX experiment, we studied the multiple scales mechanism, the impact of data assimilation, and the difference of various model physics Parameterization Schemes, with initial results achieved. We reported SCMREX progress twice in 2014, which was recognized by WMO. (Luo Yali)

2.5 Mechanism and forecast skill of warm sector heavy rainfall in South China

According to weather regimes, warm sector rainfall is divided into three types: (1) Frontal rainfall, (2) Northward motion of warm and moisture jet, (3) Eastward motion of low vortex. The above three types of warm-sector rainfall are analyzed and compared. A case study pointed out that the triggered convection in a warm sector may be closely related to its organization process, the cold cell spreading and the terrain. Besides, the instability criterion fit for the warm-sector rainfall is derived, e.g. the modified Richardson number and Brunt-Vaisala frequency. The study shows that the unstable region revealed by the modified Richardson number and Brunt-Vaisala frequency can well represent the future rainfall region. (Jiang Zhina)

2.6 On the warm-sector heavy rainfall during the early summer rainy season over South China: An EnKF data assimilation based simulation study

The Quantitative precipitation forecast (QPF) skill for the warm-sector heavy rainfall over South China during the early summer rainy season is very low. The application of the Ensemble Kalman Filter (EnKF) data

assimilation technique can potentially improve the initial conditions of simulation and thus improve the QPF skill. On the one hand, ensemble simulation experiments will be conducted using the WRF-EnKF system. Impacts of a variety of observational data, including not only the surface and sounding observations but also the Doppler radar velocity, on the initial conditions and the simulation results will be investigated. On the other hand, combining the ensemble simulation experiments with the observational analysis, we will study internal structures and organizational modes of the rainy storm, and influencing factors for the convective interactions between the rainy storm and its mesoscale environments. One case study results show that, compared to no data assimilation experiment (NODA), not only the initial conditions of EnKF data assimilation experiment (DA) are much closer to the observed fields, but also the DA predicted physical parameters are improved in terms of both biases and root-mean-square errors, which leads to a more accurate prediction of the location and magnitude of precipitation from DA. (Bao Xinghua)

2.7 Study of the ice nuclei activation parameterization and its influence on severe precipitation under the conditions of high pollution

An attempt was made to delineate the characteristics of ice nuclei (IN) over the eastern central China using the ground-based measurement data over 1960–2013. Based on the statistical results, a new parameterization was proposed for ice nuclei activation within high ice nuclei conditions. Based on the ice nuclei field observational data over the last five decades and the widely used ice nuclei activation parameterizations in numerical models, the new scheme will be coupled into the WRF model with Spectral Bin Microphysics (WRF-SBM). Based on the improved model, we will focus on the conversion among the hydrometeors (vapor, cloud water, rain water, cloud ice, snow, graupel, and hail) in a severe precipitation event which has been captured by ground-based radars, and satellites of A-train (mainly including CloudSat and CALIPSO) and Fengyun (FY). The results will be used to identify the effects of high ice nuclei concentration on the development and formation of a severe precipitation. Based on the results, the parameterization for ice nuclei activation will be improved to improve severe precipitation forecasting within polluted conditions by a numerical model. (Yin Jinfang, Wang Donghai)

2.8 The impact of land surface water on the inland behavior of landfalling typhoon

Inland water surface has remarkable differences in heat property and roughness from other land surface covers. It could lead to the uneven distribution of surface flux, which influences the mesoscale systems and rainfall of landfalling typhoon significantly. That is, inland water surface (such as Poyang Lake and wet land around it) could release heat fluxes to the boundary layer of typhoon, providing favorable condition for typhoon maintenance and rainfall. Sensitivity experiments on Poyang Lake demonstrate that a mesoscale vortex would be weakened in the absence of the lake to lead to the increase of sea level pressure in typhoon center. In addition, broader water bodies have less friction, which increases wind speed near the underground to enhance convergence over heavy rainfall area on the one hand. On the other hand, water bodies may release more surface heat fluxes to make air warmer and wetter in lower atmosphere, which is beneficial to typhoon heavy rainfall. (Li Ying)

2.9 The impact of cyclonic storms over the Bay of Bengal on the weather of China

A correlation analysis is used to investigate the relationship between rainfall of China and activities of cyclonic storms over the Bay of Bengal. Results show that the high correlation coefficient areas are mainly found in the Southwest China, southeast of Tibet plateau, southeast of Northwest China, the lower reaches of Yangtze River and Taiwan Island. Storm activities can influence rainfall of the southwest area and the lower Yangtze region concurrently, and the impact is more significant in autumn than in summer. (Li Ying)

2.10 The impact of upper tropospheric cold low on abrupt turning of tropical cyclone movement

Statistical study indicates that when the relative distance between a tropical cyclone (TC) and an upper tropospheric cold low (UTCL) is less than 5 latitudes/longitudes, the average 12 h directional change of TC movement is obviously larger than the average western North Pacific climatology. In addition, the TC average moving speed slows down under the impact of UTCL, especially that of the TCs with abrupt turning. Meranti (2010) is a typical typhoon which turned abruptly under the influence of an UTCL. A diagnostic study indicates that the UTCL changes the steering flow when it is moving from the east of the central TC to the northwest, which is an important reason for abrupt turning of Meranti (Fig. 4). (Li Ying)

2.11 The role of super typhoon Danas in extreme precipitation associated with severe typhoon Fitow

Based on surface observational data, typhoon track data and ECMWF global reanalysis data, using the objective synoptic analysis technique (OSAT), tropical cyclone (TC) track similarity area index (TSAI), and the airflow trajectory model (HYSPLIT4.9) and analyzing the characteristics and causes of the extreme precipitation over coastal Southeast China associated with the severe typhoon Fitow, this study reveals the intensification by a binary typhoon of an extreme precipitation. First, Fitow causes the maximum daily precipitation of 395.6 mm at both Yuyao and Fenghua, which rank the second most extreme daily TC precipitation in Zhejiang Province in record. The precipitation process has two distinct intense precipitation stages. Secondly, such a heavy and continuous rainfall during and after Fitow's landfall is mainly due to the existence of super typhoon Danas. In the first stage, because of the binary tropical cyclone interactions, Fitow moves much faster than before. Moreover, Danas transports about 79% moisture to the raining region, which is an important contribution to the extreme precipitation over the southern coast of Hangzhou Bay. In the second stage, as the circulation of typhoon Fitow almost dissipates, the combined interaction of super typhoon Danas and cold air mainly causes the extreme precipitation. (Ren Fumin)

2.12 Differences of bimode patterns in TC activity and their possible causes in the Bay of Bengal and the Arabian Sea

To address the inadequate tropical cyclone datasets for comparison research purpose and to analyze the regional differences in TC bimodal patterns in the North Indian Ocean, a targeted study on these issues has been carried out using the Joint Typhoon Warning Center (JTWC) TC dataset and the India Meteorological Department (IMD) TC dataset. Results are as follows: time period (1990–2012) of IMD dataset is much shorter and data recording time is irregular, while time period (1977–2012) of JTWC dataset after the abrupt change in 1977 is much longer and data recording time is regular. Thus, JTWC dataset of 1977–2012 is adopted in TC climatic characteristics analysis. During 1977–2012, the Bay of Bengal (BoB) TC frequency decreases, while the Arabian Sea (AS) TC frequency increases significantly. Average TC frequencies are 3.6 and 1.5 in BoB and AS, respectively. Meanwhile, seasonal variations in TC frequency show a bimodal pattern with two peaks in both BoB and AS but with obvious differences in bimodal peak time, intensity and strength. It is revealed that vertical zonal wind shear and seasonal changes in relative vorticity might be the key factors affecting the bimodal patterns of TC activity in BoB and AS, respectively. Meanwhile, for the whole North Indian Ocean, before the onset and after the finish of South Asian Summer Monsoon, below 10 m/s vertical zonal wind shear, positive relative vorticity, high sea surface temperature and high humidity are all favorable conditions for TC genesis. (Ren Fumin)

2.13 Sensitivity of tropical cyclone rapid intensification to the initial vortex

The multiply nested, fully compressible, non-hydrostatic tropical cyclone model is used to examine and

understand the sensitivity of the simulated tropical cyclone (TC) rapid intensification (RI) to its initial vortex structure, including the radial profile of tangential wind and the size of the vortex. The results show that when the initial vortex is with a broader profile outside but a narrower profile inside the eyewall, the slower (faster) RI is in the simulated storms. The results also show that the larger and broader (smaller and narrower) the initial vortex is, the slower (faster) the RI is but the larger (smaller) inner-core size is in the simulated storms. (Xu Jing)

2.14 Technical study of how to forecast a land-sea-breeze and associated mesoscale convective weather in Hainan island

The annual, monthly and daily changes of land-sea-breezes in Hainan Island and their relations with the temperature and rainfall fields are investigated by using the observational data of year 2013. Results show that a land-sea-breeze obviously happens throughout the year with a sea breeze occurring between 11:00 and 20:00 LST (local standard time) and a land breeze occurring between 20:00 and 11:00 (the next day) LST. A close relation is shown between the rainfall and the convergence caused by the land-sea-breeze, in which the thermal heating difference determines the evolution of the land-sea-breeze. The convergence caused by the land-sea-breeze provides a good condition for the lifting of air, which can lead to significant rainfall when accompanied with sufficient water vapor. The relative humidity near the surface is a good indicator of water vapor conditions. (Liang Zhaoming, Wang Donghai)

2.15 The characteristic analysis of hourly precipitation over eastern China

Based on the hourly rain gauge data of 2420 stations across China from June 1st to August 31st during 1951 to 2013, the hourly precipitation sequence of 1489 stations for areas in China to the east of 105°E from June 1st to August 31st during 1980 to 2012 is established with the quality controlled and no-data records rejected. The annual average precipitation frequency, rainfall intensity, hourly extreme precipitation frequency, including the distribution of the summer rainfall intensity, are analyzed. The trend of summer precipitation frequency, that of the monthly summer rainfall intensity change, and the frequency of the extreme strong precipitation events is also investigated. The results indicate that the frequency of hourly precipitation in summer mainly declines while its intensity increases on the whole over east China. The frequency of hourly extreme precipitation decreases while its intensity increases as a whole (Fig. 5). (Zhao Linna)

3 Numerical weather prediction and key techniques in numerical modeling

3.1 Study of the high-resolution physical processes

The reasons of large raindrop and high radar reflectivity simulated by CAMS cloud microphysics over the Tibetan Plateau are investigated at 1 km horizontal resolution. The relationship between cloud water content and cloud droplet concentration is analyzed using aircraft observations, and the cloud vertical structure over East Asia is explored with multi-satellite data. As a result, the performances of CAMS cloud microphysics are considerably improved over the plateau and South China. In addition, the surface exchange coefficient in a semi-arid region is assessed and modified using the observations, while the calculations about surface exchange coefficient, canopy damping parameter and surface heat flux are also improved (Fig. 6). (Gao Wenhua, Yin Jinfang, Zhang Guo)

3.2 Quasi-uniform grid GRAPES model development

Using Schwarz method, the non-hydrostatic GRAPES model is successfully established on the Yin-Yang

quasi-uniform grid with a first-type boundary condition and semi-implicit semi-Lagrangian solver. A long-term stable integration of the model dynamic core is confirmed. The application of the ILU pre-conditioner accelerates the GCR solver for Helmholtz equations, and consequently the convergence rate is speeded up significantly in the temporal integration of the model on Yin-Yang grids. An overall second-order accuracy and excellent stability of the model frame are verified in the three-dimensional idealized test cases. The frame provides a possible solution for the next-generation high-resolution GRAPES model development (Fig. 7). (Peng Xindong)

3.3 Objective correction of short-term rainfall prediction

The Anomaly Numerical-correction with Observations (ANO) method and a high-resolution precipitation analysis data are used to test the model results of correction in a Sichuan rainstorm case in July 2013, which shows the amelioration of meso-scale circulation and high-resolution rainfall forecasting. Great improvement to the high-resolution circulation, especially near surface diurnal variations, is displayed. The geopotential height, temperature and relative humidity are prominently corrected at 550 hPa and 750 hPa. Notable improvement to the short-term rainfall forecasting with the WRF mesoscale model is demonstrated (Fig. 8). (Peng Xindong)

气候系统与气候变化 Climate System and Climate Change

气候系统与气候变化研究进展

2014年,气候系统研究所在气候预测理论与方法、气候系统模式研发、东亚季风变异机理、古气候以及极地气候研究方面获得了显著进展。

1 气候预测理论与方法

1.1 夏季青藏高原积雪异常与同期梅雨降水的关联

高分辨率的卫星资料(EASE-grid)显示,在青藏高原西部、南部等高海拔地区夏季仍存在积雪。该地区的积雪异常可以调节青藏高原陆面加热,进而影响青藏高原西部的垂直运动,并通过经向垂直环流调节北印度洋地区的垂直上升运动。同时,通过热带地区的纬向垂直环流和开尔文波(Kelvin wave)响应,北印度洋异常垂直运动可以造成西北太平洋副热带高压异常,也对西太平洋暖池的对流活动具有重要的影响。因此,青藏高原高海拔地区的夏季积雪能够影响东亚-太平洋遥相关型(EAP)和相应的东亚梅雨区夏季降水异常(图1a)。

另外,青藏高原前期春季(5月)积雪异常可持续到夏季,进而影响东亚梅雨区的夏季降水(图1b)。青藏高原西部积雪异常从春至夏的持续性能部分解释前春积雪对东亚夏季降水影响的季节延迟效应。这一机制不同于以往的高原东部的冬、春季积雪异常通过调节春、夏季土壤湿度等陆面状况来影响降水的机制,是关于青藏高原积雪对我国降水预测的一个较为重要的补充(图1)。(刘舸)

1.2 气候预测新方法研究

利用分数阶积分的相关理论,成功地将给定的气候时间序列分解为两部分:历史记忆性信息及当前扰动。换言之,对于某给定时刻气候状态的预测,可以首先计算由于历史信息持续性影响造成的变化,再对当前扰动进行预测。建立了分数阶随机气候模型,并成功给出了定量计算历史记忆性信号的方法。以北半球温度序列及PDO指数为例,估算了它们的历史记忆性信号。对于这两个序列,其历史记忆性信号所占方差比很大。掌握历史信息的持续影响可以很大程度上提高我们对当前时刻气候状态的模拟、预测能力。

对当前扰动的预测,考虑从多因子相互作用出发,通过评估不同预报因子在不同时间尺度上的不同作用,尝试建立分层预测模型。目前已提出了定量评估不同预报因子在不同时间尺度上相互作用强弱的新方法,即去趋势的偏相关分析方法(DPCCA)。以长江中下游夏季降水、前冬赤道东太平洋海温异常、前冬PDO指数三者之间的关系为例,介绍了该方法。可以看到,该方法可以成功地提取出不同因子的特征作用时间尺度(图2)。(袁乃明)

1.3 中国北方冬季温度的东北—西北偶极型模态及其前兆信号

基于中国北方71个站点、NCEP/NCAR和NOAA的CIRES 20世纪再分析月平均气温(SAT)资料,对中国北方冬季温度的EOF主要模态进行了探讨。结果表明,除了第1模态一致寒冷(温暖),第2模态也占总方差相当大的比例,其特点是偶极子结构,中国西北冷(暖),则中国东北地暖(冷)。研究发现,欧亚大陆秋季气温异常与欧亚大陆积雪异常紧密相关,并对中国北方的冬季气候有延迟效应。进一步研究发现,上一年贝加尔湖($50^{\circ} \sim 60^{\circ} \text{N}$, $85^{\circ} \sim 120^{\circ} \text{E}$)地区与蒙古高原($42^{\circ} \sim 52^{\circ} \text{N}$, $80^{\circ} \sim 120^{\circ} \text{E}$)地区的秋季气温对我国东北、西北冬季气温有着重要的调节作用。(辛羽飞)

2 气候系统模式研发

气候系统研究所从2009年起成功建立了一个包括大气、陆面、海洋和海冰的气候系统模式。经数年持续发展改进,模式在去除通量订正、减小气候漂移、改进ENSO季节锁相模拟以及降水模拟等方面取得了重要进展。在自由耦合情况下,模式以T42和T63的大气水平分辨率、 1° 的海洋水平分辨率稳定积分超过1000年,显示了对全球气候平均态、季节变化以及年际变率良好的模拟性能以及对我国气候预测的潜在应用前景。

2014年模式研发在以下几个方面取得了进展:

(1) 完成了ECHAM5模式与陆面模式CoLM的双向耦合工作。耦合CoLM陆面模式后模拟的地表温度偏差较之前版本在全球大部分地区均显示减小,特别是欧亚大陆北部的冷偏差得到明显改善。

(2) 大气模式的水平分辨率提高至T255(约50 km),海洋模式水平分辨率提高至 0.5° ,耦合模式水平分辨率提高到大气模式T106、海洋模式 0.5° 。随着分辨率的增加,模式对东亚地区降水的模拟水平得到了显著提高。

(3) 对ECHAM5的动力框架进行了改进。模式的水汽输送引入了“两步保形平流方案”(TSPAS)。模拟结果显示,新方案对东亚地区降水特别是青藏高原大地形周边降水有明显改善。(荣新尧)

3 东亚季风变异机理

3.1 青藏高原大气热源对高原低涡演变东移的影响

青藏高原低涡(简称“高原低涡”)是夏季青藏高原特有的天气系统,是高原地区的主要降水系统之一。它主要在青藏高原主体上生消,一般产生于高原西半部,消失于东半部。在一定条件下,高原低涡可以移出高原,进而造成我国东部甚至更广大地区的暴雨、雷暴等灾害天气,高原下游地区一些较大规模的降水都与青藏高原低涡的移出有关。

利用NCEP的FNL资料和常规探空资料,对比研究了移出型高原低涡和不移出型高原低涡的演变东移机制。结果显示,高原低涡的演变东移是加热场和环流场相互作用的结果。对于移出型低涡,500 hPa等压面上高原北部的高压脊和孟加拉湾附近的低压槽更强,来自北部高压脊的北风和来自低压槽的南风在低涡东部的辐合更强。同时,200 hPa等压面上高空西风急流入口区右侧的辐散区正好位于高原涡的上空。高层辐散低层辐合的配置有利于低涡的维持和降水的产生,伴随降水产生的凝结潜热加热对低涡的演变东移有重要影响。

通过对位势涡度收支方程的计算和对青藏高原大气热源空间分布特征的诊断分析发现,在低涡的发展阶段,无论是移出型低涡还是不移出型低涡,其发展东移的机制是相似的,即以凝结潜热加热为主的大气热源的垂直分布对低涡的发展东移起主导作用;在衰减阶段,对于移出型低涡,其东移主要依靠低涡东部南风和北风的辐合,对于不移出型低涡,位势涡度在垂直方向上的辐散导致低涡强度减弱,且不利于其东移。(李论)

3.2 中部型厄尔尼诺的激发和发展机理

利用海洋和大气观测再分析资料,分析了中部型厄尔尼诺事件的4次主要个例(1994, 2002, 2006, 2009年)的激发和发展机理。混合层热量收支平衡诊断发现,与2000年之后的几次事件相比,1994年中部型厄尔尼诺的激发机制存在显著不同,但各次事件的发展机制大致相同。指出中部型厄尔尼诺事件的激发机制有两种:一种是(以1994年为例)赤道外侧的次表层暖水在海洋经向环流的输送下抵达赤道中太平洋,促进中太平洋变暖;一种是(以2000年后其他中部型事件为例)西太平洋暖池附近次表层暖水的堆积及其向东扩展,导致了中部型厄尔尼诺的发展。在1994年厄尔尼诺激发期,赤道太平洋海温增暖起因于太阳短波辐射的增加,这是由前期副热带太平洋暖海温异常引发的大气经向环流的改变所致。同时,副热带太平洋海洋异常能够促使赤道外侧形成反气旋式环流,这有利于赤道外侧次表层暖水的形成。赤道外侧次表层暖水能够在海洋次表层由海洋环流输运至赤道区域,形成赤道次表层暖水。受此影响赤道温跃层加深,进而增强平流反馈机制和温跃层反馈机制,因此海表温度

异常得以发展。在2000年之后的几次中部型厄尔尼诺事件的激发期，海洋动力机制起到主要作用，而海表热通量异常很弱。此类厄尔尼诺前期赤道太平洋出现次表层海温异常，可增强东向的海流进而有利于海表温度增加。这种正的海流反馈机制和温跃层反馈机制可持续至发展期，使得海表温度得以不断增温。（苏京志）

3.3 印度夏季风对南亚高压的影响及其与中国夏季降水的关系

利用逐月的ERA-40再分析资料以及降水观测资料，分析了印度夏季风对200 hPa上南亚高压的影响，以及南亚高压对中国夏季降水异常的作用。在年际时间尺度上，发现南亚高压具有显著的东西偏向特征，高压中心位于伊朗高原或者青藏高原上空。当印度季风偏强（弱）时，南亚高压位置偏西（东），中心位于伊朗（青藏）高原上空。南亚高压的东西偏向与中国夏季降水之间也存在密切关系。位置偏西（东）的南亚高压对应着江淮流域降水偏少（多），华南、华北地区降水偏多（少）。进一步提出了印度季风通过影响南亚高压进而对中国夏季降水产生影响的物理过程。当印度夏季风偏强（弱）、降水偏多（少）时，印度半岛北部地区凝结潜热释放增加（减少），为异常热（冷）源。异常热（冷）源在对流层高层，其西北和东北侧分别激发位势高度的正（负）异常和负（正）异常，表现为南亚高压位置偏西（东），中心位于伊朗（青藏）高原上空。此时，在对流层上层，青藏高原东部至中国东部上空为异常气旋（反气旋）。与该异常环流相对应的垂直运动异常影响中国夏季降水。本研究提出，南亚高压在印度夏季风影响东亚夏季风的过程中起了重要作用。（温敏）

4 古气候研究

4.1 末次间冰期以来北大西洋深层海温与青藏高原气温的千年尺度位相关系及其演变

采用代用资料研究了北大西洋深层海温和青藏高原气温自末次间冰期以来在千年尺度上的位相关系及其变化。对比分析和小波交叉谱分析表明，自末次间冰期以来二者同位相和反位相关系交替出现，同位相的持续时间相对较短，而反位相的持续时间较长，并且二者同位相和反位相关系的转换在间冰期比在冰期频繁，北大西洋深层海温与青藏高原气温的位相关系大体被北大西洋气温（格陵兰冰芯氧同位素）与青藏高原气温所验证。此外，北大西洋海表温度可能是北大西洋深层海温在千年尺度上影响青藏高原气温的一个重要因子（图3）。（肖栋）

4.2 20世纪后半叶中国石笋氧同位素对大气环流的记录

由于缺乏定量的校准，关于中国石笋氧同位素（ $\delta^{18}\text{O}_{\text{cs}}$ ）代表的意义争论激烈： $\delta^{18}\text{O}_{\text{cs}}$ 记录的是局部的还是大尺度的信号，是单一水汽源信息还是多水汽源信息？对所有的器测时段内 $\delta^{18}\text{O}_{\text{cs}}$ 趋势的统计分析结果显示，大部分 $\delta^{18}\text{O}_{\text{cs}}$ 在1960—1994年有线性增加趋势，表明 $\delta^{18}\text{O}_{\text{cs}}$ 记录了大尺度大气环流。定量计算了来自不同源区的水汽输送。用NCEP-NCAR再分析资料计算了1960—1994年孟加拉湾、南海、西太平洋夏季水汽输送强度比例。定义RSCS/BOB为南海与孟加拉湾水汽输送强度比例，RWNP/BOB为西太平洋和孟加拉湾水汽强度比例，RWNP/SCS为西太平洋和南海水汽输送强度比例。RWNP/BOB和RWNP/SCS呈现了显著的年代际增强，可能是因为1970年代末西太平洋副热带高压西伸导致从西太平洋来的水汽输送加强。进一步分析表明，赤道中东太平洋处于El Niño位相，印度洋、孟加拉湾和南海SST偏高；北太平洋中纬度SST偏低时，RWNP/BOB和RWNP/SCS偏高。1970年代以后赤道中东太平洋经常处于El Niño位相，与 $\delta^{18}\text{O}_{\text{cs}}$ 的趋势相符，说明 $\delta^{18}\text{O}_{\text{cs}}$ 记录了20世纪后半叶的大气环流。（南素兰）

5 极地气候研究

5.1 东南极冰盖气候地带性研究新发现

自1996年起，我国南极内陆考察开始布设降雪观测点，用于观测南极年降雪量的时空分布；安装

自动气象站,用于获取冰盖内陆气象信息;同时,在考察过程中对风成表面地貌形态也进行了统计。通过空间分析方法发现,东南极冰盖沿岸至内陆最高区域,共分为4个具有不同气候背景的气候带。这4个气候带大致以海拔2000 m、3000 m和3600 m为界。在分界点前后,不同地带的降雪时间变化具有相反的趋势。结合遥感和数值模拟手段发现,水汽来源的不同是造成该气候地带性的首要原因:海岸、内陆和冰穹区域具有明显不同的水汽来源,分别来自于近岸海洋、东南印度洋中高纬海洋和中低纬海洋。其次,不同天气条件下的沉积后过程,是造成内陆区域分为两个地带的重要原因。我们是国内外首个提出该地带性的团队,仍需更多的证据来证明。(丁明虎)

5.2 一种便携式大气水汽同位素连续监测装置

以往对氢氧稳定同位素的研究主要是针对液态水和固态水,其中一个主要原因是液态水和固态水的稳定性较强,易采集和保存。与这两个形态相比,气态氢氧稳定同位素比率的观测虽可以在不同季节和天气条件下进行,可提供更多的关于大气学、水文学和稳定同位素分馏过程等多方面的信息,但其样品的收集和测量甚为复杂。由于目前采样和分析技术的限制,对于大气水汽氢氧稳定同位素比率的研究,大都局限于粗空间和时间分辨率的条件。而对于海洋-大气边界层上的同位素分馏过程,也都集中于理论实验和物理过程模拟。因此,需要采用适当的装置和方法通过模拟野外自然移动条件下水汽稳定同位素比率梯度,实现水汽中 $\delta^{18}\text{O}$ 和 $\delta^2\text{H}$ 梯度和分馏过程的观测,从而实现在实时、实地、大范围、便携、低能耗等条件下大气水汽 $\delta^{18}\text{O}$ 和 $\delta^2\text{H}$ 同位素的测量与评价。本研究开发了一种可以快速、动态和准确测量野外自然条件下水汽中氢氧稳定同位素比率、梯度及其分馏过程的装置和方法。通过该装置和方法,可以客观评价并校正水汽 $\delta^{18}\text{O}$ 和 $\delta^2\text{H}$ 测量的精度,实现野外自然条件下大气水汽 $\delta^{18}\text{O}$ 和 $\delta^2\text{H}$ 的便携式观测并获取高质量数据。该发明专利于2014年12月得到授权,相应设备已经成功在我国南北极走航考察中应用,相关研究发表在*Journal of Environmental Sciences*、《冰川冻土》《地理科学进展》等杂志上(图4)。(丁明虎)

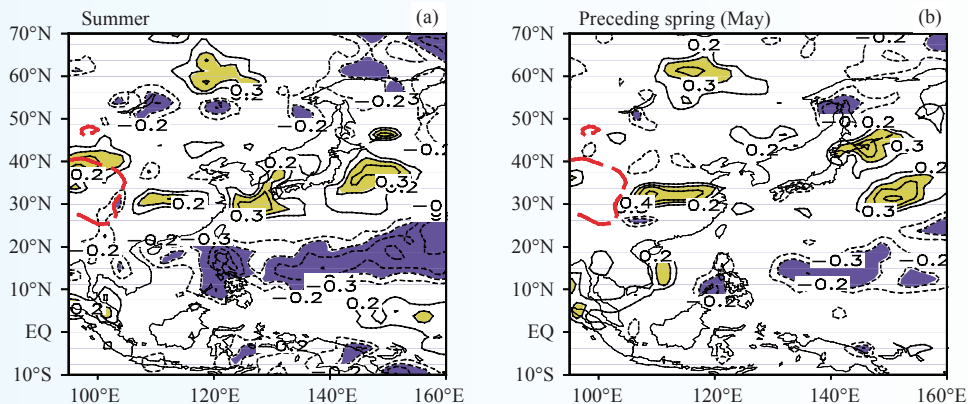


图1 夏季(a)和前期春季(b)(5月)青藏高原积雪面积异常与夏季降水的相关(阴影区超过90%统计置信度)

Fig. 1 Spatial distribution of correlation coefficients between the (a) summer and (b) preceding spring (May) snow cover area proportion (SCAP) index and summer precipitation for the period 1979–2006 (the shaded areas denote correlation significant at the 90% confidence level)

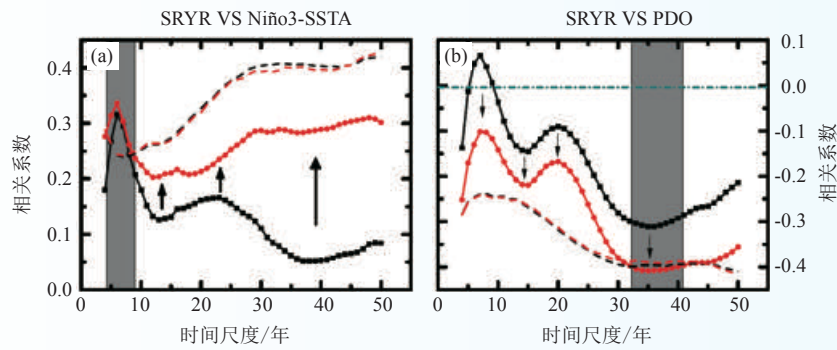


图2 DPCCA在实际气候问题研究中的应用(SRYR代表长江流域夏季降水, 红色点线为DPCCA结果, 虚线为0.05显著性边界。可以看到, Niño3海温对长江流域夏季降水的影响主要在4~7年的尺度, 而PDO的影响主要在35年的尺度)
Fig. 2 Triple relations among summer rainfall over Yangtze River (SRYR), Niño3-SSTA, and PDO index, on different time scales. Red curves are results from DPCCA, where effects of PDO (Niño3-SSTA) on SRYR are removed in a (b)

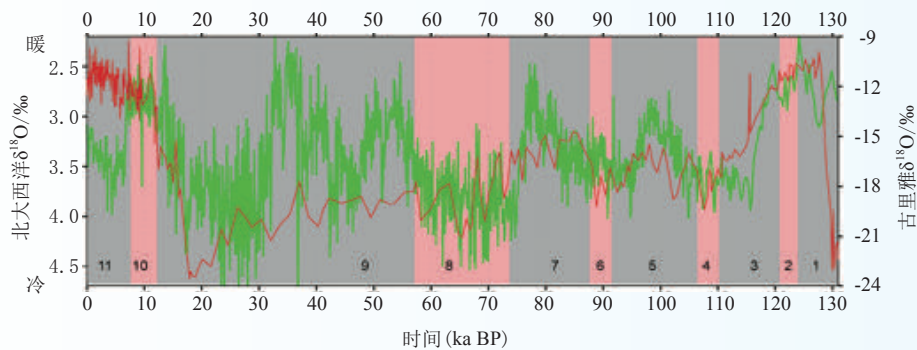


图3 末次间冰期以来北大西洋底栖有孔虫类氧同位素记录(红线)和青藏高原古里雅冰芯氧同位素记录(绿线)(按照二者位相关系的变化, 将过去131 ka 划分为11个时段, 分别用阴影和数字标记)
Fig. 3 Oxygen isotope ($\delta^{18}O$) records from the North Atlantic benthic foraminifera (red line) and from the ice core in Guliya Glacier (green line) since the Last Interglacion. Based on their phase relationship, the past 131 ka is divided into 11 epochs, which are indicated by the color shading and the serial numbers at the bottom of this figure

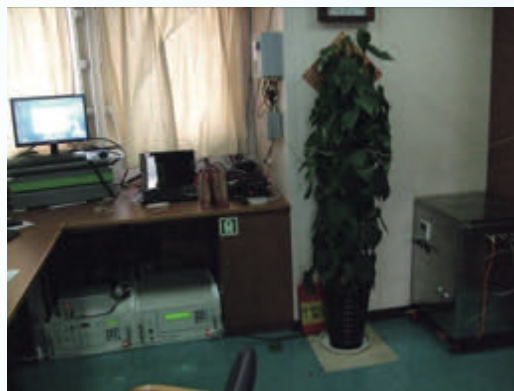


图4 大气水汽同位素实时高精度观测系统
Fig. 4 A real time-high precision instrument for monitoring atmospheric water vapor isotopes

Progress in Climate System and Climate Change Research

1 Theory and methodology of climate prediction

1.1 The summer snow cover anomaly over the Tibetan Plateau and its association with simultaneous precipitation over the Meiyu-Baiu region

The satellite-derived Equal-Area Scalable Earth grid (EASE-grid) dataset shows that snow still exists in summer in the western part and along the southern flank of the Tibetan Plateau (TP). The summer snow anomaly over the TP can directly modulate the land surface heating and, consequently, vertical motion over the western TP, and concurrently induce anomalous vertical motion over the North Indian Ocean via a meridional vertical circulation. Through a zonal vertical circulation over the tropics and a Kelvin wave-type response, anomalous vertical motion over the North Indian Ocean may result in the anomaly of the western North Pacific subtropical high and modulate the convective activity in the western Pacific warm pool, which stimulates the East Asia-Pacific (EAP) pattern and eventually affects summer precipitation over the Meiyu-Baiu (MB) region (Fig. 1a).

The snow anomaly over the TP maintains from preceding spring (May) to summer, and therefore exerts an important effect on summer rainfall over the MB region (Fig. 1b). The persistence of snow anomaly over the western TP can partly explain the season-delayed effect of TP snow on summer rainfall over East Asia, which differs from the contribution of the soil moisture appearing over the eastern TP. Therefore, the western TP snow anomaly in preceding spring could be regarded as an important supplementary factor in the forecasting of summer precipitation over East Asia (Fig. 1). (Liu Ge)

1.2 Research progress in the climate prediction: Novel methods

In 2014, we mainly focused on the research on climate prediction. By using fractal integral techniques, we have decomposed a given climatic time series into two parts: (i) climate memory signals accumulated from historical information, and (ii) weather scale excitations. When making predictions (simulations) of climate states at a given time point, we can first calculate the climate memory signals, then try to predict (simulate) the weather scale excitations.

Up to now, we have established a Fractal Integral Stochastic Model, and proposed a method which can extract the climate memory signals quantitatively and successfully. We take the North Hemisphere temperature anomalies (black curve in a) and PDO index (black curve in c) as an example, and extract their memory signals (red curves). The memory signals account for a large proportion of the total variance, which indicates that extracting climate memory signals is important and can improve our ability in climate prediction.

As for the second part, the weather scale excitations, we plan to use multi-predictors for our prediction. By determining the typical time scales which different predictors may have significant influence on, we aim to establish a hierarchical prediction model. Now we have proposed a new method, detrended partial-cross-correlation analysis (DPCCA), which can be used to diagnose quantitatively the typical time scales for different predictors. In Fig. 2, we analyzed the triple relations among the summer rainfall over Yangtze River (SRYR), the preceding winter time Niño3-SSTA, and the preceding winter time PDO index. As we can see, this method can provide us with the correlation information on different time scales, which is useful for the further development of a hierarchical model (Fig. 2). (Yuan Naiming)

1.3 Individual variations of winter surface air temperature over Northwest and Northeast China and their respective precursory signals

Based on the monthly mean surface air temperature (SAT) from 71 stations in northern China, the NCEP/NCAR and NOAA-CIRES 20th century reanalysis data, the dominant modes of winter SAT over northern China were explored. The results show that, apart from the first mode with a unanimously colder (warmer) northern China as a whole, the second mode, which is characterized by a dipole structure with a colder (warmer) Northwest China (NWC) and warmer (colder) Northeast China (NEC), also accounts for a fairly large proportion of total variance. The two components constituting the second mode, the individual variations of winter SAT over Northwest and Northeast China and their respective precursory signals were further investigated. It is found that the autumn SAT anomalies are intimately linked to persistent snow cover anomalies over Eurasia, showing the delayed effects on winter climate over northern China. Specifically, the preceding autumn SAT anomalies over the Lake Baikal (LB; 50°–60°N, 85°–120°E) and Mongolian Plateau (MP; 42°–52°N, 80°–120°E) regions play an important role in adjusting the variations of winter SAT over NWC and NEC, respectively. The preceding autumn SAT anomaly over the MP region may exert an influence on winter SAT over Northeast China through modulating the strength and location of East Asian major trough. The preceding autumn SAT over the LB region may modulate winter westerlies at the middle and high latitudes of Asia and accordingly affects the invasion of cold air and associated winter SAT over Northwest China. (Xin Yufei)

2 Development of a climate system model

Via years of work since 2009, the Institute of Climate System has successfully developed a climate system model. By several years of continuous model development, significant improvement was achieved in terms of removal of model flux correction, reduction of climate drift, and ENSO phase locking as well as precipitation bias. Both the T42 and T63 versions have steadily integrated over 1000 years without flux correction, displaying remarkable performance in simulating the global climatological mean state, seasonal cycle as well as interannual variability, hence a potential application to climate prediction in China.

In 2014, encouraging progress has been achieved in the following areas:

(1) We successfully conducted the two-way coupling between CoLM land model and ECHAM5 model. The version of the coupled CoLM land model showed notable improvement in reducing ground temperature bias for most areas of the globe, especially for the cold bias over the northern Asian-European continent.

(2) The horizontal resolutions of the atmosphere model and ocean model were increased to T255 (about 50 km) and 0.5 degree, respectively. The horizontal resolution of coupled model was also increased to T106 for the atmospheric model and 0.5 degree for the ocean model. With the model resolution increased, the simulation of precipitation over the East-Asian region was significantly improved.

(3) Modification of ECHAM5 dynamical core. The “Two-Step Shape-Preserving Advection Scheme” (TSPAS) was introduced for model vapor transportation. The result shows significant improvement in simulation of East-Asian precipitation, especially precipitation around the Tibetan Plateau. (Rong Xinyao)

3 Variability and mechanism of the East Asian monsoon

3.1 Effect of the atmospheric heat source on the development and eastward movement of the Tibetan Plateau vortices

In boreal summer, the low-level cyclonic vortices forming over the Tibetan Plateau (hereinafter the

plateau vortices) are the major mesoscale rain-producing systems over the Tibetan Plateau. Most of the vortices originate over the central-western plateau, and decay over the eastern plateau, especially over the sloping terrain at the eastern edge of the Tibetan Plateau. Some of them can maintain a long time and move eastward out of the plateau (Wang et al., 2009). The vortices moving off the plateau often trigger heavy rainfall to the east of the Tibetan Plateau, and even give rise to disastrous weather events over eastern China.

Based on the final analyses data (FNL) of the Global Forecasting System of the National Centers for Environment Prediction (NCEP) and the radiosonde data over the Tibetan Plateau, evolutions of two types of the Tibetan Plateau vortices, moving-off the plateau (Type A) and dying-out on the plateau (Type B), are investigated respectively. Compared to Type B vortices, the large-scale circulations associated with Type A vortices show a stronger ridge to the north of the plateau and a deeper trough near the Bay of Bengal at 500 hPa, and the southwesterly flow from the trough and the northwesterly flow from the ridge converge more intensely to the east of Type A vortices. Meanwhile, at 200 hPa the divergence on the right-hand side of the upper westerly jet is just over the vortices. The convergence at 500 hPa and the divergence at 200 hPa provide favorable conditions for the development and eastward motion of the vortices as well as the rainfall to the east of the vortices. The condensation latent heat related to the rainfall has a close relationship with the eastward movement of the vortices. The diagnoses of the potential vorticity (PV) budgets and spatial features of the atmospheric heat source reveal that in the developing stages of the two types of vortices, the vertical distribution of the atmospheric heat source determines both their intensity and moving direction. In the decaying stage, the maintenance and eastward movement for Type A vortices mainly depend on the convergence of the strong northwesterly and southwesterly to the east of the vortices. For Type B vortices, the vertical PV flux divergence caused by the ascending motion around the vortices reduces the intensity of the vortices and is unfavorable for their eastward motion. (Li Lun)

3.2 The initiation and development mechanisms of central Pacific El Niños

The initiation and development mechanisms of four major central Pacific (CP) El Niño events in 1994, 2002, 2006 and 2009 were investigated by analyzing oceanic and atmospheric reanalysis data. A mixed-layer heat budget analysis was conducted and the result shows that the initiation mechanism of the 1994 CP El Niño is very different from other CP El Niños in 2000s in spite that the development mechanisms are similar among these events. The initial sea surface temperature (SST) warming of the 1994 El Niño was caused by enhanced solar radiation, which was related to atmospheric meridional overturning circulation in association with the positive SST anomaly forced in the subtropical Pacific. The subtropical SST anomalies also induced anticyclonic surface wind stress curl anomalies, which caused the formation of subsurface warmer water in the off-equatorial regions. The off-equatorial subsurface warmer water was further transported equatorward by the mean subsurface ocean currents, leading to the subsurface warming in the central equatorial Pacific. The deepened thermocline anomaly at the equator further promoted a positive advective and thermocline feedback so that the SST anomaly grew. During the initiation phase of the 2000s El Niños, ocean dynamics played a dominant role while the effect of surface heat flux anomalies was minor. Pre-existing subsurface warmer water appeared in the equatorial region during its initiation phases. Such subsurface anomalies can cause the SST warming in the central Pacific through induced anomalous eastward zonal currents that transport high mean SST eastward. This positive zonal advective feedback, along with a positive thermocline feedback, continued to warm the local SST throughout the development phase of the 2000s El Niño events. (Su Jingzhi)

3.3 Impact of Indian summer monsoon on the South Asian high and its influence on summer rainfall over China

By using the monthly ERA-40 reanalysis data and observed rainfall data, we investigated the effect of the

Indian summer monsoon (ISM) on the South Asian high (SAH) at 200 hPa, and the role played by the SAH in summer rainfall variation over China. It is found that in the interannual timescale the east-west shift is a prominent feature of the SAH, with its center being either over the Iranian Plateau or over the Tibetan Plateau. When the ISM is stronger (weaker) than normal, the SAH shifts westward (eastward) to the Iranian Plateau (Tibetan Plateau). The east-west position of SAH has close relations to the summer rainfall over China. A westward (eastward) location of SAH corresponds to less (more) rainfall in the Yangtze-Huai River Valleys and more (less) rainfall in North China and South China. A possible physical process that the ISM affects the summer rainfall over China via the SAH is proposed. A stronger (weaker) ISM associated with more (less) rainfall over India corresponds to more (less) condensation heat release and anomalous heating (cooling) in the upper troposphere over the northern Indian peninsula. The anomalous heating (cooling) stimulates positive (negative) height anomalies to its northwest and negative (positive) height anomalies to its northeast in the upper troposphere, causing a westward (eastward) shift of the SAH with its center being over the Iranian Plateau (Tibetan Plateau). As a result, an anomalous cyclone (anticyclone) is formed over the eastern Tibetan Plateau and eastern China in the upper troposphere. The anomalous vertical motions in association with the circulation anomalies are responsible for the rainfall anomalies over China. Our present study reveals that the SAH may play an important role in the effect of ISM on the East Asian summer monsoon. (Wen Min)

4 Palaeo-Climate

4.1 Millennial-scale phase relationship between North Atlantic deep-level temperature and Qinghai-Tibet Plateau temperature and its evolution since the Last Interglaciatio

This study employed proxy data to investigate the phase relationship between the North Atlantic deep-level temperature and the Qinghai-Tibet Plateau (TP) surface air temperature (TP temperature) and its evolution at the millennial scale since the Last Interglaciatio. The results indicate the alternation of in-phase and anti-phase relationships since the Last Interglaciatio, with the in-phase relationships showing a shorter duration than the anti-phase relationships. Alternations between the in-phase and anti-phase relationships occurred more frequently during the Last Interglaciatio than during the Last Glaciatio. The phase relationship between the North Atlantic deep-level temperature and the TP temperature was broadly illustrated by that between the North Atlantic temperature (based on oxygen isotope data from the Greenland ice core) and TP temperature (Fig. 3). Furthermore, the North Atlantic deep-level temperature and the TP temperature may be connected through the North Atlantic sea surface temperature. (Xiao Dong)

4.2 Evaluation of the ability of the Chinese stalagmite $\delta^{18}\text{O}$ to record the variation in atmospheric circulation during the second half of the 20th century

The Chinese stalagmite $\delta^{18}\text{O}$ ($\delta^{18}\text{Ocs}$) has provoked debate worldwide over the past few years due to its lack of quantitative calibration, leading us to questions of whether $\delta^{18}\text{Ocs}$ records a local or large-scale signal and whether $\delta^{18}\text{Ocs}$ records the signal of a single remote water vapor source or multiple water vapor sources. In this study, we observe all of the $\delta^{18}\text{Ocs}$ trends within the instrumental period to verify whether they possess a common trend, which could be used as a basis to determine whether the trends reflect the large-scale signal together or whether each trend reflects the local signal. The results show that most of the $\delta^{18}\text{Ocs}$ experienced a linear increase from 1960 to 1994, which may indicate that the $\delta^{18}\text{Ocs}$ could record a trend occurring in large-scale atmospheric circulations. We then quantitatively describe the proportion of water vapor transport (WVT) from different source regions. Using the NCEP/NCAR reanalysis data from 1960 to 1994, the ratios of the intensities of three WVTs from the Bay of Bengal, the South China Sea, and the western North Pacific

during the summer are calculated. We define RSCS/BOB as the ratio of the WVT intensities from the South China Sea to those from the Bay of Bengal, RWNP/BOB as the ratio of the WVT intensities from the western North Pacific to those from the Bay of Bengal, and RWNP/SCS as the ratio of the WVT intensities from the western North Pacific to those from the South China Sea. The significant decadal increase occurs in the time series of RWNP/BOB and RWNP/SCS, most likely resulting from the strengthened WVT from the western North Pacific in the late 1970s due to the western Pacific subtropical high that extended westward. A further analysis indicates that when the equatorial central and eastern Pacific is in the El Niño phase, the sea surface temperature (SST) in the tropical Indian Ocean, the Bay of Bengal, and the South China Sea is high, and the SST at the middle latitudes in the North Pacific is low, then the RWNP/BOB and RWNP/SCS values tend to be high. Since the late 1970s, the equatorial central and eastern Pacific has often been in the El Niño phase. Therefore, we confirm that the $\delta^{18}\text{Ocs}$ indeed records the variation in atmospheric circulation during the second half of the 20th century. (Nan Sulan)

5 Polar Climate

5.1 New finding on climatic zonation in East Antarctica

Since 1996, the Chinese National Antarctic Research Expedition has started to set up the stakes to monitor snowfall, deploy the Automatic Weather Stations to monitor the surface meteorology and measure the sastrugi to identify the wind erosion. Based on these data, we explored the climatic zonation by a spatial analysis and found that from the coast to the summit of East Antarctica, there are four sections with different surface mass balance patterns. These sections are divided into heights of ~2000 m, ~3000 m and 3600 m.

Combined with studies by remote sensing and simulation, we found the coast, inland and dome areas have different moisture sources: the precipitation at coast mainly comes from offshore, the precipitation at inland comes from the southeast Indian Ocean and the dome area comes from low-mid ocean surfaces. Secondly, the post-depositional processes by wind, could determine the loss of surface snow; this is the reason that the inland area is divided into two sections with different surface mass balance tendencies. This finding has never been reported before this paper, and still needs more evidence. (Ding Minghu)

5.2 A novel instrument in monitoring atmospheric water vapor isotopes

Previously, the studies on water isotopes were mainly carried out on liquid or solid water. One of the most important reasons is that liquid or solid water is easily collected and transported. Compared with them, vapor isotopes exist in atmosphere and could be measured in all kinds of weather. It could also provide more information on global earth surface processes and hydrological cycles. During the past tens of years, the studies on atmospheric water vapor isotopes were restricted in coarse spatial and temporal resolutions for technical reasons. Besides, the isotopic fractionation processes above sea surface have been only carried out with theoretical and physical simulation experiments. So, it is necessary to develop a system, method or instrument to monitor the isotopic ratio and vertical profile. Based on the laser spectrum, we have invented an instrument to achieve a real time-mobile-high precision measurement of atmospheric water vapor isotopes (Fig. 4).

This invention was authorized with a patent in December 2014 and the instrument has been successfully applied in the Chinese National Antarctic/Arctic Research Expedition. The papers related to the instrument have been published in *Journal of Environmental Sciences*, *Journal of Glaciology and Geocryology*, *Progress in Geography*, etc. (Ding Minghu)

大气探测与雷电防护

Atmospheric Sounding and Lightning Protection

大气探测与雷电研究进展

2014年大气探测研究所以理论研究为基础,紧密联系实际应用,围绕野外观测试验和理论研究的重点方向,开展了大量卓有成效的观测和研究工作,并取得了丰硕的成果。2014年共发表期刊论文13篇,其中SCI论文4篇;申请国内发明专利3项、国际发明专利1项、实用新型专利2项;获得软件著作权授权1项;1人获得全国优秀青年气象科技工作者称号。具体成果主要体现在以下几个方面。

1 野外观测试验和闪电物理过程研究

1.1 雷电野外观测试验

2014年大气探测研究所在广州、重庆以及拉萨分别开展了雷电外场试验。5月6日到8月28日在广州从化的广州野外雷电试验基地开展的“广东闪电综合观测试验(GCOELD)”是自2006年以来的第9年度外场试验。本年度的触发闪电次数达到历年最高值,实现了共计15次包括多回击在内的人工触发闪电,总回击次数达到了45次,并获得了上述触发闪电的电磁场、光辐射、高速摄像、电流的直接测量资料。在自然闪电观测方面进一步发展了多频段同步信号的自动化观测技术,完善了低频电磁场、光辐射、宽带辐射场和高速摄像的多频段(低频-高频-甚高频-光信号)的同步综合观测平台,改善了触发记录方式,实现了自动化测量,获得了几十例闪电信号多频段观测数据,进一步深化了对闪电放电过程的研究。同时,新发展和研制的高灵敏度闪电电场变化测量系统已经架设并稳定运行,获取了大量的闪电放电的连续记录数据。在高建筑物闪电观测方面,增设了2套大量程的快慢电场变化测量仪以及2套全视野闪电通道成像仪,全年共获取综合观测个例79个,积累了更多的高建筑物自然闪电同步观测资料(图1~2)。

雷电防护技术测试获得了高压架空线在近距离闪电回击的电磁环境中的感应情况,检验了架空线的电磁兼容性能,研究了真实雷电环境下电磁脉冲在架空线的耦合机理,成功获得了数十次的架空线感应电压特征,为架空线雷电防护方案的优化提供了重要的基础数据。

重庆野外试验初步建成由9个子站和1个闪电数据处理中心站构成的地基高精度3D闪电定位系统区域示范网络,并完成基于时差定位技术的高精度闪电3D定位算法和闪电类型识别软件。拉萨外场试验主要针对“布达拉宫雷电灾害防御基础研究”项目的任务,按照计划完成了雷电光学图像和电磁信号观测设备的架设。(张阳,吕伟涛)

1.2 雷电先导3D发展特征的观测和分析

闪电通道2D图像不能反映闪电通道的真实分布情况,难以满足准确分析闪电通道3D发展特征和闪电先导相互作用的需求。本研究建立了一种利用双站摄像资料重建闪电3D通道的方法,从2幅在不同位置拍摄到的闪电2D图像上分别获取闪电通道的坐标序列,利用空间立体几何原理,寻找2组序列中相互匹配的坐标,再由匹配的坐标序列重建出最终的闪电3D通道。

利用建立的闪电通道3D重建方法,对2012年在广州观测到的6次自然负极性闪电连接过程中上行连接先导(UCL)的通道进行了3D重建,并对比分析了利用单站高速摄像资料和双站光学观测3D重建资料得到的(UCL)的2D和3D发展特征。主要结论如下:重建得到的6个UCL通道3D长度的范围为180~818 m,平均值为426 m;计算得到了38个3D发展速率,其变化范围为 $(0.8 \sim 14.3) \times 10^5$ m/s,平均值为 4.7×10^5 m/s,其中4个(11%)处于 10^6 m/s量级;对应的2D长度和发展速率的变化范

围分别为 147 ~ 610 m 和 $(0.3 \sim 10.6) \times 10^5$ m/s; 平均来看, UCL 的 3D 发展速率为 2D 的 1.3 倍; UCL 的发展速率随时间呈现逐渐增加的趋势, 4 个 10^6 m/s 量级的 3D 速率都出现在回击前的 0.2 ms 内; 对于 3D 长度短于 300 m 的 UCL, 77% (20/26) 的 3D 速率小于 5×10^5 m/s, 而对于 3D 长度超过 300 m 或者头部高度超过 650 m 的 UCL, 其 3D 速率均高于 5×10^5 m/s (图 3)。(吕伟涛, 马颖)

1.3 人工触发闪电连续电流过程与 M 分量特征

在广州野外雷电试验基地, 对 2008 年和 2011 年夏季人工触发闪电回击之后的 14 个连续电流过程和 43 个 M 分量的通道底部电流、电场变化和通道亮度进行了同步测量和分析。结果表明: M 分量的电流、快慢电场变化和亮度变化波形均近似对称; 触发闪电连续电流过程的持续时间、转移电荷量、电流平均值的几何平均值分别为 22 ms, 6.0 C 和 273 A; M 分量的幅度、转移电荷量、半峰值宽度、上升时间、持续时间的几何平均值分别为 409 A, 205 mC, 520 μ s, 305 μ s 和 1.6 ms; 连续电流持续时间与 M 分量的个数、相邻 M 分量之间的时间间隔均存在显著的正相关关系 (图 4)。(郑栋, 张阳)

1.4 闪电不规则脉冲簇事件的发生规律

分析了 2012 年广州地区 6 次雷暴过程的负地闪中不规则脉冲簇 (CPT) 放电事件的发生规律。结果表明, CPT 能够发生在首次回击之前、各个回击间以及最后一次回击之后, 是负地闪放电过程中普遍存在的一种放电现象。在 323 次负地闪中有 243 次出现了 CPT 放电事件, 比例达到了 75.2%, 并且能够发生在负地闪的首次回击之前、回击之间以及最后一次回击之后, 其中有 66.7% 的继后回击之前和 11.5% 的最后一次回击之后发生了 CPT。研究还发现, CPT 在继后回击之前有 4 种分布类型, 即单独出现一次 CPT-c (与继后回击相连的 CPT)、单独出现一次 CPT-i (与继后回击有一定时间间隔的 CPT)、同时出现 CPT-c 和 CPT-i 以及同时出现多次 CPT-i。其中, 单独出现一次 CPT-c 类型最为多见, 39.4% 的继后回击之前为此类型, 而在第 1 次和第 2 次继后回击之前更容易出现多次 CPT 的现象, 分别占到对应次序回击总数的 9.4% 和 7.7%。而随着继后回击次序的增加, 其之前发生 CPT 的概率呈减小的趋势, 并且除了第 1 次和第 2 次继后回击以外, 其他继后回击之前 CPT-c 的出现频次大于 CPT-i。另外, CPT-i 和最后一次回击之后的 CPT 均叠加在 K 变化上, 部分回击间的 CPT 也能够发生在 J 过程中 (图 5)。(张阳)

1.5 闪电不规则先导的多尺度熵分析

针对不规则脉冲簇难以判别问题, 将多尺度熵应用于不规则先导分析中, 给出了一种多尺度熵计算方法, 并通过实例说明多尺度熵在表征复杂信号方面的能力, 来区分不规则先导与直窜先导及梯级先导的不同。探讨了闪电信号不规则脉冲分析应用中多尺度熵关键参量的选择方法。在此基础上, 将不规则先导与直窜先导及梯级先导闪电信号的多尺度熵进行比较。统计分析表明: 不规则先导和直窜先导熵值随尺度先增加后趋于平稳, 但熵值有很大差异; 梯级先导熵值随尺度变化不明显, 整体呈增长趋势, 与不规则先导的熵值在大于 3 的尺度上也有所差异, 因此当尺度大于 3 时可将熵值大于 1.5 的先导归类为不规则先导, 熵值小于 1.5 的先导归类为梯级先导或直窜先导。不规则先导的特征熵平均值为 2 ~ 2.1, 最大值范围为 2.6 ~ 2.8, 最小值范围为 1.5 ~ 1.51 (图 6)。(张阳)

1.6 闪电电场变化信号测量系统及方法

为了解决闪电电场近距离测量的饱和问题并兼顾其测量的动态范围, 发明了一种闪电电场变化信号测量系统。该系统包括探测天线、电场快变化接收机、信号处理模块: 电场快变化接收机分别连接探测天线和信号处理模块; 探测天线用于将感应到的闪电产生的电场变化信号传输至电场快变化接收机; 电场快变化接收机用于处理电场变化信号, 以得到闪电电场快变化信号, 并将闪电电场快变化信号传输至信号处理模块; 信号处理模块用于采集并处理闪电电场快变化信号, 以得到闪电电场慢变化信号。同时发明了一种与上述测量系统相对应的闪电电场变化信号测量方法。所发明的闪电电场变化测量系统和方法, 可通过电场快变化接收机获取闪电电场快变化信号, 并对闪电电场快变化信号处理得到闪电电场慢变化信号, 实现了对闪电电场快、慢变化信号的集成化测量, 有效解决了近距离闪电

信号过强导致的闪电电场慢变化探测输出饱和的问题(图7)。(张阳, 孟青)

2 雷暴中闪电活动特征及其与天气现象关系研究

2.1 基于大气层结和雷暴演变的闪电和降水关系

选取2006—2008年发生在北京及其周边地区的28次雷暴过程,基于大气不稳定度参数和雷达参量对雷暴过程进行分类,分析了不同分类条件下的总闪电活动(SAFIR3000 3D闪电定位系统观测)和对流降水(雷达反演)的关系。结果表明,总闪对应降水量的平均值为 1.92×10^7 kg/fl。依据对流有效位能和抬升指数对雷暴进行分类的分析表明,较强的不稳定状态对应了较小的总闪对应降水量,同时总闪频次与对流降水量的相关性更好。基于雷达特征参数的分类分析表明,总闪对应降水量在对流运动较弱情况下最小,其次是对流运动较强的情况下,而对流运动适中时最大。(郑栋)

2.2 上海及周边地区地闪活动特征及海陆差异

利用LS8000闪电定位系统2009—2011年的地闪观测资料对上海及周边地区($120^\circ \sim 122.5^\circ$ E, $30^\circ \sim 32^\circ$ N)的地闪活动特征进行了研究。结果表明,分析区域内正地闪的比例约占8.5%,大电流地闪(电流绝对值大于50 kA)的比例约为5.6%。地闪活动主要集中在6—9月,峰值出现在8月;日间12:00—19:00闪电活动最为活跃,峰值出现在14:00,凌晨闪电活动最弱。从日变化上来说,正地闪和大电流地闪比例在地闪活动较强时段低于地闪活动较弱时段;在月分布上,在地闪活动最强的夏季,正地闪比例普遍在10%以下,在地闪活动较弱的春、秋、冬季,正地闪比例普遍在10%以上。以 31° N为界,分析区域北部地闪密度基本在 $6 \sim 12$ 次/($\text{km}^2 \cdot \text{a}$),南部基本在 $2.4 \sim 4.8$ 次/($\text{km}^2 \cdot \text{a}$)。同时陆地上的地闪密度要显著高于湖泊和海洋上的地闪密度,而海洋上的正地闪比例和大电流地闪比例要显著高于陆地。闪电空间分布的时间变化说明,下午地闪活动主要出现在陆地,而凌晨地闪主要出现在水体附近,其他时段则表现出过渡特征,这与下垫面的加热作用紧密相关。(郑栋)

3 利用 WRF-Electric 模式模拟热带气旋电荷结构的演变特征

以WRF-ARW模式为基础,在Milbrandt和Morrison2个双参数微物理方案中分别耦合了感应和非感应的起电机理,同时引入了放电参数化方案,从而构建起一个完整的中尺度起电放电模式WRF-Electric。模式不仅能够模拟风暴内电荷结构的演变,同时还具有区域闪电活动分布的预报能力。在非感应起电机理方面,不仅引入了基于液态水含量的TGZ机制和GZ机制,还将基于霰粒子结淞率的SP98机制和RR机制引入到了数值模式。图8所示为中尺度起电放电模式的架构。利用建立的中尺度起电放电模式,对于一个理想的热带气旋起电的演变进行了模拟。研究热带气旋的起电及电荷结构,有利于更进一步地理解热带气旋中的闪电活动。本研究从数值模拟的角度尝试描述热带气旋电荷结构的演变特征,已有的大部分观测事实和模拟结果从不同方面支持了本研究的结论。

模拟结果表明(图9),眼壁区对流一般表现出负的偶极性结构,有一个负电荷区在正电荷区之上。在加强阶段,眼壁区伴随的强烈上升气流的极端强对流呈现正常的3极性电荷结构,有一个主负电荷区夹在2个正电荷区之间。外螺旋雨带对流的电荷结构在不同阶段均呈现正常的偶极性电荷结构。进一步的分析表明,不同的电荷结构主要是由上升气流和粒子分布的差异造成的。在眼壁区对流的上升气流一般较弱,不同粒子的混合区域主要分布在较低的层次,导致起电过程主要发生在霰粒子的正起电区。在加强阶段,眼壁区爆发的强对流具有强的垂直上升气流,起电在霰粒子的正、负起电区同时进行。而在外螺旋雨带对流中,霰粒子和冰晶粒子的主要共存区在云的高层,起电过程也主要发生在霰粒子的负起电区,从而形成正常的偶极性电荷结构。据此,构建了热带气旋电荷结构演变的概念模型(图8~9)。(王飞,徐良韬)

4 雷电业务工作进展

4.1 雷电临近预警系统的推广培训

针对雷电业务应用系统的需求，2014年9月16—19日，按照“2013年气象监测与灾害预警工程”项目实施方案的指导精神，中国气象科学研究院大气探测所承担的第2期全国“雷电临近预警系统培训班”在中国气象局气象干部培训学院安徽分院举办，来自全国30个省（市、自治区）气象台、防雷中心以及民航华北空管局气象中心的技术人员共65名学员参加了本次培训班。

大气探测所在第1期培训班的基础上，根据培训后的反馈精心调整授课内容，更新修订了教材。培训内容涉及了雷电物理、灾害天气、雷电探测、雷电预警预报、防雷工程等多方面知识，受到了学员的好评，进一步推动了现有科研成果的业务转化和应用。（姚雯，孟青，张文娟）

4.2 雷电临近预警系统推广应用

2014年3月，雷电临近预警系统在广东省防雷中心本地化调试后，于2014年4月20日投入业务试验运行。系统运行期间，已成功对广东省多次雷暴过程提前作出了准确的雷电预警，系统POD、FAR以及TS评分较好。目前，广东省防雷中心已将雷电临近预警系统的业务产品应用于广州市超高建筑物、危化品场所等多个重点单位的雷电临近预警服务，为重点单位合理安排经营时间、规避雷击风险以及雷电应急安全生产工作提供了重要的决策参考。（姚雯，孟青）



图1 人工引雷试验场（左）和一次成功触发闪电（右）

Fig. 1 Field for artificially triggered lightning (left) and a successfully triggered lightning (right)

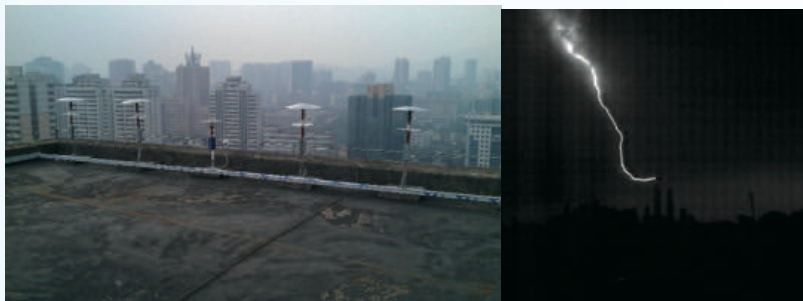


图2 新架设的观测设备（左）和一次高建筑闪电（右）

Fig. 2 A building observation system (left) and a high-building lightning (right)

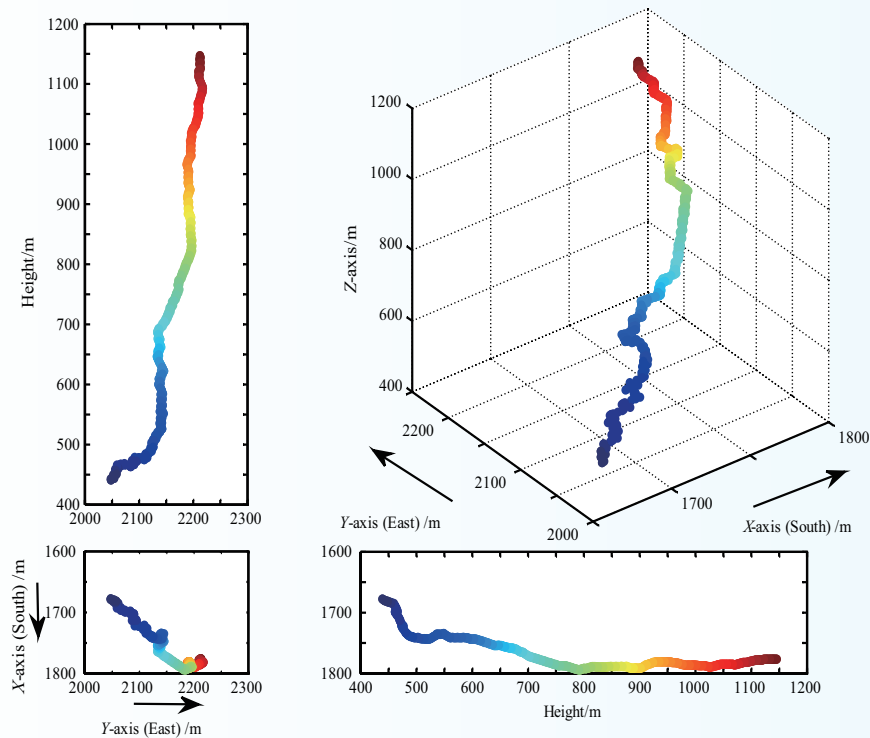


图3 广州试验观测到的一次闪电过程的上行连接先导的3D通道重建结果（右上为3D通道，左上、左下和右下分别为3D通道在Y-Z平面、X-Y平面和X-Z平面上的投影，颜色指示高度的变化）

Fig. 3 3D reconstruction results of the upward connecting leader (UCL) for a lightning flash observed in Guangzhou. It contains the 3D reconstruction channel of the UCL (top right), the projection of the 3D reconstruction channel in the Y-Z plane (top left), the X-Y plane (bottom left) and the X-Z plane (bottom right). The colors indicate height

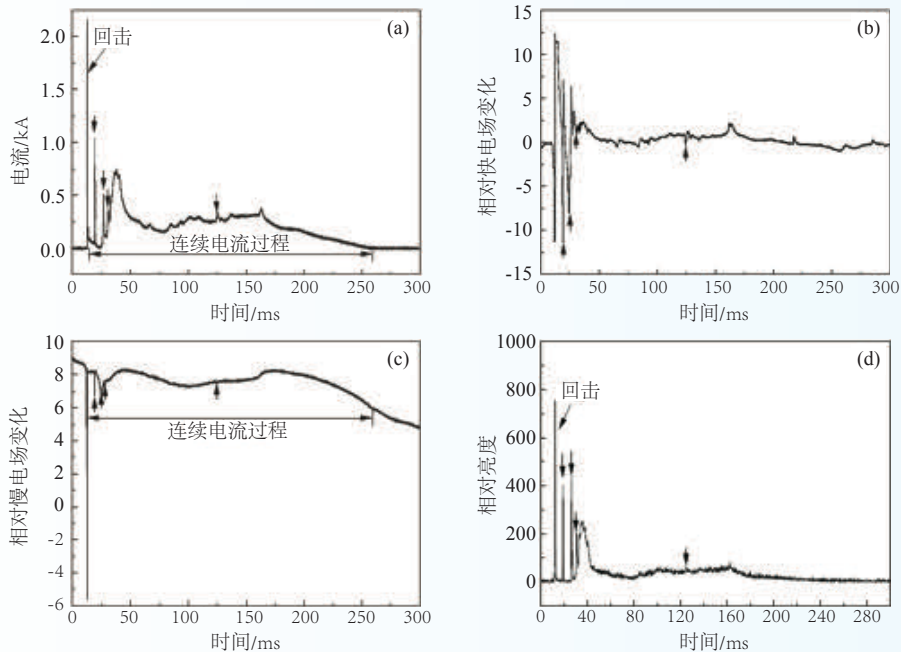


图4 触发闪电连续电流过程观测波形：(a) 电流波形；(b) 快电场变化波形；(c) 慢电场变化波形；(d) 通道亮度变化波形

Fig. 4 Observed waves of continuous current of triggered lightning: (a) current wave; (b) fast electric field waveform; (c) slow electric field waveform; (d) channel luminosity variation waveform

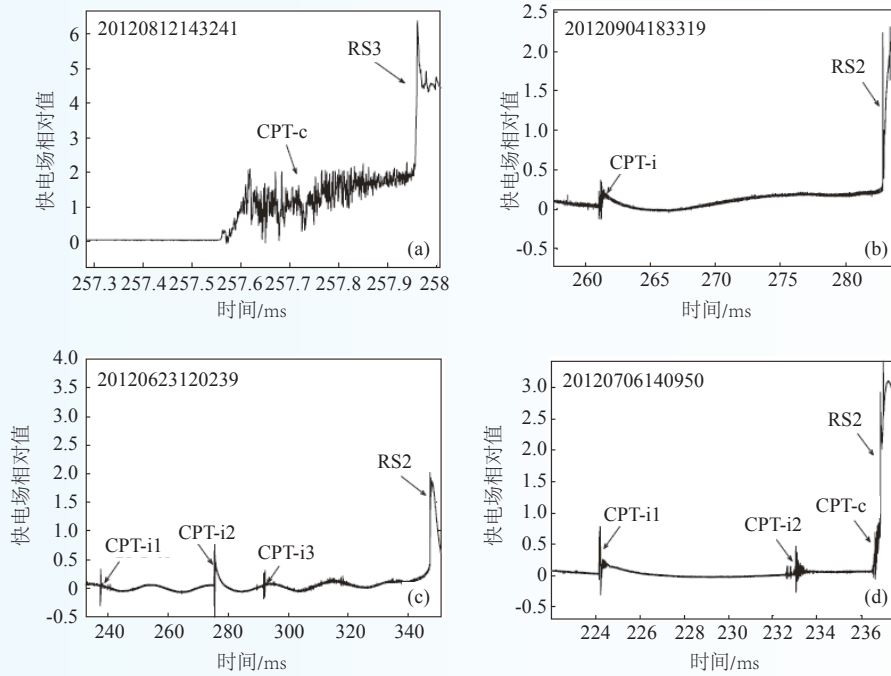


图5 不规则脉冲簇在放电波形中的位置分布
Fig. 5 Distribution of chaotic pulses in the discharge waveform

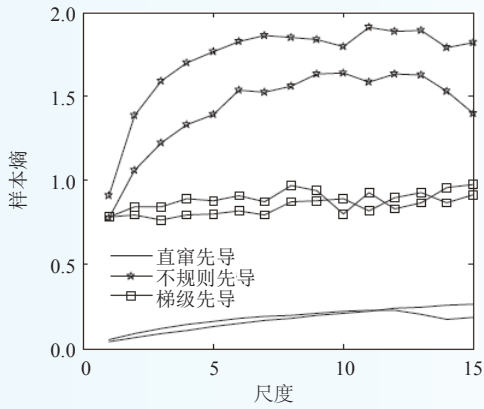


图6 不同先导的多尺度熵特征
Fig. 6 Multi-scale entropy features of different leaders

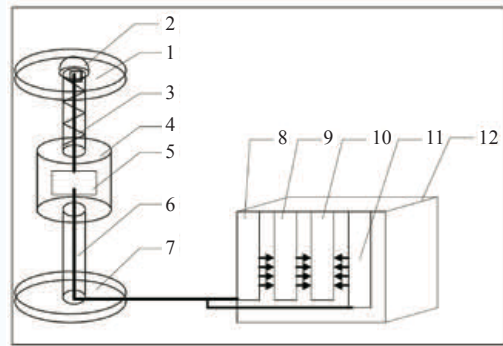


图7 闪电电场变化集成测量系统示意
Fig. 7 Integrated measurement system of lightning E-change

WRF-Elec

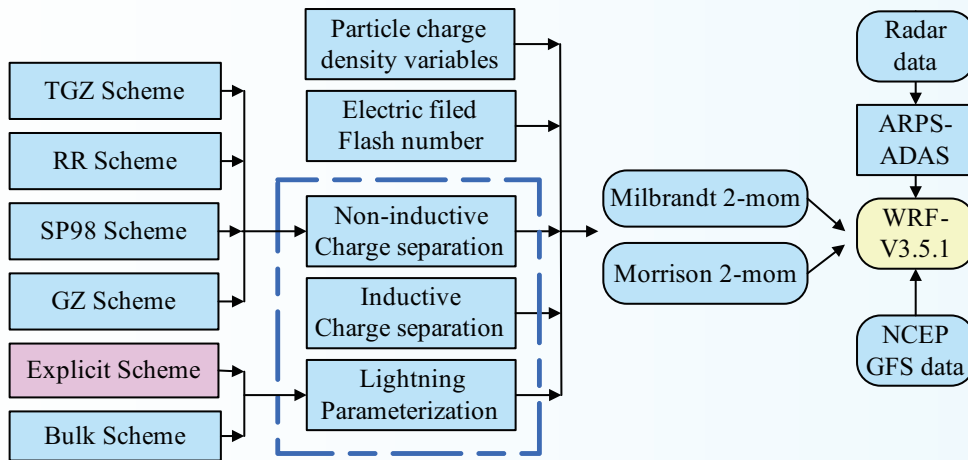


图8 中尺度起电放电模式WRF-Electric的架构
Fig. 8 Frame of the WRF-Electric model

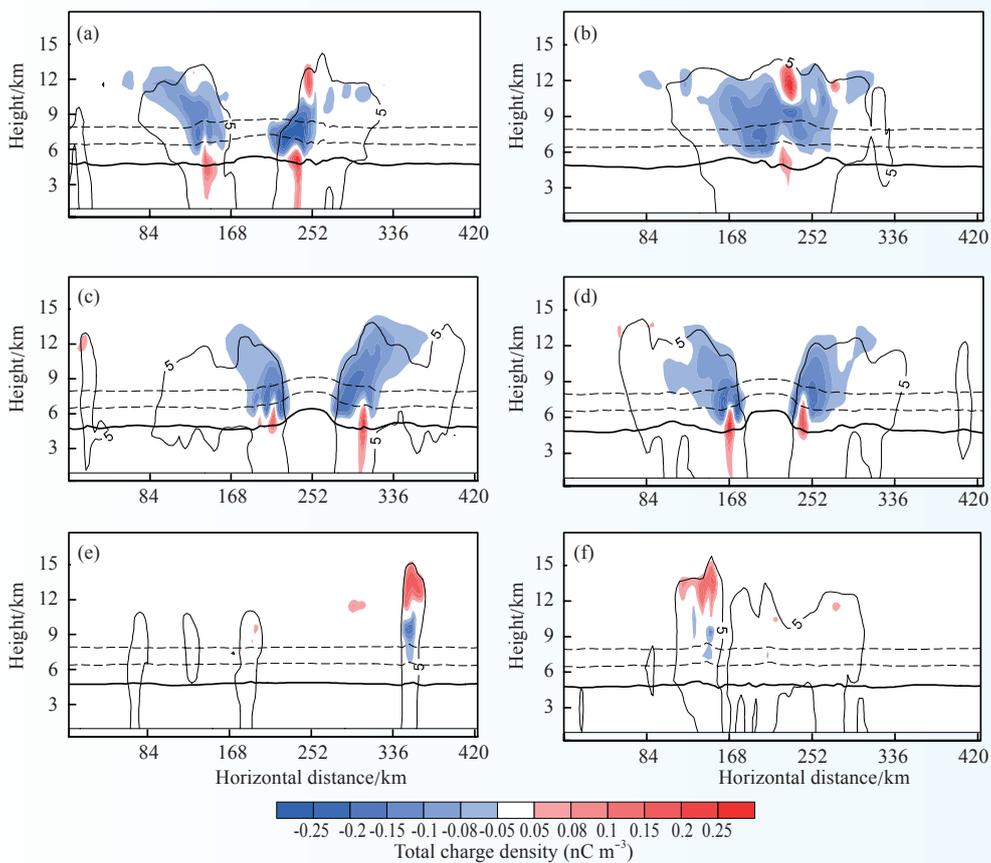


图9 热带气旋不同阶段的电荷结构演变特征（眼壁区加强阶段(a-b)和准稳态阶段(c-d)电结构；外螺旋云带加强阶段(e)和准稳态阶段(f)电结构)

Fig. 9 Evolution of the charge structure of a TC in different stages: Intensification stage (a-b) and quasi-steady stage (c-d) of an eyewall; Intensification stage (e) and quasi-steady stage (f) of the outer spiral rainband cells

Progress in Atmospheric Sounding and Lightning Research

Based on theoretical research and practical application while focused on key directions of the lightning field experiment and the theoretical research, a lot of observation and research activities were carried out and fruitful results were achieved by the Institute of Atmospheric Sounding (IAS) in 2014. 13 papers were published, 4 of which were collected by SCI/EI; one was requesting an international patent, 3 national patents for invention and 2 patents for practical novelty; one software copyright was authorized; one person obtained the title of “National Outstanding Young Meteorological Science and Technology Worker”. The concrete results are shown as follows.

1 Lightning field experiment and physical process research

1.1 Comprehensive observation experiment on lightning discharge

The IAS conducted the comprehensive observation experiment on lightning discharge in 2014. The Guangdong Comprehensive Observation Experiment on Lightning Discharge (GCOELD) carried out in Guangzhou from May 6 to Aug 28 is the ninth field experiment since 2006. 15 lightning flashes, including 45 return strokes, have been triggered successfully, which are the best results since the year of 2006 when GCOELD began. The synchronous observation data, including current, electromagnetic signal, optical radiation and high speed video, have also been acquired. As for the observation of natural lightning, the synchronous auto-observation technology of multiband lightning signals has been further developed, and the multiband observation platform, which detects LF electromagnetic signal, optical radiation, broadband radiation, and high-speed video, has been improved through a flexible triggering method and an auto-observation method. The multiband observation data for tens of flashes have been recorded, which helps further deepen the research of lightning discharge. At the same time, the novel observation system of electric field change and of high-sensitivity has been built and operated continuously, and continuous data of lightning discharge have been acquired. As for the observation of lightning on high buildings, we set up some novel observation systems, including two slow/fast antennas with a large detection range and two whole-view imagers of lightning channel, with 79 comprehensive cases of high building lightning recorded.

Additionally, the test of lightning protection technology has been conducted based on the close triggered lighting. The electromagnetic compatibility of high voltage line has been checked and 10 induction signals near the triggered lightning have been recorded, which provide fundamental data for optimizing the lightning protection scheme of high voltage line and establishing the lightning protection level in the future. Further, the coupling mechanism on electromagnetic pulse of a high voltage line has been studied.

The experiment in Chongqing has preliminarily built a local prototype network of three-dimensional (3D) lightning location system of high accuracy, which includes 9 substations and 1 central station. At the same time, the location algorithm of time-of-arrival (TOA) for lightning 3D location of high accuracy and the software for distinguishing lightning types has been developed.

The experiment in Lasa focused on the tasks as described in the project “Fundamental Research for Lightning Protection in the Potala Palace”. The instruments of optical imaging and electromagnetic signal for lightning have been installed and operated (Fig.1–2). (Zhang Yang, LüWeitao)

1.2 Observation and analysis of the 3D propagation characteristics of lightning leader

A two-dimensional (2D) image of lightning channel, which cannot reflect the real 3D spatial distribution of lightning channel, is insufficient to meet the needs of an accurate analysis of the 3D lightning channel development characteristics and the interaction between different leaders. A reconstruction method of 3D lightning channel from dual-station optical observation is established. The 2D coordinate sequence of lightning channel is obtained from each 2D lightning image captured at different positions. The principles of 3D spatial geometry are used to match the coordinates from different sequences to reconstruct the 3D lightning channel.

Six downward negative flashes terminated on tall structures in Guangzhou are analyzed. The 3D lightning channels of the upward connecting leaders (UCL) are reconstructed. For comparison, the corresponding 2D parameters are calculated using the single-station high-speed images. The main conclusions are summarized as follows: the 3D length values of the six UCLs range from 180 to 818 m with an average value being 426 m; 38 3D speed values calculated by combining the 3D UCL channel and the high-speed images for the six UCLs range from 0.8×10^5 to 14.3×10^5 m s⁻¹ (average: 4.7×10^5 m s⁻¹) and four of them (11%, 4/38) are on the order of 10^6 m s⁻¹; the corresponding 2D length and 2D speed range from 147 to 610 m and 0.3×10^5 to 10.6×10^5 m s⁻¹, respectively; the average value of the 3D speed is 1.3 times that of the 2D speed; when the time approaches the return stroke, the propagation speed of the UCL increases and all of the four 3D speed values on the order of 10^6 m s⁻¹ occur less than 0.2 ms prior to the RS; when the 3D length is shorter than 300 m, 77% (20/26) of the corresponding 3D speed values are smaller than 5×10^5 m s⁻¹, and when the 3D length is longer than 300 m or the UCL tip height is higher than 650 m, all of the corresponding 3D speed values are faster than 5×10^5 m s⁻¹ (Fig. 3). (Lǚ Weitao, Ma Ying)

1.3 Characteristics analysis of a continuing current process and M-component in an artificially triggered lightning

The Continuing Current (CC) process of cloud-to-ground lightning is a discharge process in which charges are continuously transferred to ground along the lightning channel after a return stroke. The magnitude of CC is small, but the duration of CC is commonly long. So CC often causes a lightning disaster. It's very hard to get current data due to the randomness of lightning. An artificially triggered lightning, in which the location and time of a triggered lightning can be controlled, is an effective way to measure currents of lightning. An artificially triggered lightning is different from a natural lightning, which only has CC after a return stroke. Yet an artificially triggered lightning has both CC and Initial Continuous Current (ICC) processes. Only the CC is analyzed using simultaneous observations of current, electric field change and channel luminosity by coaxial shunts, fast and slow antennas, and high-speed cameras in Guangzhou Field Experiment Site for Lightning Research and Testing, Conghua, Guangdong, China. Then, photoelectric characteristics and parameters of 14 CC and 43 M-components after return strokes of a triggered lightning observed in summer from 2008 to 2011 are analyzed. The relationships between some characteristic parameters of CC and M-component are analyzed, too.

The current waveforms of CC after return strokes are continuous and change slowly. Usually, there are current pulses ranging in size superimposed on CC waveforms. The slow electric field waveforms of CC are slowly changing, too. The lightning channel below the cloud is always luminescent during CC. The current waveforms, fast and slow electric field waveforms and channel luminosity variation waveforms of M-components are approximately symmetrical. The geometric mean of duration, charge transferred to ground, average current and action integral for CC are 22 ms, 6.0 C, 273 A, 4187 A²s, respectively. The geometric mean of magnitude, charge transferred, half peak width, rise time (10%–90%), duration, preceding CC level, inter-pulse interval, action integral for M-components are 409 A, 205 mC, 520 μs, 305 μs, 1.6 ms, 310 A,

6.5 ms, 465 A²s, respectively. There are remarkable positive correlations between the duration of continuing current and number of M-components, and between the duration of continuing current and inter-pulse interval of M-components. The correlation coefficients are 0.83 and 0.75, and both pass the significant verification of 0.01 level (Fig. 4). (Zheng Dong, Zhang Yang)

1.4 Occurrence regularity of CPT discharge events in a negative cloud-to-ground lightning

Occurrence regularity of chaotic pulse trains (CPT) discharge events in a negative cloud-to-ground (CG) lightning during six thunderstorms is analyzed. Results show that CPT is a common phenomenon throughout the negative CG lightning discharge process. 243 times of CPT discharge events occur during 323 negative CG lightning processes with a proportion reaching 75.2%. CPT in negative CG can occur before the first return stroke, between the strokes, and after the last stroke. The proportion of 66.7% of the total subsequent strokes is preceded by CPT, and CPT occurs after 11.5% of the total last strokes. It is also found that there are four distributions prior to subsequent strokes: single CPT-c (CPT connecting with subsequent strokes), single CPT-i (CPT occurring in an interval between CPT and return strokes), CPT-c and CPT-i occur concurrently, and several CPT-is appear concurrently. Single CPT-c is the most common, 39.4% of subsequent strokes are preceded by single CPT-c, and several CPTs are easier to occur before the first and second subsequent strokes, which are respectively 9.4% and 7.7% of the total corresponding strokes. With the increasing subsequent strokes, there is a decreasing occurrence of CPT, and in addition to the previous two subsequent strokes, the number of CPT-c is obviously greater than that of CPT-i. In addition, both CPT-i and CPT-c coincide with the negative CG K-change, and some also correspond to the process of J-change in the slow electric field wave (Fig. 5). (Zhang Yang)

1.5 The multi-scale entropy feature of a chaotic leader in a CG lightning

To address the difficulty in determining chaotic pulses, we apply the multi-scale entropy method to distinguish chaotic, dart and dart-stepped leaders. The calculation method of multi-scale entropy and the applicability in characterizing complex signals have been investigated. The key parameters of multi-scale entropy during their application to the analysis of lightning chaotic pulses have been researched, and the multi-scale entropies for chaotic, dart and dart-stepped leaders have been compared. The results show that although the entropies of chaotic and dart leaders both increase firstly and then stabilize with the changing scale, their values are obviously different. The entropy of a stepped leader does not change too much with the increasing scale, and its value is different from that of a chaotic leader when the scale is larger than 3. As a result, we suggest that the entropy with a value of >1.5 indicates a chaotic leader, in contrast, the entropy with a value of <1.5 corresponds to a stepped-leader or a dart leader. The average value of characteristic entropy for a chaotic leader is 2–2.1, the range of maximum values of it is 2.6–2.8, and the range of minimum values of it is 1.5–1.51 (Fig. 6). (Zhang Yang)

1.6 Lightning electric field change signal measuring system and method

To address the saturation during the close measurement of lightning, a lightning electric field change signal measuring system has been invented. The system comprises a detection antenna, an electric field rapid-change receiver and a signal processing module, wherein the electric field rapid-change receiver is respectively connected with the detection antenna and the signal processing module; the detection antenna is used for transmitting an electric field change signal generated by an induced lightning to the electric field rapid-change receiver; the electric field rapid-change receiver is used for processing the electric field change signal to obtain a lightning electric field rapid-change signal and transmitting the lightning electric field rapid-change signal to the signal processing module; and the signal processing module is used for acquiring and processing the

lightning electric field rapid-change signal to obtain a lightning electric field slow-change signal. The invention also covers a lightning electric field change signal measuring method corresponding to the measuring system. The system and method detect the electric field change signal by the reception of E-change, and then process the data to get a slow E-change waveform. As a result, it realizes an integrated measurement of lightning electric field rapid-change and slow-change signals, and solves the saturation during the close measurement of lightning (Fig. 7). (Zhang Yang, Meng Qing)

2 Characteristics of lightning activity in a thunderstorm and its relationship with weather phenomena

2.1 Relationship between lightning and precipitation based on atmospheric stratification and thunderstorm development

A total of 28 thunderstorms occurring in and around Beijing from 2006 to 2008 are collected to investigate the relationship between total lightning (observed by SAFIR3000) and convective precipitation (by radar inversion). These cases are classified according to the parameters of atmospheric stratification and the reflectivity of radar. The quantitative results provide a reference for applications of lightning data to severe weather warning and precipitation estimation. The lightning forecast can also be improved by assimilating the relationship between the hydrometeors and the lightning activities to the numerical prediction models. The analysis can extend the application of the lightning data.

The results show that the average convective rain yield per flash is $1.92 \times 10^7 \text{ kg fl}^{-1}$ on the whole, while the linear correlation coefficient between total lightning frequency and convective precipitation is 0.584. Total lightning frequency (expressed by F with the time interval being 6 min) can be used to calculate the amount of convective precipitation with the equation being $R = (2.813 \times 10^8) + (4.570 \times 10^6) F$. A total of 28 thunderstorms are classified according to the available potential convective energy (E_{cap}) and lifting index (LI) of the atmospheric stratification. It is found that strong instability of atmospheric stratification tends to be associated with smaller precipitation and there is a more pronounced correlation between total lightning and precipitation. The classified E_{cap} (no less than $1600 \text{ J} \cdot \text{kg}^{-1}$) has a correlation coefficient of 0.837. The total lightning frequency can be used to calculate the amount of convective precipitation with the equation being $R = (1.620 \times 10^8) + (5.478 \times 10^6) F$. While the classified LI (no less than 4 K) has a correlation coefficient of 0.853, the total lightning frequency can be used to calculate the area of the amount of convective precipitation with the equation being $R = (1.530 \times 10^8) + (6.276 \times 10^6) F$. Another three parameters are calculated from radar reflectivity, i.e., maximum height of 20 dBz reflectivity, maximum reflectivity at 12 km level, and volume ratio of the reflectivity larger than 30 dBz above 0°C to the reflectivity larger than 40 dBZ above 0°C , in terms of their radar volume scans. The most pronounced relationships between lightning and precipitation occur in the classification of $H_{20 \text{ dBz}} < 11.5 \text{ km}$, $25 \text{ dBz} \leq f_{12 \text{ km}} < 35 \text{ dBz}$, and $V_{40/30} < 0.39$, when the correlation coefficients are 0.804, 0.609 and 0.750, respectively. The linear correlation between lightning and precipitation shows obvious differences in different classifications. The fitting equations in different classifications will provide references for the application of relationships between lightning and precipitation according to the characteristics of thunderstorm processes. (Zheng Dong)

2.2 Characteristics of CG lightning in Shanghai and its surrounding regions and land-sea difference

With observations from the LS8000 lightning location system, cloud-to-ground (CG) lightning activities in Shanghai and its surrounding regions are studied. The percentage of positive CG lightning in the total is about 8.5% and that of large current CG lightning (with the absolute value of current larger than 50 kA) is

5.6%. CG lightning activities highly occur in the period from June to September, and peak in August. For the temporal distribution of CG lightning, 12:00 to 19:00 BT is an active period, which peaks at 14:00 BT and bottoms out in the morning. The monthly and hourly distributions of the percentage of the positive cloud-to-ground (PCG) lightning are seasonal. Setting 31°N as the boundary, the CG lightning density is generally 6 to 12 flashes/(km²·a) in the northern part and 2.4 to 4.8 flashes/(km²·a) in the southern part of the analyzed area. At the same time, the CG lightning density on land is higher than those in lake and oceanic areas, while the percentage of PCG lightning and the large current CG lightning in the oceanic area is significantly higher than those on land. The time changes of spatial distribution of CG lightning show that CG lightning activities mainly appear on the land in the afternoon and near the water in the morning, while in other periods are transitional, which is closely related to the heating effect of the underlying surface. (Zheng Dong)

3 Simulation of the electrification of a tropical cyclone using the WRF-Electric model

Inductive and non-inductive electrification schemes and a bulk discharge parameterization are introduced into the Milbrandt and Morrison two-moment microphysical schemes in the WRF-ARW model. The model with electrical processes, referred to as WRF-Electric, is able to simulate charge density and lightning distribution in storms. Four different charge separation schemes (TGZ, GZ, SP98 and RR) are introduced into the two microphysics schemes. Fig. 8 shows the frame of the WRF-Electric model.

The evolution of the electrification of an idealized Tropical Cyclone (TC) is simulated by the WRF-Electric model. The characteristics of TC lightning can be further understood by comprehending the electrification of TCs. This study makes an attempt to illustrate the evolution of the charge structure of TCs. The results of this study can be supported by most of the previous observations and simulations.

The results indicate that the eyewall generally exhibits an inverted dipole charge structure with negative being above positive. In the intensification stage, however, the extremely tall towers of the eyewall may exhibit a normal tripole structure with a main negative region found between two regions of positive charge. The outer spiral rainband cells display a simple normal dipole structure in all stages. Further analyses indicate that the differences in charge structures are associated with different updrafts and particle distributions. Weak updrafts, together with a coexistence region of different particles at lower levels in the eyewall, result in charging processes that occur mainly in the positive graupel charging zone (PGCZ). In the intensification stage, the occurrence of charging processes in both positive and negative graupel charging zones are associated with strong updrafts in the extremely tall towers. In addition, the coexistence region of graupel and ice crystals is mainly situated at upper levels in the outer rainband, so the charging processes mainly occur in the negative graupel charging zone (NGCZ). The conceptual model of the evolution of the charge structure of TCs is built (Fig. 8–9). (Wang Fei, Xu Liangtao)

4 Research working progress about lightning operational application

4.1 Promotion training of the lightning detection, nowcasting and warning system

“2013 Meteorological Monitoring and Disaster Warning Project”, the second stage of the national training on CAMS_LNWS, was held by IAS in Anhui branch of the China Meteorological Administration Training Center during 16–19 September 2014. A total of 65 staff members from meteorological stations and lightning protection centers at national level and from the Meteorological Center of the North China Air Traffic Management Bureau of Civil Aviation Administration of China participated in this course.

The IAS revised the context of the course and updated the teaching materials according to the feedback



of the first training course held in 2013. The training course covered lightning physics, lightning disaster, lightning detection, lightning warning, and lightning protection engineering. The course, which was highly praised by the participants, promoted the further application of research outputs to operations and services. (Yao Wen, Meng Qing, Zhang Wenjuan)

4.2 Application of Lightning Nowcasting and Warning System (CAMS_LNWS)

After localization test in the Lightning Protection Center of Guangdong Province, the CAMS_LNWS was put into operation in Guangdong on April 20, 2014. During the operational period, it made several successful early warnings and the evaluation results of POD (Probability of Detection), FAR (False Alarm Rate) and TS (Threat Score) showed that all warnings performed well. Now, the products of CAMS_LNWS have been used in the services for ultra-high buildings, hazardous chemicals sites and other key areas. It can provide an important reference for decisions to be made for work time arrangement, lightning risk avoidance, and safety production. (Yao Wen, Meng Qing)

大气物理与人工影响天气 Atmospheric Physics and Weather Modification

云物理与人工影响天气研究进展

1 云物理观测研究

1.1 华北一次持续性重度雾霾天气的产生、演变与转化特征观测分析

2011年12月1—7日在华北地区发生了一次比较罕见、持续1周左右的低能见度重度雾霾天气。利用气象行业专项“京津地区低能见度雾霾天气监测与预报研究”观测试验资料,研究分析了此次持续性重度雾霾天气的气溶胶、云凝结核(CCN)、雾滴谱、含水量等微物理特征及大气能见度、边界层垂直结构特征,探讨了雾霾天气的产生、演变与转化特征及机理。结果表明,此次持续1周的雾霾天气过程发生在高压天气系统和静风条件下,暖平流和辐射降温形成的稳定逆温边界层结构有利于污染气溶胶的积累和雾霾的形成和发展,尤其是来自南方持续不断的湿平流使雾霾天气得以长时间持续和发展。整个雾霾天气期间能见度均小于2 km,最低能见度达到56 m,液态水含量在 10^{-3} g/m^3 量级,最大达到 0.16 g/m^3 ,气溶胶数浓度均在 10000 cm^{-3} 以上,质量浓度范围为 $50 \sim 160 \mu\text{g/m}^3$ 。进一步的研究表明,此次长达1周的雾霾天气发生了3次强弱不同的霾气溶胶积累、霾雾转化和混合及减弱3个主要阶段。霾气溶胶积累阶段先后有爱根核模和积聚模气溶胶数浓度的积累和增加。霾向雾转化和混合阶段中,雾滴凝结释放的潜热和高浓度气溶胶环境使布朗碰并加剧,导致气溶胶尺度向粒径大的方向转移,从而提供了大量可形成云凝结核的气溶胶粒子,促进了雾的爆发性增强,浓雾过程中气溶胶向CCN活化率可达17%,而CCN向雾滴的转化效率可高达100%,此期间雾滴谱具有爆发性拓宽的特征;冷锋系统过境或辐射加热增强导致了雾霾过程的减弱和消散。(郭丽君,郭学良,方春刚,朱士超)

1.2 华北积层混合云中冰晶形态、分布与增长过程的飞机探测研究

利用国家科技支撑计划重点项目“环北京地区3架飞机联合云探测试验”数据,分析了2009年4月18日和5月1日2次积层混合云中冰晶形态、分布与增长过程。结果表明,飞机在 $0 \sim 16 \text{ }^\circ\text{C}$ 范围的云层内观测的冰晶形态主要包括板状、针柱状、柱帽状、辐枝状和不规则状。云中低层观测的冰晶形态受云顶温度影响,云顶温度不同,观测到的冰晶形态也不同,当云顶温度高于 $-8 \text{ }^\circ\text{C}$ 时,在云中低层观测到的冰晶形态以板状和针柱状为主;当云顶温度低于 $-13 \text{ }^\circ\text{C}$ 时,在云中低层可观测到辐枝状冰晶;当云顶温度低于 $-18 \text{ }^\circ\text{C}$ 时,在云中低层可观测到柱帽状冰晶。同时冰晶形态还受其所处云中位置的影响,在积层混合云的嵌入对流区和融化带中含有更多的淞附状冰晶;在融化层以上,冰晶的增长过程主要包括凝华、淞附和聚合过程,在垂直方向上,随着高度降低云中过冷水增多,冰晶的淞附增长也相应增强。积层混合云中的对流区和层云区粒子谱下落拓宽速率有明显差别,在 $4.8 \sim 4.2 \text{ km}$ ($-11.6 \sim -8 \text{ }^\circ\text{C}$)高度层,对流区粒子谱拓宽速率为 3 mm/km ,而层云区为 3.67 mm/km ,层云中粒子拓宽增长的速率略高于对流区;而在 $4.2 \sim 3.6 \text{ km}$ ($-8 \sim -5 \text{ }^\circ\text{C}$)高度层,对流区的粒子谱拓宽速率为 6.67 mm/km ,层云区为 2.33 mm/km ,对流区的粒子拓宽增长速率是层云区的近3倍,主要原因是嵌入对流的低层含有较多过冷水。(朱士超,郭学良)

1.3 探测大气温湿廓线的35通道微波辐射计设计原理与特点

总结了自主研发的MWP967KV型地基35通道微波辐射计系统设计原理和主要特点。系统将K、V双频段宽带天线及接收机、宽带调频本振、温湿压计以及电源模块紧凑集成为一台整体设备。对各传感器的测量输出实时进行一体化综合处理,采用BP神经网络实时反演大气温度、湿度廓线和汽、水总

量。廓线的垂直覆盖范围为地表至顶空 10 km，共划分为 58 层，辐射计样机于 2012 年秋冬季在北京地区开展了为期 2 个月的观测试验，利用这段时期内的 69 个探空资料样本对辐射计 2 个层次的实时观测输出都进行了对比检验，计算了水汽、氧气通道亮温和反演所得大气温湿廓线的平均偏差、均方差以及相关。结果表明，该系统能够满足实时气象监测的需求，达到国际先进水平。（卢建平，黄建平，郭学良）

1.4 L波段探空判别云区方法的研究

利用 2008 年 1 月到 2009 年 12 月的 L 波段探空资料，以及与之时空匹配的 Cloudsat 云观测资料，分析云内和云外相对湿度的累积频率分布的结果显示，以 75% 作为相对湿度阈值判断云准确率可达 81%。利用 BS (Bias Score) 和 TS (Threat Score) 评分方法对不同相对湿度阈值进行评分分析的结果显示，以 81% 作为相对湿度阈值 TS 评分可达 0.66，为最高。利用 BS 和 TS 评分方法分不同高度对相对湿度阈值进行评分分析，发现随高度的增加该高度上具有最好 TS 评分的相对湿度阈值在减小。利用这些阈值对云判断时，总的 TS 评分高于 0.6，且准确率达到 84% 以上，比利用单一相对湿度阈值判断云准确率要高。对这些阈值进行优化，得到一套适合于我国 L 波段探空秒数据的云垂直结构的判别方法。（蔡森，欧建军，周毓荃）

1.5 一次超级单体雷暴观测分析和成雹区识别研究

利用多普勒雷达资料，结合探空和常规资料，分析了 2011 年 4 月 17 日一次超级单体雷暴的流场和回波结构演变特征。该雷暴是在条件性不稳定和垂直风切变较大的环境下产生的右移风暴。垂直剖面图显示雹云初生发展阶段，逐渐形成有组织的斜上升气流促进雹云发展。成熟降雹阶段，雹云内形成一支强的斜上升气流和深厚的中气旋，主上升气流对应雹云的弱回波区。雹云维持典型的弱回波区-悬挂回波-回波墙特征结构。根据雷达径向速度和雹云移速订正得出的“零线”演变发现，随着雹云的发展，“零线”逐渐向悬挂回波靠近，并穿过悬挂回波，“零线”的走向为上翘式，附近“穴道”的汇集力较强，有利于降雹。通过对“零线”位置的判断可分析有利成雹的区域。根据高低空两层强回波的水平错位，利用两高度强中心连线所作剖面能快速准确得出特征剖面，并将 0℃ 层以上 6 km 高度处降雹潜势达到 100% 的 45 dBz 的区域识别为成雹区，与降雹实况对比发现识别效果良好。（蔡森，周毓荃）

1.6 一次西风槽过程过冷云水分布特征观测研究

过冷云水消演变规律是云物理学和人工影响天气的重要研究领域。根据 Hobbs 1974 年提出的假定，利用飞机、卫星、雷达和雨量计等观测资料，对 2012 年 9 月 21 日河北一次西风槽天气过程进行观测研究，分析其过冷云水分布特征及演变规律。结果表明，槽前云系过冷水区宽厚并且过冷水含量较高，云滴浓度和均立方根直径较大并且均匀，冷云区厚而且没有分层，没有暖云配合；近槽云系中冷云区小粒子浓度降低但云滴直径增大，冷云区夹有干层，云系变厚出现暖云配合，冷暖云液态水含量较高，冷暖云区大粒子和降水粒子浓度和尺度增大，中尺度云团移动较快；槽后云系中云滴浓度最大，但云滴均立方根直径明显减小，过冷水区出现的高度下降、厚度很薄、过冷水含量较低，冷、暖云之间有干层，暖云对应的大粒子浓度和降水粒子浓度非常大，地面降水主要由暖云过程产生；云水（过冷水）含量峰值常出现在云内逆温层的上方；利用云粒子测量系统（PMS）资料分析过冷云水消演变特征，其与卫星和雷达资料具有较高的一致性。（周毓荃，孙晶）

2 云降水物理与人工影响天气数值模拟研究

2.1 气溶胶对华北夏季对流云和降水影响的数值模拟研究

大气温室气体、气态前体物和颗粒物排放可以直接改变大气辐射收支，或间接改变云和降水过程，可能引起区域到全球尺度的气候和水循环变化。一些前期发表的大气排放对云和降水影响的定量评估研究结果并不一致。本研究利用 MODIS 卫星和 WRF-CHEM 模式，对 2008 年 7 月 4 日华北城市区一次

对流性降水个例的气溶胶特性及其对降水的可能影响进行了分析。结果表明,研究区气溶胶光学厚度超过0.9,说明存在高浓度污染气溶胶。爱根指数大于1.0,说明研究区主要气溶胶粒子属于工业和生物质燃烧所产生,粒径尺度在0.25~0.5 μm。数值模拟研究表明,污染条件下模拟区域平均降水增加17%,但大于30 mm/h的降水强度出现增强,而小于30 mm/h的降水强度减弱。污染与清洁状况下的云微物理和动力差异表明,污染对风暴初始和消散阶段的冷暖云微物理、动力过程和上升气流有明显抑制作用,而对成熟期的风暴有明显增强作用。(郭学良)

2.2 减弱对流云降水的AgI催化原理的数值模拟研究

在对流云模式中增加了AgI两个预报量,耦合了考虑受水汽过饱和度和温度影响的4种核化机制的AgI催化模块,使其具备了AgI类催化剂的模拟能力,能够研究AgI类催化剂对对流云系统的影响。利用此模式对一次华南对流云降水过程进行了AgI成冰剂催化数值模拟试验,对人工减缓对流云降水的可能性及原理进行了研究。模拟结果表明,在适当的时机对适当的部位进行大剂量的催化,可以减少总降水量,也可以减弱最大降水中心的雨强。当催化剂量达到 $2 \times 10^8 \text{ kg}^{-1}$ 时,可以减少32%的降水量,具备有效减缓对流云降水成灾的可能性。大剂量催化后,大量的AgI粒子在冷区核化后消耗了大量的过冷水。催化后霰粒子的落速和雨水的落速减小。催化阶段由于霰融化成雨水减少而使降水减弱。催化结束后在霰融化成雨水增多的情况下,雨水的蒸发大幅增加,从而导致了降水量的持续减少。AgI在此次强对流云中主要以受过饱和度影响的凝结冻结和催化剂长时间作用的浸没冻结这两种方式成核。研究所用催化方法在外场作业中具有技术可行性。(楼小凤,孙晶,史月琴,张邢)

2.3 下垫面对雹云形成发展的影响

利用中尺度模式WRF对2005年5月31日发生在北京地区的一次强冰雹天气过程进行了数值模拟研究,并与观测的雷达回波、冰雹云移动路径和冰雹落区进行比较,在此基础上探讨了城市和农田两种下垫面对雹云的影响。结果表明,由于“城市热岛”效应的作用,城市下垫面的地面感热通量显著增加,有利于雹云的发展增强和大冰雹的形成,使地面累积降雹量增加,但对雹云移动路径影响不大。农田下垫面具有较大的潜热通量,局地蒸发强,有利于大量小冰雹的形成,云中冰雹含量增加,但降雹强度较弱,地面累积降雹量小。(郭学良)

2.4 一次积层混合云降水不同尺度结构的数值模拟

利用中尺度数值模式WRF-ARW(V3.2)对2009年4月18—19日发生在张家口地区的一次积层混合云降水进行了模拟,并结合观测资料从不同尺度对这次降水过程进行了对比分析。结果表明,700 hPa西风槽、850 hPa低涡是影响这次降水的主要天气系统,来自南方的暖湿空气和西北内蒙古低涡带来的水汽是这次降水的主要水汽来源,两股水汽在张家口附近低层出现了大尺度辐合,有利于该地区云系的发展和降水的形成。降水云系呈东北—西南向带状分布,带长约1000 km,带宽300 km,在大片的云带中分布着很多个高值中心,中心区域一般在几十公里;结合雷达回波可以看到在均匀的回波层中镶嵌着柱状对流回波,具有典型的积层混合云降水回波特征;沿着雷达回波做剖面,发现云中云水含量分布无论是在水平方向还是垂直方向都是不均匀的,雨水的大值中心与上层的霰、雪的大值中心相对应,中心水平范围在10~20 km。(张微,周毓荃)

2.5 山西春季层状云系数值模拟及与飞机探测对比

采用中国气象科学研究院中尺度云参数化模式对2010年4月20日山西省一次春季层状降水云系的宏微观结构,特别是垂直方向上的微物理结构进行了数值模拟和分析。利用携带云粒子探测设备的飞机对该次层状云系进行了2次云物理探测飞行,并将飞机探测所获取的数据和图像资料与数值模拟结果进行了对比研究。模拟结果显示,该次降水过程以层状冷云降水为主,云中过冷水含量丰富,云系存在明显的3层结构,地面降水主要来自于云中高层冰晶、雪、霰等冰相粒子的融化和低层云水的转化。数值模拟与飞机探测对比分析显示,高空温度、湿度和高度的配置两者基本一致,数值模拟不同高度的云粒子相态、垂直方向云水比含水量与飞机探测获取的云粒子图像和云液态水含量的垂直结构基本吻合,但数值模拟的云中各种水成物粒子出现的高度较飞机探测偏高。(陶玥,史月琴)

3 人工影响天气关键技术研究

3.1 高炮、火箭和飞机催化扩散规律和作业设计

基于扩散计算的解析解提出了针对高炮、火箭和飞机等不同催化方式的点源、多线源和移动点源的数值计算方案，分别研究了不同催化方式催化剂扩散规律和有效范围，并利用卫星捕获的一次飞机播云实例检验了计算方案，同时研究了实现目标区充分催化的作业设计等问题。高炮作为点源催化、单个高炮作业，达到有效催化浓度的范围半径只有约0.5 km，应当采用多炮弹密集作业，比较有利于浓度和催化范围的维持，提高炮弹成核率能够明显提高高炮作业效果。火箭和飞机作为线源催化，1 h内达到有效催化浓度的宽度分别为7 km和6.6 km，此宽度可作为多线播撒作业飞行间距设计的参考依据；飞机单线播撒达不到充分催化的要求，而耕作式播撒，在风速作用下扩散区域会分散或重叠。根据风速大小设计的“8”字形来回播撒飞行路线，可使目标区得到充分播撒。在扩散计算方案研究基础上研发的各类催化扩散计算和作业设计软件系统，可方便准确地计算飞机、高炮和火箭实际作业时催化剂在云中扩散的范围、浓度及其随时间的演变，并可针对不同目标区进行充分播撒催化的作业设计，结果直观简明，为催化扩散计算的的实际业务应用和作业设计提供了帮助。（周毓荃）

3.2 北京地区人工增雨效果和防雷经济效益评估

基于全市农业气象灾情统计资料，结合近年来北京地区开展的人工增雨、防雷作业情况，利用经典的区域历史回归统计方法，对2004—2010年人工增雨效果和防雷经济效益进行了客观定量评估。结果表明：（1）在5—9月的评估期，随着作业样本数逐年累加，人工增雨平均相对增雨率逐渐趋于稳定，并维持在20%左右，在所选目标区连续7年的人工增雨作业累计增加降水量约417.8 mm，增雨效果非常显著；（2）年平均人工防雷经济效益约2.48亿元，多年平均防雷投入产出比为1:16。人工防雷效益最高、最低年份分别为2009年和2005年，对应投入产出比分别为1:27和1:6。（李宏宇）

3.3 对流云人工增雨效果检验技术方法及应用

对流云降水时空变化较大，利用Woodley & Rosenfeld提出的建立在雷达资料基础上的移动目标单元法对对流云增雨作业进行效果评估。利用塘沽、北京及秦皇岛3部雷达资料，对其进行插值处理，确定移动目标单元识别和跟踪方法，然后在移动目标单元中确定催化单元和对比单元，记录每个单元的物理参量，利用Z-R关系反演降水量，对物理参量和反演降水量作统计分析，定量计算增雨效果的同时提供人工增雨的物理证据。应用该方法对2011年7月24日对流云人工增雨作业效果进行评估的结果表明，催化剂进入云中后使得最大回波强度增强、回波顶高增加，从物理角度证明了催化对增加降水起到了一定作用。利用降雨率对增雨作业定量效果分析的结果表明，该次作业相对增雨7.69%，显著度检验值为0.043。（李宏宇）

4 人工影响天气工程建设及业务工作进展

4.1 全国人工影响天气发展规划（2014—2020年）

2014年12月，中国气象局人工影响天气中心牵头编制的《全国人工影响天气发展规划（2014—2020年）》（发改农经〔2014〕2864号）由国家发展改革委员会和中国气象局联合印发，该规划确定了全国人工影响天气的指导思想、发展目标、总体布局、主要任务、实施安排，提出了人工影响天气的组织管理体制和业务运行机制，是当前及今后一段时期全国人工影响天气发展的行动纲领，对全国人工影响天气现代化建设和科学发展具有重要指导意义。2014年10—11月，《全国人工影响天气业务发展指导意见》（气发〔2014〕95号文）、《人工影响天气专用技术装备管理办法》（气发〔2014〕106号文），相继由中国气象局正式印发颁布，标志着我国人工影响天气业务和装备管理步入规范发展的轨道。（陈添宇，周毓荃，房文）

4.2 东北人工影响天气工程建设

2014年是“东北区域人工影响天气能力建设”项目建设初见效益的重要一年。年度内,完成初步设计的修订与报批,首架新舟60增雨机试飞成功并在第10届中国国际航空航天博览会上正式亮相,完成第3架高性能增雨飞机作业系统总体方案设计并选定了11套机载人工影响天气设备,启动区域飞机作业保障中心建设,作业指挥应用系统主体功能已在东北4省区安装部署;完成高性能作业飞机卫星通信系统、79部全球定位系统气象观测(GPS/MET)设备、3部X波段移动多普勒天气雷达、GPS/MET数据处理中心软件系统以及效果检验外场试验区所有设备的采购,举办了人工影响天气前沿科学技术与飞机作业技术培训班。项目初步成果在东北区域春夏季抗旱增雨中发挥了重要作用。(李集明,陈卫红)

4.3 全国人工影响天气作业信息采集处理系统(V1.0版)投入业务运行

在多年业务工作的基础上,依托“中国气象局人工影响天气业务指挥平台”项目建设的全国人工影响天气作业信息采集处理系统(V1.0版)于5月21日通过专家组验收,成为2014年继人工影响天气预报模式系统后,第2个通过业务化验收的人工影响天气业务系统(气减函〔2014〕48号文)。

全国人工影响天气作业信息采集处理系统(V1.0版)由作业信息采集处理系统和实时上报系统2部分构成,依托全国气象业务宽带网,可实现全国人工影响天气作业信息的上报、采集、存储、监控、管理等功能;同时集成了站点信息、作业信息、人员信息、弹药信息等多种人工影响天气基础数据,为人工影响天气作业效果分析评估、联合作业指导、人工影响天气决策服务产品制作提供及时、可靠的信息来源。系统投入业务运行以来,有效地提高了地方人工影响天气部门作业信息上报效率,加强了国家级人工影响天气中心的业务指导能力和服务效益,为各地人工影响天气作业指挥和效果分析等业务的开展提供了有力支撑。(王飞,杨连英,李抗抗)

4.4 人工影响天气云降水特征参量静止卫星反演系统(CPPS-GSSL 2.0版)投入业务运行

中国气象局人工影响天气中心在多年科研积累的基础上,发展了人工影响天气云降水特征参量静止卫星反演系统(CPPS-GSSL 2.0版),该系统于2014年7月4日通过评审,并投入业务运行。

该反演系统(CPPS-GSSL 2.0版),是基于我国FY-2系列静止气象卫星和L波段探空资料等实时反演生成云黑体亮温、云顶高度、云顶温度、过冷层厚度、云光学厚度、云粒子有效半径和液水路径等云特征参量反演产品,通过与MODIS反演参量的对比检验及与CloudSat云雷达、天气雷达、雨滴谱和地面降水等多种云降水观测进行物理合理性分析,检验了反演产品的准确性和可用性。反演产品在各省应用效果好,已为重点干旱地区及跨区域增雨作业、森林草原灭火增雨作业、重大社会活动消减雨作业等提供了强有力的技术支撑。(蔡森,周毓荃)

4.5 2014年南京青奥会开、闭幕式人工消减雨取得明显效果

2014年8月16日和28日,第2届夏季青年奥林匹克运动会开、闭幕式分别于南京市奥体中心举行。为确保其顺利进行,组委会迫切要求开展人工消减雨试验和服务。江苏省气象局特邀中国气象局人工影响天气中心全程指导开展相关试验和服务工作,并取得明显消减雨效果。其中开幕式奥体中心场馆降水2 mm,场馆周边邻近站平均降水5 mm;闭幕式奥体中心场馆降水0.2 mm,场馆周边邻近站平均降水0.68 mm。确保了开、闭幕式的顺利进行。初步总结关键技术工作主要如下。

(1)在分析研究8月份南京天气和云降水特征基础上,提出并指导制定了南京青奥会人工影响天气服务技术方案,包括监测加密、通信指挥、作业防线布局和实施组织等多个分方案。

(2)利用国家近年发展的人工影响天气作业条件业务数值预报模式,提前24 h给出催化原理、催化方案(包括催化区、催化时段、催化方式及催化量的预报)。并结合天气动力预报和实况监测,利用新建的人工影响天气远程会商平台,进行国家人工影响天气指挥中心同青奥会现场指挥中心的实时互动,滚动进行作业方案的实时会商和预报方案的及时修订,并达到预期催化效果。

(3)将中国气象局人工影响天气中心近年来研究发展的云降水精细分析系统(CPAS)移植开发,建立了青奥会消减雨作业指挥系统,实现基于卫星、雷达、探空及特种仪器等各类观测的云系宏微观结构和降水演变的实时精细分析、作业条件的预判识别、最佳的作业方案的实时设计滚动修正、现场

飞机和地面多种催化的实时指挥等功能。

(4) 利用移植的CPAS平台和作业指挥系统,有效组织飞机外围侦查探测预作业和临近区域高密度火箭催化作业,有效地抑制削弱了移近场馆的云团,证实了作业前的技术原理和设计,取得了较好的预期效果(图1)。(周毓荃,刘思瑶,濮梅娟,胡志晋)

4.6 国家级人工影响天气业务平台的建设及其在业务指导和服务中的作用

2014年人工影响天气中心自主研发建设完成国家级人工影响天气业务平台,该平台主要包括4部分功能。第1部分是信息传输、收集与存储管理功能,主要收集存储常规气象观测数据、人工影响天气特种观测、业务产品和飞机、地面人工影响天气作业数据,供实时业务使用,并处理形成典型个例库数据;第2部分是产品加工、检验和中试功能,主要对数据进行加工处理,综合分析形成各种人工影响天气特征量,用于对人工影响天气作业条件进行预报和监测预警,并对预报产品进行检验和新业务开发中试;第3部分是业务指导和服务功能,包括开展作业条件潜力预报、监测预警与专题会商、设计作业方案、开展飞机作业跟踪指挥和实时监控,以及作业后效果检验分析;第4部分是产品共享发布功能,将预报和监测产品通过网站进行发布,供相关业务单位使用。

平台建成后,针对我国各地出现的旱情和可能的作业天气过程,成功进行跨省(区)联合业务会商,在实时业务指导和服务中发挥重要作用。如在2014年4月,中国气象局人工影响天气中心联合黑龙江、吉林、辽宁、内蒙古4省(区)人工影响天气中心进行会商,对整个东北区域的云系结构、云带、过冷水、冰相粒子等的分布和演变情况进行综合分析,提出了适合开展作业的时间、地点和高度等方面的建议;东北人工影响天气中心根据东北区域作业需求和作业装备的布局进行了跨省(区)联合作业的部署,标志着跨省(区)联合作业步入逐级指导、联合作业的业务模式,提高作业的科技水平和效益(图2)。(周毓荃,史月琴,孙晶,蔡森,刘卫国,陶玥,王飞)

4.7 优化空中云水资源评估

通过2011—2014年的不断探索和研究,中国气象局人工影响天气中心研发完善了空中云水资源监测评估方法(CWR-MEM)。该方法以大气水分收支平衡方程为基础,明确了包括水凝物在内的大气水物质概念,完善了各种水物质总量、降水效率、更新周期等概念和计算公式,提出了云水资源、空中云水资源总量和有效云水资源量等相关概念。

2014年,中国气象局人工影响天气中心组织专门技术力量,对该方案中三维云场和三维云水场的诊断识别等关键技术和评估时空尺度、复杂区域边界处理等评估方法进行了优化。根据云的气候特性,将中国按经纬度分为5个区域,利用2007—2008年的CloudSat云观测产品,分别统计得出各区域诊断云区的相对湿度阈值和云含水量典型值及其垂直分布,并将垂直分布随高度坐标改为温度坐标,云场物理意义更准确,明显改进优化了全国不同区域三维云场和三维云水场的诊断方案。对空中云水资源评估时,将评估区域细分为6个区域,并将各区域的边界处理成1°分辨率的闭合曲线,明显改进了对凝结和蒸发量的计算,提高了整体评估精度和计算准确率。

利用优化的CWR-MEM方案,对2008—2010年中国六大人工影响天气区域的空中云水资源进行了评估,完成了2014年空中云水资源监测评估报告。主要评估结果如下:2008—2010年,中国的水汽总量年平均均值(GQ_v)约 36.9×10^{12} t,其中从各边界输入的水汽量年平均均值约 33.1×10^{12} t,蒸发量年平均均值约 3.75×10^{12} t;水凝物总量(GQ_h)年平均均值约 7.15×10^{12} t,降水总量(GR)年平均均值约 5.02×10^{12} t,云水资源总量年平均均值(GCWR)约 2.13×10^{12} t,有效云水资源量年平均均值(CWR)约 1.23×10^{12} t。水汽降水效率年平均均值约为14%,水凝物降水效率年平均均值约为70%,水汽更新周期年平均均值约为10天,水凝物更新周期年平均均值约为7h。云水资源各特征量具有明显的时空分布差异。(周毓荃,蔡森)

4.8 研发作业效果检验技术方法

在详细分析全国人工影响天气作业信息的基础上,揭示了全国不同区域的人工增雨作业需求;开发了4种非随机化人工增雨效果统计检验技术方法,研发了针对4种统计检验方案的显著性水平检验算法,并在江西、云南、河南、重庆、安徽5个试点省进行试验试用;研发了基于TITAN技术的播云多普勒雷达识别追踪及检验算法和基于常规雷达探测资料的人工增雨效果物理检验技术方法,并在试点

省进行试验试用；对试点省2013年人工增雨作业典型个例进行了效果检验，给出了试点省人工增雨作业效果及其统计显著性水平；在试点省开展了基于历史降水资料的区域相关分析研究，为科学开展人工增雨作业和效果检验工作进行理论积累；通过分析影响试点省的主要天气系统和历史作业情况，结合试点省历史降水区域相关分析研究结果，给出试点省人工增雨主要作业影响区和对比区的区划设想；完成了2014年度全国人工增雨效果检验工作总结报告。（姚展予）

4.9 高效冷暖云催化剂的研制及新装备测试、考核和业务试用

中国气象局人工影响天气中心组织开展了WMC-IN-001、WMC-IN-002型2种冷云催化剂和WMC-CN-001型吸湿性催化剂配方的调整、改进试验研究，并对催化剂的成核率进行检测。与目前业务用的焰剂类冷云催化剂成核率相比，新型冷云催化剂成核率高一个量级以上。播撒WMC-CN-001型吸湿性催化剂后，在多个速度下，大于 $2\ \mu\text{m}$ 的粒子浓度均可达到 10^4 量级；冷暖云催化剂研究成果均通过了技术认定。研制的暖云催化剂已在福建、安徽开展地面燃烧炉的业务试用，在河北开展飞机播撒试用；对业务用机载烟条、烟弹和地面烟条等催化剂的成核率进行了统一检测，保障了催化剂的作业效率；组织了随州大方精密机电工程有限公司生产的“DF37 mm高射炮远程控制系统”和华云公司生产的“HY-1型机载焰条播撒系统”的产品定型和业务试用方案的评审。（房文，党娟，方春刚，苏正军，汪晓滨，刘汐敬）

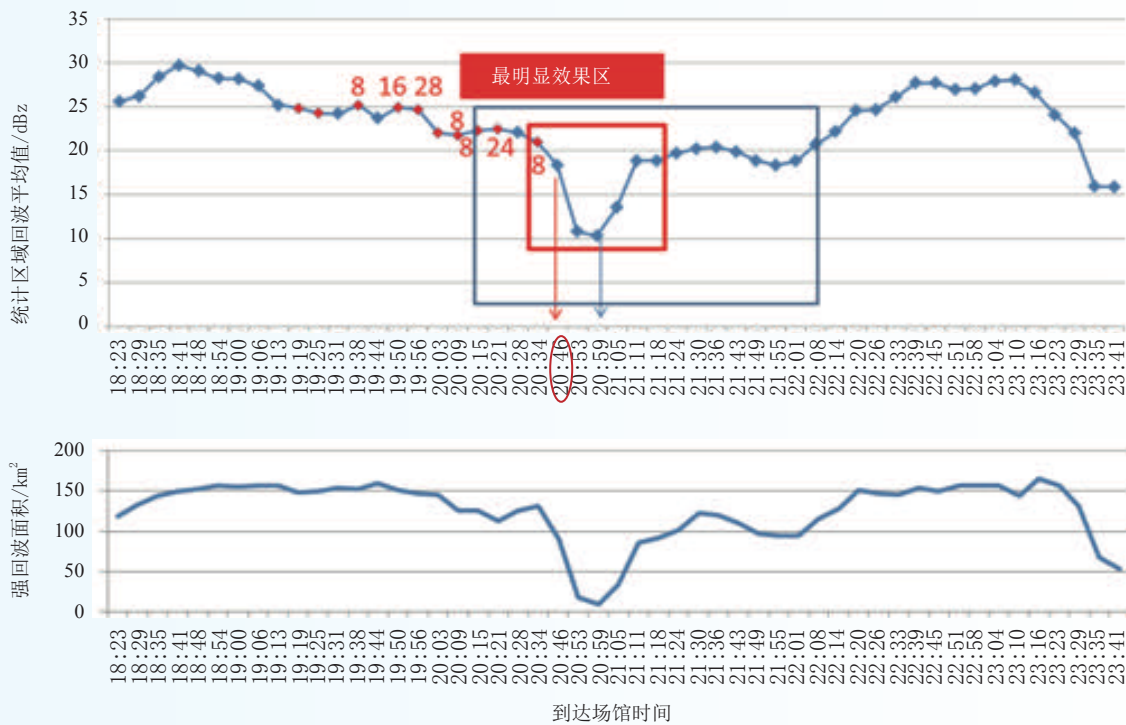


图1 2014年8月28日闭幕式主要影响云带回波平均值及强回波（大于20 dBz）面积随时间的演变（多轮次作业后保障区，保障时段（20:15—22:08）回波减弱最明显）

Fig. 1 August 28, 2014, the average echo of the statistical areas and the echo areas stronger than 20 dBz of the main influencing cloud band during the closing ceremony (The most weakened echo effect time is 20:15–22:08 after the large operations)

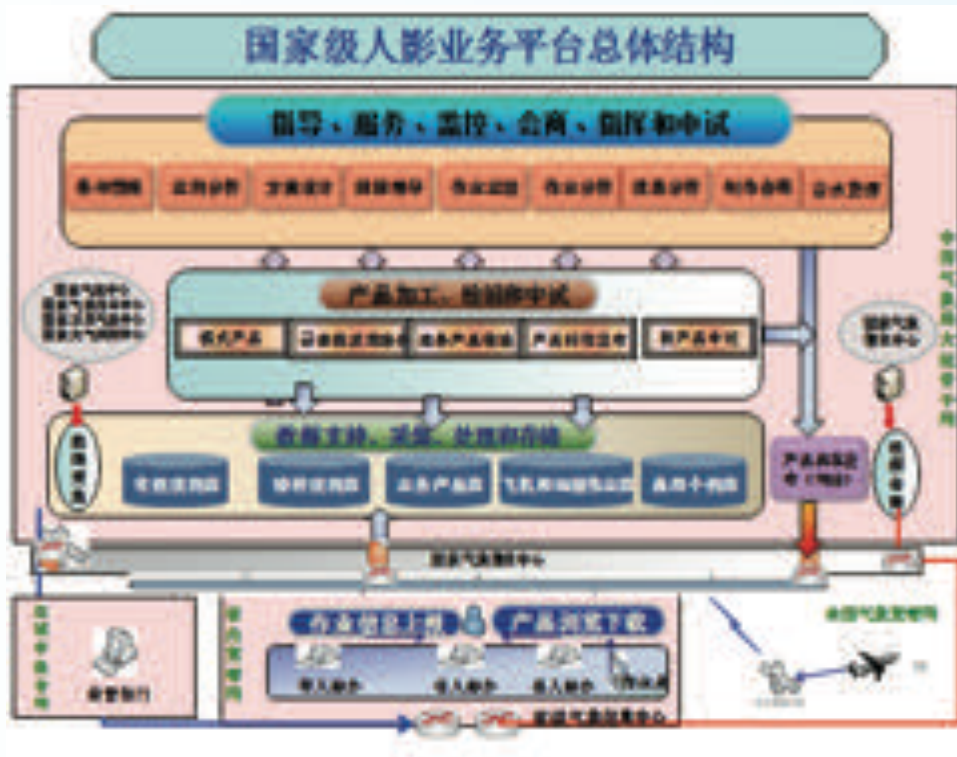


图2 国家级人工影响天气业务平台总体结构
Fig. 2 Structure of national weather modification operational platform

Advances in Cloud Physics and Weather Modification

1 Observational studies on cloud physics

1.1 Observation and analysis of characteristics of formation, evolution and transition of a long-lasting severe fog and haze episode in North China

An unusual fog and haze event lasting for one week occurred during 1–7 December 2011 over North China. To investigate the characteristics and mechanism of formation, evolution and transition of the fog and haze event, the microphysical properties such as aerosol, cloud condensation nuclei (CCN), fog droplet spectrum and liquid water content (LWC), as well as horizontal visibility and boundary layer properties were studied by using the data collected in the project of Low-Visibility Weather Monitoring and Forecasting in the Beijing-Tianjin region. The results indicate that the long-lasting fog and haze event occurred in a high pressure weather system and calm wind condition. The stable boundary-layer structure resulting from temperature inversions caused by warm advection and radiation cooling provided a favorable condition for the accumulation of polluted aerosols, and the formation and development of the fog and haze event. In particular, the continuous southerly wet advection led to a long process. The horizontal visibility was almost below 2 km in the whole process, with the lowest being only 56 m. The average LWC was about 10^{-3} g m^{-3} , with the maximum reaching 0.16 g m^{-3} . The aerosol number concentration was more than 10000 cm^{-3} , with the mass concentration ranging from 50 to $160 \mu\text{g m}^{-3}$. The further study shows that the fog and haze event experienced three main different processes in intensity during the whole period, each process being divided into three main stages: aerosol accumulation, transition and mixture of aerosol and fog, and dissipation. Each stage had different physical features: the aerosol accumulation stage was characterized by the increase of aerosol number concentration in Aitken nuclei and accumulation mode sequentially. In the transition and mixing stage of fog and haze, the latent heating produced by the fog droplet condensation process and high aerosol number concentration condition intensified the Brownian coagulation process, which induced the small size of aerosols to become larger ones and enhanced the CCN activation process, thereby promoting the explosive development of the fog event. The ratio of aerosol activated to CCN reached 17%, and the ratio of CCN converted to fog droplets exceeded 100%, showing an explosive broadening of fog droplet spectrum. The decrease and dissipation of the fog were caused by an increased solar radiation heating or the passage of cold frontal system. (Guo Lijun, Guo Xueliang, Fang Chungang, Zhu Shichao)

1.2 Ice crystal habits, distribution and growth processes in stratiform clouds with embedded convection in North China: Aircraft measurements

Ice crystal habits, distribution and growth processes in two cases of stratiform clouds with embedded convection on 18 April and 1st May 2009 are analyzed with data observed during the Beijing Cloud Experiment (BCE). The results show that ice crystal habits in clouds with temperature between $0\text{--}16 \text{ }^\circ\text{C}$ were predominantly plate, needle-column, capped-column, dendrite and irregular. Ice crystal habits were affected by the cloud top temperature (CTT), which differed with the changing CTT. Plate and needle-column were predominant habits as CTT was warmer than $-8 \text{ }^\circ\text{C}$ while dendritic and capped-column crystals were observed just as CTT was colder than $-13 \text{ }^\circ\text{C}$ and $-18 \text{ }^\circ\text{C}$ respectively. At the same time, ice crystal habits were also affected by their locations in cloud, since there were a lot of heavy rimed crystals in embedded convective

regions. Above the melting layer, ice particle grew mainly by deposition, riming and aggregation processes. The riming process became more intense in lower cloud layer due to the increase of super-cooled liquid water content. The broadening rate of particle size distributions (PSDs) is obviously different between embedded convections and stratiform clouds in the vertical direction, at levels of 4.8–4.2 km (-11.6 – -8 °C), the PSDs broadening rate in embedded convections is 3 mm km^{-1} , smaller than 3.67 mm km^{-1} in stratiform clouds, but at levels of 4.2–3.6 km (-8 – -5 °C), the PSDs broadening rate in embedded convections is 6.67 mm km^{-1} , which was almost three times as fast as 2.33 mm km^{-1} in stratiform clouds, which was mainly due to the fact that embedded convections had more super-cooled liquid water than stratiform clouds at levels of 4.2–3.6 km. (Zhu Shichao, Guo Xueliang)

1.3 A 35-channel microwave radiometer for profiling atmospheric temperature and humidity

The design principles and main characteristics of the MWP967KV ground based 35 channel microwave profiling radiometers are presented. The prototype radiometer is a compact integration of dual band (K and V) broadband radiometry antennas, two receivers, a synthesized local oscillator, a surface meteorological sensor, and a power supply in a cabinet. It has the capability of detecting down-welling atmospheric thermal emission continuously on a minute time scale. Several levels of observed data are composed and regulated. By using BP artificial neural network retrieval algorithms, the radiometer is capable of retrieving the vertical distributions (profiles) of atmospheric temperature, water vapor, relative humidity, and other variables in real time. The retrieved profiles range from the surface up to 10 km in 58 layers. The radiometer was used in atmospheric observation in Beijing in autumn to winter of 2012 for about two months. The data of 69 radiosonde cases are gathered to evaluate the radiometer's performance. The accuracies of dual band atmospheric bright temperature values are analyzed. The retrieved temperature and humidity profiles are analyzed as well, and the mean difference, root mean square difference, and correlation are calculated. The statistical results indicate that the radiometer has the ability to support real time weather surveillance, being internationally advanced. (Lu Jiangping, Huang Jiangping, Guo Xueliang)

1.4 Discriminating a cloud area by using L-band sounding data

L-band sounding data recorded from January 2008 to December 2009 and corresponding spatial and temporal CloudSat data are used to analyze the cumulative frequency distributions of relative humidity in and near clouds. It is determined that the accuracy of cloud discrimination can reach 81% against a relative humidity threshold set at 75%. In addition, various thresholds of relative humidity for discriminating clouds are evaluated on the bases of bias score (BS) and threat score (TS). By setting the relative humidity at 81%, the highest TS score of 0.66 is achieved. Moreover, relative humidity thresholds at various heights are also analyzed on the basis of BS and TS. The results show that the relative humidity threshold with the highest TS score at the same cloud height decreases when the height increases. The TS score of the discriminated cloud area with these thresholds for corresponding altitudes is higher than 0.6, and the accuracy is more than 84%, which is significantly better than that obtained by using a single relative humidity threshold for all heights. Finally, with these thresholds being optimized, a method of discriminating the cloud vertical structure is proposed by using L-band sounding data. (Cai Miao, Ou Jianjun, Zhou Yuquan)

1.5 Observation, analysis, and hail-forming area identification of a super-cell hailstorm

A detailed analysis on the evolution of stream fields and echo structures of a super-cell hailstorm that occurred on April 17, 2011, is conducted on the basis of Doppler radar data combined with radio sounding and surface observations. The main results are as follows: The hailstorm occurring in a conditional instability and significant vertical wind-shear environment was classified as a right-moving storm. A cross-section of the

development stage shows that an organized updraft was formed gradually, which promoted the formation and development of the hail cloud. During the hail-forming stage, a strong, tilted updraft and deep meso-cyclone emerged in the hailstorm; the main updraft corresponded to the weak echo region. The hailstorm maintained a typical bounded weak echo region (BWER)-overhang echo-wall echo structure. According to the evolution of zero velocity line, which connects the radar radial velocity and the speed of hailstorm, the line approached the overhang echo zone with the developing hail cloud and crossed the overhang echo. The trend of zero velocity line was upturned, and the collection power of the cave channel near the line was sufficiently strong to form hail. The hail formation area can be analyzed through the determination of the zero velocity line. A method of identifying the characteristic structure of the hail-forming region is also presented in this study. According to the strong echo dislocation of high and low levels, the characteristic structure is determined quickly and accurately from the strong echo center section at two heights. Moreover, a 45 dBz region at a 6 km height above the 0 °C layer is identified as a hail-forming region, where the potential of hail is calculated to be 100%. The identified hail region is in good agreement with the actual hail observation. (Cai Miao, Zhou Yuquan)

1.6 Observational studies of distribution characteristics of supercooled cloud water during a westerly trough process

The growth and evolution of supercooled water are always a concern in the cloud physics and weather modification science. Based on the hypothesis proposed by Hobbs in 1974, a westerly trough in Hebei Province on 21 September 2012 is analyzed by using the airplane observation, satellite monitoring, radar monitoring, and other regular observation data. Results show that (1) a wide and thick area of supercooled water exists in front of the trough where the supercooled water is abundant, the concentration and root mean cube diameter of the forward scattering spectrometer probe (FSSP) are relatively of high value, and the cold cloud is thick without dry layers or warm cloud; (2) as the trough draws near, the cloud near the trough develops rapidly, the concentration and depth of the area of the supercooled water increase significantly, the cloud becomes thicker with dry layers, the liquid water content (LWC) in cold and warm cloud is abundant, meanwhile the concentration of 2DC and 2DP is of high value, and the mesoscale structures move quickly; (3) in the rear of the trough, the root mean cube diameter of the droplets and the amount of the supercooled water are remarkably small, and the height and width of the supercooled water decrease a lot, although the cloud concentration is still high, the cold cloud is very thin with a dry layer between warm cloud and cold cloud, and the warm cloud has several layers with a high value concentration of 2DC and 2DP. The precipitation is produced by the warm rain process. Usually the peak of the LWC stays over the temperature inversion layer. The results based on the analysis of the particle measurement system (PMS) data are well consistent with those based on the satellite and radar monitoring data. (Zhou Yuquan, Sun Jing)

2 Cloud physics and artificial seeding simulation researches

2.1 A case study of aerosol impacts on summer convective clouds and precipitation over North China

The emissions of greenhouse gases, precursor gases and particulate matters may directly alter the Earth radiative budget or indirectly modify cloud and precipitation processes, and possibly induce changes in climate and the hydrological cycle at the regional to global scale. The previous publications reported a few quantitative assessments and inconsistent results on the effects of the emissions on cloud and precipitation. The aerosol properties and possible impacts on a convective precipitation case on 4 July 2008 over the urban region of North China are investigated based on the Moderate Resolution Imaging Spectroradiometer (MODIS) data and

the Weather Research and Forecast (WRF) model coupled with Chemistry (WRF-Chem). Results show that the Aerosol Optical Depth (AOD) is over 0.9 in the study area, indicating a high concentration of aerosol pollution. The value of Angstrom exponent in the study area is larger than 1.0, indicating that the main particles in the area are industrial and biomass burning pollution aerosols with a radius of less than 0.25–0.5 μm . The modeling results show that the domain-averaged precipitation amount under polluted conditions can be increased up to 17% during the whole cloud lifetime. However, the maximum rainfall rate above 30 mm h^{-1} is enhanced, whereas that below 30 mm h^{-1} is suppressed in most cloud lifetime. The differences of cloud microphysics and dynamics between polluted and clean conditions indicate that both warm and ice microphysics and updraft are suppressed at the storm's initial and dissipating stages, whereas those at the storm's mature stage are obviously enhanced under polluted conditions. (Guo Xueliang)

2.2 Theoretical research on AgI seeding simulation of the decreased convective rainfall

After two prognostic variables are added, An AgI seeding scheme is coupled with a three-dimensional cloud model, considering four nucleation modes. A case of heavy convective rainfall is simulated using this model. Numerical seeding experiments of releasing AgI in cloud are simulated to study the possibility to decrease the heavy convective rainfall. Several tests of different locations and different concentrations of seeding particles are designed. Results show that over-seeding in an updraft area with supercooled water can not only reduce the amount of rainfall, but also reduce the maximum rainfall strength. With $2 \times 10^8 \text{ kg}^{-1}$ seeding concentration, rainfall amount can be decreased up to 32%, which greatly lowers the possibility of causing flood. After seeding with large amounts of AgI, numerous AgI particles are nucleated, and these ice particles consume much supercooled water. The falling speeds of graupel and raindrops become weaker after seeding. The decrease of melting amount of graupel to rain in seeding cloud causes the decrease of rain amount, and later the much more evaporation of rain causes less rainfall amount. Results show that condensation freezing and immersion freezing are the dominant nucleation modes in this convective cloud. The over-seeding methods in this research are able to be used in a field operation. (Lou Xiaofeng, Sun Jing, Shi Yueqin, Zhang Xing)

2.3 Effects of underlying surface on the formation and evolution of hail cloud

A severe hailstorm in Beijing on 31 May 2005 was simulated using mesoscale model WRF and compared with the observed radar echo, hailstorm moving path and hail fall area. The effects of underlying surface of cities and farmland on hailstorm was investigated. The results show that due to the effect of Urban Heat Island (UHI), the sensible heat flux is obviously increased, which is favorable for the development of hail cloud and enhancement of vertical velocity and formation of larger-sized hailstones, and the increase of the surface accumulated hail fall. But the influence of urban surface on the moving path on hail cloud is smaller. The farmland surface has larger latent heat flux and higher evaporation, which is favorable for the formation of a large amount of smaller-sized hailstones, and induces weak vertical velocity and small mean diameter of hailstones in the cloud. The surface accumulated hailfall decreases due to the weakening intensity of hail clouds for farmland surface. (Guo Xueliang)

2.4 Numerical simulation of a convective stratiform mixed cloud precipitation at different scales

The precipitation of a convective stratiform mixed cloud in Zhangjiakou during 18–19 April 2009 is simulated using the mesoscale numerical model WRF-ARW (V3.2) and comparatively analyzed with the observation data at different scales. Results show that the west wind trough at 700 hPa and the low vortex at 850 hPa are the main weather systems responsible for convective stratiform mixed cloud. The warm wet air from the southern China and the low vortex from northwest Inner Mongolia are main water vapor suppliers, which converge in Zhangjiakou region and thus are conducive to cloud system development and precipitation

formation. The cloud system shows a NE-SW banded distribution, which is 1000 km long and 300 km wide, and has lots of cloud water centers, covering tens of kilometers. The cloud system has the echo characteristics of typical convective stratiform mixed cloud precipitation, such as columnar echo of cumulus cloud embedded in a uniform echo layer. The cross-section of radar echo shows that the cloud water content is heterogeneous either horizontally or vertically. The centers of rainwater are corresponding with the centers of graupel and snow in the upper layer, with a horizontal range of 10–20 km. (Zhang Wei, Zhou Yuquan)

2.5 Numerical simulation and flight observation of stratiform precipitation clouds in spring in Shanxi Province

The CAMS meso-scale cloud model was introduced and operationally applied in Shanxi Province in 2009. The macro and micro structure of stratiform precipitation clouds, especially the vertical micro-physical structure are simulated and analyzed of a spring stratiform precipitation process in Shanxi Province on April 20th, 2010 by using this model. Two times of cloud physical detection flights are carried out by using a weather modification plane equipped with Droplet Measurement Technologies (DMT) in the same place during the same period of that day. The data and images from flight detection and the results of numerical simulation are compared and studied. Simulation results show that the precipitation process mainly comes from cold stratiform cloud. The cloud contains a lot of supercooled water, and the thickness of the rich supercooled water layer is about 4000 meters. The temperature of the supercooled layer was 0– -40 °C, and the ratio content of the supercooled cloud water is 0.1–0.7 g kg⁻¹ with some ice crystals distributed unevenly. The structures of the stratus precipitation cloud can be roughly divided into three layers. The first layer (upper layer) is mainly composed of ice crystals; snow, sleet, and supercooled cloud water is mixed in the second layer (middle layer); and the third layer (lower layer) is mainly of liquid raindrops. The vertical distribution and the transformation of different hydrometers in different stages of the precipitation are analyzed. The precipitation mainly comes from the melting of the ice phase particles such as ice crystals, snow, sleet and the transformation of liquid cloud droplets. A comparison of the numerical simulation results and the plane observation shows that the relationship between temperature and altitude is in good agreement. The simulated vertical structure of the different cloud particle phase and the vertical distribution of the cloud liquid water ratio content are nearly the same as the vertical distribution of different cloud particle images and the cloud liquid water content of the flight detection. The difference is that the simulated height where various hydrometeors appear is higher than the actual flight detection. (Tao Yue, Shi Yueqin)

3 Research on technology of weather modification

3.1 Study of anti-aircraft-gun, plane and rocket cloud seeding diffusion and operation designing

This article gave out the diffusion law of different seeding ways such as anti-aircraft-gun, rocket and plane, based on the analytical solution of cloud seeding agent diffused in cloud, by the diffusion calculation model of point source, multi-line source and mobile point source. It studied the diffusion law and effective range of different seeding ways and examined the calculation scheme by using a flight seeding track caught by a satellite, and discussed such problems as adequate seeding flight designing. The main conclusions were as follows: As a point source, when using a single anti-aircraft-gun for work, the operation range was only 0.5 km, it would be better to use multi-shell for keeping concentration and diffusion range, the work effect can be improved largely when nucleation rate was raised. The work of rockets and planes was calculated as a line source, the widths beyond threshold value 1 h after seeding were about 7 km and 6.6 km, which could be taken as a reference for the multi-line seeding flight interval. Due to the effect of wind, the diffusion areas would disperse or overlap when

using ‘S’ seeding way. The best flight design which could make the target area get adequately seeded was a ‘8’ shaped flight route. The cloud seeding diffusion calculation and work designing software developed based on diffusion calculation model could calculate the diffusion range, concentration and evolution by time of agents released from a plane, an anti-aircraft-gun and a rocket in real work, and could design the seeding ways for effective work in different target areas. The results, which were direct and clear, helped with the actual work application and seeding diffusion calculation as a guidance to weather modification in our country. (Zhou Yuquan)

3.2 Evaluation of precipitation enhancement and hail suppression programs in Beijing region

Seeding effects investigation or evaluation is one of the most important parts of weather modification. It also acts as a crucial standard of assessing the scientific and technological level of weather modification activities, and plays an extremely important role in promoting the development in this connection. Taking into account the activities implemented in Beijing region in recent years, we assessed the seeding effects of precipitation enhancement and the economic benefits of hail suppression between 2004 and 2010, based on the classical method of historical regional regression and the agricultural disaster data collected around the whole region. The results indicate that: (1) in the assessment period from May to September, the average ratio of precipitation enhancement efficiency tends to stand at about 20 percent with the sample numbers being accumulated year by year. In the target area selected, cloud seeding totally increased the precipitation amount by 417.8 mm during the 7 years. The statistical seeding effect is of high significance; and (2) the estimated average annual economic benefit of hail suppression is nearly 248 million yuan. The average cost-benefit ratio is about 1:16. The highest and the lowest economic benefit appeared in 2009 and 2005, with a corresponding cost-benefit ratio of 1:27 and 1:6, respectively. The methods studied for seeding effects evaluation and results help to strengthen the exploitation and utilization of cloud water resource in a scientific and technological sense in Beijing and its neighboring regions, which firmly supports the approval of local disaster prevention and mitigation projects as well. (Li Hongyu)

3.3 Research on and application of a method to evaluate the effectiveness of convective cloud precipitation enhancement

The reliability of convective cloud-seeding effectiveness evaluation is poor when a traditional statistical test method is used because of its large spatial and temporal variation. The floating-target area method, a new one proposed by Woodley, is introduced, which is based on radar echoes. Some changes are made to this scheme taking into account Tianjin’s terrain and weather modification operation characteristics. The radar based data are used to determine the floating target cell recognition and tracking methods, then determine the catalytic units and control units in the floating target cells; the physical parameters and the retrieved precipitation of each unit are recorded, and the precipitation enhancement effect is calculated to provide physical evidence on artificial rainfall. The method is used to evaluate the effectiveness of convective cloud-seeding on 24 July 2011 in Tianjin, for example, and the objective evaluation results are obtained, which show that: the value of the maximum echo intensity and echo top height increased as the catalyst got into the clouds. It proves that artificial catalysis takes effect in precipitation enhancement. The effectiveness of precipitation enhancement is 7.69% at a significance of 0.043. (Li Hongyu)

4 Progress in weather modification

4.1 National Weather Modification Development Plan (2014–2020)

In December 2014, National Weather Modification Development Plan (2014–2020), formulated by CMA

Weather Modification Centre, was jointly issued by NDRC (National Development and Reform Commission) and CMA (China Meteorological Administration). The plan identifies the guidelines, goals, overall layout, main tasks and implementation arrangements of the nationwide weather modification program, and also proposes an organization, management and operation mechanism for weather modification work. The plan serves as a program of action for nationwide weather modification at present and in the near future, and is of guiding significance to weather modification modernization and its scientific development. From October to November of 2014, National Weather Modification Operations Development Guidance, Weather Modification Dedicated Technology and Equipment Management Regulations were formally issued by CMA, marking that China's weather modification operations and equipment are managed by standards. (Chen Tianyu, Zhou Yuquan, Fang Wen)

4.2 Northeast Regional Weather Modification Capability Building project

The year 2014 showed signs of benefits in the project of Northeast Regional Weather Modification Capability Building. Within one year, primary design revision and approval were completed; the first Xinzhou 60 artificial rainfall aircraft finished its test flight and made its debut in the 10th China International Aviation & Aerospace Exhibition; the third high performance artificial rainfall aircraft was completed in overall design, with 11 sets of airborne equipment having been selected; regional aircraft operation support center started its construction; main features of control system were deployed in the four northeastern provinces; the procurement was finished for high performance operation of aircraft satellite communications system, including 79 GPS/MET devices, 3 X-band Doppler weather radars, GPS/MET data processing center software system and all the devices for external field test areas; training classes were held for weather modification frontier technology & aircraft operations. The initial fruit of the project has played an important role in drought relief and rainfall enhancement efforts in the Northeast China region. (Li Jiming, Chen Weihong)

4.3 The Collection and Processing System of Weather Modification Operation Information OICPS V1.0 being in operational use

Based on years of professional work, the OICPS V1.0, part of Weather Modification Centre (WMC) Operational Control System project, was accepted by experts on 21th May. The OICPS V1.0 is the second operationally accepted system following the weather modification forecast model system. The OICPS V1.0 composes two parts, a real-time upload system and information acquisition & processing system. Relying on the national meteorological network, it makes it possible for the national weather modification operating information to be uploaded, collected, monitored, stored, displayed and managed. A variety of basic data, including information on stations, operations, practitioners and ammunitions, are integrated to offer timely and reliable information for effectiveness analysis and evaluation, joint guidance to an operation and production of decision services. Since the system's running, the uploading of operation data has been effectively improved, the strength of WMC capability in guidance and service has been enhanced as a strong support to all other operators in control and evaluation. (Wang Fei, Yang Lianying, Li Kangkang)

4.4 Geostationary satellite-based retrieval system for cloud precipitation characteristics in weather modification (CPPS-GSSL 2.0) was put into operation

With many years of efforts, Weather Modification Centre of CMA developed the geostationary satellite-based cloud characteristics retrieval system (CPPS-GSSL 2.0), which was accepted in a technical review organized by the Department of Disaster Alleviation, CMA. The conclusion has been published and notified: the retrieved products are open to operational use.

The retrieval system (CPPS-GSSL 2.0) is based on FY-2 series geostationary meteorological-satellite and

L-band sounding data and their real-time retrieved cloud characteristics related products such as Tbb, cloud top height, cloud top temperature, supercooled layer thickness, cloud optics thickness, cloud particle effective radius and liquid water path. By comparing with MODIS retrieval parameters along with a physical analysis of CloudSat cloud-radar, weather radar, raindrop size distribution and ground precipitation data, the accuracy and the usability of the system have been examined. The retrieval products have been used smoothly in all the provinces throughout China as a technical support to multi-regional cloud seeding, forest-grassland fire extinguishing and rain suppression for important social activities. (Cai Miao, Zhou Yuquan)

4.5 The successful weather modification for opening and closing ceremonies of the 2014 Second Summer Youth Olympic Games

On August 16 and 28, 2014, the opening and closing ceremonies of the Second Summer Youth Olympic Games were held in Nanjing Olympic Sports Center. In order to ensure the smooth ceremonies, the organizing committee raised the need to carry out cloud seeding tests and services. Meteorological Bureau of Jiangsu Province invited the Weather Modification Centre of the CMA (WMCMA) to guide the relevant tests and services for the whole operations, with rainfall obviously suppressed. In the opening ceremony, the precipitation at the stadium is about 2 mm, while the average precipitation around it is 5 mm. The numbers in the closing ceremony are 0.2 mm and 0.68 mm. The operations ensured the success of the ceremonies. The preliminary summary of the key technical work mainly includes:

(1) Based on the analysis of the characteristics of the cloud precipitation and the weather in Nanjing in August, the WMCMA put forward and guided the technical scheme for the weather modification for the ceremonies, including the intensive monitoring, the communication command, the layout design of operations, implementation organization and so on.

(2) Thanks to the numerical prediction model for the weather modification operation conditions the WMCMA developed, the catalytic principle and scheme were given 24 h in advance. Combined with the weather forecast and the monitoring of the actual situation, a real-time interaction between the WMCMA and Youth Olympic Command Center was maintained for the discussion on and the revision of the scheme and the estimation of the result.

(3) The Cloud and Precipitation Precision Analysis System (CPAS) developed by the WMCMA was transplanted to establish a command system of rain decreasing operation for the Youth Olympics. The real-time precision analysis of the macro and micro structures of the cloud and the evolution of the precipitation, recognition and discrimination of the operating conditions, the rolling correction of the optimal design for the operation, the real-time command of the multi-catalytic (plane and rocket) by satellite, radar, sounding and many other special instruments were realized.

(4) Thanks to the transplanted CPAS platform and operation command system, planes were used to do the periphery reconnaissance for the pre-operation and for the highly dense rocket based catalytic operation in the adjacent zones. The clouds that were moving towards the venue were successfully weakened, which proved the technical principle and the design before the operation, with expected effects being observed (Fig. 1). (Zhou Yuquan, Liu Siyao, Pu Meijuan, Hu Zhijin)

4.6 National weather modification (WM) operational platform plays an important role in WM guidance and service

National weather modification (WM) operational platform was developed by Weather Modification Center (WMC) in 2014. The platform mainly includes 4 parts. First part is to transfer, collect, store and manage information for real time use, such as meteorological observation data, WM special observation data, WM

seeding data and ground operation data, based on which a database of case studies is developed. Second part is to process, verify and test products. By synthesizing various data, WM characteristic cloud and precipitation variables are produced to be used to forecast and warn seeding potential conditions. Third part is WM operational guidance and service, including forecasting seeding potential conditions, early warning, designing field seeding scheme, monitoring and commanding, and seeding effect evaluation and so on. The last part is to share various WM products by website to be used by relevant professionals.

The operational platform plays an important role in real time weather modification service. For example, a video consultation was held together by CMA-WMC, Northeast Regional-WMC, Heilongjiang Weather Modification Office, Jilin Weather Modification Office, Liaoning Weather Modification Office and Inner Mongolia Weather Modification Office in April 2014. In this consultation, the structure of cloud system and distribution of cloud band, supercooled water and ice particles in the northeast of China were analyzed. The seeding time, area, and height of rain enhancement were also discussed. The Northeast Regional-WMC arranged the inter-provincial joint operation according to rain enhancement demand. All of these marked the beginning of the operation model which features joint actions through a level-based guidance. As a result, weather modification is improved in science and in benefit (Fig. 2). (Zhou Yuquan, Shi Yueqin, Sun Jing, Cai Miao, Liu Weiguo, Tao Yue, Wang Fei)

4.7 Optimizing the evaluations of air cloud-water resources

As a result of continuous research and experiment during 2011–2014, Weather Modification Centre of CMA developed and improved the monitoring evaluation method for cloud water resources (CWR-MEM). The method is based on the atmospheric water vapor budgeting equation, clarifying the concept of atmospheric water substance including hydrometeor. It improved the calculation equation and concept of water substance mass, precipitation effectiveness and update period etc. It proposed such new concepts as cloud water resources, aggregation of cloud water resources and effective cloud water quantities.

In 2014, Weather Modification Centre of CMA organized the technical forces to optimize the evaluation methods of diagnosis and identification of three-dimensional water and cloud field, temporal-spatial scales and the processing of complex area boundaries. China was divided into five areas by longitude and latitude and by climate. 2007–2008 CloudSat's observation data were used to count the relative humidity threshold, typical liquid water content values and their vertical distribution of each diagnosed cloud field. The height coordinate was changed into temperature coordinate, which made the cloud field concept more accurate, sharply optimizing the diagnosis scheme of three-dimensional cloud and water field in each area. To evaluate the cloud water resources, it is desirable to take six weather modification areas into consideration, before subdividing each area into six sub-areas, the borderline of which is made a loop curve with the resolution at 1° . This improves the calculation of condensation and evaporation values, including the integral resolution and accuracy.

The 2014's cloud water resources monitoring report was prepared using the optimized CWR-MEM scheme with which the cloud water resources in six weather modification areas throughout China from 2008 to 2011 were evaluated. The results are as follows, from 2008 to 2010, the gross quantity of vapor in China was averaged around 36900 billion tons of which 33100 billion tons was input from the boundaries while evaporation was averaged around 3750 billion tons. The gross quantities of hydrometeor (GQh) were averaged at 7150 billion tons. The total precipitation volumes were averaged at approx. 5020 billion tons. Gross cloud water resources were averaged at 2130 billion tons whilst cloud water resources at 1230 billion tons. Annual water vapor precipitation effectiveness was averaged at around 14% while effectiveness of the hydrometeor precipitation was 70%. The update period for the vapor was averagely about 10 days and 7 hours

for the hydrometeor. It can be concluded that the cloud water resources differ distinctly in temporal-spatial distribution. (Zhou Yuquan, Cai Miao)

4.8 Evaluation techniques and methods for cloud seeding effect

Based on the detailed analysis of the information from weather modification operations in the whole country, the specific rain enhancement requirements in different regions are revealed. Four kinds of methods have been developed and integrated to evaluate the effect of nonrandomized rain enhancement operation, and the relevant testing algorithms of the significance level have been researched and developed as well. These algorithms have been applied in Jiangxi, Yunnan, Hainan, Chongqing and Anhui provinces. The Doppler radar identification, tracing and testing algorithms have been developed based on TITAN techniques and the physical evaluation methods based on regular radar data, which have been applied in the piloted provinces. Typical cloud seeding examples in 2013 in the piloted provinces have been analyzed and tested, and the evaluated effects as well as the statistical significance levels have been released. The regional correlation analysis has been made based on the historical rainfall data in the piloted provinces, which is useful for the theoretical accumulation in the field of rain enhancement operation and effect evaluation. According to the analysis of the synoptic systems and historical operations in the piloted provinces, as well as the regional correlation analysis, a designed mapping of the target areas and control areas for the cloud seeding in these provinces has been proposed. The summary report 2014 of rain enhancement effect evaluation in China has been prepared. (Yao Zhanyu)

4.9 The development of efficient seeding agents for warm and cold cloud, and testing, assessment and trial of new devices

The Weather Modification Center (WMC) of CMA developed three types, WMC-IN-001, WMC-IN-002 and WMC-CN-001, of cloud seeding flare agents, tested their nucleation rate in cloud chamber, and compared them with those flare agents used in recent rain-enhancement operation. The result shows that the nucleation rates of WMC-IN-001 and WMC-IN-002, which are for cold cloud seeding, are higher by one order of magnitude at least than those used in operation. Under different wind speeds, the particle spectrum of WMC-CN-001, which is hygroscopic type seeding agent, is tested in a wind tunnel. The result shows that the number concentration of particles whose diameter is more than 2 μm is up to 10^1 . The above three cloud seeding agents have been recognized by the Department of Science & Technology and Climate Change of CMA.

WMC carried out the trial use of hygroscopic flare for warm cloud in Fujian, Anhui and Hebei provinces, for ground smoke stove in Fujian and Anhui provinces, and for airborne flare in Hebei Province. Working jointly with Shanghai Material Management Division of CMA, WMC tested the nucleation rates of airborne and ground-flare, and flare bomb. A review of product design and operation oriented trial plan for “the remote control system for DF37 mm anti-aircraft guns” produced by Suizhou Dafang Precision Mechanical Engineering Co. Ltd. and “HY-1 type airborne flame strip seeding system” produced by China cloud company was organized. (Fang Wen, Dang Juan, Fang Chungang, Su Zhengjun, Wang Xiaobin, Liu Xijing)

生态环境与农业气象

Ecological Environment and Agrometeorology

生态与农业气象研究进展

1 生态和农业气象基础理论与应用技术研究

1.1 高时空分辨率数据融合模型研究

本研究对基于MODIS产品（高时间分辨率、低空间分辨率）和Landsat卫星数据（高空间分辨率、低时间分辨率）光谱相似性、像元空间尺度和时间差异的数据融合模型STARFM进行如下改进：（1）将MODIS双向反射率数据校正为天顶方向，根据地表覆盖类型数据实现BRDF产品的缺测值填图；（2）利用滑动窗技术，计算得到MODIS和Landsat数据的最大相关系数，进而实现MODIS和Landsat数据的几何精度校正；在此基础上构建集成的数据融合模型框架（Integrated STARFM, ISTARFM），实现模型半自动化运行。该模型框架可以实现两类数据在时间分辨率和空间分辨率的向上融合，为高时频、精细化冬小麦区域干旱监测服务。（王培娟）

1.2 Landsat地表参数反演及空间尺度转换

利用LEDAPS（Landsat Ecosystem Disturbance Adaptive System）模型，将最新发射的Landsat8卫星数据的DN值转换为地表反射率，以地表反射率数据为基础，计算得到归一化植被指数（NDVI）、叶面积指数（LAI）和地表温度（LST）。反演30 m分辨率地表温度数据时，首先将Landsat8的30 m反射率数据进行降尺度转换到100 m，得到与热红外波段空间分辨率相同的地表反射率数据，建立地表反射率和地表温度的回归模型T-R（Temperature-Reflectance），而后利用该模型和30 m分辨率的地表反射率数据，实现地表温度的精细化空间尺度转换（图1）。（王培娟）

1.3 精细化逐日多层土壤墒情和灌溉预报系统研发

基于土壤水分、土壤质地、蒸散、遥感水分亏缺指数等数据集，通过像元匹配、误差分析和神经网络等方法，研究了土壤水分人工、自动、遥感监测等多资料融合技术。利用中国103个站1961—2010年逐日总辐射和日照时数资料，分析了 a 、 b 系数时空变化规律，确定了中国不同区域各年代 a 、 b 系数参考值。在前期冬小麦农田水量平衡简化模型和精细化逐日多层土壤墒情和灌溉预报模型研究基础上，构建了3个省级预报系统（试用版），并在2014年冬小麦主要生长季进行试用。进一步开发了基于数据管理、数据处理、土壤墒情预报、灌溉量预报、产品制作、效果检验6个模块的业务应用平台，并在河北省进行了初步本地化应用，发布服务产品3次。（毛飞）

1.4 夏玉米生理生态与生长特性对干旱过程的响应研究

夏玉米在七叶期灌水处理15天后发生轻旱，1个月后发生中旱，2个月后发生特旱。轻旱条件下，拔节期玉米叶片光合作用存在“午休”现象，顶部第一片展开叶光合速率、蒸腾速率、气孔导度和水分利用效率对干旱响应敏感，具有指示作用。全生育期内玉米叶片光合速率、蒸腾速率和气孔导度均随干旱发生发展呈下降趋势，叶片水分利用效率则呈上升趋势。叶片光合速率、蒸腾速率和气孔导度前期下降幅度较大，处理间差异显著，随干旱发展，土壤相对湿度差异减小，后期下降幅度减小，处理间差异也减小。叶片水分利用效率前期上升幅度较小，处理间差异也较小，干旱发展后期上升幅度较大，处理间差异也较大。夏玉米生育期内叶片含水率随干旱发生发展呈线性下降趋势，并与土壤相对湿度显著相关，可表征玉米的受旱程度。随着干旱的发生发展，玉米光合限制因素由气孔限制向非气孔限制转换，干旱强度越大、持续时间越长，叶片光合限制因素转换时间越早，且转换发生时叶片

含水率越高。夏玉米茎含水率在拔节期达到最大值（93%左右），茎含水率对土壤水分胁迫的响应没有叶片含水率灵敏。土壤相对湿度较高处理的叶面积指数在抽雄期达到最大，土壤相对湿度较低处理的叶面积指数在灌浆期达到最大。比叶面积前期呈迅速下降趋势，后期维持稳定并略有下降趋势；比叶重在开花期前呈明显上升趋势，开花期后呈稳定并略有上升趋势，比叶重在生长末期显著高于生长初期。夏玉米地上生物量累积对土壤水分变化反应灵敏，玉米各生育期的生物量干重均随土壤相对湿度的下降而减少。拔节期和抽雄期干旱造成的夏玉米地上生物量增幅明显下降。干旱条件下夏玉米地上生物量平均每天增幅速率在1.15 ~ 1.74 g/d之间，增幅速率随土壤相对湿度的下降而下降（图2）。（周广胜）

2 农业气象防灾减灾技术研究

2.1 基于TIGGE和分布式水文模型的农业干旱预警

采用全球三大TIGGE数据归档中心（中国气象局、欧洲中期天气预报中心和美国国家环境预报中心）的TIGGE资料，基于NOAH_LSM对TIGEE资料进行动力降尺度、神经网络ANN、TOPMODEL和新安江水文模型构建了新的水文模型XXT。研究把土壤蓄水容量曲线和地下水水位线紧密关联，形成新的蓄水容量曲线概念，并与TOPMODEL土壤分层结构及地下产流方程结合，提取了新产流方程和新的水量平衡方程，在此基础上构建了新型降雨-径流模型——XXT。虽然，此时的XXT模型通过大量试验验证了其比传统的TOPMODEL和新安江水文模型性能优越，但由于该模型的本质是基于物理过程的模型，所以在预测精度上仍然比经典的基于人工智能技术的统计模型（如神经网络，支持向量机等）要差。为了提高其模拟精度，我们首次将神经网络模块嵌入到XXT模型的产流方案中，这与传统方法显著不同，因为传统方法是将神经网络模块集成到基于物理过程的水文模型的汇流方案中。（赵俊芳）

2.2 冬小麦干旱预测预警模式研发

在山东农业大学国家重点实验室试验站利用美国Li-COR公司生产的Li-6400便携式光合作用测定系统测定了干旱条件下作物光合生理生态参数变化情况，用英国Hansatech公司生产的FMS-II脉冲式调制荧光测定仪测定了叶片叶绿素荧光参数。研究表明：随着干旱胁迫的加剧， Φ_{PSII} 呈现出明显的下降趋势，表明严重干旱胁迫时，叶片PSII的实际量子效率的影响显著， F_v/F_m 与 F_v/F_0 均与 Φ_{PSII} 一致；随着干旱胁迫程度加剧呈持续降低，或呈现降低—升高—降低趋势，表明夏玉米在经受适度水分胁迫时，可以作出一定的适应性调节反应，其调节程度与品种有关。基此，将农业干旱识别模式中的相关模块进行了相应改进，在此基础上利用C++与Fortran混合编程技术，建立起了适用于我国山东、河北及河南3省的农业干旱预测预警模式，小麦干旱综合预测预警准确率达到85%以上。（刘建栋）

2.3 华南地区龙眼寒害时空分布规律及演变趋势

基于华南4省（福建、广东、广西、海南）64个气象站点1961—2012年逐日资料，根据《龙眼寒害等级标准》，选取影响龙眼寒害的主要影响因子，计算龙眼寒害指数，确定各级别寒害的发生频率；通过对龙眼寒害指数矩阵、主要发生月份（11月至次年3月）寒害指数矩阵的经验正交分解（EOF），提取第一时间分量，分析了近52年华南龙眼寒害时空分布特征。结果表明：受气候变暖影响，华南地区平均积寒随年代呈减少趋势，有利于龙眼寒害的减少；时间分布特征为1—2月为寒害发生频率最高的月份，体现了年寒害分布的主要特征，是年寒害发生的最主要时段，但发生频率随年代呈现明显减少趋势。11—12月和3月不是年寒害发生的主要时段，发生频率相对低，但个别年份仍有可能出现较重寒害；龙眼寒害空间分布呈明显纬向分布，寒害发生频率由南至北增加，寒害还与地理位置有关，发生频率由沿海至内陆增加，研究结果与历史记载情况基本一致。对闽东地区龙眼寒害风险分析表明，1981—2010年闽东沿海龙眼寒害发生概率较大（0.42 ~ 0.43），风险概率为0.10 ~ 0.16。（赵俊芳）

2.4 西南地区农业与水稻洪涝灾害发生等级评价指标构建

针对西南地区农业与水稻洪涝灾害监测预警的需求，基于西南农业区341个气象站1961—2010年

的逐日降水量、分省农业洪涝灾情、分县水稻产量等资料,以重庆市单站洪涝等级指标(过程降水量)为原型,通过对原型指标中不同等级洪涝的降水量临界值进行幅度为 $-50 \sim +50$ mm、步长为1 mm的增减,得到各单站共101个洪涝指标,在此基础上,分别构建单站、分省逐年洪涝指数以及平均每站分省逐年洪涝指数,采用灰色关联度方法确定不同等级洪涝对实际灾情的影响权重,综合考虑由101个洪涝指标计算得到的洪涝指数与农业洪涝实际受灾程度的相关性、指标与历史洪涝灾害记录的吻合性以及分省指标的可比性,优选构建了分省农业洪涝等级指标。基于分县水稻减产率与洪涝指数、洪涝过程日数、过程降水量,构建了水稻洪涝等级指标。依据构建的指标,揭示了西南地区农业与水稻洪涝灾害的时空分布特征。近50年云南、贵州、四川、重庆农业洪涝发生较严重的年代分别为20世纪80年代、20世纪90年代、20世纪80年代和21世纪初。近50年洪涝的多发区分别位于云南西南和东南部、贵州西南部和四川盆地的西部和东北部。一季稻洪涝危险性指数高值区主要位于四川中北部、云南南部以及贵州西南部(图3)。(霍治国)

2.5 重大病虫害发生的气候背景指示指标与长期预测、动态预警模型优化

针对重大病虫害(小麦白粉病、稻飞虱)发生气象条件监测、预警与评价的业务应用需求,基于1971—2010年病虫害发生面积、发生程度、74项大气环流特征量、北太平洋海温场格点资料,采用因子膨化、空间拓扑分析、最优化处理、因子独立性检验等方法,补充构建了全国小麦白粉病发生面积率等级的大气环流、北太平洋海温指示指标;经验证检验,指示因子对小麦白粉病发生流行等级指示效果较好。补充研发了全国稻飞虱发生程度、小麦白粉病发生面积率等级的大气环流预测模型、北太平洋海温预测模型,对应的模型等级预测正确率分别为97.5%、82.5%、82.5%、80%。补充研发了基于fisher判别分析的广西桂林地区稻飞虱发生程度等级、河北地区小麦白粉病发生程度等级的动态预警模型,桂林地区稻飞虱发生程度等级的回代检验、预测检验基本一致,准确率分别为84.6%、88.2%,河北地区小麦白粉病发生程度等级回代检验、预测检验基本一致,准确率分别为97.8%、95.0%。(霍治国)

2.6 南方双季稻低温灾害时空分布特征及风险分析

针对中国南方双季稻区早稻播种移栽期低温灾害、晚稻抽穗扬花期寒露风灾害,基于169个气象站1981—2010年的逐日平均气温资料、气象行业标准规定的双季稻低温灾害等级指标,综合考虑不同低温灾害等级及其出现的风险概率,构建了低温灾害综合风险指数,揭示了双季稻不同低温灾害等级发生次数的时空变化以及等级风险和综合风险的地理分布特征。近30年南方早稻低温灾害、晚稻寒露风(粳稻、籼稻)轻、中、重度发生次数以及总次数总体均呈减少趋势,但部分区域呈增加趋势,按灾害呈增加趋势覆盖面积的大小依次为粳稻寒露风、早稻低温灾害和籼稻寒露风。中重度灾害风险高值区:早稻低温灾害主要位于湖南、江西、福建3省的部分地区,发生概率中度为20%~40%、重度在10%以下;粳稻寒露风主要位于云南种植区中部、陕西种植区、四川成都西部以及四川种植区东北部等地,发生概率中度为20%~30%、重度为20%~45%;籼稻寒露风主要位于云南、湖南、安徽、陕西、四川的部分地区,发生概率中度为20%~40%,重度为50%~95%(图4)。(霍治国)

2.7 华南荔枝寒害风险评估

构建了包括灾害危险性、承灾体暴露性和脆弱性3个方面的华南荔枝寒害风险动态评估指标体系。致灾因子及孕灾环境的危险性由灾害强度乘以其月或年发生的频率确定。寒害强度即由最大降温幅度、极端最低气温、日最低气温 ≤ 5.0 °C的持续日数、日最低气温 ≤ 5.0 °C的积寒等要素构造的综合寒害指数,分为极重、重度、中度、轻度和无寒害5个等级。承灾体的脆弱性由荔枝减产(相对气象产量)等级与其发生频率之积确定,减产等级分为4级。承灾体的暴露性根据荔枝收获面积与耕地面积的比值确定。运用自然灾害风险指数法(风险指数=危险性 \times 暴露性 \times 脆弱性)构建了华南荔枝寒害的月或年风险评估模型。据此模型对广东和海南省的荔枝进行逐月或年的寒害风险区划。结果表明,广东荔枝从11月开始即有发生寒害的中度风险,至12月、1月及2月发展为较高风险及以上。其中,广宁、高要到台山一线为寒害的高风险区。另外,年度寒害风险区较月的范围有所扩大。海南荔枝月的寒害风险在中度及以下,而年的风险级别达到了较高(图5)。(马玉平)

2.8 重大农业气象灾害立体监测与动态评估技术研究

针对西南地区农业干旱、南方双季稻低温和黄淮海小麦干热风灾害,取得了以下几个方面的研究成果。完善了灾害立体监测指标。建立了以遥感植被指数为指标的遥感监测大面积干热风灾害的方法。建立了基于干热风危害指数的黄淮海地区冬小麦干热风灾损评估模型。采用经验指标模型或将指标嵌入ORYZA2000模型作为水稻低温冷害的动态评估方法,并可以从站点和区域尺度进行灾害的动态评估。站点尺度的评估紧跟水稻生长过程,监测到低温影响后,及时作出冷害评估,提供定量的冷害评估结果。区域评估以遥感反演信息作为数据源代入指标模型或作物模型中计算或更正评估结果,并以MODIS为例,探索了低温造成生育期延迟的评估方法。对于西南作物干旱,建立了基于干旱累积指数(DI)的产量损失评估模型和基于WOFOST模型的干旱影响作物评估模型。在前期研究成果的基础上,初步完成了黄淮海干热风 and 西南作物干旱省级灾害监测与评估业务平台。(赵艳霞)

2.9 华北冬小麦灌浆期高温热害指标研究

在冬小麦灌浆中后期,短期(3天、6天或9天)高温胁迫导致灌浆速率下降、灌浆持续时间缩短,千粒重与高温胁迫期间午间平均冠层气温呈显著性的负线性相关关系。通过对千粒重数据进行标准化处理,得到了不同年型间表现一致的千粒重相对值与高温特征值的关系,并据此提出了冬小麦灌浆中后期短期高温热害的温度指标。由3年不同长度的短期高温胁迫试验结果提炼出了一个反映灌浆中后期全阶段高温热害当量的特征量-高温有效度时,并得出适应于不同年型的千粒重相对值与高温有效度时的统计相关关系,并由此给出了不同减产程度的致灾高温积热指标。(谭凯炎)

2.10 长江中下游地区双季早稻冷害、热害风险识别技术

以长江中下游地区48个站点1961—2012年的气象资料为基础,利用统计分析、Mann-Kendall和小波分析的方法研究早稻生长季前期冷害、后期冷害、后期热害的时空变化。结果表明:近52年来早稻生长季气温呈极显著升高趋势($>0.5\text{ }^{\circ}\text{C}/10\text{a}$);前期冷害和后期冷害均从21世纪初开始出现减弱趋势,前期冷害变化存在2~4年的短周期,后期冷害变化存在2~4年和4~6年2个周期;后期热害从21世纪初开始有显著增强趋势,无明显周期特征;空间分布上,前期冷害高风险区基本与山脉地形特征相吻合而后期冷害与水系的分布相关性很高。全球变暖背景下长江中下游地区低温灾害减弱、高温灾害增强。(王春乙)

2.11 东北地区玉米主要气象灾害风险评价

利用东北地区35个农业气象站1961—2010年气象资料、1981—2010年玉米发育期资料、1961—2010年产量面积资料、近50年东北3省的灾情资料以及近10年东北3省各县的社会经济统计资料,以玉米出苗-抽雄、抽雄-成熟两个生长阶段里发生的干旱及冷害为研究对象,基于水分亏缺指数和热量指数分别建立了干旱指标和冷害指标,对东北地区玉米干旱、冷害进行风险分析。建立了包括危险性、脆弱性、暴露性和防灾减灾能力4个方面的东北地区玉米干旱、冷害风险评价模型,指出危险性和防灾减灾能力是风险评价模型中最重要的2个影响因子。给出了东北地区玉米干旱、冷害高风险值区位于黑龙江西南部和东北部,以及辽宁西部建平县一带,风险指标值在0.8以上;吉林西北部、东南部、辽宁东北部为次高值区,风险指标值在0.6~0.7之间;低值区位于辽宁中南部及辽东半岛,风险值在0.3左右。(王春乙)

3 农业应对气候变化研究

3.1 全球变化影响下主要作物的脆弱性及评价指标

研究表明,显著增温对春小麦生育期和关键发育期的影响是气候变化背景下春小麦产量脆弱性的主要原因。春小麦生育阶段气温升高,使拔节期、抽穗期、开花期和成熟期显著提前,从而使春小麦生育期显著缩短。然而,播种期调制、耕作方式改变和新品种引入等适应性措施的不断实施,弥补了由于生育期缩短和发育期变化等对小麦产量的可能影响。统计分析表明,由于增温趋势和适应性措施

实施水平的区域性差异影响, 增温对春小麦生育期缩短和发育期变化的贡献率在23%~68%, 平均达到40.3%; 每增温1℃, 生育期可能缩短6~7天, 产量可能减少522 kg/hm²。另外, 应该清晰地认识到, 人类的适应性措施伴随气候变化而持续实施, 到目前为止的作物生育期和发育期变化是气候变化和人类适应气候变化的共同结果。(俄有浩)

3.2 东北玉米生产对气候变化的响应与适应

进一步细化了作物发育期, 以平均资源适宜指数(I_{sr})、平均效能适宜指数(I_{se})和平均资源利用指数(K)作为评价指标, 评价了近50年东北地区玉米气候资源的适宜情况和利用率。从年际、潜在生长季和作物生长期3个时间尺度方面, 确定影响春玉米生长发育的关键气象因子, 分析了近30年来东北春玉米关键发育期的变化特征和演变趋势, 构建了玉米生长期对气候变化的响应关系模型, 探讨了春玉米发育期对不同时间尺度气象因子的响应规律。提出了分离东北玉米气候产量的最优方法, 分离出气候变化对东北春玉米产量的影响, 确定了影响东北春玉米气候产量的关键气象因子, 建立了反映不同地区气象因子和春玉米气候产量关系的区域模型。(赵俊芳)

3.3 大气CO₂浓度升高和增温影响作物需水量变化机理研究

利用开顶式生长箱(OTC)与大田试验, 对比研究了增温和CO₂浓度升高对冬小麦需水量的影响。结果表明, 冬小麦生长期(2013年10月11日至2014年6月10日), 日平均增温3.1℃, 并且日平均施加CO₂浓度到760×10⁻⁶, 冬小麦生育期缩短17天(7%)。日均耗水量增加0.7 mm(OTC日均2.7 mm, 大田日均2.0 mm), 全生育期增加需水量123.5 mm(25.5%)。另外, 利用半封闭OTC(无CO₂施加)与大田对比试验表明, 半封闭式OTC比大田日平均增温0.7℃, 冬小麦生育期缩短7天, 日均耗水量增加0.65 mm, 全生育期增加需水量138.8 mm(28.7%), 与封闭式OTC中日均耗水量和全生育期增加的需水量接近。出现这种情况的原因可能有两方面: 一是虽然封闭式OTC增温幅度明显大于半封闭式OTC, 但是封闭环境下空气流动性比半封闭环境下差, 不利于水汽流动, 导致封闭式OTC中蒸散量较小; 二是许多文献资料提到增加CO₂浓度能够减少蒸散量, 增加水分利用效率。由于该试验观测结果是增温和CO₂浓度增加的综合表现, 无法分离各自作用对需水量的影响及贡献, 因此, 还需要进一步试验观测和分析。(俄有浩)

3.4 增温和CO₂增加对华北主要作物产量影响的试验研究

偏冷年的增温将促进小麦的分蘖, 有效穗数显著增加, 籽粒产量较对照大幅度增加; 偏暖年的增温也显著促进冬小麦有效穗数和穗粒数增加, 尽管使得千粒重显著降低, 但并未导致产量下降。OTC小麦增温+CO₂的试验也得出, 增温+CO₂对产量没有产生影响, 与单纯CO₂增加试验不同, 即没有预期的CO₂施肥效应在小麦增温+CO₂中表现出增产的结果。玉米大田增温试验得出: 增温可能降低玉米产量, 可能与玉米生长期处于夏季高温期, 如再升温就可能超出玉米适应高温的能力有关。预期的CO₂施肥效应在玉米增温+CO₂中表现出增产的效应(图6)。(房世波)

3.5 近30年东北春玉米发育期对气候变化的响应

基于1981—2010年东北地区55个农业气象观测站发育期数据、16个气象站逐日气象资料, 采用趋势变率、秩相关分析、主成分分析和结构方程模型等方法, 分析了近30年东北春玉米关键发育期的变化特征, 探讨了春玉米发育期对不同时间尺度气象因子的响应规律。结果表明, 1981—2010年春玉米关键发育期(播种期、抽雄期、成熟期)均有延后趋势, 大部分地区春玉米生长前期(播种期—抽雄期)日数减少, 生长后期(抽雄期—成熟期)日数增加, 全生育期日数增加。在绝大多数年份, 春玉米播种期在温度适播期之后, 成熟期在初霜日之前。近30年对东北春玉米生育期日数影响最大的气象要素为温度, 主成分分析结果显示, 年际尺度的升温、温度生长期的延长和作物生长期的高温对生育期日数影响显著; 结构方程模型指出, 作物生长期的最高温度和最低温度对生育期日数影响有间接效应, 主导气象要素能够解释生育期日数变异的44%。全球变暖背景下, 东北春玉米发育期变化是作物响应气候变化和农业生产适应气候变化的共同结果。(郭建平)

3.6 气候变化和科技进步对中国玉米产量影响的定量评估

农作物产量受气候变化和科技进步的共同影响，客观和定量评价气候变化和科技进步对农作物产量的影响有利于保障农业的可持续发展。本研究利用农业生态区域法计算了作物光合生产潜力、光温生产潜力和气候生产潜力，并结合主要作物主产省实际产量变化趋势，系统分析了近50年来不同气候资源要素变化对作物气候生产潜力的影响，分析了近30年来气候变化和科技进步对主要作物产量的影响。研究表明：近50年辐射减少对我国主要农作物产生了显著的不利影响；近50年温度升高对玉米和双季稻有不利影响，但对小麦有正效应；近50年降水变化对农作物的影响地区间有显著差异，对不同作物也有差异，但以正效应为主；近30年气候变化对农作物产量均以负面影响为主，农业增产主要是科技进步的贡献。如果没有气候变化的不利影响，我国粮食作物的实际增产幅度可能比现在更大。（郭建平）

3.7 东北种植制度变化下作物气候生产潜力和气候资源利用效率分析

利用已有的种植制度界限指标体系，综合考虑水、热资源对东北地区农业种植制度的影响，分析了种植制度界限变化敏感区作物气候生产潜力和气候资源利用效率的变化。结果表明：随着未来气候变化，综合考虑热量和降水资源，东北一年两熟的北界明显的北移东扩，2071—2100年黑龙江哈尔滨附近的小部分区域可以实现一年两熟，而黑龙江西南地区由于水资源的缺乏，仍只适宜一熟制作物种植；由于高温胁迫，研究区域内春玉米气候生产潜力会随时间下降，种植模式的调整是提高气候生产潜力的一种有效方式。但在热量相对较高的地区，过高的温度导致冬小麦、夏玉米生育期的缩短，冬小麦与夏玉米两熟模式下的气候生产潜力总和也会降低，但仍然高于一熟种植方式；随着气候变暖，积温相应增加，一熟制种植方式出现了资源浪费的现象。改一熟为两熟，延长了作物的生长季节，可以很好地利用气候资源，有利于提高农业气候资源利用效率。（郭建平）

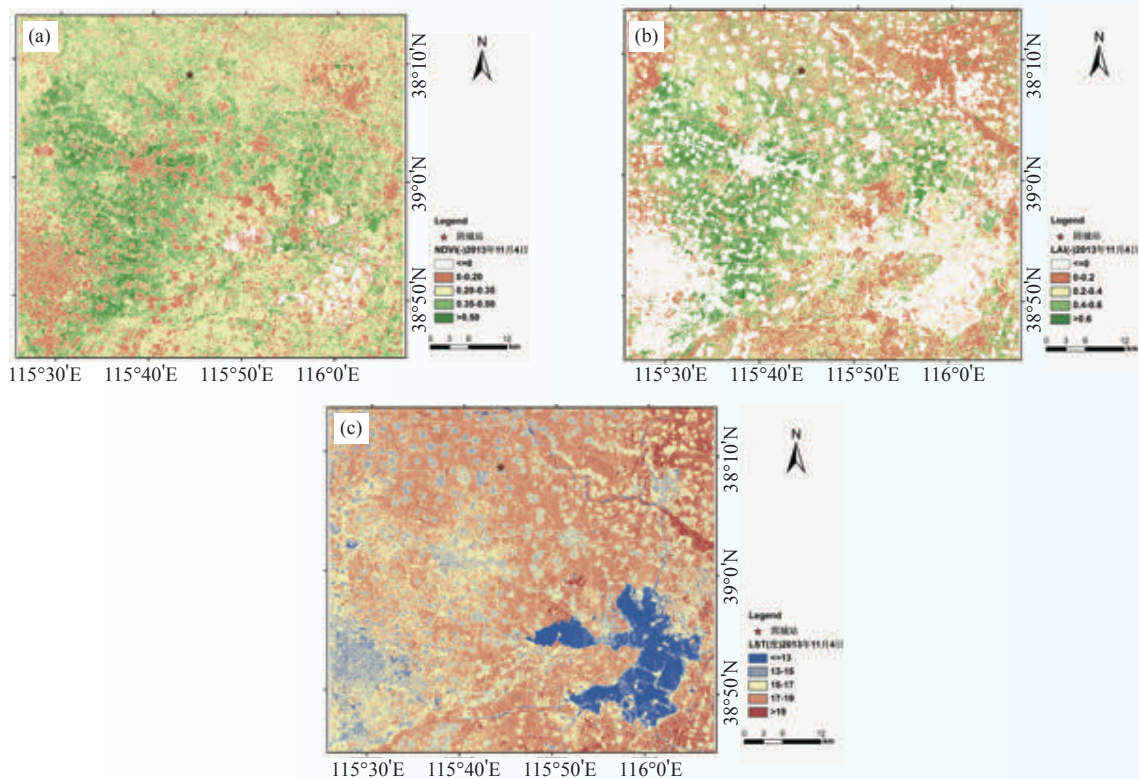


图1 Landsat8数据地表参数反演结果(a: 归一化植被指数(NDVI); b: 叶面积指数(LAI); c: 地表温度(LST))
Fig. 1 Inversion maps of Landsat8 surface parameters (a: NDVI; b: LAI; c: LST)

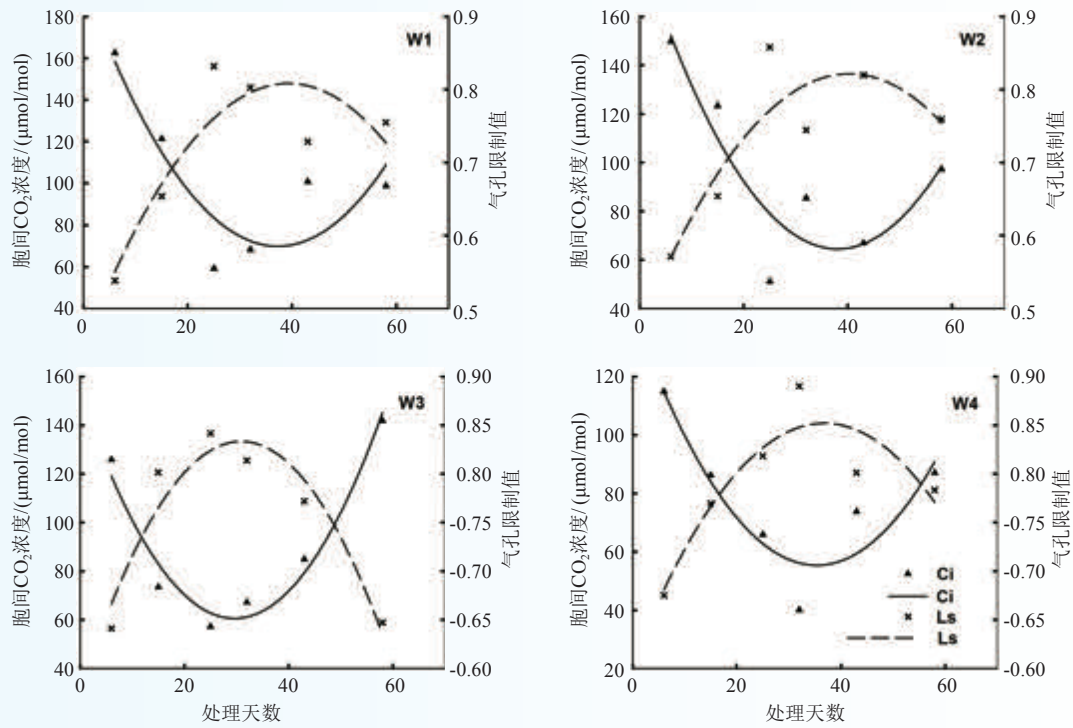


图2 玉米全生育期叶片光合作用限制因素

Fig. 2 Factors limiting leaf photosynthesis of summer maize during growing season

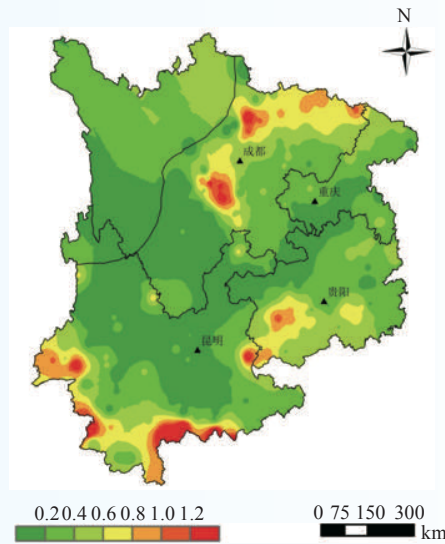


图3 1961—2010年中国西南地区农业洪涝平均次数

Fig. 3 Average agricultural flood frequency in Southwest China during 1960–2010

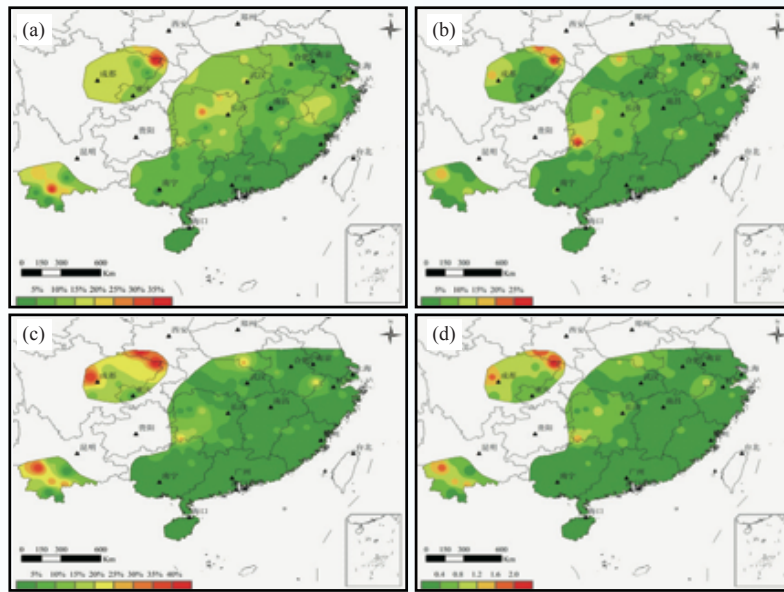


图4 南方地区晚稻（粳）寒露风风险概率及综合风险指数地理分布（a：轻度寒露风；b：中度寒露风；c：重度寒露风；d：寒露风风险指数）

Fig. 4 Geographical distribution of risk probability of each-level cold dew wind to japonica rice during 1981 to 2010 (a: the occurring probability of mild cold dew wind; b: the occurring probability of medium cold dew wind; c: the occurring probability of severe cold dew wind; d: risk index of cold dew wind)

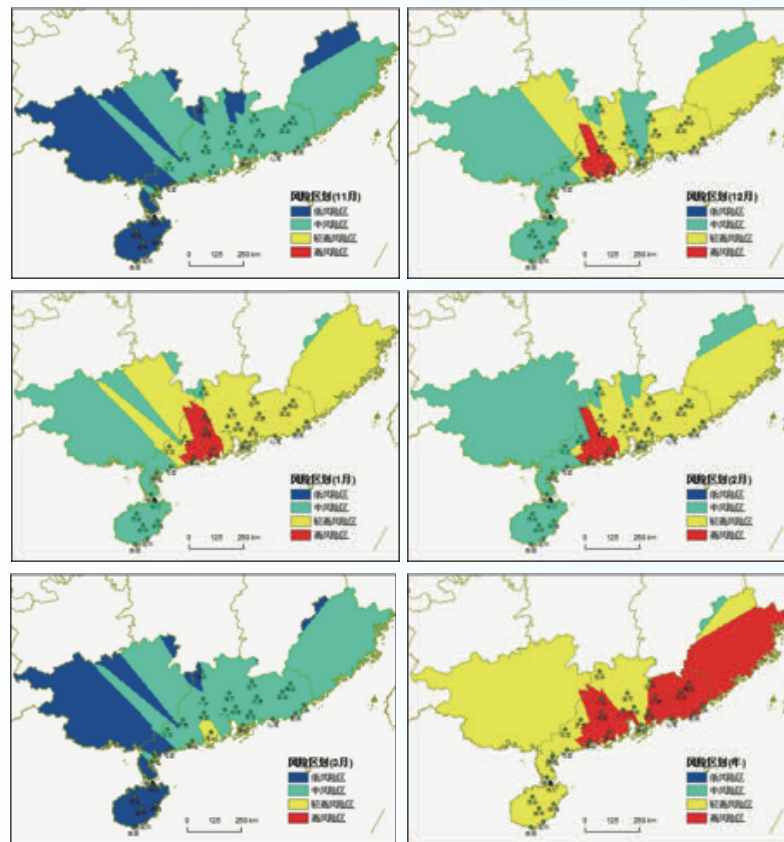


图5 广东和海南省荔枝月及年寒害风险区划

Fig. 5 The monthly or annual risk zoning of litchi chilling injury in Guangdong and Hainan provinces

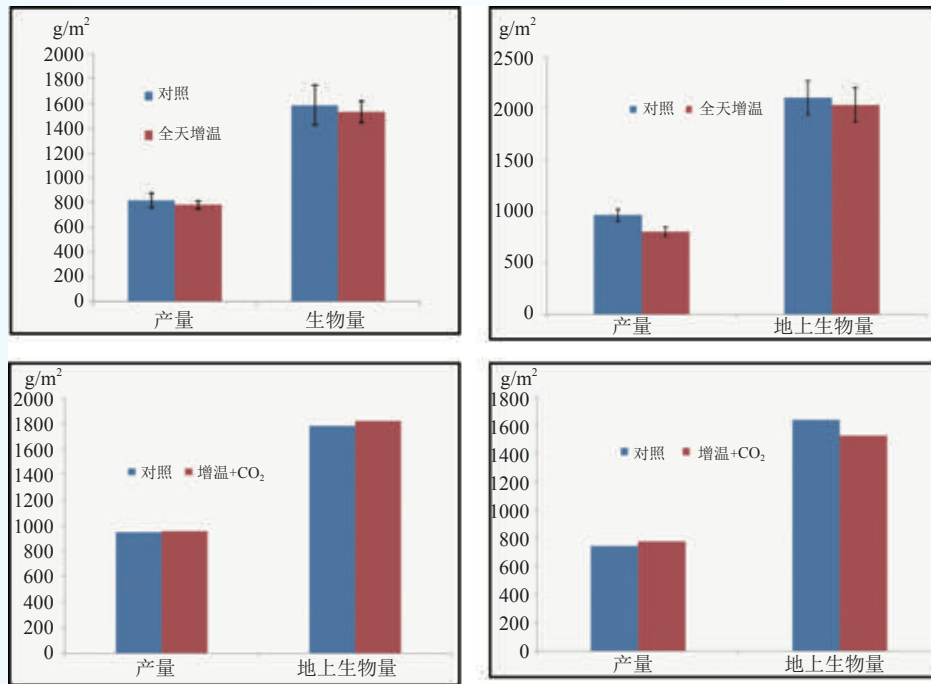


图6 单独增温和增温+CO₂复合对玉米产量影响的差异

Fig. 6 The different effects between warming treatments and warming combined CO₂ enrichment

Research Progress in Ecology and Agrometeorology

1 Ecological and agrometeorological theories and application techniques

1.1 A study on data fusion model for high temporal and spatial resolution remote sensing data

The Spatial and Temporal Adaptive Reflectance Fusion Model (STARFM) was used to blend Landsat and MODIS surface reflectance based on their spectral similarities and spatio-temporal differences. An operational data fusion framework was built by integrating STARFM (referred to as ISTARFM hereinafter). Compared with STARFM, several improvements have been incorporated in the ISTARFM. These include: (1) viewing angular correction on the MODIS daily bidirectional reflectance to get daily NBAR (Nadir BRDF (Bidirectional Reflectance Distribution Function) - Adjusted Reflectance), and filling gap values in BRDF products with BRDF lookup table obtained from MODIS International Geosphere-Biosphere (IGBP) land cover and MODIS BRDF products, (2) precise and automated co-registration on MODIS and Landsat paired images by looking for maximum correlation coefficient with the moving-window technique. The ISTARFM provides a feasible and cost-effective way to build dense time-series surface reflectance at Landsat spatial resolution, which can serve as regional drought monitoring for winter wheat precisely at high spatial and temporal resolutions with remote sensing images. (Wang Peijuan)

1.2 Landsat surface parameters inversion and spatial down-scaling

Digital number (DN) was converted to surface reflectance based on LEDAPS (Landsat Ecosystem Disturbance Adaptive System) model for Landsat8. And then several surface parameters were inverted using surface reflectance at their own spatial resolution, which include normalized difference vegetation index (NDVI) at 30 m resolution, leaf area index (LAI) at 30 m resolution, and land surface temperature (LST) at 100 m resolution. A Temperature-Reflectance (T-R) model was developed with LST and down-scaled surface reflectance at 100 m resolution. Therefore, LST can be down-scaled spatially based on T-R model and surface reflectance at 30 m resolution to get LST at 30 m resolution (Fig. 1). (Wang Peijuan)

1.3 Research on and development of fine daily multi-layer soil moisture and irrigation forecasting system for winter wheat

Based on data sets of soil moisture, soil texture, evapotranspiration, water deficit indices of remote sensing and so on, the fusion technologies of soil moisture observation data by manual, automatic and remote sensing were studied with the methods of pixel matching, error analysis, neural network and others. Using daily total radiation and sunshine time data in 103 stations from 1961 to 2010 in China, the spatial and temporal distribution of the a coefficients and b coefficients were analyzed and the a coefficients and b coefficients for each age (ten years) in every region of China were given. Based on earlier stage research on the simplified models of water balance and daily multi-layer soil moisture and irrigation forecast models for winter wheat, three provincial forecasting systems (probation) were established, and tried in main winter wheat growth period in 2014. The operational application platform based on six modules of data management, data processing, soil moisture forecasting, irrigation quantity forecasting, product making and results testing was developed and tried in Hebei Province preliminarily. Three service products were issued. (Mao Fei)

1.4 Study on responses of summer maize ecophysiological and growth characteristics to drought process

During the manipulation experiment of summer maize drought occurrence and development, light drought occurred after 15 days of water control, and moderate drought happened one month later, extreme drought appeared two months later. The midday depression phenomenon of leaf photosynthesis occurred during the jointing stage under the conditions of light drought. The photosynthetic rate, transpiration rate, stomatal conductance and water use efficiency of the first maize leaf were sensitive to drought, implying they were able to be indicative indices. The photosynthetic rate, transpiration rate and stomatal conductance of maize leaves during growing season decreased significantly with the decrease of soil relative moisture. The difference of all these parameters between water treatments declined with the development of consecutive drought. The water use efficiency showed a rising trend and its difference between water treatments was small at earlier stage, but enlarged at later stage with the aggravation of consecutive drought. The leaf water content decreased linearly with the drought occurrence and development during growing season and it was significantly correlated with soil relative moisture, implying that the leaf water content is able to be an index of crop drought. The limiting factor of maize photosynthesis was a conversion process from stomatal limitation to non-stomatal limitation during growing season. The occurrence time of the conversion process was in correspondence with drought intensity and duration. The leaf SPAD value was not as sensitive as the photosynthetic rate to drought, which reflected its hysteretic nature. Electron transfer rate, photochemical quenching coefficient and photochemical efficiency decreased significantly from filling stage to milk stage. The summer maize stem water content reached the maximum at jointing stage (about 93%) and it was not as sensitive as leaf water content to drought. The leaf area index reached the maximum at tasseling stage for the treatment under higher soil relative moisture, while for the treatment under lower soil relative moisture it reached the maximum at filling stage. The specific leaf area declined rapidly in the early stage, while it showed a stable trend. The specific leaf weight showed an opposite trend, and it was significantly higher in the late stage than in the early stage. The summer maize aboveground biomass was sensitive to soil water content, and it decreased with the decrease of soil relative moisture at all stages. The reduction caused by drought at jointing and tasseling stages was obvious. The average daily increase of summer maize aboveground biomass was between 1.15 g to 1.74 g, and the increase rate declined with the decrease of soil relative moisture (Fig. 2). (Zhou Guangsheng)

2 Agrometeorological disaster prevention and mitigation

2.1 Agricultural drought warning based on TIGGE and distributed hydrological model

In this study, three global ensemble weather prediction systems from the China Meteorological Administration (CMA), the European Centre for Medium-Range Weather Forecasts (ECMWF), and the US National Centers for Environmental Prediction (NCEP) in THORPEX (The Observing System Research and Predictability Experiment) Interactive Grand Global Ensemble (TIGGE) archive were used. A new distributed hydrological model XXT was built based on TIGEE dynamical downscaling through NOAH_LSM, neural network ANN, TOPMODEL and Xin'anjiang hydrological models. It was based on the soil moisture storage capacity distribution curve (SMSCC), some essential modules of the Xin'anjiang model, together with the simple model framework of the TOPMODEL (a topography based hydrological model). The innovation of XXT was that the water table was incorporated into SMSCC to connect the surface runoff production with base flow production. This improved the description of the dynamically varying saturated areas that produced runoff and also captured the physical underground water level. XXT was tested and found to have better performance

against the TOPMODEL and the Xin'anjiang model. However, due to the fact that XXT model was based on physical processes, the prediction accuracy was still poorer than the classical statistical model which was based on artificial intelligence techniques (such as neural networks, support vector machines, etc.). In order to improve its simulation accuracy, we firstly embedded neural network module in the runoff program of XXT model, which was significantly different from the conventional method. Because the traditional method was that the neural network module was integrated into the scheme of hydrological model with physical processes. (Zhao Junfang)

2.2 Development of the agro-drought prediction model for the winter wheat in North China Plain

Variation of the physiological parameters of the winter wheat under drought conditions, including photosynthesis rate of the winter wheat leaves etc., was measured with Li-6400 portable photosynthesis analyzers in the National Key Laboratory of Shandong Agricultural University. Green fluorescence parameters of the leaves were also determined with FMS-II pulse modulated fluorescence detector. The results indicate that ϕ PSII decreased obviously with the evolution of the drought in the field, which means that the real quantum efficiency of PSII would be seriously affected under severe drought conditions. Variations of the Fv/Fm and Fv/F0 agreed quite well with that of the ϕ PSII. All of the parameters would decrease steadily with the development of the drought, or fluctuate like a wave of decreasing-increasing-decreasing. These variations indicate that the crop can somewhat regulate itself to adapt to the consecutive drought conditions. However, the adaptability changes with varieties. Based on these achievements mentioned above, the researchers have successfully improved some of the related modules in the agro-drought prediction model. An agro-drought prediction model was also established by using the hybrid programming technology of C⁺⁺ and Fortran, with comprehensive prediction accuracy as high as 85%. The model is quite suitable for agro-drought prediction in Shandong, Hebei and Henan provinces in North China Plain. (Liu Jiandong)

2.3 Spatial and temporal distribution characteristics of longan caused by chilling injury in South China

According to the meteorological service standards "Grade of Chilling Injury to Dimocarpus Longan Trees" (QX/T168-2012), the main influencing factors of chilling injury in longan production were selected, and the chilling injury indexes (Hi) of longan in the 64 stations in four provinces of South China from 1961 to 2012 were calculated. The occurrence frequencies of each level of chilling injury were determined. Based on the empirical orthogonal function (EOF), the matrix of longan chilling injury indexes of 52 years, and the matrix of chilling injury indexes in main months (November-March) were analyzed, while the first time components of the above matrix were extracted. The results show that under climate warming, the average accumulated harmful temperature ($<5\text{ }^{\circ}\text{C}$) presented a significant decreasing trend along with decadal time in South China, and it was helpful to reduce disaster of chilling injury. Changes in temporal characteristics of chilling injury indicated the highest frequency was found in January and February, reflecting the main distribution features of chilling injury. These two months were the most important period of chilling injury occurring in a year. November-December and March were not the main period for chilling injury, with a relatively low frequency. But in some years, it might still experience severe chilling injury. Spatial distributions of chilling injury presented obvious latitudinal distribution. The occurrence frequency of chilling injury increased from south to north and from coast to inland areas, which was related to geographic location. A comparative analysis of the historical records indicated that the spatial and temporal distributions of chilling injury could reflect the main actual characteristics of historical record. The frequency of chilling injury from 1981 to 2010 in the eastern coastal Fujian was high (0.42-0.43), with the risk probability standing at 0.10-0.16. (Zhao Junfang)

2.4 The evaluation indicators of agricultural and rice flooding level

For the demand of agricultural and rice flood monitoring and early warning in Southwest China, the single station flood indicators, provincial flood indicators year by year and provincial flood indicators year by year in each station have been developed based on daily precipitation data, agricultural flood disaster information and the rice yield by county from 341 weather stations in southwest agricultural areas from 1961 to 2010. In the progress of building the indicators, flood indicators of Chongqing as the prototype, through increasing and decreasing precipitation threshold by the amplitude which was $-50\sim+50$ mm and step size was 1 mm, 101 groups of flood indicators were obtained in each province. Agricultural flood level indicators of each province were constructed which used grey correlation method to determine weights of different levels of flood impact on actual situation, comprehensive consideration of correlation between flood intensity calculated by 101 indicators and crop flood real seriousness, coincidence between indicators and historical flood records and comparability of indicators of each province. Rice flood level indicators were constructed based on yield reduction rate of each county and flood index, days of flood disaster process and process rainfall. According to the flood level indicators, temporal-spatial distribution features of flood disaster in southwest agricultural areas were revealed. The ages in which flood disaster appears very serious are 1980s in Yunnan, 1990s in Guizhou and 1980s and 2000s in Sichuan and Chongqing in recent 50 years. The areas in which flood frequently occurred are located in southwest and southeast of Yunnan, southwest of Guizhou and west and northeast of Sichuan basin in recent 50 years. Regions of high value flood dangerous index of single-season rice are mainly located in northern and central Sichuan, south of Yunnan and southwest of Guizhou (Fig. 3). (Huo Zhiguo)

2.5 The climate background indicator of major pests diseases occurrence and long-term prediction, dynamic early warning model optimization

For operational application needs of major pests diseases (powdery mildew, planthoppers) occurrence weather conditions monitoring, early warning and assessment, data on the national occurrence area and degree of rice planthopper and wheat powdery mildew from 1971 to 2010, 74 kinds of atmospheric circulation characteristics from 1970 to 2010, and North Pacific SST data from 1969 to 2010 were reviewed. Atmospheric circulation and North Pacific SST data level indicators of rice planthopper and wheat powdery mildew occurrence area level were also used including factor puffing, topological analysis, optimization process, and factor independence test. After the test, indication factor method showed a better result for the powdery mildew of occurrence epidemic level. The whole nation rice planthopper occurrence degree model, the rice planthopper occurrence rate of atmospheric circulation model and North Pacific SST model were established, the accuracy of which are 97.5%, 82.5%, 82.5% and 80%, respectively. Early dynamic warning models were developed based on fisher discriminant analysis of rice planthopper occurrence degree in Guangxi Guilin and wheat powdery mildew in Hebei. The level evaluation accuracy of rice planthopper model in Guilin is 84.6%, while the prediction accuracy is 88.2%. The level evaluation accuracy of wheat powdery mildew model in Hebei achieves 97.8%, while the prediction accuracy is 95.0%. (Huo Zhiguo)

2.6 Low temperature disaster temporal/spatial distribution characteristics of double cropping rice in southern China and its risk analysis

For cold damage in early rice seeding transplanting period and cold dew wind damage of late rice in heading flowering stage in double cropping rice areas in southern China, the risk index of cold temperature damage was established which was based on the community standard and the data of daily average temperature from 169 weather stations during 1981–2010. It revealed the characteristics of geographical distribution of the occurrence probability and integrated risk index for double cropping rice from different low temperature

disasters by level. In recent 30 years, the cold damage of early rice in southern China, the frequency of light, moderate and severe occurrence of late rice cold dew wind (japonica rice and indica rice), and the number of total occurrences showed a decreasing trend. But some regions showed an increasing trend. According to the disasters showing an increasing trend in terms of coverage, they are japonica cold dew wind, cold rice disasters and indica cold dew wind. High value areas of moderate to severe disaster risk: Cold damage of early rice mainly in parts of Hunan, Jiangxi and Fujian provinces, moderate probability of 20% to 40%, severe below 10%. Japonica rice cold dew wind is mainly located in the middle of Yunna, Shaanxi planting area, western Sichuan and Chengdu, and in northeastern of Sichuan growing areas, where the moderate probability of occurrence is 20% to 30%, and the severe probability of occurrence is 20% to 45%. Indica rice cold dew wind is located in parts of Yunnan, Hunan, Anhui, Shaanxi and Sichuan, where the moderate of occurrence is 20% to 40%, and the severe probability of occurrence is 50% to 95% (Fig. 4). (Huo Zhiguo)

2.7 Risk assessment of litchi chilling injury in South China

The risk evaluation index system of litchi chilling injury was firstly constructed, which included risk of disasters, exposure and vulnerability of litchi in South China. The risk of the disaster factor and its environment was determined by the intensity of disaster multiplied by the frequency of its occurrence in a month or year. Chilling intensity was the integrative chilling damage index constructed by maximum temperature drop, extreme minimum temperature, persisting days of low temperature and harmful chilling accumulation in which the minimum temperature stays below 5 °C. Chilling intensity was classified as severe, heavy, moderate, mild and no chilling injury. The vulnerability was determined by the grades of litchi yield decrease multiplied by its occurrence frequency. The grade was divided into 4 levels. Exposure was determined by the ratio of litchi harvest area to cultivated land area. The monthly or annual risk assessment model of litchi chilling in South China was then constructed by using natural disaster risk index method which was risk multiplied by vulnerability and exposure. Based on this model, the monthly or annual chilling injury risk zoning was carried out in Guangdong and Hainan provinces. The results show that moderate risks of litchi chilling injury have begun in November and gradually developed into higher risk from December, January to February in Guangdong Province, in which the high risk area of litchi is in Guangning, Gaoyao to Taishan regions. Moreover, annual chilling risk area is greater than that for monthly one. Monthly chilling risk grade is in moderate and below but the annual is rather high in Hainan Province (Fig. 5). (Ma Yuping)

2.8 Study on the stereo monitoring of and the dynamic assessment technology for major agrometeorological disasters

The findings about the dry-hot wind for winter wheat in Huanghuaihai areas, low-temperature damage for double cropping rice in southern China and the agricultural drought in Southwest China have been summarized as follows. Indicators for stereo monitoring were improved. Vegetation indexes were developed to monitor the large-scale dry-hot wind disastrous to wheat. The model based on the hazard index of dry-hot wind was constructed to assess the wheat loss due to dry-hot wind. For low-temperature damage to rice, loss was assessed at site and regional scale based on ORYZA2000 and empirical models. The assessment at site scale followed the rice growth process. Once the impact of low temperature was monitored, the quantitative evaluation results would be made in time. At regional assessment, remote sensing inversion was used as input data to ORYZA2000 or empirical model to calculate and modify the results. And taking MODIS data coupled with model as example, the methods were investigated for evaluating the impact of low temperature on delaying rice growth. For crop drought, yield loss was assessed based on drought accumulation index (DI) and WOFOST model. The operational platforms of monitoring and evaluation of dry-hot wind in Huanghuaihai

areas and drought disasters in Southwest China at the provincial level have been established. (Zhao Yanxia)

2.9 Study on high temperature stress at grain filling stage of winter wheat in North China

High temperature stress at the mid to late grain filling stage of winter wheat reduced the grain filling rate and shortened the grain filling duration, resulting in a significant reduction of grain yield. After taking into account the other influencing factors, a significant negative linear relationship was found between the grain weight and the midday canopy air temperature in this period. This study suggest that the extent of the high temperature stress effects on winter wheat grain yield depends on both the strength and duration of the stress, which can be represented by the effective accumulated heat (summation of the hour's temperature differences above a threshold value during the mid to late grain filling stage of winter wheat). There were significant negative linear relationships between the normalized grain weight of winter wheat and the effective accumulated heat above 30 °C during the mid to late grain filling stage ($P \leq 0.05$). This proved that the high temperature stress index is a useful parameter for quantitative evaluation of the impacts of high temperature at the grain filling stage on winter wheat yield. (Tan Kaiyan)

2.10 Risk identification techniques for cold and heat damage to double-season early rice (DSER) in the middle and lower reaches of Yangtze River

Based on daily meteorological data of 48 meteorological stations during 1961–2012 in the middle and lower reaches of Yangtze River (MLRYR), spatial and temporal distribution of early cold damage, late cold damage and late heat damage of early rice was analyzed using such methods as statistical analysis, Mann-Kendall and wavelet analysis. Results show that over the past 52 years, average temperature increased significantly (>0.5 °C/10a) during early rice growing season in MLRYR. Both the early and late cold damage showed a downtrend from 2000. There was a short cycle of cold damage of two to four years in early period and two to four, four to six years in late period. Late heat damage showed a significant increase trend from 2000 with no obvious periodicity. High risk area of early cold damage was consistent with spatial distribution of mountain terrain while that of late cold damage was consistent with distribution of water system. Cold damage weakened and heat damage increased in MLRYR under global warming. (Wang Chunyi)

2.11 Risk assessment of main meteorological disasters to maize in Northeast China

The meteorological data from 1961 to 2010, maize growth data from 1981 to 2010, production data from 1961 to 2010 in 35 agro-meteorological stations, disaster record for the latest 50 years in three provinces of Northeast China, and social and economic statistics for the latest 10 years in the counties of these three provinces were employed in this study. The drought and chilling injury at two stages of the maize including emergence-tasseling and tasseling-mature were studied, and the risk of the drought and cold injury to corn in Northeast China was evaluated. The creation of index systems of drought and cold injury was based on water deficit index and heat index. The indices of drought and chilling injury risk assessment model of the maize included hazard, vulnerability, exposure, and emergency response and recovery. Hazard and emergency response and recovery were the two most important factors in the model. For the whole growth and development period of the maize, the high values of risk index were in the southwest and northeast of Heilongjiang Province and west of Liaoning Province, standing above 0.8. The moderate values were found in the northwest and southeast of Jilin Province and the northeast of Liaoning Province, standing between 0.6 and 0.7. The low values were in the central south of Liaoning Province and Liaodong Peninsula, standing around 0.3. (Wang Chunyi)

3 Response of agriculture to climate change

3.1 Vulnerability and evaluation index of main crops under global change

The research results indicate that the impact of climate warming on growth periods and critical growth stages of spring wheat was the primary reason for vulnerability of spring wheat yield under the background of climate change. Increased temperature during the growing season accelerated the phenological development, including internode elongation, heading, anthesis and stage of grain ripening, resulted in a shorter growth period. The application of adaptation strategies, such as adjusting the sowing dates, introducing new cultivars and changing the tillage practices, likely compensated some effects of shorter growth period on wheat yield. A correlation analysis reveals that the increase in temperature during the growing season was responsible by 23% to 68%, with an average of 40.3% for the shortening growth period and altered farming practices based on phenological events, in spite of regional differences in increased temperature trend and in application of adaptation strategies. The trend analyses reveal that rising temperature has shortened the growth period by 6 to 7 days per 1 °C, resulting in the decrease in spring wheat yield of averagely 522 kg ha⁻¹. In addition, the fact should be recognized that the adaptive strategies continue to be performed along with the changing climate since the changes in growth period and phenology of spring wheat up to now both result from climate change and human adaptive activities. (E Youhao)

3.2 Response of maize production to climate change and its adaptation in Northeast China

The growth period of spring maize was further subdivided into four stages: germination to emergence, emergence to jointing, jointing to tasseling, and tasseling to maturity. The average resource suitability index (I_{sr}), average efficacy suitability index (I_{se}), and average resource utilization index (K) were used as indicators of agricultural climatic resource suitability and utilization for maize production. The utilization dynamics of agricultural climatic resource during spring maize cultivation from 1961 to 2010 in Northeast China were analyzed. The key climatic factors limiting the spring maize growth were identified from three time scales of interannual, potential growth season and crop growing period. The variations of key growth stages of spring maize in Northeast China over the past 30 years were analyzed. The regression models on the growing period of maize in response to climate change were also established. The response of growing period of maize to climate change at different time scales was investigated. Compared with the methods of moving average and harmonic average, logistic regression optimally decoupled the climate induced yield of spring maize. The contribution of climate change to spring maize yield over the past three decades in Northeast China was decoupled. The key meteorological factors limiting the climate-induced yield were determined. Finally, the models between climatic variables and climate-induced yield of spring maize in Northeast China were also established to reflect geographical differences. (Zhao Junfang)

3.3 Study on the impact of extreme temperature and CO₂ enrichment on crop water demand

The control experiments in open top chambers (OTC), side half closed chambers and field were performed to investigate the effects of elevated atmospheric carbon dioxide concentration [CO₂] and increase in temperature on winter wheat water requirement. The results show that, compared to the field, in open top chambers the air temperature increased by mean daily temperature of 3.1 °C and [CO₂] elevated to 760×10⁻⁶, the whole growing period was shortened by 17 days (7%), and the average daily water requirement increased by 0.7 mm. Consequently, the water requirement increased by 123.5 mm (25.3%) during the growth period. While in side half closed chambers in which using the ambient [CO₂], the air temperature increased by mean

daily temperature of 0.7 °C, the whole growing period was shortened by 7 days and the average daily water requirement increased by 0.65 mm. So, the water requirement increased by 138.8 mm (28.7%) during the growth period, indicating the approximately equivalent water requirement both in open top chambers and in side half closed chambers. There would be two reasons to explain these results. For one thing, in OTC, the air exchange with outside is less than that in side half closed chambers, leading to less evapotranspiration though significantly warmer in OTC than in side half closed chambers. For another, the elevated [CO₂] may decrease the evapotranspiration by raising water use efficiency as mentioned in literatures. However, we have not separated the positive effect by elevated [CO₂] on evapotranspiration from increased air temperature, due to the compounded effects of both elevated [CO₂] and increased air temperature. Further experiments still need to be made to separate the impacts of elevated [CO₂] and increased air temperature. (E Youhao)

3.4 Experimental study on the impacts of extreme temperature and CO₂ enrichment on crop yield in North China

The heated treatments of winter wheat showed higher values of panicles per square meter, and no significant difference in the 1000 grain weight, which had significantly increased the yield compared to CK in the colder year (2011). The warm year (2012) showed higher values of panicles per square meter and grain number in each panicle, while the 1000 grain weight is significantly reduced compared with CK, but the heated treatments did not lead to yield reduction. Warming and CO₂ enrichment could hardly show any difference with CK, and no fertilizer effects of CO₂ were shown in this experiment. The warmed treatment of maize had the potential to reduce the yield compared with CK, which maybe come from the negative effect of extreme temperature in summer. But warming and CO₂ enrichment could set off the negative effect of extreme temperature, which increased the yield in 2012 (Fig. 6). (Fang Shibo)

3.5 Response of growth stages of spring maize to climate change in Northeast China over the past 30 years

Based on the observation data of spring maize from 55 agricultural meteorological stations, and daily meteorological data of 16 meteorological stations in Northeast China, the variations of key growth stages of spring maize in Northeast China over the past 30 years were analyzed, using such methods as trend rate, spearman correlation analysis, principal component analysis and structural equation modeling. Finally, the responses of growth period of spring maize to meteorological factors over the past 30 years were further analyzed at different time scales. The results show that the spring maize's critical growth stages in Northeast China over the past 30 years were postponed. The number of days decreased during the early maize growth period (from sowing to tasselling), while both days during the late maize growth period (from tasselling to maturation) and days of whole growth period increased. In most years, the sowing date of spring maize was later than suitable planting date, and the maturing date was earlier than the first frost date. Temperature was the most notable meteorological factor responsible for the altered spring maize growth period during the past 30 years. A principal component analysis showed that the increased temperature at the inter-annual timescale, the prolonged temperature growth period and the high temperature in the crop growth period were more notable than other meteorological factors. While, in the structural equation modeling, the effects of temperature on days of growth period partly were indirect, and significant meteorological factors could explain 44% of variation in growth period's days. Changes in the growth stages of spring maize were caused by the response of crops and the adaptation of agricultural production to climate change under global warming. (Guo Jianping)

3.6 Attribution of crop yield increase in China to climate change and technological advancement

Crop yields are affected by climate change and technological advancement. Objectively and quantitatively



evaluating the attribution of crop yield change to these two factors will ensure sustainable development of agriculture under climate change. The relative impacts of different climate variables on climatic potential productivity of maize from 1961 to 2010 in China are then evaluated based on Agro-Ecological Zones (AEZ) model. In the AEZ model, the climatic potential productivity was examined through three steps or levels: photosynthetic potential productivity, photosynthetic thermal potential productivity, and climatic potential productivity. Combined with the observations of maize, the contributions of climate change and technological advancement to maize yield from 1981 to 2010 in China were separated. The results show that, from 1961 to 2010, decreased radiation was the main factor leading to the decrease of climatic potential productivity of crops. Increased temperature had a significant adverse impact on the climatic potential productivities of maize and double cropping rice in China. However, it had a positive effect on wheat. Climate change had a significant adverse impact on the crop yield in China from 1981 to 2010. This suggests that technological advancement had offset the negative effects of climate change on maize yield. Our findings highlight the fact that agronomic technological advancement has contributed dominantly to crop yield increases in China in the past three decades. (Guo Jianping)

3.7 Effects of adjusted cropping systems on climatic potential productivity and utilization efficiency of climatic resources in Northeast China

Based on the existing limitation indicators of cropping systems, while considering the impact of water and thermal resources on cropping systems in Northeast China, changes in climatic potential productivity and utilization efficiency of climatic resources in the sensitive areas of cropping systems were analyzed. The results show that the planting boundaries of different cropping systems in Northeast China obviously shifted toward the north and the east along with the heat and precipitation resources. However, in southwestern Heilongjiang Province, only one crop in a year could be planted because of the shortage of precipitation resources. Due to high temperature stress, the climatic potential productivity of spring maize would be reduced in the future. In certain small areas nearby Harbin in the Heilongjiang Province, two crops in a year could be planted from 2071 to 2100. Therefore, adjusting the cropping system was an effective way to improve the climatic potential productivity and climate resource utilization. In some thermal resource rich areas, the climatic potential productivity of summer maize or winter wheat decreased because of the shortened growth season caused by a warming and drying climate. However, if the one crop in one year pattern (spring maize) becomes a two crops in one year pattern (summer maize and winter wheat), the total climatic potential productivities of two crops would be higher than that of one crop. This finding further illustrates that after a paradigm shift from one crop in one year to two crops in one year, the thermal resources, which were not originally used, would become fully utilized. (Guo Jianping)

大气成分和大气化学

Atmospheric Composition and Atmospheric Chemistry

大气成分和大气化学研究进展

2014年,大气成分研究所圆满完成了承担的各项任务,在分析方法建立、比对校验、质量控制,大气成分及相关特性的观测、环境气象模式发展应用,影响评估等方面均取得了明显的进展。

1 分析方法、比对校验和质量控制研究

1.1 中国气溶胶遥感网Cimel太阳光度计积分球标定方法的建立

参考美国国家标准技术研究院对于积分球标定的方法,建立了中国气溶胶遥感网络(CARSNET) Cimel太阳光度计的积分球标定方法和流程。利用该标定方法和操作流程对4台CE318太阳光度计进行了标定试验。结果显示,与出厂参数相比,本方法获得的可见光波段标定系数相对偏差小于3%,而红外波段相对偏差约5%。太阳等纬圈(ALMUC)和主平面(PPLAN)现场验证实验数据显示,天空散射辐亮度在 $\pm 6^\circ$ 表现出良好的一致性,所有波长的差异小于1%,表明该标定方法和流程适合CARSNET太阳光度计的校准,并有利于提高数据质量和网络观测的精度。(车慧正)

1.2 四级杆质谱与全二维气相色谱联用鉴定大气中的挥发性有机物

大气挥发性有机物的准确测量对空气质量评估、大气光化学机理研究和污染控制政策制定等具有重要意义。全二维气相色谱技术有助于准确测量复杂的大气挥发性有机物,但是对快速检测器的要求限制了全二维气相色谱与四级杆质谱的联用。通过研究将四级杆质谱与全二维气相色谱联用,并应用于大气挥发性有机物的鉴定。在对标准混合气体和北京城市空气测量中,鉴定了包括烷烃、烯烃、芳香烃、含氧烃以及卤代烃等125种挥发性有机物,并将鉴定化合物逐一对应至全二维气相色谱-氢火焰离子化检测结果中,从而完成了后者的谱图解析和进一步定量分析。对谱图中部分色谱峰保留时间随二维调制周期环绕的现象进行了详细讨论。全二维气相色谱分别与四级杆质谱和氢火焰离子化检测器联用进行定性和定量分析的方法不仅可靠实用,而且降低了仪器成本。该方法和研究结果可应用于其他挥发性有机物的分析中(图1)。(王瑛)

1.3 本底大气CO₂观测分析过程中QA/QC方法的建立与评估

建立科学规范的本底大气CO₂采样观测分析过程中的质量保证与质量控制方法,是实现该数据资源同化和共享的基础。本研究以中国气象局温室气体网络化采样观测经验为基础,以便携式采样观测尧波长扫描光腔衰荡光谱(WS_CRDS)分析技术为例,系统介绍了我国青海瓦里关全球本底站大气中CO₂采样观测过程中的质量保证措施、样品分析过程中的玻璃瓶质量保证措施和样品分析过程中的系统质量控制方法、数据处理过程中的校正方法、数据分级质量标记和数据拟合插补方法等;并重点对该方法中几个关键步骤进行了评估验证;最后,应用本研究方法,对我国3个区域大气本底站CO₂的采样观测数据进行了处理和浓度变化特征分析。本研究方法也可以较好地捕捉区域和局地环境因素对观测结果的影响,并客观、准确地反映该区域的自然和人为活动特征。(刘立新)

1.4 龙凤山本底站大气CO₂数据筛分及浓度特征研究

针对黑龙江龙凤山区域大气本底站2009年1月至2011年12月底层(离地10 m)和高层(离地80 m)大气CO₂在线观测数据,选取底层数据重点开展研究,分析地面风向和风速等因素对观测CO₂浓度的影响。结果表明,龙凤山底层大气CO₂浓度明显受局地源汇影响,其与高层观测结果差异在白天

08:00—17:00相对较小, 小于 $(0.5 \pm 0.5) \times 10^{-6}$ (物质的比量)。春、夏和秋这3季节E-ESE-SE-SSE扇区来向的地面风会明显抬升大气CO₂浓度、而冬季N-NNW-NW-WNW扇区CO₂浓度明显较高。该站4个季节近地面CO₂浓度随着风速增大而逐渐减小, 在冬季尤为明显。结合日变化及地面风的影响对低层观测数据进行初步本底/非本底筛分, 筛选出代表东北区域混合均匀CO₂水平的本底数据占总数据的30.7%。本底CO₂浓度季节变化显示该站大气CO₂浓度呈现冬季高夏季低的趋势, 季振幅为 $(36.3 \pm 1.4) \times 10^{-6}$, 明显大于同期WMO、GAW同纬度站点观测结果, 2009—2011年龙凤山大气CO₂年平均增长率为 2.4×10^{-6} 。(方双喜)

1.5 MeteoInfo: 气象数据显示分析GIS软件

MeteoInfo是为气象数据分析和显示开发的一套软件工具, 包括一个面向软件开发人员的.Net类库和一个面向最终用户的桌面软件。MeteoInfo包含了一些基本的GIS功能, 并能读取气象领域中常用的数据格式, 如NetCDF和GRIB。对于格点和站点数据提供了能够进行复杂气象分析的数据模型。类库提供了丰富的空间和气象数据操作方法和控件, 可以方便地用于相关业务软件开发。桌面软件具备友好的用户界面, 是查看和探究气象数据的一个方便和强有力的工具。通过编写IronPython脚本程序, MeteoInfo可以自动运行并进行批处理操作。MeteoInfo是一个免费软件, 已经在国内外有广泛的应用(图2)。(王亚强)

2 大气成分及相关特性变化的观测研究

2.1 我国上甸子区域本底站大气六氟化硫(SF₆)在线观测研究

通过国际合作, 采用欧亚地区卤代温室气体观测网(SOGE)和改进的全球大气实验网(AGAGE)技术, 利用自组装气相色谱-电子捕获检测系统和气相色谱-质谱联用系统, 在我国上甸子区域本底站自2009年6月至2011年5月开展了2个完整年度的在线观测。观测期间SF₆平均本底和非本底浓度分别为 7.22×10^{-12} 和 8.66×10^{-12} 。上甸子站本底浓度与AGAGE同纬度本底站(Trinidad Head站和Mace Head站)浓度一致, 大于南半球本底站(Cape Grim站和Cape Matatula站)浓度。观测期间SF₆本底浓度快速增长, 年增长率达到 0.30×10^{-12} 。SF₆本底浓度季节振幅为 0.07×10^{-12} , 非本底浓度季节振幅则达到 2.16×10^{-12} 。SF₆的浓度峰值出现在秋季, 地面风向来自W-WSW-SW-SWS-S, 而SF₆低浓度出现在地面风来自N-NE-NE-ENE-E扇区。(姚波)

2.2 我国瓦里关和上甸子本底站大气CO₂及其稳定同位素变化

利用2007—2010年瓦里关和上甸子站大气CO₂及其碳稳定同位素观测数据, 对二者的变化特征、相关关系和源汇特征进行了分析研究。结果显示, 瓦里关站大气CO₂及其δ¹³C具有显著的长期变化趋势和季节变化规律, 同时二者呈明显的镜像关系, 年际变化规律显示出北半球中高纬度陆地生态系统源汇季节变化特征。CO₂年均浓度呈线性增长趋势, 年均增长率为 $(2.1 \pm 0.1) \times 10^{-6}$; δ¹³C年均值则呈线性下降趋势, 年均增长率为 $(-0.02 \pm 0.001) \text{‰}$ 。在上甸子站, 受陆地生态系统和人类活动共同影响下, 大气CO₂年均值亦呈线性增长趋势, 年均增长速率为 $(1.8 \pm 0.1) \times 10^{-6}$; 同时CO₂季振幅达到 23.0×10^{-6} 。2009—2010年度δ¹³C年均值由 -8.27‰ 降至 -8.36‰ 。瓦里关和上甸子站δ_s分别为 $(-25.44 \pm 0.72) \text{‰}$ 和 $(-21.70 \pm 0.67) \text{‰}$; 在瓦里关站, 冬春季δ_s偏负; 而在上甸子站, 由于受到夏季C₄植物光合作用和冬季生物质燃烧的影响, 其δ_s全年偏重并较瓦里关站更偏正。(刘立新)

2.3 我国4个大气本底站大气CO₂浓度观测研究

利用基于光腔衰荡光谱技术, 于2009—2011年对我国4个世界气象组织/全球大气观测网(WMO/GAW)全球或区域本底站(浙江临安、黑龙江龙凤山、北京上甸子和青海瓦里关)大气CO₂浓度进行连续观测研究。其中临安站位于经济发达区域(上海), 龙凤山站位于农田和森林区域, 离省会哈尔滨较近, 而上甸子站距离北京约150 km。瓦里关站代表我国内陆本底清洁大气水平, 该站也拥有国内最长的大气CO₂观测记录。观测期内4站大气CO₂浓度年增长率分别为 $(3.7 \pm 1.2) \times 10^{-6}$ (临安)、

$(2.7 \pm 0.8) \times 10^{-6}$ (龙凤山)、 $(3.5 \pm 1.6) \times 10^{-6}$ (上甸子)、 $(2.2 \pm 0.8) \times 10^{-6}$ (瓦里关)。相比而言, 临安站 CO_2 浓度最高, 在2011年平均浓度为 $(404.2 \pm 3.9) \times 10^{-6}$ 。通过对各站大气 CO_2 浓度日变化、季节变化以及局地源汇影响分析, 研究了各站浓度特征以及影响因素。以上研究为认识我国大气 CO_2 浓度特征以及模式研究提供了基础支撑。(方双喜)

2.4 长三角区域临安站大气 CO_2 本底信息的评估

结合气溶胶观测记录和气象资料, 对长三角地区大气中混合均匀的 CO_2 本底信息进行了提取研究。基于新研发的方法, 对浙江临安站2009—2011年观测的 CO_2 浓度记录进行筛分, 并评估了人为活动对观测浓度的影响。结果表明, 通过本方法提取的 CO_2 本底浓度与R筛分提取的信息基本一致, 在重污染条件下, 本方法对于区域本底 CO_2 信息的提取明显优于R筛分法。2009—2011年临安站年平均 CO_2 浓度分别为 $(404.7 \pm 8.2) \times 10^{-6}$ 、 $(405.6 \pm 5.3) \times 10^{-6}$ 、 $(407.0 \pm 5.3) \times 10^{-6}$, 明显高于全球平均。人为活动排放对临安区域大气本底 CO_2 浓度有明显影响, 抬升约 9.1×10^{-6} 。(方双喜)

2.5 上甸子本底站卤代温室气体大气浓度短期波动的个例分析

利用轨迹分析法、印痕分析和流场分析法, 结合上甸子站卤代温室气体H-1301、HCFC-22、CFC-11和 SF_6 在线浓度观测数据, 选取2012年9月7—12日上甸子测站卤代温室气体浓度短期波动典型个例进行分析。轨迹分析结果表明: 9月7日12:00污染发生前, 气团主要来自较远的偏西北、偏北方向, 水平输送距离长、移速快、垂直高度高, 对应的卤代温室气体浓度偏低, H-1301、HCFC-22、CFC-11和 SF_6 的体积分数分别为 4×10^{-12} 、 350×10^{-12} 、 260×10^{-12} 、 10×10^{-12} ; 9、10日有一定比例的气团在测站的偏南区域近地面回旋打转, 水平输送距离短、垂直高度低, 在边界层内缓慢移动, 不利于污染物在边界层内扩散, 导致卤代温室气体浓度偏高, 对测站浓度的短期抬升贡献较大, 9日12:00 H-1301、HCFC-22、CFC-11的峰值体积分数分别达到 45×10^{-12} 、 200×10^{-12} 、 310×10^{-12} , 10日03:00 SF_6 的峰值体积分数达到 28×10^{-12} ; 11日西南方向回旋气团消失; 12日气团完全来自较远的西北方向且轨迹移动较快。印痕分析与轨迹分析结果一致: 7、8日敏感性系数较高区域主要分布在测站以北, 9、10日敏感性系数较高区域分布在测站偏南, 11、12日测站偏南的敏感性系数较高区域消失。流场分析结果表明: 9、10日环流形势有利于污染物在测站区域累积, 造成测站浓度的短期抬升。(安兴琴)

2.6 北京上甸子区域大气本底站甲基氯仿 (CH_3CCl_3) 在线观测研究

利用GC-ECD在线观测系统, 在北京上甸子区域大气本底站开展了 CH_3CCl_3 2年在线观测, 利用逐步逼近回归法进行本底值筛分, 讨论了上甸子站 CH_3CCl_3 浓度水平及其变化趋势。该站2009年和2010年的年均大气 CH_3CCl_3 本底浓度(摩尔分数, 下同)分别为 $(9.03 \pm 0.53) \times 10^{-12}$ 和 $(7.73 \pm 0.47) \times 10^{-12}$, 本底数据出现频率为61.1%(2009年)和60.4%(2010年)。上甸子站 CH_3CCl_3 浓度水平与北半球同纬度带本底站观测结果基本一致, 低于文献报道的2001—2005年间我国华南区域和城市观测的结果。观测期间本底浓度呈下降趋势, 年下降率为 1.39×10^{-12} 。结合风向分析, 该站 CH_3CCl_3 平均浓度最高的风来自西南扇区, 而平均浓度最低的风来自东北扇区, 不同风向的浓度差值分别为 0.77×10^{-12} (2009年)和 0.52×10^{-12} (2010年)。2010年各风向 CH_3CCl_3 平均浓度比2009年降低 $1.03 \times 10^{-12} \sim 1.68 \times 10^{-12}$ 。(姚波)

2.7 气团垂直输送对中国西南香格里拉区域大气本底站近地面臭氧浓度的影响

根据2007年12月到2009年11月在中国西南香格里拉区域大气本底站(28.006°N , 99.726°E ; 3580 m)的近地面臭氧、一氧化碳以及气象数据的现场观测, 发现臭氧和一氧化碳的季节峰值在春季而臭氧的谷值在夏季、一氧化碳的谷值在冬季。根据月均归一化的臭氧、一氧化碳和水汽值的变化, 提出了一个用于指示来自高层大气、富含臭氧气团向下输送到近地面的归一化指示因子(标为Y)。这个组合的因子具有较少受季节或偶然个例变化影响的优点。通过对Y值的分析, 发现大多数有效的向下输送经常发生在冬季(占总数的39%, 当Y的指示值大于4时), 导致了近地面臭氧浓度显著地上升。来自较强的向下输送事件导致冬季近地面臭氧浓度增加 9.6×10^{-9} (21%)。基于Y值与位势涡度、臭氧总量和后向轨迹很好地分析了一个由西风槽主导下较强的臭氧向下输送个例。亚洲季风在压制夏、秋

季近地面臭氧的积累中扮演了一个很强的角色，而由Y值指示的香格里拉高层臭氧向下输送的季节变化与青藏高原地区的平流层-对流层输送、副热带高空急流的季节变化有一致性。(郑向东)

2.8 超大城市北京冬季过氧乙酰硝酸 (PAN): 化学与气象过程的作用

亚洲超大城市大气过氧乙酰硝酸 (PAN) 的测量研究过去很少，而且主要局限于夏季较短的时段。本研究给出了2010年1月25日至3月22日北京市区中国气象局大院同步观测的PAN、O₃、NO_x等的分析结果。PAN小时平均浓度为 0.70×10^{-9} ($0.23 \times 10^{-9} \sim 3.51 \times 10^{-9}$)，与NO₂浓度呈较好的正相关，但与O₃浓度却不相关，这表明冬季城市PAN和O₃是脱钩的。风速风向和气团输送条件对O₃、PAN等污染物有非常显著的影响。到达测点的气团来自严重污染N-S-W扇区的边界层或者来自W-N扇区的自由对流层。自由对流层的下沉空气富含O₃，其平均PAN/O₃比值小于0.031，而污染扇区边界层空气含高浓度PAN和一次污染物，其平均PAN/O₃比值为0.11。这些有关输送条件的事实可较好地解释观测到的PAN与O₃的脱钩现象。北京冬季光化学生成对于PAN仍是重要的。形成PAN需要的PA自由基浓度估算值介于 0.0014×10^{-12} 和 0.0042×10^{-12} 之间。计算了PAN的生成反应和热分解反应对PAN浓度变化的相对贡献，发现即使在北京较冷的时期，两者的作用都是显著的，其中生成作用超过分解作用(图3)。(徐晓斌)

2.9 北京及周边地区3个典型站点NO_x和CO的变化特征

为了研究华北平原北部区域不同类型站点光化学前体物的共性与差异，在华北平原北部地区西南—东北主导风向上选取间距大于100 km的3个站点，即中国气象局(CMA)、上甸子(SDZ)和固城(GCH)依次代表北京城区、华北本底地区和相对污染的农村地区，进行了近地面NO_x和CO观测。结果表明：2008年6月至2009年5月，CMA、SDZ和GCH 3站NO_x体积分数的年均值依次为 $(42.4 \pm 21.8) \times 10^{-9}$ 、 $(13.8 \pm 5.5) \times 10^{-9}$ 和 $(26.9 \pm 15.2) \times 10^{-9}$ ；CO体积分数的年均值依次为 $(1.13 \pm 0.37) \times 10^{-6}$ 、 $(0.67 \pm 0.17) \times 10^{-6}$ 和 $(1.11 \pm 0.62) \times 10^{-6}$ 。3站的NO_x月均值体积分数以及CMA、GCH 2站的CO月均值体积分数呈现出冬季高夏季低的特点，而SDZ站的CO 6月均值体积分数 (1.03×10^{-6}) 为一年中最高。SDZ站的NO_x和CO体积分数在中午12:00前后出现一个低谷，比CMA和GCH站的提前3~4 h，此后呈上升趋势，体现了午后西南风输送对SDZ站的影响。尽管不同的源排放和大气输送影响导致3站的NO_x和CO体积分数在日变化特征上有所差异，但3站的NO_x和CO日平均体积分数之间存在极其显著的相关性，体现了区域性污染和气象条件共同影响的特征(图4)。(徐晓斌)

2.10 浙江临安大气本底站CO浓度及变化特征

利用基于光腔衰荡光谱(CRDS)技术自组装的大气CO在线观测系统，于2010年9月至2012年2月在浙江省临安大气本底站对大气CO进行了在线观测。结果表明，临安站四季CO日变化明显受人为活动影响，分别在每日07:00—10:00和19:00—20:00出现峰值，夏季CO日平均浓度和振幅均最低，分别为 $(314.3 \pm 7.6) \times 10^{-9}$ (摩尔比，下同)和 $(50.1 \pm 47.9) \times 10^{-9}$ 。该站全年大气CO浓度呈现冬春季高、夏季低的趋势、与北半球瑞士Jungfrauioch站、青海瓦里关等站基本一致，但平均浓度明显高于其他国际站点，全年CO月均值振幅为 $(286.8 \pm 19.2) \times 10^{-9}$ 。轨迹聚类和地面风结果分析表明，临安站非本底CO浓度主要来自N-NNE-ENE扇区内城市及工业等人为排放，春、夏和冬季最大的浓度抬升均出现在NEN风向，冬季抬升值最大为 $(106.3 \pm 58.0) \times 10^{-9}$ 。(方双喜)

2.11 长江三角洲区域本底站氨气和铵盐气溶胶季节变化特征

2009年9月至2010年12月在位于经济快速发展的华东长江三角洲之临安区域本底站使用被动采样器对大气氨进行了强化观测，同时在2010年对该站大气细粒子PM_{2.5}开展了为期1年的观测。观测期间临安站NH₃浓度变化范围为 $(0.1 \sim 41.8) \times 10^{-9}$ ，2010年NH₃年均浓度是 $(16.5 \pm 11.2) \times 10^{-9}$ 。2010年临安站PM_{2.5}中的NH₄⁺质量浓度变化范围为 $0.02 \sim 19.2 \mu\text{g}/\text{m}^3$ ，年均浓度为 $(4.3 \pm 3.5) \mu\text{g}/\text{m}^3$ 。NH₃浓度季节变化明显，夏季最高冬季最低，其主要与周边农业活动和气温呈正相关。NH₄⁺浓度在秋季最高可能是受到农业残余生物质燃烧的影响。2010年临安站NH₃/NH_x的比值为 0.8 ± 0.1 ，说明NH_x主要是受到当地源的影响。后向轨迹分析表明，临安站因受到长江三角洲区域及偏北气流引起的污染长距离传

输影响, 呈现出高细粒子水平特征。临安区域本底站高 NH_x 沉降说明了在长江三角洲区域减少 NH_3 排放的紧迫性。(孟昭阳)

2.12 北京 $\text{PM}_{2.5}$ 中水溶性离子的变化、形成以及酸性特征

总结了北京城区2009年6—11月期间 $\text{PM}_{2.5}$ 日均浓度、 $\text{PM}_{2.5}$ 中水溶性无机离子小时平均浓度以及 $\text{PM}_{2.5}$ 气态前体物浓度。结果表明, 水溶性离子总浓度为 $44 \mu\text{g}/\text{m}^3$, 占 $\text{PM}_{2.5}$ 的38%, 其中硫酸盐、硝酸盐和铵盐是主要的离子成分。硫酸盐在夏季和秋季浓度差异在30%以内, 而硝酸盐和铵盐的浓度在两个不同季节差别明显。由于源排放、生成机理以及气象条件的不同, 导致多数离子成分及其前体物浓度的日变化特征明显。硫酸盐、硝酸盐和铵盐的氧化/转化率分别为63%, 15%和15%。尽管环境大气中存在大量氨气, 但铵盐的转化率仍然很低, 说明气态氨的浓度水平不是铵盐生成主导因子。铵盐的日变化特征也与气态氨的日变化特征不同。对 $\text{PM}_{2.5}$ 中氢离子浓度以及气溶胶酸度的估算结果显示, 有75%的样品显强酸性, 只有极少部分样品显碱性。(张养梅)

2.13 我国中东部高山站 PM_1 中主要化学组分和粒径分布特征

自2010年6月至2012年1月, 对泰山高山站亚微米气溶胶主要化学组分质量浓度和粒径分布特点进行了归纳和总结。结果表明, 该站点亚微米气溶胶中有机物、硫酸盐、硝酸盐、铵盐和氯化物的年平均质量浓度分别为11.2、9.2、7.2、5.8和0.95 $\mu\text{g}/\text{m}^3$ 。这个浓度水平明显高于美国和高山站, 但比我国城市近地面站点浓度要低。在整个观测阶段, 主要化学组分浓度具有明显的季节变化规律、边界层高度的季节变化特点, 近地面污染物浓度以及区域传输过程等因素是导致秋季浓度低、夏季浓度高的主要原因。

为了更好地探讨不同类型污染天气对亚微米气溶胶特性的影响, 本研究将气团分成了受边界层影响(PBL)、受自由对流层影响(LFT)、新粒子生成事件(NPF)、云中过程和污染过程等5类。其中, 有机物在新粒子生成事件中占有主导地位, 而硫酸盐在云中过程中对亚微米气溶胶的贡献最大。

整个研究期间, 有机物、硫酸盐、硝酸盐和铵盐的质量谱均值粒径分别为539、585、542和545 nm。该均值粒径比在华北地区地面观测的均值粒径要偏大, 说明高山站气溶胶粒子相对老化并混合均匀。在PBL、NPF和污染事件中, 有机物在小粒子范围贡献最大, 尤其在污染事件中, 在100~200 nm之间, 有70%的组分是有机物。在云中过程中, 无机物在整个亚微米粒径范围贡献70%, 其中硫酸盐在小粒子范围贡献40%, 表明硫酸盐在云形成过程中起到至关重要的作用。

根据气团轨迹特点将该站点受到的主要气团来向分为7条, 大多数气团来源于短距离的区域扩散, 主要气团来自站点南方, 其中有机物和硫酸盐是这类气团的主要污染物种。远距离传输气团通常载带着清洁和干燥的气团影响泰山站点。

利用正矩阵因子分析方法对有机物进行的分类解析结果表明, 泰山站有机气溶胶中, 氧化类有机气溶胶在春、夏、秋、冬4个季节分别占总有机物的49%、56%、51%和41%, 说明夏季有机物氧化程度较严重。此外, 生物质燃烧类有机气溶胶夏季占有机气溶胶的34%, 燃煤类有机气溶胶在冬季占有机气溶胶的22%。(张养梅)

2.14 中国不同区域大气气溶胶化学成分浓度、组成与来源特征

为获得中国不同区域大气气溶胶化学组成的总体“图景”, 进一步探讨污染治理方向, 需要分区域评估其化学成分浓度水平、组成与来源特征。通过对近地层中国内陆大气气溶胶中6种主要化学成分(硫酸盐、硝酸盐、铵、有机碳、黑碳和矿物气溶胶)至少有1年观测研究的评估分析, 获得不同区域气溶胶化学成分质量浓度水平与组成的评估结果。在气溶胶污染最严重的4大区域(即北京以南的华北与关中平原区域、以长三角为主体的华东区域、以珠三角为主体的华南区域以及四川盆地)的 PM_{10} 中矿物气溶胶(所占20%~38%)、硫酸盐(占14%~24%)、有机碳(占11%~18%)是3个主要组分; 其中华北与关中平原气溶胶污染在中国最重, 硫酸盐浓度为35~47 $\mu\text{g}/\text{m}^3$ (远高于北京的(13~18 $\mu\text{g}/\text{m}^3$))、有机碳为28~45 $\mu\text{g}/\text{m}^3$ (约是北京(19~22 $\mu\text{g}/\text{m}^3$)的1.8倍)、硝酸盐为19~22 $\mu\text{g}/\text{m}^3$ (约是北京(9.9~12 $\mu\text{g}/\text{m}^3$)的2倍)、铵为14~16 $\mu\text{g}/\text{m}^3$ (比北京(6.2~8.4 $\mu\text{g}/\text{m}^3$)高1倍), 黑碳在北京和北京以南城市的浓度差别不大(9.1~12 $\mu\text{g}/\text{m}^3$)。这其中燃煤对硝酸盐和有机

碳气溶胶的贡献超过50%，农业活动是铵的最重要来源。华东、华南和东北城市区域气溶胶化学成分浓度水平与北京相近，但四川盆地城市站各组分浓度均高于北京，污染较重。西北兰州城市站，除了黑碳浓度低很多、硝酸盐浓度稍高外，其他气溶胶化学成分浓度水平与北京相当。西北偏远区域沙漠站点，各种气溶胶化学成分浓度都远低于北京。青藏高原和云贵高原城市站气溶胶化学成分浓度与北京相比也明显偏低。不同区域气溶胶化学组成分析显示，燃煤、机动车、城市逸散性粉尘和农业活动是4个最需要关注的污染源，加强除发电行业外的燃煤脱硫，进一步消减燃煤氮氧化物、一次有机碳和挥发性有机物排放，并有效减少农业活动排放到大气中的氨，更有效限制硫酸盐和硝酸盐的形成是已有大气污染治理对策基础上，未来应特别关注的控制方向。（张小曳）

2.15 泰山PM₁₀及其中化学成分变化特征

为研究具有区域背景代表性的气溶胶成分及其变化特征，在泰山顶从2010年6月至2011年7月采集了64个PM₁₀滤膜样品，分析了样品的PM₁₀及其中无机盐离子和有机碳（OC）、元素碳（EC）的质量浓度，并对各成分相关性等进行了分析。泰山PM₁₀年均质量浓度约为68.4 μg/m³，其中无机盐离子约占总质量的64.8%，碳气溶胶约占17.4%。无机盐离子的质量浓度从春季逐渐增大，夏季达到峰值，秋季下降，冬季最小；OC质量浓度从春季至秋季逐渐增高，冬季最低，EC变化类似，但夏秋两季差别不大。二次有机碳（SOC）与OC的比值四季均在50%以上，年均值约为58.5%。通过后向轨迹聚类分析，发现在经过城市的较短轨迹以及南方较短混合轨迹的影响下，泰山PM₁₀质量浓度较高，而西北长距离传输气团PM₁₀浓度均较低。（王亚强）

2.16 北京上甸子典型天气个例的大气气溶胶数谱分布特征

使用差分滴度粒径分析仪（TDMPs）和空气动力学粒径分析仪（APS）对上甸子区域本底站颗粒物（直径3 nm ~ 10 μm）数谱分布特征进行观测。利用2008年的观测结果，分析了不同天气（包括沙尘天气、干洁天气和雾霾天气）条件下大气气溶胶数谱分布及其与气象要素和气团来源的关系。结果表明，沙尘天气条件下，上甸子站受西北方向的气团控制，风速较大，粗粒子数浓度明显增加，PM₁₀的质量浓度可以迅速增加到毫克每立方米的量级。典型的“香蕉型”新粒子生成事件通常发生在比较干洁晴朗的天气条件下，西北气团主导，大气中背景气溶胶数浓度较低，核模态气溶胶数浓度迅速增长，气溶胶的粒径呈现明显的增长过程，核模态可以平稳地增长到80 nm左右，达到成为云凝结核的尺度。雾霾天气通常是在西南气团影响下，细颗粒物（1 μm以下）的不断累积、相对湿度不断升高的条件下发生的。雾霾天气条件下数谱分布的几何中值粒径出现在积聚模态，积聚模态数浓度也高于非雾霾天。个例研究表明，雾霾天气条件下PM_{2.5}质量浓度可以达到非雾霾天的10倍左右，其中以细颗粒物的贡献为主。在雾霾天气条件下，上甸子地区数浓度较高的积聚模态颗粒物主要来自城区的传输，因此对背景地区气溶胶数谱的研究可以为解析城区气溶胶复杂来源提供依据。（沈小静）

2.17 基于地基太阳光度计测试的2013年中国华北平原严重雾霾月数据进行的柱状气溶胶光学特性和气溶胶辐射强迫研究

2013年1月，华北平原经历了几次严重的雾霾事件，在2013年1月1—30日，基于Cimel太阳光度计在华北背景、郊区和城市等7个站点进行了观测，研究气溶胶光学参数的时空变化和气溶胶辐射强迫。研究发现，500 nm气溶胶光学厚度在无污染时期每个站点都低于0.30，在污染事件发生时期，气溶胶光学厚度显著大于1.00。在大多数时间段，所有的站点Angstrom指数都大于0.80。污染和非污染时期，在北京的3个城市站点，500 nm平均气溶胶光学厚度从北向南逐渐增加。在城市站点污染期间细模态气溶胶光学厚度大约是无污染时期的2.5倍，而在郊区和农村站点达5.0倍左右。在2013年1月，对于所有站点675 nm细模态气溶胶光学厚度所占比例大于80%。污染时期，675 nm气溶胶光学厚度吸收在农村站点约为0.01，而在其他地区的污染和非污染时段，分别为0.03 ~ 0.07和0.01 ~ 0.03，单次散射反照率在0.87和0.95之间。雾霾最严重时期，北京城区气溶胶粒子谱分布呈现出明显的3峰分布特征。在污染时期，细模态气溶胶有效半径为0.01 ~ 0.08 μm，大于非污染时段；而粗模态粒子有效半径，在污染时段为0.06 ~ 0.38 μm，比非污染时期小。总体、细模态和粗模态气溶胶体积变化分别为0.06 ~ 0.34 μm³，0.03 ~ 0.23 μm³和0.03 ~ 0.10 μm³。在雾霾最严重的时期（1月1—16日），气溶

胶辐射强迫在农村、郊区、城市分别超过了 -50 W/m^2 、 -180 W/m^2 和 -200 W/m^2 。在大气层顶,农村和城市地区气溶胶辐射强迫数值分别为 -30 W/m^2 和 $-40 \sim 60 \text{ W/m}^2$ 。由于积雪覆盖导致的高反照率,惠民城市站点大气层顶正的气溶胶辐射强迫不同于其他站点。(车慧正)

2.18 2013年1月中国东部一次重度霾污染事件的天气成因分析

应用加密地面气象要素观测资料、经纬仪气球探空资料、NCEP再分析资料以及T639模式输出产品,采用大气环流三维结构合成分析、稳定边界层物理量诊断分析以及轨迹模式HYSPLIT4跟踪等方法,研究2013年1月6—16日中国华北大范围雾霾天气过程发生和持续的气象成因,探讨气象条件在2013年1月10—12日北京 $\text{PM}_{2.5}$ 质量浓度连续上升过程中的作用与影响。结果表明:(1)大气环流从经向波型调整成为纬向波型的过程为中国华北地区提供了有利于雾霾天气发生的静稳型环流形势;(2)边界层大气层结稳定、对流高度值低,使边界层湍流运动受到抑制,为雾霾的形成提供了有利的气象条件;(3)黄河河套以东广大地区(包括山西、河北等地)在对流层低层存在一支低空西南气流($6 \sim 11 \text{ m/s}$),有利于这些地区的污染物向北京方向远距离输送,加剧北京的空气污染程度;(4)美国NOAA研制的HYSPLIT4模式对气团72 h后向轨迹追踪与高空探测结果相吻合,具有参考价值。(王宏)

2.19 中国北京严重雾霾条件下气溶胶光学特性的研究

2013年1月,在中国华北地区发生了几次严重的霾污染事件。基于中国气象科学研究院站点2013年1月1—30日期间的Cimel太阳光度计的数据,详细研究了气溶胶的光学特性。研究发现,2013年1月雾霾期间,当北京城区气溶胶光学厚度大于0.60时,Angstrom指数大多大于0.80。在霾发生之前,北京城市地区气溶胶光学厚度大约可以稳定在0.40,而之后,伴随霾的产生,500 nm气溶胶光学厚度急剧上升超过1.50。在严重的霾污染时期,细模态大气气溶胶是粗模态的20倍。在440、675、870和1020 nm 4个波段,单次散射反照率接近 0.90 ± 0.03 ,细模态粒子单次散射反照率在440 nm波段相对一致,而在675、870和1020 nm波段变化很大。除1月12日和18日外,所有的细粒子体积都高于粗粒子体积,表明由人为产生的细粒子是雾霾产生的主要因素。对2013年1月严重雾霾污染事件气溶胶类型分类分析表明,占主导地位的气溶胶类型能够被分为“混合”和“城市/工业/生物体燃烧”两种类别。混合型约为31%,而城市/工业型约为69%。(车慧正)

2.20 使用Prede天空辐射计在北京城市站点反演的气溶胶光学特性

SKYNET是基于Prede天空辐射计的国际气溶胶光学特性观测网络,主要目的是研究气溶胶-云-辐射相互作用。利用最新SKYRAD.pack软件(版本5.0)反演了北京城市站点气溶胶光学特性,包括气溶胶光学厚度(AOD),波长指数(α),粒子体积谱分布及单散射反照率(SSA)等。研究结果表明,北京500 nm的AOD值变化区间在0.11(第5百分位)到1.14(第95百分位),中值为0.34,季节平均的 α 最大值出现在夏季,为 1.05 ± 0.36 ,最小值出现在春季,为 0.82 ± 0.39 。500 nm的SSA值在夏季和春季有相似的较高值,为 0.96 ± 0.03 ,但在冬季较低,为 0.93 ± 0.04 。在北京全年的气溶胶粒子清楚地表明了双峰尺度分布:春季粗粒子,夏季细粒子。 α 随着AOD增大而变大,表明在北京细粒子在气溶胶光学特性中起着重要作用。根据沙尘标准阈值($\alpha < 0.47$ 并且 $\text{SSA}_{400 \text{ nm}} - \text{SSA}_{1020 \text{ nm}} < 0.018$),在所有的观测数据中沙尘类型气溶胶发生率在春、夏、秋和冬季分别占4.1%,5.1%,0.5%和1.2%。(车慧正)

2.21 2013年1月一次持续性重度霾污染事件的综合观测研究

针对2013年1月6—16日中国东部地区的一次强污染过程,对其能见度、 PM_{10} 、 SO_2 和 NO_2 浓度、550 nm的ODIS AOD、440 nm的CARSNET AOD和CLIPSO 532 nm的气溶胶消光系数等观测资料进行了综合分析。研究发现,东部地区这次持续性大面积霾污染过程伴随着低能见度、高 PM_{10} 和AOD。污染最为严重的地区是京津冀以及河北中南部、山东西部和河南北部在内的紧邻周边地区。霾污染扩散到了中国东部到 125° E 的海面,甚至对整个 140° E 以西的洋面都有所影响。京津冀及其周边地区 PM_{10} 的变化趋势呈现出很大的相似性,显示该地区污染物跨城市输送的可能影响。在这次严重霾污染事件中,超级城市群的郊区显示出和城市非常相似的严重污染状况。大部分污染物集中在地面以上1500 m高度,特别是100 ~ 800 m高度是污染物最为集中带。(王宏)

2.22 中国华北平原地区区域背景大气柱状整合的气溶胶光学和物理特性

基于兴隆站2006年2月到2011年7月的气溶胶光学特性数据研究了北方平原区域背景气溶胶光学和物理特性以及在沙尘和霾条件下的时间变化情况。结果表明,兴隆年平均气溶胶光学厚度和消光波长指数分别为 0.28 ± 0.30 和 1.07 ± 0.38 。季节平均的 $AOD_{440\text{ nm}}$ 在春季(0.40 ± 0.3)和夏季(0.40 ± 0.42)高于秋季(0.20 ± 0.22)和冬季(0.19 ± 0.21)。兴隆站的消光波长指数约为1.25,吸收波长指数为1.0~1.5,这表明占主导地位的类型是混合气溶胶(当AAE>1.0时占88.2%)。几乎所有的沙尘观测都发生在春季。细模态和粗模态颗粒的体积浓度随AOD的增加而增加。在春季,粗粒子气溶胶的增加程度大于细粒子;然而,在其他季节观测到相反的现象。兴隆站的高值AOD可能与细模态气溶胶增长及粗模态粒子有关。该背景站不仅受来自中国西北和蒙古国南部沙尘气溶胶的影响,也受到来自南方城市和工业化地区人为气溶胶远距离输送的影响。沙尘天气的平均AOD为1.49,而霾天的AOD为1.10。沙尘天和霾天的平均波长指数分别为0.09和1.43。(车慧正)

2.23 1980—2009年塔克拉玛干沙漠沙尘气溶胶对驱动表面太阳辐射呈上升趋势

研究了塔克拉玛干沙漠在1980—2009年表面太阳总辐射(SSR)的长期趋势及其与总云量(TCC)、低云(LCC)、水汽含量(WVC)和气溶胶光学厚度(AOD)的关系。该地区年平均SSR每10年增加了 1.21 W/m^2 ,除了冬季,SSR均呈上升趋势。TCC, LCC和WVC有所增加,而AOD和严重沙尘时间发生频次均呈减少趋势,表明在塔克拉玛干沙漠是沙尘气溶胶而不是云层和水蒸汽驱动SSR的长期上升。(车慧正)

2.24 中国四川盆地基于地面测量的气溶胶光学特性

测量并分析了2007年2月到2009年12月中国四川盆地成都站点的气溶胶光学厚度(AOD)和Angstrom指数以及气溶胶光学厚度与 PM_{10} 之间的关系。观测中发现AOD月平均高值出现在3月、8月和12月而相对较低的值出现在10月,Angstrom指数在3月和8月的变化与AOD相反,平均 PM_{10} 呈显著的季节性差异,冬季存在高峰值,总的AOD值与近地面层的 PM_{10} 之间存在一个复杂的(非线性)正相关关系。沙尘和雾霾条件下的3个案例表明,AOD值在沙尘天气条件下最大而在霾天气条件下最小,然而3种天气条件下Angstrom指数分布与AODs相反。3天的后向轨迹分析表明,空气质量的起源很大程度上影响四川盆地上方的气溶胶光学特性。(车慧正)

2.25 利用CloudSat卫星资料分析云微物理和光学性质的分布特征

利用2007年1月至2010年12月高垂直分辨率CloudSat卫星的2B数据产品,对云微物理特征量(包括云中液态水/冰水含量、液态水/冰水路径、云滴有效半径等)以及云光学参数(云光学厚度等)的全球分布和季节变化进行了统计分析,并研究了云微物理性质对光学性质的影响。结果表明,冰水路径分布在北美南部、南美大陆、非洲大陆、澳大利亚和南亚的陆地上空,以及太平洋、大西洋和印度洋的洋面上空,高值区最大值达 600 g/m^2 以上,垂直方向上高值区位于赤道地区8 km附近以及中纬度地区4~8 km高度上。液态水路径在 300 g/m^2 以上的高值区主要位于太平洋、印度洋和大西洋的中低纬度海域上空,垂直方向上液态水含量随高度递减。冰云有效半径在高纬度地区近地面层达 $200\text{ }\mu\text{m}$ 以上,在赤道附近4~8 km上有1个高值区,南北半球中纬度地区2~4 km上有2个高值区,最大值均达到 $80\text{ }\mu\text{m}$ 以上。在1 km以下的边界层水云有效半径值较大,达到 $12\text{ }\mu\text{m}$ 以上。总云光学厚度在全球大部分地区 < 40 ,高值区普遍位于中高纬度的广阔地区和低纬度靠近大陆的洋面上空;垂直方向上云光学厚度的高值集中在2 km以下的边界层。云光学厚度的分布受云量、云水含量和云滴有效半径的影响,云量大的地区基本为云光学厚度的大值区。(王志立)

2.26 青藏高原及其周边地区卫星Aura-MLS的臭氧与水汽廓线产品的验证分析

根据Aura卫星微波临边探测(MLS)2.2、3.3版水汽和臭氧廓线,采用线性内插方法,将夏季在青藏高原(西藏的那曲和拉萨)及其周边地区(云南腾冲)通过冷冻霜点仪(CFH)和电化学反应池型(ECC)探空仪分别测得的水汽和臭氧数据插值到与卫星产品规定的气压高度进行比较分析,以检验MLS水汽和臭氧廓线产品。结果表明:MLS 2.2、3.3版水汽相对误差在100 hPa的对流层

顶附近分别为 $(9.8 \pm 46.0)\%$ ($n=18$)、 $(23.0 \pm 45.8)\%$ ($n=17$)；在小于并包含 82.5 hPa 在内的下平流层则分别为 $(2.2 \pm 15.7)\%$ ($n=74$)、 $(0.3 \pm 14.9)\%$ ($n=75$)；而在对流层 316 ~ 121 hPa 高度则分别为 $(21.5 \pm 90.6)\%$ ($n=104$)、 $(6.0 \pm 83.4)\%$ ($n=99$)。相应 MLS 2.2、3.3 版臭氧的误差分别为： $(-3.5 \pm 54.4)\%$ ($n=27$)、 $(-8.7 \pm 41.6)\%$ ($n=38$) (100 hPa)； $(-11.7 \pm 16.3)\%$ ($n=135$)、 $(15.6 \pm 24.2)\%$ ($n=305$) (下平流层)； $(18.0 \pm 79.1)\%$ ($n=47$)、 $(34.2 \pm 76.6)\%$ ($n=160$) (对流层上层)。MLS 水汽和臭氧的误差垂直分布在对流层上层-平流层低层振荡和离散分布明显，部分误差可能由此高度层水汽和臭氧浓度梯度大和用线性插值探空数据引起。“臭氧低谷”期间，拉萨地区 70 hPa 高度以下 MLS 卫星臭氧浓度误差明显增加；腾冲、那曲与拉萨 3 地的 MLS 臭氧误差的垂直分布特征较一致。卫星产品与探空测值的初步关系表明，MLS 廓线的灵敏度与水汽和臭氧在大气中垂直分布有密切联系，3.3 版水汽产品的灵敏度在 82.5 hPa 以上高度略有提高，臭氧产品灵敏度没有明显变化。对 MLS 水汽和臭氧廓线产品误差的可能因素也进行了讨论。(郑向东)

3 大气成分模式的发展应用及大气成分的影响研究

3.1 APEC 环境空气质量预测和减排效果评估

实施了 APEC 会议 1 个月前的污染趋势预报，在临近 APEC 和 APEC 期间，实施了精细化预报。对北京城区和会议区域（怀柔）的空气质量进行了 7 ~ 10 天的预报。与此同时，对 APEC 期间的减排措施进行了评估和分析。综合分析表明，2014 年 11 月 3—12 日 APEC 会议期间，北京及周边采取的大气污染物减排措施使北京城区 PM_{2.5} 浓度约降低 35%，NO₂ 浓度约降低 33%，有效避免了重污染天气发生。APEC 会议期间，由于南风弱，大气污染物跨区域输送不明显，北京本地减排对改善空气质量的贡献率为 83% ~ 89%，周边地区减排的贡献率为 11% ~ 17%。分析还发现，APEC 会议期间，周边 300 km 范围内采取减排措施对北京的影响效果与 600 km 范围内的减排效果相当；外地机动车的减排措施对北京影响不大；周边区域高架点源减排对降低北京地区 PM_{2.5} 浓度的贡献约为 9%。(龚山陵，刘洪利)

3.2 气溶胶-气候在线耦合模式 BCC_AGCM2.0.1_CUACE/Aero 中云微物理过程的改进、评估以及更新的气溶胶间接效应

将一套能同时预报云滴和冰晶质量浓度和数浓度的双参数云微物理方案应用到气溶胶-气候在线耦合模式 BCC_AGCM2.0.1_CUACE/Aero 中，详细评估了模式对气溶胶、云性质和气象场的模拟性能，计算了气溶胶的间接辐射强迫。较之前模式，新模式能更真实地模拟出气溶胶的质量浓度和光学厚度。新模式模拟的全球年平均柱云滴数浓度为 $3.3 \times 10^{10} \text{ m}^{-2}$ ，与卫星反演结果 $4.0 \times 10^{10} \text{ m}^{-2}$ 相当。新模式模拟的全球年平均云顶云滴有效半径为 8.1 μm ，小于相应的观测结果 10.5 μm 。新模式模拟的云液态水路径明显低于旧模式的结果，特别是在中纬度一些区域，年平均的云液态水路径低了近 100 g/m^2 ，但是与卫星观测结果更加一致。新模式对云辐射强迫和降水的模拟在一定程度上也有所改进。新模式模拟的大气顶辐射能量收支为 -0.6 W/m^2 ，相比旧模式的结果 (1.8 W/m^2) 有明显的差异。当没有设置云滴数浓度的较低限制时，新模式模拟的大气顶人为气溶胶的间接辐射强迫的全球年平均值为 -1.9 W/m^2 。但是，当设定一个云滴数浓度的最低限制时，气溶胶的间接辐射强迫明显减小。(王志立)

3.3 气溶胶-气候耦合模式系统 BCC_AGCM2.0.1_CAM 气候态模拟的初步评估

讨论了国家气候中心第 2 代大气环流模式 BCC_AGCM2.0.1 和加拿大气溶胶理化模式 CAM 所组成的耦合模式系统对 5 种典型气溶胶（硫酸盐、黑碳、有机碳、沙尘和海盐）和气候要素的模拟效果。结果表明，耦合系统对 5 种典型气溶胶的模拟总体上比较合理，尤其是对硫酸盐、沙尘和海盐的模拟比 BCC_AGCM2.0.1 原有的月平均气溶胶资料有很大的改进。耦合系统模拟的全球平均气候态参量与观测/再分析资料比较一致，在总云量、陆地表面温度和降水等方面要略优于原月平均气溶胶资料的模拟结果。耦合系统对沙尘和海盐气溶胶模拟的改进使得撒哈拉沙漠和南半球中纬度海洋大气顶净太阳辐射的模拟也有所改进，而这将直接影响地表温度尤其是陆地表面温度。而不同气溶胶方案在赤道海洋上引起的云反馈不仅引起辐射的改变，还将对降水产生明显影响。(王志立)

3.4 不同时刻污染减排对北京市PM_{2.5}浓度的影响

利用空气质量模式 Model-3/CMAQ 及京津冀地区高分辨率排放源清单, 针对有代表性的污染时段(2012年2月7—16日), 设置了5种不同时刻的减排方案(在污染峰值提前4天、提前3天、提前2天、提前1天及当天减排), 对比在同样的减排比例下, 不同时刻开始减排的效果差异。研究发现, 提前采取减排控制措施比污染峰值当天开始减排对降低PM_{2.5}浓度的影响更为明显, 而且提前采取应急减排的时间越早, PM_{2.5}浓度下降越明显。提前1天、2天、3天减排海淀站和城6区峰值浓度下降率分别为23%和22%、31%和30%、39%和38%, 均明显高于当天减排的峰值浓度下降率10%和9%。但随着提前天数的增加, PM_{2.5}峰值浓度进一步下降的幅度越来越小, 减排效益较之前显著降低。提前4天减排海淀站和城6区峰值浓度下降率分别为40%和39%, 提前4天减排和提前3天减排对降低污染峰值日PM_{2.5}浓度的效果已没有太大差别。同时针对另一个污染时段(2012年1月11—20日)进行了相似的敏感性试验, 得出了类似的结论。因此, 针对某些污染事件的应急减排, 综合考虑减排成本和减排效果, 根据气象条件的预报, 在可能引起重污染事件的不利气象条件来临时提前2~3天采取减排措施效果最好, 既能有效降低PM_{2.5}浓度, 也可以避免因盲目长时间减排造成的成本过大。(安兴琴)

3.5 NASA / Goddard长波辐射方案在GRAPES_Meso模式中的应用研究

将NASA/Goddard的长波辐射方案引入到GRAPES_Meso模式中, 对2006年4月中国地区进行了1个月的模拟试验, 并与相应的NCEP再分析资料进行了对比分析。试验结果表明: 在模拟区域内, GRAPES_Meso模式24 h、48 h预报晴空大气顶向外长波辐射通量(OLRC)、地面接收到向下长波辐射(GLWC)分布形势与NCEP再分析资料具有较好的对应关系; 模式24 h、48 h预报OLRC和相应NCEP再分析资料月平均误差百分比控制在-10%~+10%以内, GLWC月平均误差百分比比OLRC略大, 但总体上两者误差在合理和可接受范围之内。模式24 h、48 h预报的OLRC和GLWC的距平相关系数都在0.93以上, 标准误差都在31 W/m²以内, GLWC预报与NCEP再分析资料的相关性比OLRC略好, OLRC与NCEP再分析资料的标准误差比GLWC小。本文研究结果表明, 引入NASA/Goddard的长波辐射方案后的GRAPES_Meso模式整体上能够较好地预报OLRC和GLWC, 该辐射方案可以作为模式GRAPES_Meso的备选辐射方案之一。(王宏)

3.6 对流层气溶胶的直接气候效应对平流层的影响

通过WACCM-3模式中气溶胶光学厚度与卫星资料的对比发现, 模式可以很好地再现全球气溶胶的主要分布特征, 但在一些区域还存在数值上的差异。利用数值试验研究了对流层气溶胶的直接气候效应对平流层气候的影响。结果表明, 对流层气溶胶对平流层气候有明显影响, 平流层化学过程在这一影响中起重要作用, 而对流层气溶胶对平流层辐射的影响不是其直接气候效应对平流层影响的主要原因。其机制可能是对流层气溶胶改变对流层的辐射平衡, 影响对流层的温度和大气环流, 进而影响行星波的上传, 使得平流层气候发生变化; 影响区域主要位于高纬度和极地地区, 南半球的变化比北半球大, 温度变化最大达10 K, 纬向风变化最大可达12 m/s, 臭氧体积分数最多减少 0.8×10^{-6} 。(刘煜)

3.7 城市排放与输送对北京上甸子站温室气体本底观测的影响分析

以北京上甸子区域大气本底站CO₂和几种典型卤代温室气体(HFC-134a、PFC-218和HCFC-22)浓度在线观测为例, 统计分析并匹配计算了各风向浓度距平与浓度载荷, 探讨了各季节城市排放和输送对上甸子站温室气体本底观测的影响。研究期间, CO₂本底数据比例约为21.2%, 受局地 and 城市排放与输送影响, 非本底浓度比本底浓度偏高 $(3.7 \pm 1.3) \times 10^{-6}$; HFC-134a和PFC-218浓度距平和浓度载荷的特征反映了2个物种源区特征的差别; HCFC-22浓度特征与空调制冷剂夏高冬低的季节排放规律相一致。(姚波)

3.8 利用FLEXPART模式反演中国区域SF₆排放量

六氟化硫(SF₆)是一种长寿命卤代温室气体, 被列为《京都议定书》限排物质。随着经济高速发展, 中国的排放量受到世界各国的关注。采用传统的“自下而上”清单方法估算排放量时, 所需排放因子、

活动水平数据的准确性和时效性存在较大局限。因此,本文利用拉格朗日粒子扩散模式FLEXPART,结合2009年北京上甸子区域大气本底站浓度观测资料,尝试建立中国区域排放量的反演方法。结果表明,初步反演的2009年中国区域排放量为 1.25×10^3 ($0.53 \times 10^3 \sim 1.97 \times 10^3$) t,与文献结果相当,源排放量的不确定性从 1.05×10^3 t减小到 0.72×10^3 t。与先验源相比,反演源的相关系数从0.37提高到0.43,均方根误差减小了2.64%。(安兴琴)

3.9 不同气象条件下的气溶胶对暖云特征变化影响的卫星观测研究

考虑不同气象条件,研究了长时间序列的夏季长三角地区(YRD)和下风向的中国东海(ECS)等2个区域的气溶胶-暖云相互作用(ACI)。气溶胶和云特征数据来自于MODIS/Aqua Level 2,气象场数据来自NCEP再分析资料。为了减少气象条件对气溶胶-暖云相互作用统计分析的影响,本研究主要考察了不同云顶气压(CTP)、相对湿度(RH)、气压垂直速度(PVV)和下对流层稳定度(LTS)条件下的ACI。结果表明,ECS地区的云滴有效半径(CDR)随气溶胶光学厚度增加而减少,而在YRD存在相反的变化趋势。再研究气溶胶对云量(CF)影响时,考虑了CTP和RH等2个气象参数。当气溶胶变化较小时,无论RH大小,YRD地区的CF随气溶胶的增长速度明显快于ECS地区。因此,本研究认为云的水平覆盖特征的改变主要由气溶胶而非相对湿度这一气象特征驱动。同时,针对AOD-CF、AOD-CTP的联合统计分析结果表明,CTP对AOD-CF相互作用非显著。本研究也考察了不同LTS和PVV条件下的CDR-AOD相互关系,发现了2个地区在大气热力条件相对稳定时,CDR随AOD增加而减少。而在大气不稳定时,存在截然相反的结果。通过研究不同动力条件对ACI的影响,发现在大气上升的时候,陆地和海洋2个典型地区的CDR随气溶胶变化存在一个更显著的改变,一个可能的解释是上升气流更有利于促进云滴的形成。总之,在云内存在更为复杂的热力和动力条件影响下,很难把观测到的云特征的改变完全归结为气溶胶。(郭建平)

3.10 西藏地面和卫星观测降水的日变化特征及其影响因子

基于2010—2011年2年夏季加密的西藏地区自动气象站和卫星降水产品(CMORPH),首次得到了该地区空间覆盖度最为广阔而全面的降水日变化特征。约60%站点的最大降水量和降水频次的峰值出现在下午-傍晚时分。由CMORPH数据也得到了同样的日变化特征,但它没有抓住有些站点临近中午的上午峰值。观测到的降水峰值时刻基本与该时刻附近容易出现降水的天气条件吻合。从空间上来说,没有明显的自西到东的日变化传输过程,表明该地区的降水主要由局地对流或环流而非大尺度环流导致,因此,该地区的降水日变化特征主要取决于地形和地形特征。进一步研究发现,降水峰值存在明显的地理依赖,即从山区的白天降水峰值过渡到山谷和湖泊(地形较低地区)的傍晚-夜间降水峰值。位于山峰(山谷)的站点在接近中午或午后时刻(傍晚时分)容易出现降水峰值。总体而言,无论降水量或降水频次,均出现类似的地形依赖特征,表明山谷环流效应(山谷风)在大(中)尺度降水特征比较弱的情况下对本地的降水峰值存在显著影响。同时,针对西藏空间异质的降水日变化特征提出了一种可能的机制,即在分析青藏高原降水日变化时空分布特征时,不仅需要考虑高原尺度的大尺度环流特征,更要考虑由复杂地形导致的局地环流因子的影响。(郭建平)

3.11 基于观测和模式模拟的华北地区山区和平原站点的降水和大气污染研究

利用华北太行山地区7个站点(4个平原站+3个高山站)40年夏季的日平均能见度和小时降水数据,分析了其时间变化趋势。发现所有站点的夏季降水量均没有出现明显的变化趋势,而同期随着能见度减少,出现了小雨减少而大雨增加的趋势。小雨的减少表现在由地形降水和中尺度层云降水等产生的两类降水上。同时观测到的不同能见度、降水和地形因子变化趋势表明存在明显的气溶胶间接效应。同时,也深入分析了诸如可降水、对流有效位能、垂直风切变等大尺度环境因子对降水的潜在影响,发现他们之间不存在明显的内在直接联系。为了验证由观测得到的关于存在的气溶胶间接效应假设,使用了带谱分辨微物理方案的WRF模式进行云解析尺度模拟研究。模式模拟结果进一步确认了气溶胶间接效应是导致山区小雨雨量和降水频次减少的主要原因。当不考虑地形影响时,小雨对大气污染的效应出现相反的结果,表明地形可能是山区和平原站观测到不同的小雨变化的原因之一。(郭建平)

3.12 沙尘输送和沉降以及对黄海浮游植物生长的影响

利用地面PM₁₀浓度、天气现象观测和卫星反演的气溶胶和海洋颜色数据,结合沙尘的数值模拟和后向追踪轨迹,对发生于2010年19—22日的一次强沙尘过程及其对黄海浮游植物的影响进行了研究。研究发现,沙尘天气发生期间叶绿素a增加了4倍,而且10~14天之后,浮游植物量显著增加。严重沙尘天气带来的铁离子使得黄海南部的叶绿素a增加了10%~68%。研究表明,沙尘暴发生时给黄海地区带来的生物性养分有利于该地区浮游植物的成长。(王宏)

3.13 中国及东亚其他地区不同区域至酸性物质的湿沉降: 采样升级的NAQPMS模式模拟研究

研究源与受体关系的传统方法是开展敏感性模拟,但是这种方法对涉及到非线性的二次形成的污染物(如臭氧、硝酸盐等)的研究存在弱点。本研究在嵌套空气质量预测模拟系统(NAQPMS)基础上建立了一种在线源追踪方法,并首次将其与云过程模块耦合。新的模式不仅能更精确地确定硫酸盐、硝酸盐和铵盐总的湿沉降量,而且可追踪酸性物质的前体物。研究表明:(1)华东和华中是2个主要的污染物输出区,对其他区域的湿沉降分别具有15%~30%和10%的影响;(2)除了以上2区域外,我国西南和东北区域的酸沉降也达到或超过了各自环境条件下的临界负荷(图5)。(徐晓斌)

3.14 1-硝基苊和1,2-萘醌的联合细胞毒性和致DNA损伤

以人肺上皮细胞A549为研究对象,运用MTT方法检测1-硝基苊(1-NP)处理后A549的细胞存活率;测定细胞培养液中乳酸脱氢酶(LDH)的漏出率,评价细胞膜损伤;运用彗星试验检测DNA损伤;通过荧光探针的方法测定细胞内产生的活性氧自由基(ROS)。通过1,2-萘醌(1,2-NQ)预先染毒24h,再使用1-NP染毒24h的方法,评估1-NP和1,2-NQ对A549的联合细胞毒性和DNA损伤。结果表明,1-NP对A549暴露24h和48h的半致死浓度(LC₅₀)分别为5.2 μmol/L和2.8 μmol/L。LC₅₀随着染毒时间的增加而降低,提示暴露时间越长1-NP的细胞毒性越强。A549在1、2、3和4 μmol/L浓度的1-NP染毒下,DNA损伤显著增强,ROS水平不断升高,呈现剂量-效应关系($P < 0.05$);但LDH漏出率无显著变化。1,2-NQ(5 μmol/L)预染毒A549细胞24h,能明显减弱1-NP造成的DNA损伤和ROS升高。结果说明,1,2-NQ预处理可能通过抑制1-NP暴露产生的ROS,来降低A549的DNA损伤。(李怡)

3.15 大气颗粒物携带醌类物质引发细胞毒性以及DNA损伤: 氧化应激作用

大气颗粒物对人体有重要的健康影响。已有证据表明,颗粒物上携带的醌类物质可能通过氧化应激造成损伤,但是,肺部细胞的DNA损伤是否与醌类物质氧化应激有关,还缺乏相关研究。本研究选择了5种代表性醌类物质,在肺部上皮A549细胞中,研究了它们引发氧化应激的能力以及相应的DNA和其他生物学意义的损伤。这些醌类物质能够因剂量-效应引发细胞内Ca²⁺浓度增加,表明氧化应激是一个重要的途径。本研究结果再次证明了大气颗粒物对健康影响的重要性(李怡)

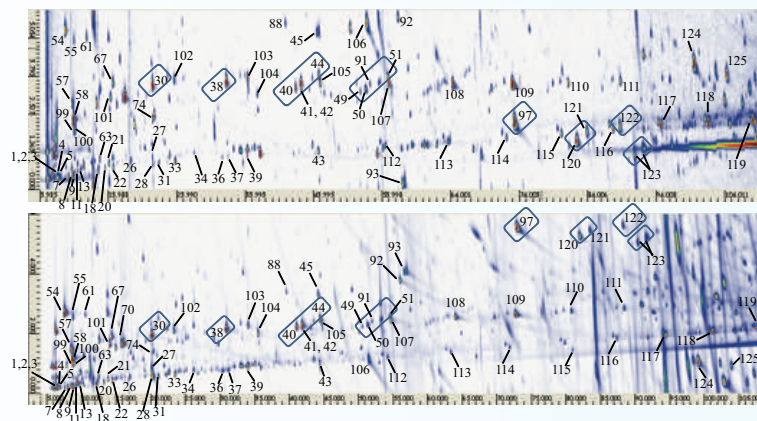


图1 北京空气样品GC×GC-qMS (a) 和GC×GC-FID (b) 的色谱图

Fig. 1 GC × GC-qMS (a) and GC × GC-FID (b) chromatograms of a Beijing air sample

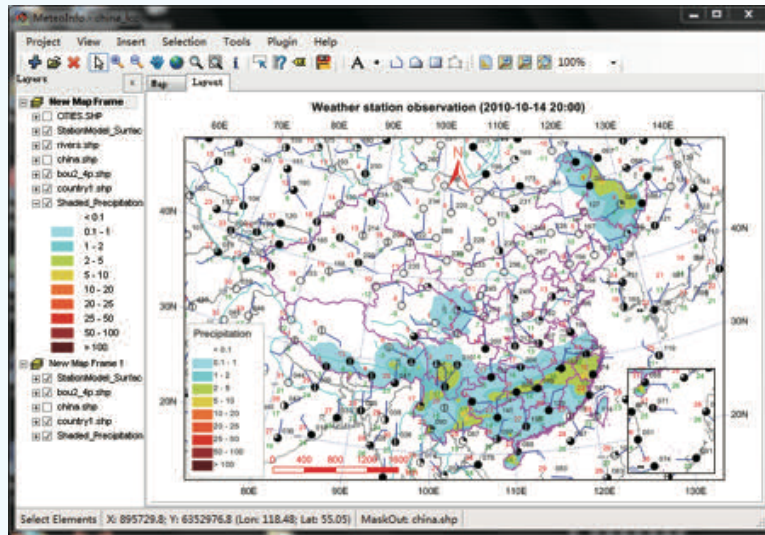


图2 MeteoInfo软件主界面及站点数据图形示例
Fig. 2 MeteoInfo GUI and sample plot from station data

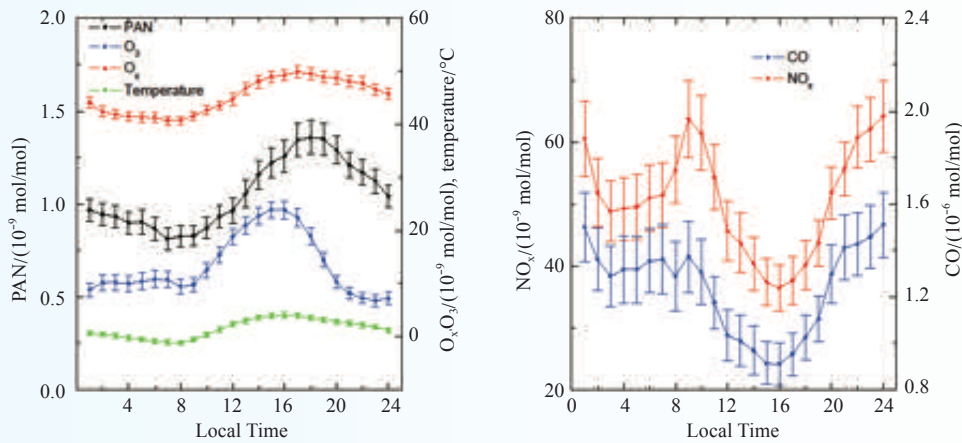


图3 中国气象局大院站点冬季PAN、O₃、O_x、CO、NO_x和气温的平均日变化(垂直线段表示各平均值的平均标准偏差)
Fig. 3 Diurnal cycles of PAN, O₃, O_x, CO, NO_x, and air temperature at the CMA site during the wintertime. The vertical bars represent one standard error of the mean

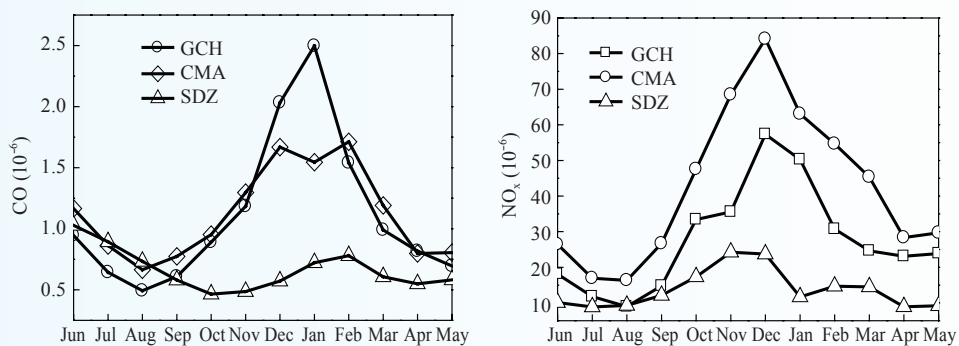


图4 中国气象局(CMA)、上甸子(SDZ)和固城(GCH)3个站点CO和NO_x均值体积分数变化
Fig. 4 Variation of the monthly CO and NO_x concentrations at the CMA, SDZ and GCH stations

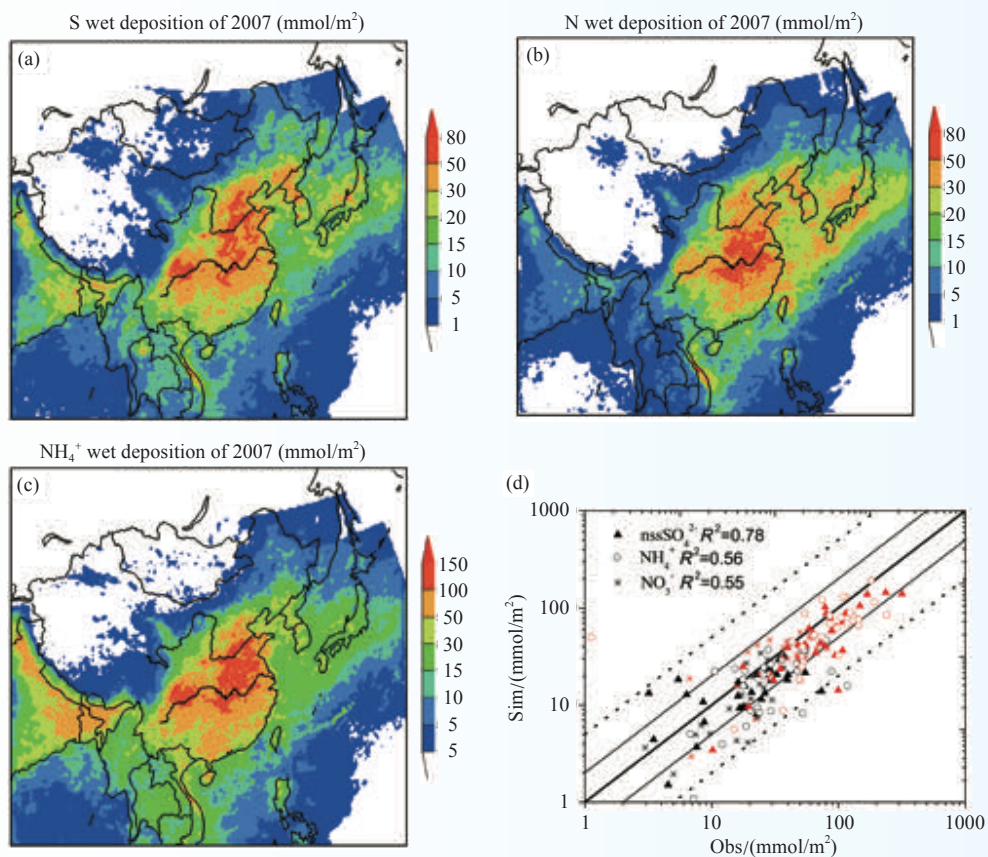


图5 模拟的S (a)、N (b)、 NH_4^+ (c) 的沉降空间分布以及东亚区域2007年3种致酸性物质模拟值和观测值的比较 (d) ((d) 中的黑点和红点分别表示来自东亚其他站点和中国境内站的观测数据)

Fig. 5 Simulated patterns of wet deposition of (a) S, (b) N, (c) NH_4^+ and (d) scatter plot of the three acidifying substances over East Asia during 2007. Black and red points in (d) represent the observation data from other sites located in other East Asia and in China, respectively

Progress in Atmospheric Composition and Atmospheric Chemistry Research

In 2014, the Institute of Atmospheric Composition completed several tasks and made obvious progress in analytical methods, comparison and verification, quality control, observation of atmospheric composition and atmospheric chemistry process, model development and implementation, and in assessing the impact of atmospheric composition and related factors on climate, weather, and human health.

1 Analytical methods, comparison and verification and quality control

1.1 Establishment of the integrating sphere calibration method for China aerosol remote sensing network Cimel sunphotometer

Based on the integrating sphere traced from the National Institute of Standards and Technology (NIST, USA), a sphere calibration method and protocol for the China aerosol remote sensing network (CARSNET) Cimel sun photometer was established. Four CE318 sun photometers were verified using the proposed calibration method and operational protocol. The calibration results showed that the instrument coefficients differed by less than 3% for visible (~5% for infrared) wavelengths from the original ones stated by Cimel electronique. In situ validation experiment data showed that radiances at $\pm 6^\circ$ measured by a sun collimator (aureole) were consistent with those measured by a sky collimator (sky), under both almucantar (ALMUC) and principal plane (PPLAN) scenarios. Differences at all wavelengths were less than 1%, indicating that the method and protocol are suitable for CARSNET field sun photometer calibration, and would benefit data quality and accuracy of network observations. (Che Huizheng)

1.2 Coupling of comprehensive two-dimensional gas chromatography with quadrupole mass spectrometry (GC×GC-qMS): Application to the identification of atmospheric volatile organic compounds

Observation data of atmospheric volatile organic compounds (VOCs) are highly needed in air quality assessment, photochemical mechanism study, and emission control policy-making, while it has been a challenge to accurately and comprehensively measure them. Comprehensive two-dimensional gas chromatography (GC×GC) is one of the advanced techniques in analysis of complex mixtures, providing a good choice for measurement of VOCs. However, the requirement for a fast detector limits the application of quadrupole mass spectrometry (qMS) in GC×GC analysis. This paper presents a method on how to apply a common qMS detector coupled with GC×GC to the identification of atmospheric VOCs. About 125 VOCs including alkanes, alkenes, aromatics, oxygenated hydrocarbons, and halocarbons were identified in the measurement of standard gas mixtures and/or urban air samples from Beijing. The results were applied to the analysis of GC×GC-FID by one to one correspondence of the equivalent peaking compounds between the GC×GC-FID and GC×GC-qMS chromatograms, and the retention times of the identified components in GC×GC-FID in turn underwent the qualitative analysis without the further help of MS. The wrap-around phenomenon which may confuse the match of peaks was discussed in detail. The co-use of GC×GC-FID and GC×GC-qMS in the identification process makes the GC×GC device more affordable and the qualitative and quantitative analysis more robust. The method and the identified results can be further used to analyze other volatiles (Fig. 1). (Wang Ying)

1.3 QA/QC method for and assessment of atmosphere background CO₂ sampling and analysis

To strengthen scientific management and sharing of greenhouse gas data obtained from atmospheric background stations in China, it is important to ensure the standardization of quality assurance and quality control methods for background CO₂ sampling and analysis. The observation and study of atmospheric greenhouse gases in the Waliguan station (Qinghai) by CMA were begun in 1980s, with rich experience in data sampling, analysis and processing having been accumulated. In this study, the QA/QC method for atmospheric CO₂ concentration observation and analysis by portable flask sampling and the CRDS system are discussed in detail. Then, several key steps of this method are evaluated. Finally, by using this method, the variation features of the three typical regions', atmospheric background CO₂ concentration are preliminarily analyzed. (Liu Lixin)

1.4 Study of atmospheric CO₂ mole fractions at the Longfengshan WMO/GAW regional station

Out of the in-situ observation results of atmospheric CO₂ mole fractions from two levels (10 m and 80 m above the ground) at Longfengshan (LFS) regional background station in Heilongjiang Province from January 2009 to December 2011, this study mainly focused on the lower (10 m) level (a.g.l.). The results indicate that the observed data from 10 m were strongly affected by the local sources/sinks. The differences between the 10 m and 80 m results were relatively small during the daytime (08:00–17:00) with values being lower than $(0.5 \pm 0.5) \times 10^{-6}$. In spring, summer and autumn, higher CO₂ mole fractions were observed when surface winds came from the E–ESE–SE–SSE sectors, while, in winter, surface winds from the N–NNW–NW–WNW sectors obviously enhanced the observed values. Generally, lower CO₂ values were accompanied with higher wind speed in the four seasons. This phenomenon was most obvious in winter. Based on the analysis of the observed diurnal cycle and the local meteorological conditions, the observed data from 10 m were filtered into background/non-background events. About 30.7% valid hourly data turned out to be regional background representative. The background CO₂ variation displayed a peak in winter and a valley in summer with a seasonal peak to peak amplitude of $(36.3 \pm 1.4) \times 10^{-6}$, which was higher than the values at similar latitudes from marine boundary layer (MBL) references and WMO/GAW stations. The annual CO₂ increasing rate at LFS was roughly estimated to be 2.4×10^{-6} . (Fang Shuangxi)

1.5 MeteoInfo: GIS software for meteorological data visualization and analysis

MeteoInfo is a suite of software tools which has been developed for meteorological data visualization and analysis. It includes a .NET class library for software developers and a desktop application for end users. MeteoInfo also supports several basic GIS functions and can read common meteorological data formats such as NetCDF and GRIB. Complex meteorological analyses of grid and station data can be processed using provided data models. The class library can be conveniently used to develop software routines for manipulating spatial and meteorological data. The desktop application has a user friendly GUI and is a powerful tool to view and examine meteorological data sets. MeteoInfo can also be run automatically using the IronPython scripting language (Fig. 2). (Wang Yaqiang)

2 Observational studies of atmospheric compositions and related properties

2.1 Atmospheric sulfur hexafluoride (SF₆) in-situ measurements at the Shangdianzi regional background station in China

We present in-situ measurements of atmospheric sulfur hexafluoride (SF₆) conducted by an automated gas chromatograph-electron capture detector system and a gas chromatography/mass spectrometry system

at a regional background site, Shangdianzi, in China, from June 2009 to May 2011, in which the system for observation of greenhouse gases in Europe and Asia and Advanced Global Atmospheric Gases Experiment (AGAGE) techniques were used. The mean background and polluted mixing ratios for SF₆ during the study period were 7.22×10^{-12} and 8.66×10^{-12} respectively. The averaged SF₆ background mixing ratios at Shangdianzi were consistent with those obtained at other AGAGE stations located at similar latitudes (Trinidad Head and Mace Head), but larger than AGAGE stations in the Southern Hemisphere (Cape Grim and Cape Matatula). SF₆ background mixing ratios increased rapidly during our study period, with a positive growth rate at $0.30 \times 10^{-12} \text{ yr}^{-1}$. The peak to peak amplitude of the seasonal cycle for SF₆ background conditions was 0.07×10^{-12} while the seasonal fluctuation of polluted conditions was 2.16×10^{-12} during the study period. Peak values of SF₆ mixing ratios occurred in autumn when local surface horizontal winds originated from W/WSW/SW/SWS/S sectors, while lower SF₆ mixing ratios appeared as winds originated from N/NNE/NE/ENE/E sectors. (Yao Bo)

2.2 Background variations of atmospheric CO₂ and carbon-stable isotopes at Waliguan and Shangdianzi stations in China

Observational data from 2007 to 2010 at the Waliguan (WLG) and Shangdianzi (SOZ) stations in China are used to study atmospheric CO₂, its $\delta^{13}\text{C}$ composition, and their potential relationship with sources and sinks. Results suggest that at WLG station, both CO₂ and $\delta^{13}\text{C}$ feature a long-term variation and seasonal cycle that correlate well with each other. CO₂ and $\delta^{13}\text{C}$ inter-annual variations indicate terrestrial ecosystem's alteration in source-sink by season in the mid- to high-latitude Northern Hemisphere. CO₂ annual means vary from 384.0×10^{-6} to 390.2×10^{-6} , increasing in an approximately linear manner averagely at an annual growth rate of $(2.1 \pm 0.1) \times 10^{-6}$. The $\delta^{13}\text{C}$ annual means vary from -8.30‰ to -8.35‰ , decreasing almost linearly and averagely at an annual rate of $-0.02\text{‰} \pm 0.001\text{‰}$. Given the terrestrial biosphere and anthropogenic activities at SDZ station, the CO₂ annual means vary from 385.1×10^{-6} to 390.6×10^{-6} , approximately increasing linearly and averagely at an annual growth rate of $(1.8 \pm 0.1) \times 10^{-6}$. The peak-to-peak annual seasonal amplitude is 23.0×10^{-6} . The $\delta^{13}\text{C}$ annual means vary from -8.27‰ to -8.36‰ between 2009 and 2010. Mean values of $(-25.44 \pm 0.72)\text{‰}$ and $(-21.70 \pm 0.67)\text{‰}$ for the respective sources are obtained at WLG and SDZ. The estimated δ_s values are rather negative in winter and spring than in summer and autumn at WLG. While because substantial C₄ photosynthesis occurs in summer and biomass burns in winter, the estimated δ_s values at SDZ are heavy throughout the year and rather positive than those at WLG. (Liu Lixin)

2.3 In situ measurement of atmospheric CO₂ at the four WMO/GAW stations in China

Atmospheric carbon dioxide (CO₂) mole fractions were continuously measured from January 2009 to December 2011 at four atmospheric observatories in China with cavity ring-down spectroscopy instruments used. The stations are Lin'an (LAN), Longfengshan (LFS), Shangdianzi (SDZ), and Waliguan (WLG), which are either regional (LAN, LFS, SDZ) or global (WLG) under the World Meteorological Organization's Global Atmosphere Watch program (WMO/GAW). LAN is located near the megacity of Shanghai, in China's most economically developed region. LFS is in a forest and rice production area, close to the city of Harbin in northeastern China. SDZ is located 150 km northeast of Beijing. WLG, boasting the longest record of measured CO₂ mole fractions in China, is a high-altitude site in northwestern China registering background CO₂ concentration. The CO₂ growth rates are $(3.7 \pm 1.2) \times 10^{-6} \text{ yr}^{-1}$ for LAN, $(2.7 \pm 0.8) \times 10^{-6} \text{ yr}^{-1}$ for LFS, $(3.5 \pm 1.6) \times 10^{-6} \text{ yr}^{-1}$ for SDZ, and $(2.2 \pm 0.8) \times 10^{-6} \text{ yr}^{-1}$ for WLG during the period of 2009 to 2011. The highest annual mean CO₂ mole fraction of $(404.2 \pm 3.9) \times 10^{-6}$ was observed at LAN in 2011. A comprehensive analysis of CO₂ variations, their diurnal and seasonal cycles as well as an analysis of the influence of local sources on the CO₂ mole fractions allow for a characterization of the sampling sites and of the key processes driving the

CO₂ mole fractions. These data form a basis to improve our understanding of atmospheric CO₂ variations in China and the underlying fluxes using atmospheric inversion models. (Fang Shuangxi)

2.4 Estimation of regional background concentration of CO₂ at Lin'an station in Yangtze River Delta, China

A new method of extracting regional background concentration of CO₂ in Yangtze River Delta was developed based on the observations of both black carbon concentration and meteorological parameters. The concentrations of CO₂ and black carbon were observed at Lin'an regional background station from 2009 to 2011. The regional background concentration of CO₂ in Yangtze River Delta was obtained by means of this new method, and the impact of human activities on CO₂ concentration in this area was also assessed. The results show that the regional background concentration of CO₂ extracted by this approach was comparable to the values obtained by R statistical filter method, and moreover this new method was better at picking up episodes heavily polluted by anthropogenic emissions. The annual regional average background concentration of CO₂ in Yangtze River Delta from 2009 to 2011 was approximately $(404.7 \pm 8.2) \times 10^{-6}$, $(405.6 \pm 5.3) \times 10^{-6}$ and $(407.0 \pm 5.3) \times 10^{-6}$, respectively, much higher than global average value, indicating the distinct characteristic of this region. The anthropogenic emissions from Yangtze River Delta had significant influence on the concentration of CO₂ in this area, increasing the local value by roughly 9.1×10^{-6} . (Fang Shuangxi)

2.5 A case study of short-term fluctuation in atmospheric concentration of halogenated greenhouse gases at Shangdianzi regional background monitoring station

By means of trajectory analysis method and footprint analysis method, combined with the online observed concentration of H-1301, HCFC-22, CFC-11 and SF₆, a typical case about short-term fluctuation of halogenated greenhouse gases at Shangdianzi background station during 7–12 September 2012 was analyzed. The results show that before the occurrence of pollution, air masses at 12:00 BT 7 September 2012 are mainly from the far-away north and northwest, with a long horizontal transport distance, rapid moving speed and high vertical height; meanwhile, the corresponding halogenated greenhouse gases concentrations are relatively low, which are 4×10^{-12} , 350×10^{-12} , 260×10^{-12} and 10×10^{-12} for H-1301, HCFC-22, CFC-11 and SF₆, respectively. However, on 9–10 September 2012, a certain percentage of air masses convolutes over the south of the station with a short horizontal transport distance and low vertical height, moving slowly in the boundary layer, thus hindering the spread of pollutants in the boundary layer and resulting in relatively high halogenated greenhouse gases concentrations. Such situation contributes a lot to the short-term rapid growth of concentration levels and H-1301, HCFC-22 and CFC-11 respectively reach the peak concentrations of 45×10^{-12} , 200×10^{-12} and 310×10^{-12} at 12:00 BT 9 September and SF₆ reaches 28×10^{-12} at 03:00 BT 10 September. On 11 September, the convoluting air mass in the southwest direction disappears and on 12 September, air masses all flow from the far-away northwest and have rapid moving trajectories. The result by footprint analysis method is the same as that by the trajectory analysis, which is that on 7–8 September, regions with a high sensitivity coefficient are mainly located in the north of the station; on 9–10 September, they are seen mainly in the south of the station. Then on 11 and 12 September, the regions with high sensitivity coefficients in the south of the observation station disappeared. In addition, a flow field analysis also showed that the circulation pattern on 9 and 10 September is favorable for the accumulation of pollutants in the observed region, resulting in the short-term lift of pollutants' concentrations. (An Xingqin)

2.6 In-situ measurement of atmospheric methyl chloroform at the Shangdianzi GAW regional background station

An in-situ GC-ECD monitoring system was established at the Shangdianzi GAW regional background

station (SDZ) for 2-year atmospheric methyl chloroform (CH_3CCl_3) measurement. Robust extraction of baseline signal filter was applied to the CH_3CCl_3 time series to separate background and pollution data. The yearly averaged background mixing ratios of atmospheric CH_3CCl_3 were $(9.03 \pm 0.53) \times 10^{-12}$ in 2009 and $(7.73 \pm 0.47) \times 10^{-12}$ in 2010, and the percentages of the background data to the whole data were 61.1% in 2009 and 60.4% in 2010, respectively. The yearly background CH_3CCl_3 mixing ratios at SDZ were consistent with the Northern hemisphere background levels observed at Mace Head and Trinidad Head stations, but lower than the results observed at sites in South China and some Chinese cities from 2001 to 2005. During the study period, background mixing ratios exhibited a decrease at a rate of $1.39 \times 10^{-12} \text{ yr}^{-1}$ in trend. The wind direction with the maximum CH_3CCl_3 mixing ratio was from the southwest sector and with the minimum one was from northeast sector. The differences between the maximum and the minimum average mixing ratios in the 16 wind directions were 0.77×10^{-12} (2009) and 0.52×10^{-12} (2010). In the different 16 wind directions, the averaged mixing ratio of CH_3CCl_3 in 2010 was lower than those in 2009 by 1.03×10^{-12} – 1.68×10^{-12} . (Yao Bo)

2.7 Influence of downward air mass transport on the variability of surface ozone at Xianggelila regional atmospheric background station, Southwest China

In situ measurements of ozone (O_3), carbon monoxide (CO) and meteorological parameters were made from December 2007 to November 2009 at the Xianggelila regional atmospheric background station (28.006°N, 99.726°E, 3580 m.a.s.), Southwest China. It was found that both O_3 and CO peaked in spring while the minima of O_3 and CO occurred in summer and winter, respectively. A normalized indicator (marked as “Y”) on the basis of the monthly normalized O_3 , CO and water vapor, is proposed to evaluate the occurrence of O_3 downward transport from the upper, O_3 -rich atmosphere. This composite indicator has the advantage of being less influenced by the seasonal or occasional variations of individual factors. It is shown that the most frequent and effective transport occurs in winter (accounting for 39% of the cases when Y is larger than 4), which makes a significant contribution to surface O_3 at Xianggelila. A 9.6×10^{-9} increase (21.0%) of surface ozone is estimated based on the impact of deep downward transport events in winter. A case of strong O_3 downward transport event under the synoptic condition of a deep westerly trough is studied by a combined analysis of the Y indicator, potential vorticity, total column ozone and trajectory. Asian monsoon plays an important role in suppressing O_3 accumulation in summer and fall. The seasonal variation of O_3 downward transport, as suggested by the Y indicator at Xianggelila, is consistent with the seasonality of stratosphere-to-troposphere transport and the subtropical jet stream over the Tibetan Plateau. (Zheng Xiangdong)

2.8 Wintertime peroxyacetyl nitrate (PAN) in the megacity Beijing: The role of photochemical and meteorological processes

Previous measurements of peroxyacetyl nitrate (PAN) in Asian megacities were scarce and mainly conducted for relatively short periods in summer. Here, we present an analysis of the measurements of PAN, O_3 , NO_x , etc. made at an urban site (CMA) in Beijing from 25 January to 22 March 2010. The hourly concentration of PAN averaged 0.70×10^{-9} (0.23×10^{-9} – 3.51×10^{-9}) was well correlated with that of NO_2 but not O_3 , indicating that the variations of the winter concentrations of PAN and O_3 in urban Beijing are decoupled with each other. Wind conditions and transport of air masses exert very significant impacts on O_3 , PAN, and other species. Air masses arriving at the site originated either from the boundary layer over the highly polluted N-S-W sector or from the free troposphere over the W-N sector. The descending free-tropospheric air was rich in O_3 , with an average PAN/ O_3 ratio being smaller than 0.031, while the boundary layer air over the polluted sector contained higher levels of PAN and primary pollutants, with an average PAN/ O_3 ratio being 0.11. These facts related with transport conditions can well explain the observed PAN- O_3 decoupling. Photochemical

production is important to PAN in the winter over Beijing. The concentration of the peroxyacetyl (PA) radical was estimated to be in the range of 0.0014×10^{-12} – 0.0042×10^{-12} . The contributions of reaction from the formation and thermal decomposition to PAN's variation were calculated and found to be significant even in the colder period in air over Beijing, with the production exceeding the decomposition (Fig. 3). (Xu Xiaobin)

2.9 Changing characteristics of NO_x and CO emission at three sites in Beijing and its surrounding areas

To study the similarity and dissimilarity in the characteristic features of the ambient NO_x and CO emission in different parts of the North China Plain (NCP), we observed the mixing ratios of CO and NO_x in the surface layer air at three sites in the NCP, which are over 100 km apart from each other and in the prevailing SW–NE wind directions. The three sites are China's Meteorological Administration (CMA), the Shangdianzi station (SDZ), and the Gucheng station (GCH), representing typically the urban area of Beijing, the regional background area of the NCP, and the rather seriously polluted rural area in North China, respectively. The results of our investigation show that from June 2008 to May 2009, the annual average concentration of NO_x at CMA, GCH, and SDZ were $(42.4 \pm 21.8) \times 10^{-9}$, $(26.9 \pm 15.2) \times 10^{-9}$, and $(13.8 \pm 5.5) \times 10^{-9}$, respectively, and those of CO were $(1.13 \pm 0.37) \times 10^{-6}$, $(1.11 \pm 0.62) \times 10^{-6}$, and $(0.67 \pm 0.17) \times 10^{-6}$, respectively. At CMA and GCH, the monthly average concentrations of NO_x and CO reached the corresponding maximum in winter and minimum in summer, whereas the highest monthly average concentration of CO at SDZ was observed in June (1.03×10^{-6}). The concentrations of NO_x at CMA, GCH, and SDZ turned to be 3.4, 3.6, and 1.8 times higher in winter than those in summer, respectively. The concentrations of CO at CMA, GCH, and SDZ were 1.8, 2.9, and 0.8 times higher in winter than in summer, respectively. The average diurnal variations indicated that the CO and NO_x concentrations of SDZ decreased to their minimum around noon, about 3–4 h earlier than those of GCH and CMA, and then increased gradually till evening, in response to the impact of transported pollutants on the gas concentrations of SDZ. The above dissimilarities in the diurnal variations can probably account for the different effects of emission sources and the air-mass transport on the concentrations of pollutants at the three sites. The time series of the daily average CO and NO_x concentrations show great similarities among the sites, revealing that the characteristic features were influenced by the common regional pollution and similar meteorological conditions. The observation data we have gained indicate fairly high CO level in the North China Plain in summer, which was probably caused by the outdoor combustion of wheat straw in large amount (Fig. 4). (Xu Xiaobin)

2.10 Characteristics of CO at Lin'an Station in Zhejiang Province

Background CO mole fractions were continuously measured at Lian'an background station in Zhejiang Province from September 2010 to February 2012 with Cavity Ring Down Spectroscopy (CRDS) system used. The diurnal variation of CO was strongly influenced by anthropogenic activities with two peaks occurring at 07:00–10:00 and 19:00–20:00 (Local time). The average daily mole fraction and amplitude in summer were the lowest among the four seasons with values being $(314.3 \pm 7.6) \times 10^{-9}$ (mole fraction, the same below) and $(50.1 \pm 47.9) \times 10^{-9}$, respectively. The seasonal variations displayed peak values during winter-spring period and valley in summer, which was roughly consistent with those observed variations at other sites located in the Northern hemisphere such as Jungfraujoch in Switzerland and Waliguan in China. However, the average mole fractions were much higher than other stations. The amplitude of monthly CO mole fractions was $(286.8 \pm 19.2) \times 10^{-9}$. The analysis of cluster to backward trajectories and surface wind influence might suggest that the non-background CO mole fractions at Lin'an station were mainly affected by the emissions from the megacities and industrial areas in the N–NNE–ENE sectors. The maximum enhancements in spring, summer

and winter all occurred in ENE sector, with a maximum value being $(106.3 \pm 58.0) \times 10^{-9}$ in winter. (Fang Shuangxi)

2.11 Seasonal variation of ammonia and ammonium aerosol at a background station in the Yangtze River Delta region, China

The measurement of atmospheric NH_3 was conducted by means of passive samplers from September 2009 to December 2010 at Lin'an regional background station located in the economically booming Yangtze River Delta (YRD) region in East China. NH_4^+ in fine particles was also measured in 2010 at this site. The NH_3 concentration ranged from 0.1×10^{-9} to 41.8×10^{-9} , with the annual average being $(16.5 \pm 11.2) \times 10^{-9}$ in 2010. The daily NH_4^+ concentrations ranged from 0.02 to $19.2 \mu\text{g m}^{-3}$, with an annual average of $(4.3 \pm 3.5) \mu\text{g m}^{-3}$. NH_3 concentrations were highest in summer and lowest in winter, showing positive correlations with agricultural activities and temperature. The highest concentrations of NH_4^+ were in autumn coinciding with the period of active open burning of agricultural residues. The mean mass ratio of NH_3/NH_x is estimated to be (0.8 ± 0.1) during 2010, indicating that NH_x was mainly influenced by local sources around Lin'an. The air mass back trajectory analysis suggests that both local sources and long-distance transport play an important role in the observed ammonium aerosol at Lin'an station. High NH_x deposition in this regional background station suggests the urgency of reducing NH_3 emission in the YRD region. (Meng Zhaoyang)

2.12 Variability, formation and acidity of water-soluble ions in $\text{PM}_{2.5}$ in Beijing

Daily $\text{PM}_{2.5}$ and hourly water-soluble inorganic ions in $\text{PM}_{2.5}$ and gaseous precursors were measured during June–November 2009 at an urban site in Beijing. The average mass concentration of the total water-soluble ions was $44 \mu\text{g m}^{-3}$, accounting for 38% of $\text{PM}_{2.5}$. Sulfate (SO_4^{2-}), nitrate (NO_3^-) and ammonium (NH_4^+) were dominant ions. The summer-fall difference in seasonal average mass concentrations was smaller than 30% for SO_4^{2-} , but was up to a factor of 2.0 for NO_3^- and NH_4^+ . A pronounced diurnal cycle was found for most ions and gaseous precursors and could be explained by their respective sources, formation mechanisms and meteorological conditions. The average oxidation/conversion ratios for SO_4^{2-} (SOR), NO_3^- (NOR) and NH_4^+ (NHR) were estimated to be 63%, 15% and 15%, respectively. The low NHR value suggests that NH_3 was mainly from local sources, the excessive existence of which thus was not a limiting factor in the formation of NH_4^+ . As a result, the diurnal pattern of NH_4^+ was similar to that of SO_4^{2-} to some extent, but differed significantly from that of NH_3 . Based on the estimated H^+ concentration and acidity purity (f), 75% of data samples were strongly acidic and a few percentages might be alkaline. Seasonal variations in aerosol acidity and chemical forms of major ions were also briefly discussed. (Zhang Yangmei)

2.13 Chemical composition and mass size distribution of PM_1 at an elevated site in central east China

Size-resolved aerosol chemical compositions were measured continuously for 1.5 year from June 2010 to January 2012 with an aerosol mass spectrometer (AMS) to characterize the mass and size distributions (MSDs) of major chemical components in submicron particles (approximately PM_1) at Mountain Tai (Mt. Tai), an elevated site in central east China. The annual mean mass concentrations of organic, sulfate, nitrate, ammonium, and chloride were 11.2, 9.2, 7.2, 5.8, and $0.95 \mu\text{g m}^{-3}$, respectively, which are much higher than those at most mountain sites in the USA and Europe, but lower than those at the near-surface urban sites in China. A clear seasonality was observed for all major components throughout the study, with low concentration in fall and high in summer, which is believed to be caused by seasonal variations in planetary boundary layer (PBL) height, near surface pollutant concentrations and regional transport processes. Air masses were classified into categories impacted by PBL, lower free troposphere (LFT), new particle formation (NPF), in-cloud

processes, and polluted aerosols. Organics dominated the PM_{10} mass during the NPF episodes, while sulfate contributed most to PM_{10} in cloud events. The average MSDs of particles between 30 and 1000 nm during the entire study for organics, sulfate, nitrate, and ammonium were approximately log-normal with mass median diameters (MMDs) of 539, 585, 542, and 545 nm, respectively. These values are slightly larger than those observed at ground sites within the North China Plain (NCP), likely due to the relative aged and well-mixed aerosol masses at Mt. Tai. There were no obvious differences in MMDs during the PBL, LFT, in-cloud and polluted episodes, but smaller MMDs, especially for organics, were observed during the NPF events. During the PBL, NPF, and polluted episodes, organics accounted for major proportions at smaller modes, and reached 70% at 100–200 nm particles in the polluted events. In cloud episodes, inorganics contributed 70% to the whole size range dominated by sulfate, which contributed 40% to small particles (100–200 nm), while organics occupied 20%, indicating that sulfate is a critical chemical component in cloud formation. Seven clusters of air masses were classified based on 72 h back-trajectory analysis. The majority of the regionally dispersed aerosols were found to be contributed from short distance mixed aerosols, mostly originating from the south with organics and sulfate as major components. Air masses from long range transport always brought clean and dry aerosols which resulted in low concentrations at Mt. Tai. AMS-PMF (positive matrix factorization) was employed to resolve organics into subtype. Oxygenic organics aerosols (OAs) occupied 49%, 56%, 51%, and 41% of OAs in the four seasons respectively, demonstrating that most OAs were oxidized in summer due to strong photochemical reactions. Biomass burning OAs (BBOAs) accounted for 34% of OA in summer, which was mainly from field burning of agricultural residues, and coal combustion OAs (CCOAs) accounted for 22% of OA in winter, which was from heating. (Zhang Yangmei)

2.14 Characterization of chemical components of aerosol particles in various regions over China

In order to obtain the overall chemical “picture” of the aerosol pollution in various regions of China and discuss the further direction in pollution control, we need to assess and evaluate the concentration level, chemical composition and pollution sources region-by-region in China. Features of the chemical aerosol particles in China have been obtained, based on the analysis of six major chemical components (sulfate, nitrate, ammonium, mineral aerosol, organic and elemental carbon) from ground-based observation, all of which have undergone at least one-year-long measurement. The four most hazy regions out of the nine with characteristics of synchronous changes in visibility within China are also identified in areas like the region to the south of Beijing (also called the Hua Bei Plain and Guanzhong Plain); mostly the East China region with Yangtze River Delta; the South China region focused on the Pearl River Delta; and also the region of Sichuan Basin. Of the total mass of PM_{10} in China, three major components account for ~20%–38% for mineral aerosol, ~14%–24% for sulfate, and ~11%–18% for organic carbon.

The heaviest aerosol pollution was found in the Hua Bei and Guanzhong Plain regions, with the annual mean concentrations being 35–47 $\mu\text{g m}^{-3}$ of sulfate (much higher than the 13 to 18 $\mu\text{g m}^{-3}$ of urban Beijing), 28–45 $\mu\text{g m}^{-3}$ of organic carbon (about 1.8 factors higher than 19–22 $\mu\text{g m}^{-3}$ of Beijing), 19–22 $\mu\text{g m}^{-3}$ for nitrate (2 times higher than 9.9–12 $\mu\text{g m}^{-3}$ of Beijing), 14–16 $\mu\text{g m}^{-3}$ for ammonium (still one factor higher than the 6.2–8.4 $\mu\text{g m}^{-3}$ of Beijing mean concentration), and the 9.1–12 $\mu\text{g m}^{-3}$ of elemental carbon which was similar to the level of Beijing. More than 50% mass of nitrate and organic carbon is attributable to coal-combustion, and the agricultural activity is the most important source for ammonium.

In the urban areas of East, South and Northeast China, the concentration levels of aerosol chemical components were similar to that in Beijing, but in urban areas of the Sichuan Basin, the annual mean concentrations were higher than that in Beijing, exhibiting heavy aerosol pollution there. In Lanzhou of Northwest China, the urban concentrations of aerosol chemical components were also similar to that in Beijing,

except for much lower concentration in elemental carbon and slightly higher concentration of nitrate observed. In the remote desert area of Northwest China, the chemical concentrations of aerosol particles were far lower than that in Beijing, so were in the Tibetan and Yunnan-Guizhou Plateaus.

Coal-combustion, motor vehicle, urban fugitive dust and agricultural activities are found to be the four major pollution sources according to the aerosol chemical composition analysis made in different regions. Therefore, the future control of atmospheric aerosol pollutants should be directed to the following: strengthening coal desulfurization in addition to the power generation industry, further reducing coal produced emissions of NO_x , organic carbon and its precursor gases, and effectively reducing ammonia emissions from agricultural activity, and effectively limiting the formation of secondary aerosol, especially sulfate and nitrate. (Zhang Xiaoye)

2.15 Characteristics of PM_{10} and its chemical components at Mount Tai

In order to better understand the chemical components and their variations of background aerosols in the North China Plain, 64 PM_{10} samples were collected on the top of Mount Tai from June 2010 to July 2011. The mass concentration and seasonal variations of PM_{10} as well as its nine water soluble ions, organic carbon (OC) and elemental carbon (EC) have been analyzed. The correlation analysis of various chemical components has also been performed. The annual average mass concentration of PM_{10} is $68.4 \mu\text{g m}^{-3}$, of which inorganic salt accounts for 64.8%, carbon aerosol for 17.4%. The mass concentration of inorganic salt increases gradually from the Spring Festival, reaches its peak in summer, then decreases in autumn and comes to the lowest in winter. The mass concentration of OC increases from the Spring Festival to autumn and reaches the minima in winter. Similar pattern has been found in the mass concentration of EC; however, the concentrations of EC between summer and autumn are much smaller in difference. The ratio of secondary organic carbon (SOC) to OC is above 50% for all seasons with an annual average of 58.5%. A back trajectory analysis shows that when Mount Tai is mainly influenced by air masses from the south and megacities, mass concentrations of PM_{10} and its components are high; while it is mainly influenced by air masses from the Northwest China through long distance transport, the mass concentrations of PM_{10} and its components are much lower. (Wang Yaqiang)

2.16 The characteristics of particle number size distribution under typical meteorological conditions at Shangdianzi regional station in Beijing

By using the instruments of Twin Differential Mobility Particle Sizer (TDMPs) system and an Aerodynamic Particle Sizer, measurements of particle number size distribution (PNSD) in the range of 3 nm–10 μm were performed at Shangdianzi regional station. Based on the dataset in 2008, the characteristics of particle number size distribution at different meteorological conditions such as dust storm, new particle formation event and fog-haze day were investigated. On the dust storm day, the air mass originated from the northwest, with high wind speed. The coarse particle number concentration increased sharply and PM_{10} mass concentration could reach up to milligrams per cubic meter. A typical “banana shape” new particle formation event occurred when the atmosphere background was quite dry, clean and clear, with the air mass coming from the northeast. The nucleation mode particle could grow significantly in size to around 80 nm, which has the potential to be activated as cloud condensation nuclei. The fog-haze day usually occurred when southwest air mass arrived, with the meteorological conditions being of high humidity. The conditions favored the fine particles (<1 μm) for accumulation. The case study showed the PNSD on haze-fog day was dominated by the accumulation mode and higher number concentration than on a haze-fog free day. The mass concentration of $\text{PM}_{2.5}$ could increase by 10 times on a haze-fog day, which is mainly contributed by fine particles. On fog-haze days, the accumulation mode particles of high number concentration were mainly transported from the urban

area. Thus the study of PNSD at rural sites could also provide information for the analysis of the complex emission sources in urban areas. (Shen Xiaojing)

2.17 Column aerosol optical properties and aerosol radiative forcing during a serious haze-fog month over North China Plain in 2013 based on ground-based sunphotometer measurements

In January 2013, North China Plain experienced several serious haze events. Cimel sunphotometer measurements at seven sites over rural, suburban and urban regions of North China Plain from 1 to 30 January 2013 were used to further our understanding of spatial-temporal variation of aerosol optical parameters and aerosol radiative forcing (ARF). It is found that Aerosol Optical Depth at 500 nm (AOD_{500nm}) during non-pollution periods at all stations was lower than 0.30 and increased significantly to greater than 1.00 as pollution events developed. The Angstrom exponent (Alpha) was larger than 0.80 for all stations most of the time. AOD_{500nm} averages increased from north to south during both polluted and non-polluted periods at the three urban sites in Beijing. The fine mode AOD during pollution periods is about a factor of 2.5 times larger than that during the non-pollution period at urban sites but a factor of 5.0 at suburban and rural sites. The fine mode fraction of AOD_{675nm} was higher than 80% for all sites during January 2013. The absorption AOD_{675nm} at rural sites was only about 0.01 during pollution periods, while 0.03–0.07 and 0.01–0.03 during pollution and non-pollution periods at other sites, respectively. Single scattering albedo varied between 0.87 and 0.95 during January 2013 over North China Plain. The size distribution showed an obvious tri-peak pattern during the most serious period. The fine mode effective radius in the pollution period was 0.01–0.08 μm , which was larger than that during non-pollution periods, while the coarse mode radius in pollution periods was 0.06–0.38 μm , which was less than that during non-pollution periods. The total, fine and coarse mode particle volumes varied by 0.06–0.34 μm^3 , 0.03–0.23 μm^3 , and 0.03–0.10 μm^3 , respectively, throughout January 2013. During the most intense period (1–16 January), ARF at the surface exceeded $-50 W m^{-2}$, $-180 W m^{-2}$, and $-200 W m^{-2}$ at rural, suburban, and urban sites, respectively. The ARF readings at the top of the atmosphere were approximately $-30 W m^{-2}$ in rural and -40 – $60 W m^{-2}$ in urban areas. Positive ARF at the top of the atmosphere at the Huimin suburban site was found to be different from others as a result of the high surface albedo due to snow cover. (Che Huizheng)

2.18 A study of the meteorological causes of a prolonged and severe haze episode in January 2013 over central-eastern China

This paper employs meteorological observation data from surface and high-balloon stations, China Meteorological Administration (CMA) model T639 output data, NCEP reanalysis data, $PM_{2.5}$ observations and modeled HYSPLIT4 trajectory results to study the meteorological causes, including large-scale circulation and planetary boundary layer features, which led to the extended haze episode on January 6–16, 2013 in central-eastern China. It discusses the possible impact of pollutants transported from southern Hebei Province on Beijing. The results show that: (1) the re-adjustment of atmospheric circulation from a longitudinal to a latitudinal model provides a valuable interpretation of the large-scale circulation background to the haze episode experienced in the metropolitan regions of Beijing, Tianjin, Hebei and their surrounding regions; (2) the regional atmospheric stratification of the planetary boundary layer is stable and the mixing height is low, suppressing air turbulence in the planetary boundary layer and providing favorable meteorological conditions for the formation of haze; and (3) the southwesterly jet stream with wind speeds of 6–11 $m s^{-1}$ at a height of 850–950 hPa and the below-700 m air mass trajectory tracking established using the HYSPLIT4 model interdependently suggest a transport of pollutants from southern Hebei Province to Beijing at 850–950 hPa. (Wang Hong)

2.19 Aerosol optical properties under the condition of heavy haze over an urban site in Beijing, China

In January 2013, several serious haze pollution events happened in North China. Cimel sunphotometer measurements at an urban site in Beijing (Chinese Academy of Meteorological Sciences—CAMS) from 1 to 30 January 2013 were used to investigate the detailed variation of aerosol optical properties. It is found that Angstrom exponents were mostly larger than 0.80 when aerosol optical depth values were higher than 0.60 in the urban region of Beijing during January 2013. The aerosol optical depth (AOD) in the urban region of Beijing remained steady at approximately 0.40 before the haze happened and then increased sharply to more than 1.50 at 500 nm with the onset of haze, which suggests that the fine mode AOD is a factor of 20 of the coarse-mode AOD during a serious haze pollution event. The single scattering albedo was approximately 0.90 ± 0.03 at 440, 675, 870 and 1020 nm during the haze pollution period. The single scattering albedo at 440 nm as a function of the fine-mode fraction was relatively consistent, but it was highly variable at 675, 870 and 1020 nm. Except on January 12 and 18, all the fine-mode particle volumes were larger than those of coarse particles, which suggested that fine particles from anthropogenic activities made up most of the haze. An analysis of aerosol type classification showed that the dominant aerosol types can be classified as “mixed” and “urban/industrial (U/I) and biomass burning (BB)” categories during the heavy haze period of Beijing in January 2013. The mixed category occurrence was about 31%, while the U/I and BB was about 69%. (Che Huizheng)

2.20 Aerosol optical properties retrieved from a Prede skyradiometer over an urban site in Beijing, China

SKYNET is an international research network of ground-based Prede sky radiometers for the observation and monitoring of aerosol-cloud-radiation interactions in the atmosphere. The algorithm developed by SKYNET is SKYRAD.pack, which can be used to process the measurement data by Prede instruments. In this study, the latest SKYRAD.pack software (Version 5.0) has been used to retrieve the aerosol optical properties measured by a SKYNET Prede sky radiometer over an urban site in Beijing, China. Continuous data have been processed over a two-year period, and inversion products, including aerosol optical depth (AOD), Ångström exponent (α), volumes of different aerosol particle size distributions, and single-scattering albedos (SSA), have been analyzed. AOD values were found to vary from 0.11 (5th percentile) to 1.14 (95th percentile) with a median of 0.34 at 500 nm, and the maximum and minimum seasonal α values in Beijing were 1.05 ± 0.36 in summer and 0.82 ± 0.39 in spring. SSA values are higher in summer and spring with a similar value of 0.96 ± 0.03 , but lower in winter with a value of 0.93 ± 0.04 at 500 nm. Aerosol particles in Beijing clearly demonstrated bimodal size distributions throughout the year: there were coarser particles in spring and finer particles in summer. The α values increased with AOD, indicating that fine particles play an important role in the optical properties of aerosols in Beijing. Dust type aerosol occurrence accounted for 4.1%, 5.1%, 0.5%, and 1.2% of all measurements data in spring, summer, autumn, and winter, respectively, according to the dust criteria threshold ($\alpha < 0.47$ and $SSA_{400 \text{ nm}} - SSA_{1020 \text{ nm}} < 0.018$). (Che Huizheng)

2.21 A multi-source observation study of the severe prolonged regional haze episode over eastern China in January 2013

By employing visibility observation of PM_{10} , SO_2 and NO_2 concentration, MODIS AOD at 550 nm, CARSNET AOD at 440 nm, and CALIPSO extinction coefficient at 532 nm, we studied the air pollution condition of a severe haze episode occurring on 6–16 January 2013 over eastern China. It is found that this severe pollution episode of large area haze was accompanied with low visibility, high PM_{10} and AOD in

eastern China. The most polluted regions are the Jing-Jin-Ji and its closely neighboring ones including central and southern Hebei, western Shandong and northern Henan provinces. The haze pollutants were spread to the offshore area of from 125°E to the east of China, and even affected the whole ocean surface to the west of 140°E. The PM₁₀ variation trend shows a strong linkage among the big cities in Jing-Jin-Ji, and their closely surrounding cities, indicating the possible inter-transport of pollutants among them. The suburban areas of megacities suffered the similar serious pollution to the urban regions during this severe haze episode. Most aerosol pollutants concentrated in boundary layers of below 1500 m vertical height, in particular, the vertical heights of 100–800 m above the ground which are most intensive. (Wang Hong)

2.22 Column-integrated aerosol optical and physical properties at a regional background atmosphere in North China Plain

The AERONET level 2.0 data at Xinglong station from February 2006 to July 2011 were used to characterize the aerosol optical and physical properties, including temporal variability, aerosol absorption, classification and properties under dust and haze conditions. The annual mean aerosol optical depth (AOD) and extinction Angstrom exponent (EAE) are 0.28 ± 0.30 and 1.07 ± 0.38 , respectively. The seasonal variations of AOD_{440nm} are higher in spring (0.40 ± 0.3) and summer (0.40 ± 0.42) than in autumn (0.20 ± 0.22) and winter (0.19 ± 0.21). The EAE is low in spring (0.96 ± 0.43) and high in summer (1.22 ± 0.38). The EAE is ~ 1.25 with an absorption Angstrom exponent (AAE) of ~ 1.0 – 1.5 at Xinglong station, which indicates that the dominant type is mixed aerosol (accounting for 88.2% at AAE > 1.0). Almost all of the dust observations occurred in spring. The volume concentrations of both fine and coarse mode particles increase with increasing AOD. In spring, the increase of coarse particles is greater than that of fine aerosols; however, the reverse phenomenon is observed for other seasons. The high AOD at Xinglong station could be associated with the growth of fine mode aerosols and the addition of coarse mode particles. This background station is not only impacted by dust aerosols from northwest China and south Mongolia but also influenced by long-range transport of anthropogenic aerosols from southern urban and industrial regions. The mean AOD was 1.49 on the dust day, while AOD was 1.10 on the haze day. The mean EAEs were 0.09 and 1.43 on dust and haze days, respectively. (Che Huizheng)

2.23 Dust aerosol drives upward trend of surface solar radiation during 1980–2009 in the Taklimakan Desert

Long-term trend of surface solar radiation (SSR) in the Taklimakan Desert (TD) during 1980–2009 and its relationship with total cloud cover (TCC), low cloud cover (LCC), water vapor content (WVC) and aerosol optical depth (AOD) were investigated. Annual mean SSR has increased by $1.21 \text{ W m}^{-2} \text{ decade}^{-1}$. Upward SSR trends were observed in seasons except winter. TCC, LCC and WVC have increased while, however, AOD and occurrences of severe dust storms have decreased, which indicates that it is dust aerosol rather than cloud cover and water vapor drive long-term upward trend of SSR in the TD. (Che Huizheng)

2.24 Study of aerosol optical properties based on ground measurements over Sichuan Basin, China

The characteristics of aerosol optical depth (AOD) and Ångström exponent as well as the relationship between the AOD and particulate matter (PM₁₀), were measured and analyzed at the Chengdu station over the Sichuan Basin in China from February 2007 to December 2009. High monthly AODs were observed in March, August and December, while a low value was observed in October. Monthly variations in Ångström exponent were opposite to that of AODs in March and August. The averaged PM₁₀ showed a significantly seasonal variation with a peak in winter. There is a complicated (not linear) positive correlation between total AOD and near-surface PM₁₀. Three typical cases under the conditions of dust and haze were studied, and the results show that the AODs on the dust days were largest while minimum AODs occurred on haze days. On the contrast, the

Ångström exponent distributions among three weather conditions were opposite to that of AODs. The 3-day back-trajectory analysis indicates that the origin of the air masses largely affects the aerosol optical properties over the Sichuan Basin. (Che Huizheng)

2.25 Analysis of global distribution characteristics of cloud microphysical and optical properties based on the CloudSat data

The global distribution and seasonal variation of the cloud physical characteristics (including the cloud liquid and ice water content, liquid and ice water path, the effective radius, etc.) and cloud optical parameters (the cloud optical depth, etc.) were analyzed with the CloudSat 2B data from January 2007 to December 2010. The results show that the distribution of ice water paths is mainly over the North America, South America, Africa, Australia and the South Asia, as well as the Pacific, Atlantic and Indian Ocean, with the highest values reaching 600 g m^{-2} or more. In the vertical direction, the high values of ice water content are located near the height of 8 km over the equatorial regions and from 4 to 8 km over the middle latitude regions. The high values of liquid water paths are located over the Pacific Ocean, the Indian Ocean and the mid and low latitudes of Atlantic. In the vertical direction, the value of liquid water content decreases with height. The ice effective radius reaches its maximum of over $200 \mu\text{m}$ near the surface at high latitudes, while having a maximum of over $80 \mu\text{m}$ at the height of 4–8 km in the equatorial region and at the height of 2–4 km in the mid-latitude. The liquid effective radius is large at the boundary layer under 1 km, with a value of over $12 \mu\text{m}$. The total cloud optical depth is below 40 around the globe, with largest values located in the vast middle and high latitudes as well as over the oceans off the west coasts of low-latitude continents. Large cloud optical depths are concentrated below the boundary layer. The distribution of the cloud optical depth is closely linked to cloud amount, which is in good spatial accordance with the former, and also to cloud water content, and cloud effective radius. (Wang Zhili)

2.26 Validation of Aura Microwave Limb Sounder (MLS) water vapor and ozone profiles over the Tibetan Plateau and its adjacent region during boreal summer

We present validation studies of MLS V2.2 and V3.3 water vapor (WV) and ozone profiles over the Tibetan Plateau (Naqu and Lhasa) and its adjacent region (Tengchong) respectively by using the balloon-borne Cryogenic Frost point Hygrometer and Electrochemical Concentration Cell ozonesonde. Coincident in situ measurements were selected to compare the MLS V2.2 and V3.3 WV and ozone profiles for understanding the applicability of the two version MLS products over the region. MLS V2.2 and V3.3 WV profiles respectively show their differences within $(2.2 \pm 15.7) \%$ ($n=74$) and $(0.3 \pm 14.9) \%$ ($n=75$) in the stratosphere at and above 82.5 hPa. Accordingly, at 100 hPa, the altitude approaching the troposphere height, differences are within $(9.8 \pm 46.0) \%$ ($n=18$) and $(23.0 \pm 45.8) \%$ ($n=17$), and they are within $(21.5 \pm 90.6) \%$ ($n=104$) and $(6.0 \pm 83.4) \%$ ($n=99$) in upper troposphere. The differences of MLS ozone are within $(-11.7 \pm 16.3) \%$ ($n=135$, V2.2) and $(15.6 \pm 24.2) \%$ ($n=305$, V3.3) at and above 82.5 hPa. At 100 hPa, they are within $(-3.5 \pm 54.4) \%$ ($n=27$) and $(-8.7 \pm 41.6) \%$ ($n=38$), and within $(18.0 \pm 79.1) \%$ ($n=47$) and $(34.2 \pm 76.6) \%$ ($n=160$) in the upper troposphere. The relative difference of MLS WV and ozone profile is significant in oscillation and scattering at upper troposphere and lower stratosphere partly due to the stronger gradients of WV and ozone concentrations here as well as the linear interpolation of sounding data for the inter-comparison. At and below 70 hPa, the relative differences of MLS ozone are significantly larger over Lhasa during the Tibetan Plateau “ozone valley” season, which is also the Asian summer monsoon period. The MLS ozone differences over the three sites are similar in their vertical distributions during that period. A simple linear correlation analysis between MLS and sounding profiles indicates that the sensitivity of MLS profile products is related to concentrations at each pressure level. The MLS V3.3 product sensitivity is slightly improved for WV at and above 82.5 hPa, whereas it is not for

ozone. The possible factors contributing to the differences of the MLS profile products of WV and ozone are discussed. (Zheng Xiangdong)

3 Model development and implementation, the impacts of atmospheric compositions on climate, weather, and human health

3.1 Air quality forecasts and assessment of control measures during APEC

With the climate forecasting results and the CMA operational air quality (AQ) forecast model CUACE, the AQ trends and detailed forecasts were carried out. One month before the APEC, we provided the day to day variation trend for the APEC period to capture the main pollution episodes. Ten days before the APEC, high resolution forecasts were obtained for the proper Beijing and the APEC meeting venue in Huairou district. With the same CUACE model and observational results, the impacts of pollution reduction control measures were also assessed. It is shown that the control measures had reduced the $PM_{2.5}$ by 35% and NO_2 by 33% in Beijing City, contributing to the “APEC Blue”. It is found that the local contribution by Beijing City to the overall control impacts was 83%–89%, where the outside contribution was only 11%–17%, due to the weak southerly winds during the APEC period. Spatially, the most efficient control measures were those taken within a circle of 300 km around Beijing and the contribution of vehicle control measures outside Beijing was not significant. The reduction at the point sources outside Beijing contributed about 9% of the reduced $PM_{2.5}$ in Beijing. (Gong Shanling, Liu Hongli)

3.2 Improvement of cloud microphysics in the aerosol-climate model BCC_AGCM2.0.1_CUACE/Aero, evaluation against observations, and updated aerosol indirect effect

A two-moment cloud microphysical scheme, which predicts both the mass and number concentrations of cloud droplets and ice crystals, is implemented into the aerosol-climate model BCC_AGCM2.0.1_CUACE/Aero. The model results for aerosols, cloud properties, and meteorological fields are evaluated, and the anthropogenic aerosol indirect effect (AIE) is estimated. The new model simulates more realistic aerosol mass concentrations and optical depth as compared with the former version using a one-moment bulk cloud microphysical scheme. The global annual mean column cloud droplet number concentration (CDNC) from the new model is $3.3 \times 10^{10} \text{ m}^{-2}$, which is comparable to the $4.0 \times 10^{10} \text{ m}^{-2}$ from satellite retrieval. The global annual mean cloud droplet effective radius at the cloud top from the new model is $8.1 \mu\text{m}$, which is smaller than the $10.5 \mu\text{m}$ from observation. The simulated liquid water path (LWP) in the new model is significantly lower than that in the former model. In particular, the annual mean LWP is lower in the new model by more than 100 g m^{-2} in some mid latitude regions, hence more consistent with satellite retrievals. Cloud radiative forcing and precipitation are improved to some extent in the new model. The global annual mean radiation budget at the top of the atmosphere is -0.6 W m^{-2} , which is considerably different from the value of 1.8 W m^{-2} in the former model. The global annual mean anthropogenic AIE is estimated to be -1.9 W m^{-2} without a lower bound of CDNC being imposed, whereas it is reduced significantly when a higher lower bound of CDNC is prescribed. (Wang Zhili)

3.3 Primary assessment of the simulated climatic state by a coupled aerosol-climate model BCC_AGCM2.0.1_CAM

With the coupled model system of the second generation Global Circulation Model of the National Climate Center (BCC_AGCM2.0.1) and Canadian Aerosol Model (CAM), the simulation of five typical aerosols (sulfate, black carbon, organic carbon, soil dust, and sea salt) and possible effects on the modeled

climate are discussed. The results show that in general, the coupled system simulates the five aerosols reasonably well, and there are obvious improvements in that for sulfate, dust, and sea salt aerosols compared to the original monthly mean aerosol data used in BCC_AGCM2.0.1. The climatic statistics simulated by the coupled system mainly agree well with observational/reanalyzed data, and are a little better than the monthly mean aerosol data in terms of the total cloud amount, land surface temperature, and precipitation. The enhanced representation of dust and sea salt improves the simulation of net solar radiation at the top of the atmosphere in the Sahara Desert and mid-latitude ocean in the Southern Hemisphere, which directly affects the land surface temperature. The cloud feedback above the tropical ocean caused by the change in an aerosol scheme not only alters radiation but also markedly influences precipitation. (Wang Zhili)

3.4 Effects of emission-sources reduction at different time points on $PM_{2.5}$ concentration over Beijing

The Model-3 Community Multi-scale Air Quality (CMAQ) modeling system with a high resolution inventory data over Beijing-Tianjin-Hebei area was used to investigate the effects on $PM_{2.5}$ concentrations over Beijing of emission-sources reduction, the rates of which were the same but the 5 time points of which were different: 4 days, 3 days, 2 days, 1 day and 0 day in advance of the most polluted day. Simulations were made for a representative air pollution episode (Feb 7th–16th, 2012), in which Feb 13th was found to be the most polluted day. The results show that the $PM_{2.5}$ concentration was likely to decline more significantly if emission-sources reduction measures were taken before the most polluted day than were taken on the most polluted day. In addition, the earlier emission-sources reduction measures were taken, the more significantly the $PM_{2.5}$ concentration would decline. Reducing emission-sources 1 day, 2 days, 3 days ahead of the most polluted day led to the reduction of the peak value of $PM_{2.5}$ concentration at the Haidian station by 23%, 31%, and 39%, and in urban Beijing by 22%, 30%, and 38%, respectively. However, as the number of days ahead of the most polluted day (Feb 13th) to take reduction measures increased further, the additional decrease of the peak $PM_{2.5}$ concentration became smaller, thus the emission-sources reduction became less effective. The peak $PM_{2.5}$ concentration would decrease by 40% and 39% at Haidian station and urban Beijing if the reduction measures were taken 4 days before the most polluted day, which shows almost no improvement compared with those taken 3 days in advance. Similar results were obtained from simulations for another pollution episode (Jan 11th–20th, 2012). For controlling severe air pollution, both reduction costs and benefits should be considered. Our study indicates that the most effective way of emission-sources reduction is to take reduction actions 2–3 days ahead of a possible severe pollution event, the timing of which can be obtained from meteorological condition prediction. In this way, a substantial decrease of the peak $PM_{2.5}$ concentration can be achieved with less cost for implementing the reduction measures. (An Xingqin)

3.5 Research on the application of the NASA/Goddard Long-Wave Radiative Scheme to the GRAPES_Meso model

The National Aeronautics and Space Administration (NASA)/Goddard Long-Wave Radiative Scheme is integrated into the Global/Regional Assimilation and Prediction System Mesoscale (GRAPES-Meso) model in this study. One month of simulation experiments conducted in China and its nearby areas are compared with the corresponding National Centers for Environmental Prediction (NCEP) reanalysis data recorded in April 2006. The results show that the distribution of the clear-sky outgoing long wave radiation flux (OLRC) at the top of atmosphere and downward long wave radiation flux at ground (GLWC) of 24-h and 48-h forecasts by using the GRAPES Meso model are in good agreement with the NCEP reanalysis data. The monthly average percentage error of the OLRC of these forecasts is within -10% and 10%. Although the monthly average percentage error of the GLWC is slightly larger than that of the OLRC, both are within a reasonable and

acceptable range. The comparison study of the daily averaged anomaly correlation coefficient and standard error of these fluxes of the two forecasts show that the monthly averaged anomaly correlation coefficients of the OLRC and the GLWC of the 24-h forecast are 0.96 and 0.98 respectively, and that the monthly averaged standard errors are 24.54 W m^{-2} and 27.23 W m^{-2} respectively. Those of the OLRC and the GLWC of the 48-h forecast are 0.95 and 0.98 and 22.43 W m^{-2} and 27.64 W m^{-2} respectively. Overall, the daily averaged anomaly correlation coefficients of the OLRC and the GLWC of both 24-h and 48-h forecasts are above 0.93, and the daily standard error is within 31 W m^{-2} . Moreover, the correlation of the GLWC and the NCEP reanalysis data is stronger than that of the OLRC, whereas the standard error of the OLRC and the NCEP reanalysis data is smaller than that of the GLWC. A comparison of the long wave radiative schemes of the rapid radiative transfer (RRTM) and the NASA/Goddard models reveals that the forecasting by the two schemes is essentially identical. The results of OLRC and the GLWC show that NASA/Goddard long wave radiative scheme may be appropriate for application to the GRAPES_Meso model. (Wang Hong)

3.6 Direct effect of tropospheric aerosols on stratospheric climate

Satellite data are used to be compared with WACCM-3 model results. It is found that model results have a very good consistency with satellite data in such areas: central Africa, the Arabian Peninsula, Indian subcontinent, and most of China; however, in southern central Africa, Caribbean, Europe and the Americas, the model results are low. In short, model results can well reproduce the global distribution of aerosols, and there still exist numerical differences in some areas.

Simulation tests indicate that the changes of stratospheric temperature are neither caused by changes of stratospheric short-wave radiation nor decided by the changes of long-wave radiation. It is not the main reason of the tropospheric aerosol effect on the stratospheric temperature, the changes of temperature are caused by dynamic processes, the change of the long wave radiative heating rate is in response to temperature changes. The stratospheric chemical, dynamic and radiation processes are tightly coupled together. The stratospheric chemical process is of vital importance to the effect of the tropospheric aerosols on stratospheric climate. The stratospheric chemical process has different effects in different seasons and different regions. Polar and high-altitude regions are considered to be mostly affected. In addition, the stratospheric chemical process also has a great influence to the upper stratosphere.

Planetary wave propagation changes make the stratospheric climate change: Stratospheric temperature, and wind field. Stratospheric ozone and radiation and dynamic processes are closely linked and influence each other. The temperature and wind changes then influence the concentration of ozone. Polar and high-altitude regions are considered to be mostly affected and impact on high southern altitude is greater than that on high northern altitude. The temperature variation could reach 10 K at most, while zonal wind variation could reach 12 m s^{-1} and ozone mixing ratio could decline for 0.8×10^{-6} at most at 20 hPa in the lower Antarctic stratosphere. In most other areas the temperature change does not exceed 1 K. (Liu Yu)

3.7 Study on impact of city emission and transport on greenhouse gases background observation at Shangdianzi station, Beijing

In-situ measurements of Carbon dioxide (CO_2) and several halogenated greenhouse gases (HFC-134a, PFC-218 and HCFC-22) were chosen for case study. We did a statistical analysis and calculation of concentration anomalies and loadings from each wind direction, discussing impact of city emission and transport on greenhouse gases background observation at Shangdianzi station in different seasons. In the study period, the ratio of background concentration of CO_2 was about 21.2%. The difference between non-background concentration and background concentration was $(3.7 \pm 1.3) \times 10^{-6}$ due to local and city emission and

transport. Anomalies and loadings of HFC-134a and PFC-218 reflected differences in source characteristics of these two compounds. The seasonal trend of HCFC-22 was in consistency with the emission pattern of refrigerant. (Yao Bo)

3.8 Retrieve emission of SF₆ in China using FLEXPART

SF₆ is one of long-lived halogenated greenhouse gases and listed as the restricted emission species in “Kyoto Protocol”. Along with the rapid economic development, SF₆ emission in China is increasing, which attracts attention in the world. For the traditional “bottom-up” method for SF₆ emission estimation, the required highly accurate and timely updated emission factors and activity data constitute a bottleneck. This paper presents the results on the estimation of SF₆ emissions in China for the year 2009 by using the Laprange particle dispersion model of FLEXPART and based on the in-situ measurement data obtained from the Shangdianzi regional atmospheric background station (SDZ). The preliminary estimations of SF₆ emissions in China for the year 2009 is $1.25 \times 10^3 (0.53 \times 10^3 - 1.97 \times 10^3)$ t, which is similar to the results reported by other studies in the literature. Compared to the a-priori emission, the retrieved emission boasts an improved correlation coefficient which increases from 0.37 to 0.43 and an improved root-mean-square (RMS) which decreases by 2.64 %. (An Xingqin)

3.9 Satellite observed aerosol effect on warm cloud properties under different meteorological conditions over eastern China

By taking meteorological conditions into account, this paper studies aerosol indirect effect on summertime warm clouds over the Yangtze River Delta (YRD) and East China Sea (ECS). The observed aerosol and cloud data are from MODIS/Aqua Level 2 datasets, and meteorological variables are from NCEP Final Analyses Operational Global Analysis datasets. To minimize meteorological effect on statistical analyses of aerosol-warm cloud interaction, several meteorological variables such as cloud top pressure (CTP), relative humidity (RH), pressure vertical velocity (PVV) and lower tropospheric stability (LTS) are considered in this study. Results show that cloud droplet radius (CDR) decreases with increasing aerosol optical depth (AOD) over ECS, while increases with increasing aerosol abundance over YRD. By taking CTP and RH into account, aerosol effects on cloud fraction (CF) are investigated. When aerosol loading is relatively small, CF is found to increase more sharply over YRD than over ECS in response to aerosol enhancement regardless of RH conditions. Therefore, we argue that the horizontal extension of cloud is prone to be driven by aerosol rather than meteorological conditions. Meanwhile, a joint correlative analysis of AOD-CF and AOD-CTP reveals that CTP effect on AOD-CF is not significant, indicating CTP makes little contribution to observed AOD-CF relationship. Constrained by lower LTS and pressure vertical velocity (750 hPa), CDR variation in response to AOD is analyzed. In general, CDR tends to decrease as aerosol increases over both ECS and YRD under stable conditions (higher LTS value). In contrast, CDR positively responds to aerosol over land under unstable conditions. Dynamically, CDR has stronger effects on the ascending motion than on the sinking motion with the same aerosol loading over both land and ocean. The reason can be partially explained by the phenomenon that updrafts favor the growth of cloud droplets. Overall, the observed cloud variations can be extremely difficult to be attributed to aerosol particles alone due to dynamical and thermodynamical processes in cloud systems. (Guo Jianping)

3.10 Diurnal variation and influential factors of precipitation from surface and satellite measurements in Tibetan Plateau

Some new features concerning the diurnal variation of precipitation over the Tibetan Plateau (TP) are revealed from rainfall data acquired by a network of rain gauge stations and estimated by the Climate

Precipitation Center Morphing (CMORPH) technique during the summer of 2010 and 2011. Maxima in precipitation amount and frequency are associated with the afternoon-to-evening precipitation regime as recorded at approximately 60% of the stations in the network. CMORPH data also capture this pattern, but miss the late morning peak that occurs at some stations. The timing of maximum occurrence agrees well with the diurnal cycle of synoptic conditions favoring the development of precipitation over this area. There is no distinct west-to-east propagation of the diurnal cycle, implying that the diurnal cycle is more driven by local effects than by large-scale circulation. It turns out that the diurnal cycle in precipitation frequency depends largely on topography and landscape. The geographical transition in precipitation peaking is distinct from hilly regions (daytime peak) towards lakes and valleys (evening-to-nocturnal peak). Stations located in mountainous regions (valleys) tend to experience more precipitation in either late morning or early afternoon (late afternoon or evening). Overall, precipitation amount shows a similar topographic dependence, as does the precipitation frequency, suggesting that local-scale effects, such as the mountain valley circulation effect, have a great impact on the diurnal variation in precipitation when large-scale dynamical processes are weak. A possible mechanism for the non-uniform diurnal cycle of precipitation over the TP is proposed. The major conclusion is that plateau-scale synoptic systems, as well as local circulation systems caused by the complex topography, should be taken into account when the diurnal variation in precipitation over the TP is determined. (Guo Jianping)

3.11 Precipitation and air pollution at mountain and plain stations in North China: Insights gained from observations and modeling

We analyzed 40-year datasets of daily average visibility (a proxy for surface aerosol concentration) and hourly precipitation at seven weather stations, including three stations located on the Taihang Mountains in North China during the summertime. There was no significant trend in summertime total precipitation at almost all stations. However, light rain decreased, whereas heavy rain increased as visibility decreased over the period studied. The decrease in light rain was seen in both orographic-forced shallow clouds and meso-scale stratiform clouds. The consistent trends in observed changes in visibility, precipitation, and orographic factor appear to be a testimony to the effects of aerosols. The potential impacts of large-scale environmental factors, such as precipitable water, convective available potential energy, and vertical wind shear, on precipitation were investigated. No direct link was found. To validate our observational hypothesis about aerosol effects, Weather Research and Forecasting (WRF) model simulations with spectral-bin microphysics at the cloud-resolving scale were conducted. Model results confirmed the role of aerosol indirect effects in reducing the light rain amount and frequency in the mountainous area for both orographic-forced shallow clouds and meso-scale stratiform clouds and in eliciting a different response in the neighboring plains. The opposite response of light rain to the increase in pollution when there is no terrain included in the model suggests that orography is likely a significant factor contributing to the opposite trends in light rain seen in mountainous and plain areas. (Guo Jianping)

3.12 The transport and deposition of dust and its impact on phytoplankton growth in the Yellow Sea

Observed surface PM_{10} mass concentrations and weather records, satellite-derived aerosol and ocean color data, dust simulations, and a backward trajectory analysis were used to investigate a severe dust storm episode during 19–22 March 2010 and its impact on phytoplankton growth in the Yellow Sea. The observed PM_{10} concentrations and weather records show that heavy dust pollution occurred along the transport pathway. The high MODIS AOD regions were consistent with the simulated high dust emission and deposition ones. Based on the CALIPSO satellite observations, the high dust aerosol layer was below 2 km above ground,

indicating the dust transported to the sea was centered within the lower layer. The model simulation estimated that the total deposition flux over the southern Yellow Sea during 19–22 March 2010 was about 1.5 g m^{-2} . Consequently, the chlorophyll a concentration was calculated to have increased four-fold. Ten to thirteen days later, a phytoplankton bloom occurred. The iron deposited by the severe dust episode could have increased the chlorophyll a concentration in the southern Yellow Sea by 10%–68%. Our results suggest that severe dust storms containing readily bioavailable nutrients may enhance phytoplankton growth in the southern Yellow Sea. (Wang Hong)

3.13 Wet deposition of acidifying substances in different regions of China and the rest of East Asia: Modeling with updated NAQPMS

The traditional way to study Sources-Receptor Relationships (SRRs) of wet deposition is based on sensitivity simulation, which has weakness in dealing with the non-linear secondary formation pollutants (e.g. ozone and nitrate). An on-line source tracking method has been developed in the Nested Air Quality Prediction Modeling System (NAQPMS) coupled with the cloud-process module for the first time. The new model can not only quantify the total volume of the sulfate, nitrate and ammonium wet deposition with more accuracy, but also trace these acidic species to their emitted precursors. Compared with previous studies, our result clearly shows: (1) East China and Central China, which are the two primary export regions, have 15%–30% and 10% effect on wet deposition in other areas, respectively; (2) Besides the above two regions, the total acid deposition in Southwest and Northeast China has reached or exceeded the critical loads under the environmental conditions of the two regions (Fig. 5). (Xu Xiaobin)

3.14 Combined effects of 1-nitropyrene and 1,2-naphthoquinone on cytotoxicity and DNA damage in A549 cells

With human lung epithelial A549 cells treated with 1-nitropyrene (1-NP), viability was measured by MTT assay; lactate dehydrogenase (LDH) leakage was determined to evaluate the cellular membrane injury; DNA damage was detected with comet assay; reactive oxygen species (ROS) generation was measured with fluorescent probe. The combined toxic effects of 1-NP and 1,2-naphthoquinone (1,2-NQ) on A549 were also evaluated. 1-NP caused a significantly concentration-dependent and time-dependent viability decrease. The LC_{50} for 24 h and 48 h were $5.2 \mu\text{mol L}^{-1}$ and $2.8 \mu\text{mol L}^{-1}$, respectively. DNA damage and intracellular ROS levels were also increased significantly through a dose-dependent manner after exposure to 1-NP. The LDH leakage was not significantly changed. Compared with the groups treated with 1-NP alone, the viability and LDH leakage were not changed significantly in combined-treated groups with 1-NP and 1,2-NQ. However, the DNA damage and ROS levels were significantly reduced in the combined-treated groups compared with the groups treated with 1-NP alone. These results suggest that 1-NP may mediate the genotoxic and cytotoxic effects through ROS generation and pretreatment with 1,2-NQ, and may inhibit the ROS generation induced by 1-NP, thereby reducing the DNA damage in A549 cells. (Li Yi)

3.15 Airborne quinones induce cytotoxicity and DNA damage in human lung epithelial A549 cells: The role of reactive oxygen species

Ambient particulate matter (PM) is associated with adverse health effects. Quinones present in PM are hypothesized to contribute to these harmful effects through the generation of reactive oxygen species (ROS). However, whether the ROS induced by quinones is involved in mediating DNA damage as well as other biological responses in pulmonary cells is less well known. In this study, the toxic effects of five typical airborne quinones, including 1,2-naphthoquinone, 2-methylanthraquinone, 9,10-phenanthrene-quinone, 2-methyl-1,4-naphthoquinone, and acenaphthenequinone, on cytotoxicity, DNA damage, intra-cellular



calcium homeostasis, and ROS generation, were studied in human lung epithelial A549 cells. An antioxidant N-acetylcysteine (NAC) was used to examine the involvement of ROS in adverse biological responses induced by quinones. The quinones caused a concentration-dependent viability decrease, cellular LDH release, DNA damage, and ROS production in A549 cells. 1,2-Naphthoquinone, but not the other four quinones, increased intracellular calcium (Ca^{2+}) levels in a dose-dependent manner. These toxic effects were abolished by administration of NAC, suggesting that ROS played a key role in the observed toxic effects of quinones in A549 cells. These results emphasize the importance of quinones in PM on the adverse health effects of PMs, which has been underestimated in the past few years, and highlight the need, when the effects on health and exposure management are evaluated, to always consider their qualitative chemical compositions in addition to the size and concentration of PMs. (Li Yi)

消息与动态 News and Notes



2014年1月13—14日，灾害性天气预报理论与方法研讨会暨灾害天气国家重点实验室2013年度学术年会在京召开。开幕式由气科院副院长赵平主持，中国气象局有关职能司领导、气科院院长端义宏以及灾害天气国家重点实验室、北京大学等研究所和高校的200多名学者出席了会议，会议收到投稿论文85篇。

On 13–14 January 2014, the Workshop on Severe Weather Forecasting Theories and Methods, i.e. the 2013 Academic Annual Meeting of State Key Laboratory on Severe Weather (LaSW) was held in Beijing. Prof. Zhao Ping, Vice President of CAMS, presided over the opening of the meeting. Director-

Generals from relevant departments of CMA headquarters, CAMS President, Dr. Duan Yihong, and over 200 researchers from research institutes and universities such as LaSW, Peking University, etc, attended the meeting. 85 research papers were submitted to the meeting.



2014年1月16日，气科院召开2014年工作会议，院长端义宏主持会议并做工作报告，全院职工参加了会议。报告总结了2013年气科院在科技创新、人才培养、国内外学术交流等方面取得的成绩，明确了2014年的工作思路以及将进一步提高科技创新能力等7个方面的重点工作任务。

On 16 January 2014, the 2014 Annual Meeting of CAMS was held and presided over by Dr. Duan Yihong, President of CAMS, who presented the annual working report. The entire staff of CAMS attended the meeting. In his report, Dr. Duan reviewed the working highlights of CAMS in 2013 including scientific and technical innovation, talents development, domestic and international academic exchanges, etc. He also confirmed the working arrangement of 2014 and the seven targeted assignments such as further improving the capability of scientific and technical innovation.



2014年3月25日，中国气象科学研究院与国家气象中心就加强科研业务结合、协同推进环境气象及雾-霾预报关键技术研发、提升中国雾-霾数值预报水平等问题进行了交流和研讨。气科院院长端义宏、气象中心主任毕宝贵及双方单位相关专家参加了会议。

On 25 March 2014, CAMS and National Meteorological Centre (NMC) held joint workshop on how to enhance co-efficiency of scientific research and operations, how to promote the development of environmental meteorology, development of key technologies of fog-haze forecasting, and how to improve the fog-haze forecasts in China. Dr. Duan Yihong, CAMS President, and Dr. Bi Baogui, Director-General of NMC as well as experts from CAMS and NMC attended the workshop.

2014年3月，中组部公布了“万人计划”（国家高层次人才特殊支持计划）第一批科技创新领军人才入选名单，气科院张小曳研究员入选“万人计划”。张小曳研究员是大气成分领域的学科带头人，先后主持过科技部、国家自然科学基金项目多项，并获得过包括国家自然科学二等奖在内的多项奖励。

In March 2014, the Organization Department of the CPC Central Committee released the namelist of the first group of scientists selected as leading scientific and technical innovation talents in the “Ten Thousand Talents Project” (a specially sponsored project for national high-level talents). Prof. Zhang Xiaoye, researcher from CAMS, was selected into the project, who was a leading scientist in atmospheric composition.

He has led several research projects sponsored by Ministry of Science and Technology, and the National Natural Science Foundation of China. He has also won a number of awards including the second prize of the National Natural Science Awards.



2014年4月1—2日，气科院2013年学术年会在京召开。院长端义宏主持开幕式，中国气象局副局长许小峰等领导出席开幕式并听取了学术报告。年会邀请了两院院士及相关研究领域的知名专家做大会特邀报告13个。年会设立灾害天气、雷电和云物理、农业气象、气候以及大气成分和城市气象学4个分会，中国气象局相关业务单位和8个专业研究所的专家也参加了年会。

On 1–2 April 2014, the 2013 Academic Annual Meeting of CAMS was held in Beijing, the opening of which was presided over by Dr. Duan Yihong, President of CAMS. CMA leaders, including Dr. Xu Xiaofeng, CMA Deputy Administrator, attended the opening of the meeting and listened to relevant academic reports. The meeting arranged 13 invited presentations delivered by academicians from the Chinese Academy of Sciences and the Chinese Academy of Engineering, as well as renowned experts in relevant research fields. The meeting had four sub-committees for areas including severe weather, lightning and cloud physics, agrometeorology and climate, atmospheric composition and urban meteorology. Experts from CMA operational facilities as well as eight specialized institutes also attended the Annual Meeting.



2014年4月9日，第3次青藏高原大气科学试验领导小组第1次会议在京召开。试验领导小组组长、中国气象局局长郑国光主持会议，领导小组成员、专家指导组成员、试验实施组负责人等出席了会议。会上，气科院副院长赵平汇报了第3次青藏高原大气科学试验总体实施方案，徐祥德院士报告了2014年的试验方案。

On 9 April 2014, the first meeting of the leading group for the Third Tibetan Plateau Scientific Experiment on Atmosphere was held in Beijing, which was chaired by Dr. Zheng Guoguang, head of the experiment leading group and CMA Administrator. Leading group members, steering group members and implementation group heads, etc, attended the meeting. During

the meeting, Prof. Zhao Ping, Vice President of CAMS, presented the overall implementation scheme of “the Third Tibetan Plateau Scientific Experiment on Atmosphere”. Prof. Xu Xiangde, Academician of Chinese Academy of Engineering, reported the experiment scheme for 2014.

2014年4月11日，由灾害天气国家重点实验室（LaSW）和中科院大气物理研究所大气科学和地球流体力学数值模拟国家重点实验室（LASG）、大气边界层物理和大气化学国家重点实验室（LAPC）联合举办的第2届“百叶箱”论坛在北京举行。此届论坛的主题为“极端天气气候研究进展及面临的科学问题”。论坛旨在促进3个实验室的共同发展，提升大气科学学科研究水平。

On 11 April 2014, the Second Forum on Thermometer Screen was held in Beijing, which was jointly hosted by LaSW of CAMS, State Key Laboratory of Numerical Modeling for Atmospheric Sciences and Geophysical Fluid Dynamics (LASG) as well as State Key Laboratory of Atmospheric Boundary Layer Physics and Atmospheric Chemistry (LAPC) of the Institute of Atmospheric Physics (IAP) of Chinese Academy of Sciences (CAS). The theme of the forum was “Research Progress in Extreme Weather and Climate and the Scientific Challenges”, which aimed at promoting the joint development of the three laboratories and improving the research in atmospheric sciences.



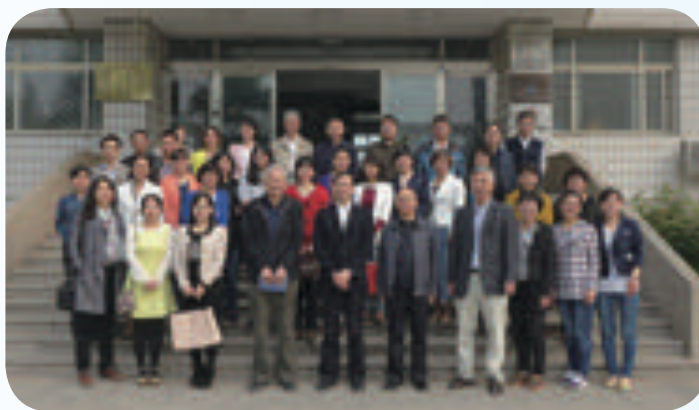


2014年4月11日，布达拉宫雷电灾害防御基础研究项目启动实施会议在北京召开。气科院副院长王怀刚主持了会议，西藏气象局、西藏文物局等单位领导和专家、项目负责人气科院张义军研究员及协作单位负责人参加了会议。该项目旨在建立布达拉宫周边的雷暴和闪电活动探测系统和预警平台，推进西藏地区古建筑防雷设计标准的研究。

On 11 April 2014, the meeting that marked launching the implementation of Basic Lightning Protection Research Project for Potala Palace was held in Beijing. CAMS Vice President, Mr. Wang Huaigang, chaired the meeting. Leaders and experts from Tibet Meteorological Service, Tibet Bureau of Cultural Relics, etc, as well as the project leader, Dr. Zhang Yijun, who was a researcher from CAMS, and experts from brother institutes attended the meeting. The project aimed at establishing the thunder storm and lightning detection system and warning platform surrounding Potala Palace, and promoting the research on ancient architecture lightning protection design in Tibet.

2014年4月14—18日，中国气象局气象干部培训学院与气科院灾害天气国家重点实验室合作举办了台风和暴雨监测与预报技术高级培训班。培训班邀请国内外知名学者就登陆台风降水机理及预报理论、台风暴雨短临预报方法等问题进行授课，国家气象中心以及受台风和暴雨影响较大省气象局的预报人员参加了培训。

On 14–18 April 2014, CMA Training Centre and LaSW of CAMS jointly held the Advanced Training Workshop of Monitoring and Forecasting Techniques for Typhoons and Rainstorms. The training invited renowned domestic and international scholars to give lectures on the rainfall mechanism and forecasting theories of landing typhoons, short-range forecasting and nowcasting methods of typhoons and rainstorms. Forecasters from NMC and meteorological services of the provinces that were seriously affected by typhoons and rainstorms attended the training.



2014年4月24—25日，国家973项目我国持续性重大天气异常形成机理与预测理论和方法研究2013/2014年度学术年会召开。首席科学家翟盘茂研究员主持了会议。项目5个课题负责人对两年多来各课题的实施情况、取得的成果、存在的问题等方面内容进行了综述性的报告。

On 24–25 April 2014, the 2013/2014 Annual Academic Meeting of National 973 Project “Research on Theories and Methods of Abnormal Formation Mechanism and Prediction for Sustained Significant Weather” was held. The project chief scientist, Dr. Zhai Panmao chaired the meeting. Five project experts reported on the implementation, progress, problems of relevant sub-projects over the past two years.

2014年4月29日，中央国家机关“五一”劳动奖颁奖仪式在北京人民大会堂举行，气科院张义军研究员获中央国家机关“五一劳动奖章”。张义军研究员是中国气象局雷电科学研究领域的领军人物。他牵头组建了“雷电物理和防护工程”实验室，并建立了国内唯一的雷电野外试验基地。他曾获得“全国优秀科技工作者”、国家科技进步二等奖等多项称号和奖项。

On 29 April 2014, the Awarding Ceremony for “May 1st Workers Award Medal” by the Central Government was held at the Great Hall of the People in Beijing. Dr. Zhang Yijun, researcher from CAMS won the medal. He was a leading scientist of CMA in the field of thunder and lightning research. He led the establishment of the laboratory of “Lightning Physics and Protection Project” and set up the only field lightning testbase in China. He has won several national honorary titles and awards such as “Excellent National Science and Technology Staff” and second prize of National Scientific and Technological Advancement.



2014年5月10日，中国气象局局长郑国光一行到气科院就气象科技体制改革进行调研。郑局长听取了气科院有关气象现代化建设的情况汇报并与气科院领导班子成员座谈。郑国光局长肯定了气科院改革发展进程中取得的成绩，分析了制约气科院未来发展的关键问题，表示中国气象局将积极推动气科院提升气象科技对气象业务现代化的支撑能力。

On 10 May 2014, Dr. Zheng Guoguang, CMA Administrator, visited CAMS to study the reform of scientific and technological mechanism. Dr. Zheng listened to the report of CAMS’ progress on meteorological modernization and held

discussions with CAMS leaders. Dr. Zheng appreciated the development of CAMS’ reform and helped analyzing the potential key problems that prevented the future advancement. He expressed CMA’s proactive support for CAMS’ developing its supporting capability in accelerating meteorological modernization by improving science and technology.

2014年5月22日，中国气象局人工影响天气中心暨云雾物理环境重点实验室在北京召开了2013年度学术年会。年会围绕人工影响天气数值模式和应用，以及人工影响天气效果检验等主题进行了交流和讨论。来自中国气象局人工影响天气中心、北京大学等高校、中科院大气物理研究所等研究所以及部分省市的人影专家参加了学术报告及讨论。

On 22 May 2014, CMA Weather Modification Centre, i.e. the Key Laboratory of Cloud-Fog Physical Environment held the 2013 Annual Academic Meeting in Beijing. The exchanges and discussions of the meeting focused on the numerical models of

weather modification and their applications, as well as verification of weather modification effects. Weather modification experts from CMA Weather Modification Centre, Universities like Peking University, the Institute of Atmospheric Physics (IAP) of CAS, as well as provincial meteorological services attended the parts of academic reports and discussions.





2014年6月5日，国家自然科学基金重点项目“光化学过程对华北区域臭氧和二次气溶胶形成的影响”的野外综合观测试验在河北省衡水展开。首批仪器设备主要探测地面臭氧、气溶胶前体物和光解系数等。综合观测试验由气科院组织，中国气象局气象探测中心、中科院大气物理研究所、部分省气象局以及中国环境科学研究院等协作单位也将参加试验及相关研究工作。

On 5 June 2014, the field integrated observation experiment of the Key Project of National Natural Science Foundation, Impacts of Photochemical Processing on the Formation of Regional Ozone and Secondary Aerosols over North China, was carried out in Hengshui of Hebei Province. The first sets of equipments were for the sounding of surface ozone, aerosol precursor and photolysis coefficient, etc. The integrated observation experiment was organized by CAMS, while cooperative partners including CMA Meteorological Observation Centre, IAP of CAS, some meteorological services of the provinces and Chinese Academy of Environmental Sciences would participated in the experiment and relevant research.



2014年6月6日，李建博士被中央国家机关工委授予第3届中央国家机关“五四青年奖章”。李建是气科院气候系统研究所副研究员，在我国气候特征及异常机理的研究方面开展了一系列具有创新性的研究工作，先后主持国家自然科学基金项目两项，是国家自然科学基金创新研究群体项目的骨干成员。

On 6 June 2014, Dr. Li Jian was awarded the third “May 4th Youth Medal” by the Central Government Working Committee. Dr. Li Jian was an associate researcher from CAMS’ Institute of Climate Systems. He has carried out a series of innovative researches in China’s climate features and abnormal

mechanisms. He has led two National Natural Science Foundation projects and is also a cadre member of the National Natural Science Foundation Innovation Research Team.

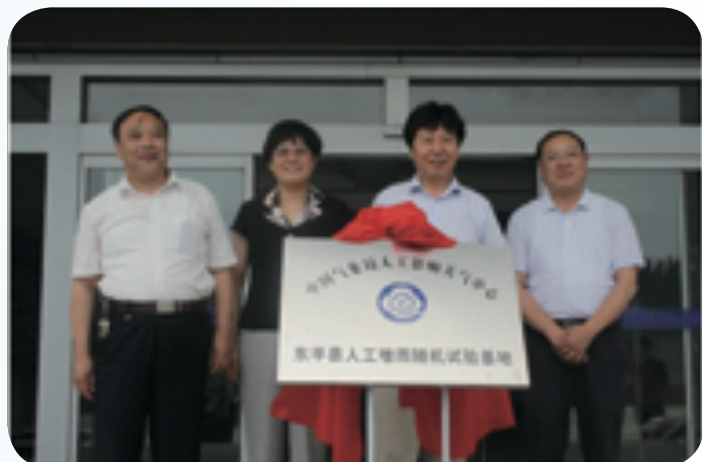


2014年6月17日，天津市科学技术委员会张勇勤副主任一行赴气科院就“协同发展寻求合作——百家院所进天津”活动开展深入调研，王怀刚副院长主持了座谈。天津市近年来经济快速发展成效显著，引进了一大批高科技院所和高水平的领军人才。张勇勤副主任代表天津市科委诚挚邀请气科院能够参与百家院所走入天津活动，双方就开展深层次合作进行了交流。

On 17 June 2014, the Deputy Director-General of Tianjin Science and Technology Committee, Mr. Zhang Yong, led a study group to CAMS seeking cooperation for better joint development, which was part of the “One Hundred Institutes in Tianjin” project. Mr. Wang Huaigang, Vice President of CAMS, chaired the discussion. In recent years, Tianjin has witnessed rapid development and fruitful outcomes, which successfully attracted a number of high-level leading talents from high-tech research institutes. On behalf of Tianjin Municipal Government, Mr. Zhang Yong extended cordial invitation to CAMS for participating in the project. The two sides exchanged ideas about deep cooperation.

2014年6月20日，中国气象局人工影响天气中心人工增雨随机试验基地揭牌仪式在山东东平县举行。中国气象局人工影响天气中心主任李集明、山东省气象局阎丽凤副局长等领导及相关专家出席了揭牌仪式。

On 20 June 2014, the launching of Testbase of Precipitation Enhancement of CMA Weather Modification Centre was held in Dongping, Shandong Province. The Director-General of CMA Weather Modification Centre, Mr. Li Jiming, and the Deputy Director-General of Shandong Provincial Meteorological Service, Ms. Yan Lifeng, etc, and relevant experts attended the launching ceremony.





2014年6月21—22日，“十二五”国家科技支撑计划重点项目“农林气象灾害监测预警与防控关键技术研究”中期检查暨2014年度工作会议在长春市召开。来自气科院、中国农业科学院和北京林业大学等研究机构的30余位专家出席了会议。会议由项目负责人王春乙研究员主持，5个课题负责人就课题实施3年多来的成果进行了汇报。

On 21–22 June 2014, the mid-term assessment of the implementation for the Key Project of National Twelfth Five-Year Plan, “Key Techniques for Meteorological Disasters Monitoring, Warning and Prevention in Agriculture and Forestry”, i.e. the 2014 Annual Meeting, was held in Changchun. Over 30 experts from research institutes including CAMS, Chinese Academy of Agricultural Sciences and Beijing Forestry University, etc, attended the meeting. The meeting was chaired by Dr. Wang Chunyi, project leader and researcher. Five project researchers reported on the outcomes achieved over the three years for the implementation of the project.



2014年7月上旬，第3次青藏高原大气科学试验综合观测全面展开。雷达和飞机观测取得了宝贵的相关资料。加密探空和边界层观测也如期进行，卫星地面校验网建设已完成部分设备安装调试和预备试验。

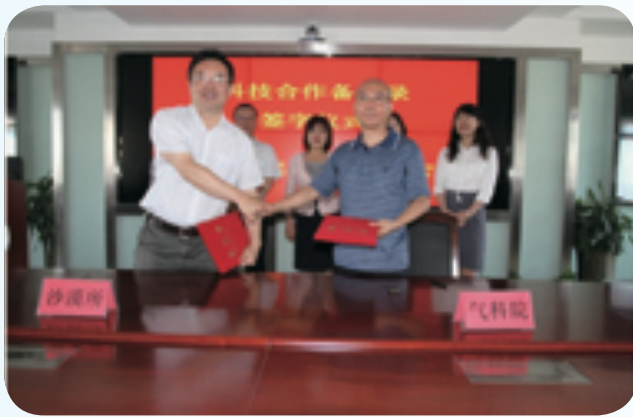
In the first half of July, 2014, the integrated observation of the Third Tibetan Plateau Scientific Experiment on Atmosphere was fully implemented, in which valuable data were obtained by radar and aircraft observation. Intensified upper-air sounding and boundary

layer observation were carried out as planned. Besides, the establishment of satellite ground verification network also partially completed the equipment installation and test as well as the pre-operational test.

2014年8月18日，中国气象局气象干部培训学院和中国气象局人工影响天气中心联合举办了第4期人工影响天气国际培训班。来自美国国家大气研究中心（NCAR）、科罗拉多州立大学（CSU）、美国人工影响天气公司（WMI）及国内人工影响天气领域的9名知名专家进行了授课，国内外的50名学员参加了培训与讨论。

On 18 August 2014, CMA Training Centre and CMA Weather Modification Centre jointly held the Fourth International Training Workshop on Weather Modification. Nine renowned experts from US National Centre for Atmospheric Research (NCAR),

Colorado State University (CSU), US Weather Modification Incorporated (WMI), and domestic weather modification community, gave lectures, in which over 50 trainees both at home and abroad attended the workshop and discussions.



2014年8月21日，赵平副院长一行赴乌鲁木齐沙漠气象研究所商讨合作事宜并签署灾害实验室与沙漠气象研究所的合作备忘录。新疆维吾尔自治区气象局张守保局长和崔彩霞副局长对气科院一行人员表示欢迎，崔彩霞副局长出席了合作备忘录的签字仪式。签字仪式后，双方就灾害实验室和沙漠研究所的科研工作进行了学术交流。

On 21 August 2014, Prof. Zhao Ping, Vice President of CAMS, led the team to the Institute of Desert Meteorology (IDM) in Urumqi to discuss cooperation and signed the MoU between LaSW and IDM. The Director-General of Xinjiang Meteorological Service, Mr. Zhang Shoubao, and

Deputy Director-General, Ms. Cui Caixia, welcomed the CAMS delegation. Ms. Cui Caixia attended the signing ceremony of MoU. After the ceremony, the two sides exchanged ideas in the research work of LaSW and IDM.

2014年9月16—19日，由中国气象局气象干部培训学院和气科院大气探测研究所共同组织的第2期全国雷电临近预警系统业务推广培训班在安徽举行。大气探测研究所主要承担了培训任务的计划编制、教材编写授课、预警系统安装使用培训等工作。65名从事相关业务的人员参加了培训。

On 16–19 September 2014, the Second National Lightning Nowcasting System Training Workshop was jointly held in Anhui, by CMA Training Centre and CAMS Atmospheric Sounding Institute. CAMS Atmospheric Sounding Institute took the main responsibilities of planning the training task, editing the training material and giving lectures, as well as warning system installation and application training, etc. 65 technical staff attended the training.





2014年9月23日，中国第6次北极考察队圆满完成考察任务乘雪龙船抵达上海。气科院逯昌贵、丁明虎两位队员在考察中完成了温室气体、黑碳气溶胶的走航观测等多项科考任务，获取了东海和西北冰洋等海表大气成分等多种观测数据并实时传输回国内。他们还协助其他单位完成了海冰雷达观测等科研任务。两位队员均被评为“中国第6次北极考察队优秀共产党员”。

On 23 September 2014, China's Sixth Arctic Scientific Expedition Team completed its assignment and arrived in Shanghai by the Snow Dragon Ship. Lu Changgui and Ding Minghu from CAMS took the responsibility of greenhouse gases and black carbon aerosol observation on excursion and successfully fulfilled the task. They obtained a variety of observation data including sea surface atmospheric compositions of East China Sea and North-West Arctic Ocean, etc, and transmitted to domestic offices on a real time basis. They also supported the completion of sea ice radar observation for other research institutes. They were awarded "Excellent CPC Members of China's Sixth Arctic Scientific Expedition".



2014年10月17日，气科院组织召开了中国气象局雾-霾监测预报创新团队启动暨学术交流研讨会。中国气象局副局长许小峰等领导和专家、创新团队成员等人员出席了会议。气科院院长端义宏主持了会议。团队带头人龚山陵教授介绍了团队总体目标、拟解决的关键技术和工作计划。与会专家就团队要解决的关键技术和面临的难点问题进行了讨论。

On 17 October 2014, CAMS organized the Academic Workshop of CMA Fog-Haze Monitoring and Forecasting Innovation Team. CMA Deputy Administrator, Dr. Xu Xiaofeng and other leaders,

experts, innovation team members, etc, attended the meeting, which was presided over by Dr. Duan Yihong, President of CAMS. The team leader, Prof. Gong Shanling introduced the overall target, key techniques to be solved and the working plans of the team. Experts discussed about the key techniques and challenges to be solved.



亚太经合组织第22次领导人非正式会议（APEC峰会）于2014年11月10—11日在北京举行。气科院积极组织院属有关科研业务单位配合预报部门做好APEC峰会期间雾霾预报和人工影响天气服务保障工作。

The 22nd Informal Meeting of APEC Leaders (APEC Summit) was held during 10–11 November 2014 in Beijing. CAMS provided service support in fog-haze forecasting and weather modification during APEC Summit by organizing its subordinating institutes and cooperating with forecasting operational bodies.



2014年11月24日，第3次青藏高原大气科学试验2014年度工作总结会在北京召开，中国气象局、基金委和中科院相关领导、项目专家指导组和项目组成员参加了会议，气科院副院长赵平主持了会议。2014年，青藏高原大气科学试验取得积极进展，全面开展了卫星、飞机、多种雷达等综合观测，对观测数据进行质量控制，在高原地区地气能量交换特征和对流系统的变化、高原大气加热场异常变化对我国旱涝的影响等方面取得了可喜的研究成果。

On 24 November 2014, the 2014 Annual Summarizing Meeting for the Third Tibetan Plateau Scientific Experiment on Atmosphere was held in Beijing. Leaders from CMA, NNSF and CAS, Steering Group experts and project members attended the meeting, which was presided over by Prof. Zhao Ping, Vice President of CAMS. In 2014, the Tibetan Plateau Scientific Experiment on Atmosphere made positive progress in which integrated observations of satellites, aircrafts and radars of different types were completed and observation data were controlled in quality. Satisfactory research outcomes in many aspects have been achieved such as gas energy exchange features on plateau and convective system variation, impact of abnormal change of atmospheric heating field on plateau on drought and flood in China, etc.



2014 新项目

New Projects in 2014

课题名称 Title	项目类别 Project/Fund	执行期间 Duration	负责人 Principal Investigator
登陆台风精细结构的观测、预报与影响评估 The observation, forecasting and impact evaluation of a landfall tropical cyclone fine structure	科技部: 973 计划项目 MOST: national basic research program	2015—2019	端义宏 Duan Yihong
我国雾-霾监测与不同分辨率数值预报业务系统研究 Research on the haze-fog monitoring and its numerical forecasting system at different resolutions in China	科技部: 科技支撑计划项目 MOST: technology support program	2014—2016	周春红 Zhou Chunhong
雾-霾观测研究 Study on haze-fog observations	科技部: 科技支撑计划项目 MOST: technology support program	2014—2016	郭建平 Guo Jianping
青藏高原与太平洋/大西洋热力作用对北半球陆地夏季风年际变化的协同影响 Collaborative influences of the Tibetan Plateau and Pacific/Atlantic thermodynamic functions on interannual variations of summer land monsoon over the Northern Hemisphere	基金委: 重大研究计划重点项目 NSFC: key program	2015—2018	赵平 Zhao Ping
青藏高原科学试验关键区物理协调大气分析模型与数据集的构建研究 The constrained variational analysis model and its dataset for the field experiment regions over the Tibetan Plateau	基金委: 重大研究计划重点项目 NSFC: key program	2015—2018	王东海 Wang Donghai
多种设备联合探测资料研究青藏高原对流云的微物理参数化方案 Study on the microphysical parameterization for convective clouds over the Tibetan Plateau by combining multiple observation data	基金委: 重大研究计划培育项目 NSFC: key program	2015—2017	高文华 Gao Wenhua
青藏高原热力作用对我国南方持续性强降雨影响机制研究 Study on mechanisms governing influence of the Tibetan Plateau's heating effect on the persistent heavy rainfall over southern China	基金委: 重大研究计划培育项目 NSFC: key program	2015—2017	罗亚丽 Luo Yali
青藏高原大气绕流和爬流三维结构异常变化对下游地区暴雨天气的影响研究 Impacts of abnormal 3D structures of flow around and flow over the Tibetan Plateau on rainstorms over its downstream areas	基金委: 重大研究计划培育项目 NSFC: key program	2015—2017	姚文清 Yao Wenqing
青藏高原复杂地形优化网格与多源信息同化研究 Study on the optimization grid meshes of complex terrain and the multivariate information assimilation in the Tibetan Plateau	基金委: 重大研究计划培育项目 NSFC: key program	2015—2017	王光辉 Wang Guanghui
中国雾-霾及其对暖云降水垂直分布影响的立体观测及建模研究 Study of the three-dimensional observation and modelling of haze-fog and its impact on the vertical structure of warm cloud and precipitation in China	基金委: 面上项目 NSFC: general program	2015—2018	郭建平 Guo Jianping
下行梯级先导诱发的上行先导的观测与研究 Observation and study of the upward leader induced by the downward stepped leader	基金委: 面上项目 NSFC: general program	2015—2018	吕伟涛 Lǚ Weitao
C波段调频连续波雷达降水云结构研究及降水参数反演 Precipitation cloud structure analysis and micro-physical parameters retrieval using C-FMCW radar	基金委: 面上项目 NSFC: general program	2015—2018	阮征 Ruan Zheng
南亚季风区近地层向平流层大气输送“烟囱”的三维结构及其形成和维持机制 Three-dimensional structures and formation/maintenance mechanisms of the “chimney” in atmospheric transport from boundary layer into the stratosphere over the South Asian monsoon region	基金委: 面上项目 NSFC: general program	2015—2018	陈斌 Chen Bin
基于超级集合预报的定量降水概率预报方法研究 The method of probabilistic quantitative precipitation forecasts based on super ensemble prediction system	基金委: 面上项目 NSFC: general program	2015—2018	赵琳娜 Zhao Linna

课题名称 Title	项目类别 Project/Fund	执行期间 Duration	负责人 Principal Investigator
西北太平洋高空冷涡对台风路径突变影响的机理研究 Study on impacts of upper tropospheric cold lows on sudden changes of typhoon motion over the Northwest Pacific	基金委: 面上项目 NSFC: general program	2015—2018	李英 Li Ying
北半球冬季中高纬大气环流低频变率成因的低维随机学动力学研究 Low-order stochastic dynamical study on the formation of the boreal winter extratropical low-frequency variability	基金委: 面上项目 NSFC: general program	2015—2018	赵南 Zhao Nan
东亚夏季风环流的齿轮耦合模态年际变化对中国降水多样性的影响 The impacts of coupling wheels of East Asian summer monsoon on the interannual diversity of rainfall in China	基金委: 面上项目 NSFC: general program	2015—2018	祝从文 Zhu Congwen
北极海冰消融与欧亚大陆中、高纬度地区盛行天气型以及极端天气之间的联系 Linkages between Arctic sea ice loss and dominant weather patterns and extreme weather events over the mid-high latitudes of Eurasia	基金委: 面上项目 NSFC: general program	2015—2018	武炳义 Wu Bingyi
基于光学特性测量的气溶胶吸湿增长因子观测研究 Hygroscopic growth factor measurement based on the aerosol scattering coefficient	基金委: 面上项目 NSFC: general program	2015—2018	孙俊英 Sun Junying
多源数据淮河流域水稻洪涝灾害遥感监测方法与应用研究 How remote sensing is applied to rice flood monitoring based on multi-source data: A case study of Huaihe River Basin	基金委: 青年科学基金项目 NSFC: youth program	2015—2017	王慧芳 Wang Huifang
西北太平洋热带气旋眼壁闪电爆发特征研究 Characteristics of eyewall lightning outbreaks in tropical cyclones over the Northwest Pacific	基金委: 青年科学基金项目 NSFC: youth program	2015—2017	张文娟 Zhang Wenjuan
闪电始发过程高低频同步观测及放电特征研究 Study about the features of lightning initial breakdown process by using synchronous VHF and VLF/LF dual band location observation	基金委: 青年科学基金项目 NSFC: youth program	2015—2017	刘恒毅 Liu Hengyi
高污染区大气冰核活化参数化方法及对强降水影响的研究 Study of the ice nuclei activation and its influence on heavy precipitation under a high ice nuclei concentration condition	基金委: 青年科学基金项目 NSFC: youth program	2015—2017	尹金方 Yin Jinfang
多种下垫面湍流扩散特征的对比研究 Study on turbulent dispersion on various complex underlying surfaces by a comparison between experiments	基金委: 青年科学基金项目 NSFC: youth program	2015—2017	全利红 Quan Lihong
基于 EnKF 资料同化方法的华南前汛期暖区暴雨集合数值模拟 Ensemble numerical simulation of warm-sector heavy rainfall during early summer rainy season over South China based on EnKF data assimilation	基金委: 青年科学基金项目 NSFC: youth program	2015—2017	宝兴华 Bao Xinghua
青藏高原低涡环流场与加热场之间的相互作用及其对低涡演变东移的影响 Interaction between the circulation related to the Tibetan Plateau vortex and the heating field and its effect on the evolution and eastward movement of the vortex	基金委: 青年科学基金项目 NSFC: youth program	2015—2017	李论 Li Lun
气候变率中长期记忆性信号的提取及其在中国气候预测中的应用 On the extraction of long-term climate memory signals in climate variability and their application to the climate prediction in China	基金委: 青年科学基金项目 NSFC: youth program	2015—2017	袁乃明 Yuan Naiming
近 30 年北半球平均费雷尔环流强度变化及其在东亚夏季风演变中的作用 Variation of the intensity of Northern Hemisphere Mean Ferrel Cell and its role in the evolvement of East Asia summer monsoon during past 30 years	基金委: 青年科学基金项目 NSFC: youth program	2015—2017	肖栋 Xiao Dong
基于求解反问题改进数值天气预报的一个新方法 A new method for numerical weather prediction improvement based on solving an inverse problem	基金委: 青年科学基金项目 NSFC: youth program	2015—2017	薛海乐 Xue Haile



课题名称 Title	项目类别 Project/Fund	执行期间 Duration	负责人 Principal Investigator
丙酮醛非均相反应过程对二次有机气溶胶的贡献研究 Study of the heterogeneous reaction of methylglyoxal on the formation of secondary organic aerosols	基金委：青年科学基金项目 NSFC: youth program	2015—2017	吴玲燕 Wu Lingyan
我国 WMO/GAW 本底站大气 N ₂ O 浓度及特征研究 Concentration and characteristics of atmospheric N ₂ O at the four WMO/GAW stations in China	基金委：青年科学基金项目 NSFC: youth program	2015—2017	方双喜 Fang Shuanxi
长三角地区雾-霾天气条件下大气黑碳气溶胶混合状态特征的观测研究 The measurement of black carbon mixing state under haze-fog conditions in Yangtze River Delta	基金委：青年科学基金项目 NSFC: youth program	2015—2017	沈小静 Shen Xiaojing
基于天气分型和污染输送的北京持续污染成因和控制研究 Research on the cause and control of the persistent air pollution in Beijing based on weather types and pollutants transport	基金委：青年科学基金项目 NSFC: youth program	2015—2017	王郁 Wang Yu
贝尔蒙特论坛国际研讨会 International Workshop of Belmont Forum	基金委：国际合作与交流项目 NSFC: projects of international cooperation and exchanges	2014—2014	王东海 Wang Donghai
NO ₃ 自由基参与的有机硝酸酯生成及老化机制研究 Formation and aging of organic nitrates via NO ₃ radical reaction	人事部：博士后基金项目 SHRM: postdoctoral fund projects	2014—2016	刘畅 Liu Chang
雹暴过程中雹粒子与闪电活动的时空配置关系研究 Spatial-temporal relationship between hail particles and lightning activity in hailstorms	人事部：留学回国人员基金项目 SHRM: scientific research foundation for returned chinese scholars	2014—2015	郑栋 Zheng Dong
中国灰霾多源数据的三维立体观测及其与云降水相互作用研究 Study of the three-dimensional observation of haze and its interaction with cloud and precipitation in China	人事部：留学回国人员基金项目 SHRM: scientific research foundation for returned chinese scholars	2014—2015	郭建平 Guo Jianping
近 50 年我国干旱频发地区的区域性气象干旱事件的检测与变化 Detection and changes of regional meteorological drought events over China's drought-prone areas during the past 50 years	中国气象局：气候变化专项 CMA: special fund for meteorological service	2014—2015	任福民 Ren Fumin
北极关键地区气候变化检测分析 Detection and analysis of climate change in key regions of Arctic	中国气象局：气候变化专项 CMA: special fund for meteorological service	2014—2015	张东启 Zhang Dongqi
人工影响天气地面作业信息实时采集分析系统 Development and application of a real-time information acquisition and analysis system for weather modification ground-based operations	中国气象局：关键技术集成应用项目 CMA: project of key technology integration and application	2014—2015	李宏宇 Li Hongyu
降水现象自动观测系统的集成应用 Integration and application of photographic precipitation recognizer	中国气象局：关键技术集成应用项目 CMA: project of key technology integration and application	2014—2015	马颖 Ma Ying

MOST: Ministry of Science and Technology (科技部)

NSFC: National Natural Science Foundation of China (国家自然科学基金)

SHRM: State Human Resource Ministry (国家人事部)

CMA: China Meteorological Administration (中国气象局)

人才培养 Education and Training



2014年5月4日，在“五四青年节”来临之际，气科院举办“优秀青年国外访学经验成果交流报告会”。气科院副院长王怀刚和50余名青年科技人员、研究生等参加报告会，院青联主席温敏主持了报告会。会上，吕伟涛研究员、郭建平和陈军明副研究员3位优秀青年汇报了国外访学成果。2008年开始气科院通过项目支持、出国培训和奖励评选等多种方式加强对优秀青年的培养，为青年人才快速成长搭建平台。

On 4 May 2014, the Youth Day, CAMS held the Workshop for Foreign Visits Outcome Exchange by Excellent Youths. Mr. Wang Huaigang, Vice President of CAMS, together with over 50 youth scientists and graduate students attended the workshop. The head of the Youth League of CAMS, Wen Min chaired the workshop. Three excellent young scientists presented their study outcomes from the visits abroad during the workshop, including Dr. Lü Weitao, Dr. Guo Jianping, and Dr. Chen Junming. Since 2008, CAMS has devoted great efforts in youth development by project sponsorship, training abroad and awards, etc, which has set up an excellent platform for young talents' rapid development.



2014年7月11日，气科院举行表彰会，端义宏院长为获得优秀博士生导师称号的周广胜、郭学良、吴统文研究员和获得优秀硕士生导师称号的武炳义、李维京、彭新东、张人禾、李伟平、翟盘茂、陈德辉研究员颁发了证书，希望全体研究生导师以优秀导师为榜样，继续为气科院研究生教育事业做出更大的贡献。

On 11 July 2014, CAMS held the commendation meeting to award certificates for excellent PhD supervisors including Zhou Guangsheng, Guo Xueliang, Wu Tongwen as well as excellent graduate supervisors including Wu Bingyi, Li Weijing, Peng Xindong, Zhang Renhe, Li Weiping, Zhai Panmao and Chen Dehui. All graduate students were encouraged to follow the good example of their supervisors and continue to make greater contributions to the graduated education of CAMS.

中国气象科学研究院2014年度博士、硕士毕业生合影

2014.07.11 北京



2014年7月11日，气科院2014年度研究生学位授予仪式暨毕业典礼隆重举行，共有11名博士研究生、44名硕士研究生顺利完成学业。2014年气科院共招收研究生61名，其中硕士研究生45名、博士研究生16名。博士后科研工作站今年共有3名博士后完成研究工作出站，有3名博士后进站。

On 11 July 2014, the Master Degree Awarding Ceremony, i.e., the 2014 Graduation Ceremony of CAMS was held with 11 PhD and 44 MSc degrees conferred. In 2014, CAMS enrolled 61 graduate candidates, including 45 MSc and 16 PhD students. Three candidates completed their work at the Post-Doctoral working station and three new candidates joined the station.



2014年8月7日，气科院青联邀请周秀骥院士为青年职工做了以“科学与人生”为主题的报告。院青联主席温敏主持了报告会。周秀骥院士结合自身60余年的科研究生涯感悟，讲述了老一辈气象科技工作者为气象事业奋斗的历程和成才故事，令广大青年科技人员深受鼓舞。

On 7 August 2014, the Youth League of CAMS invited Mr. Zhou Xiuji, Academician of CAS, to deliver a presentation themed “Science and Lifetime” for the young staff of CAMS. The presentation was chaired by head of the Youth League, Wen Min. Based on his own working experience over 60 years in scientific research, Mr. Zhou Xiuji told the success stories of the older generation of meteorological staff which were filled with hard work and great efforts. The young scientists were deeply moved and inspired by the Academician’s presentation.



2014年8月22日，气科院首届全国大气科学领域优秀大学生培训班（暑期学校）圆满结束。本次暑期学校邀请了丁一汇院士、倪允琪、张小曳、周广胜、陈德辉和陆龙骅6位知名科学家为学员做了学术报告，学员们参观了国家气象中心、北京南郊观象台等多家单位和台站。通过学习和参观，来自各大学不同专业背景的40名学员们开拓了视野，了解了气象行业的业务和科研情况。

On 22 August 2014, the first National Training Workshop (Summer School) in Atmospheric Sciences for Excellent Undergraduates was successfully completed. The Summer School invited six renowned scientists to give scientific lectures for the students, including Mr. Ding Yihui, Mr. Ni Yunqi, Mr. Zhang Xiaoye, Mr. Zhou Guangsheng, Mr. Chen Dehui and Mr. Lu Longhua. The students visited the National Meteorological Centre and the Observatory of Beijing Southern Suburb, etc. By learning and visiting, more than 40 undergraduates with different academic backgrounds broadened their horizon and had a basic understanding of the operations and researches in meteorology.

合作与交流 Cooperation and Communication



2014年1月3日，美国阿拉斯加大学张向东教授应邀到气科院进行学术交流，并做了题为“大气环流的根本改变及反气旋的加强：近期欧亚大陆极端寒冷天气事件的原因”的学术报告。张向东指出，近年来冬季反气旋环流加强导致极地冷空气向中纬度欧亚大陆渗透，是欧亚大陆冷事件的原因之一。赵平副院长主持了报告会。

On 3 January 2014, Prof. Zhang Xiangdong from University of Alaska, USA visited CAMS for academic exchange and presented the report titled “Radical Shifts of Atmospheric Circulation

and Intensification of Anticyclones: Causes of Recent Extreme Cold Weather Events in Eurasia”. Prof. Zhang pointed out that in recent years, the intensification of winter anticyclone circulation led to the permeation of cold air of polar regions into the mid and high latitude of Euro-Asian Continent, which was one of the causes of cold events on the Euro-Asian Continent. The presentation was chaired by Prof. Zhao Ping, Vice President of CAMS.



2014年1月20日，应灾害天气国家重点实验室的邀请，美国国家大气科学研究中心（NCAR）黄向宇博士访问气科院，并做了题为“WRFDA同化系统研究进展及应用”的报告。气科院副院长赵平主持了报告会，院长端义宏及相关科研业务人员、学生参加了报告会。黄向宇博士现任NCAR资料同化测试中心主任，主管WRF模式资料同化系统的发展，是国际公认的资料同化专家。

On 20 January 2014, Dr. Huang Xiangyu of US National Center for Atmospheric Research (NCAR) was invited by State Key Laboratory on Severe Weather (LaSW) of CAMS to present the report titled “Research and Application of WRFDA Assimilation System”, which was presided over by Prof. Zhao Ping, Vice President of CAMS. Dr. Duan Yihong, President of CAMS, many researchers, and students of CAMS attended the meeting. Dr. Huang is the head of NCAR’s Data Assimilation Testing Center who is responsible for the development of WRF model data assimilation system. He is a well acknowledged expert in the international community of data assimilation.



2014年2月26日，应大气探测所邀请，美国VAISALA公司气象学家Amitabh Nag博士到气科院进行学术交流，并做了题为“雷电研究的最新热点及防护技术”的学术报告。报告会由吕伟涛研究员主持，会后双方就全球闪电定位资料的共享与使用等未来可能的合作领域进行了深入的交流。

On 26 February 2014, Dr. Amitabh Nag, meteorologist from VAISALA Company US was invited by the Atmospheric Sounding Institute of CAMS to present the report titled “Recent Topics in Lightning Research and Detection Technology”, which was chaired by Dr. Lü Weitao, researcher from CAMS. After the presentation, the two sides exchanged on potential cooperation in the share of global lightning positioning data and application



2014年3月4日，应灾害天气国家重点实验室邀请，美国佐治亚理工学院地球大气科学系邓毅博士到气科院交流，并做了题为“把天气与气候联系起来”的报告。邓博士指出，从天气学角度分析气候现象的动力学机制，可为传统的气候学研究提供重要的补充。

On 4 March 2014, Dr. Deng Yi of Geo-Atmospheric Science Branch of US Georgia Institute of Technology was invited by LaSW to present the report titled “Linking Weather and Climate”, in which Dr. Deng pointed out that significant supplement could be available to traditional climate research by analyzing the dynamic mechanism of climate phenomena from synoptic point of view.

2014年3月21日，中加合作项目“气候变化背景下，西藏高寒草地牧草长势遥感监测及主要气象灾害遥感监测系统研制”项目总结会在气科院召开。加拿大使馆商务处贸易专员Stephen Kester主任和Linda Lee博士、课题负责人生态环境与农业气象研究所房世波研究员及相关领域的专家出席了会议。房世波汇报了项目内容、研究方法和取得的成果以及未来的目标等情况。

On 21 March 2014, the Project Summarizing Meeting of the Sino-Canada joint project “Crop and Grassland Health Monitoring and Productivity Estimation System in Tibet under Climate Change” was held at CAMS. Mr. Stephen Kester and Dr. Linda Lee from Business Office of Canadian Embassy to China, Dr. Fang Shibo from Institute of Ecological Environment and Agrometeorology of CAMS as well as other experts attended the meeting. Dr. Fang Shibo reported on the content of project, research methods, outcomes and future objectives.





2014年3月17日，应灾害天气国家重点实验室邀请，美国国家航空航天局（NASA）戈达德太空飞行中心陶为国博士访问气科院，并做了题为“云解析模式及其在降水过程研究中的应用”的报告。实验室王东海研究员主持了报告会。陶为国博士在报告中阐述了云微物理参数化方案的发展、存在的问题和未来发展方向等问题。

On 17 March 2014, Dr. Tao Weiguo from NASA Goddard Space Flight Center was invited by LaSW to present the report titled “Cloud-Resolving Model and its Application on Precipitation Processes”, which was chaired by Dr. Wang Donghai, research of CAMS. In his report, Dr. Tao covered several points including cloud micro-physics parameterization scheme and its problems, as well as future development, etc.



2014年4月15日，美国农业部农业研究中心高峰博士到生态环境与农业气象研究所进行访问交流，并做了题为“集成多源遥感数据的植被物候期和水分状况高时空分辨率填图研究”的学术报告。报告由王培娟博士主持。高峰博士介绍了MODIS和Landsat数据融合模型（STARFM）在地表蒸散、干旱、物候期监测等方面的应用现状和未来发展方向。

On 15 April 2014, Dr. Gao Feng from Agriculture Research Centre of US Ministry of Agriculture was invited to Institute of Ecological Environment and Agrometeorology of CAMS to present the report titled “Mapping 30-m Phenology and Water Use through Integrating Multiple Remote Sensing Data”, which was chaired by Dr. Wang Peijuan. In Dr. Gao’s representation, the application of STARFM (Spatial and Temporal Adaptive Reflectance Fusion Model) in evapor

transpiration, drought, phenology, and so on were introduced, and the future research focuses of the data fusion model were also analyzed.

2014年5月19日，澳大利亚气象局天气气候研究中心(CAWCR) Noel Davidson博士应邀到气科院访问交流，并做了题为“CAWCR的热带气旋业务和研究”以及“放大的罗斯贝波对热带气旋强度、结构和降水的影响”的学术报告。灾害天气国家重点实验室副主任徐晶主持了报告会。

On 19 May 2014, Dr. Noel Davidson from Australian Weather and Climate Research Centre (CAWCR) of Bureau of Meteorology (BoM) was invited to CAMS to present the reports titled “Operational and Research Activities on Tropical Cyclones at CAWCR” and “Influence of Amplifying Ross by Waves on Tropical Cyclone Intensity, Structure and Rainfall”, which was chaired by Dr. Xu Jing, Deputy Director of LaSW.



应极地气象研究所武炳义所长邀请，德国亥姆霍兹海洋极地研究中心的Doerthe Handorf博士和Thomas Jung教授分别于2014年5月9日和12日来气科院做了题为“北极海冰和大气环流——区域和全球的交互作用”和“北极对中纬度地区天气气候的影响”的学术报告。Doerthe Handorf博士指出，近几十年8、9月份北极海冰有减少趋势，将导致海洋中热量的增加，大气稳定度降低，进而导致秋季斜压系统的增强。Thomas Jung教授在报告中指出，观测资料显示北极和中纬度天气和气候有密切联系，北极海冰减少的同时欧洲和北美冷冬的发生频次增多，而目前对于其内在机制尚不清楚。



At the invitation of Dr. Wu Bingyi, Director of CAMS' Institute of Polar Meteorology, Dr. Doerthe Handorf and Thomas Jung from the German Helmholtz Ocean and Polar Research Centre visited CAMS on 9 May and 12 May 2014 respectively to present reports titled "Arctic Sea Ice and Atmospheric Circulations—Regional and Global Interactions" and "Arctic Influence on Mid-latitudes Weather and Climate". Dr. Doerthe Handorf pointed out that in recent decades, there was a tendency of Arctic sea ice decrease in August and September, which would lead to the heat increase in the ocean and decrease of atmospheric stability, hence strengthening the autumn baroclinic system. Prof. Thomas Jung pointed out in his report that the observation data show that the Arctic Region was closely related to the weather and climate of mid and high latitude areas. With the decrease of Arctic sea ice, more frequent cold winters occurred in Europe and North America. However, the mechanism is still not clear.



2014年5月22日，日本东京大学教授Kazuhiko Kobayashi来气科院进行了学术交流，并做了题为“农户如何适应气候变化”的学术报告。该报告通过实例阐明了气候变暖对作物以及农户的影响，以及如何利用农业气象知识使作物适应气候并使农民受益。副院长周广胜研究员主持了报告会，生态环境与农业气象研究所、国家气候中心、中国科学院植物研究所等单位的科技业务人员及学生参加了报告会。

On 22 May 2014, Dr. Kazuhiko Kobayashi from Tokyo University visited CAMS and presented the report titled "Farmers Bottom-up Adaptations to Climate Change". The presentation explained the impact of the warming climate on crops and farmers by examples, as well as how the farmers could apply agrometeorological

knowledge to make crops better adapt to climate change. Dr. Zhou Guangsheng, Vice President of CAMS, presided over the presentation. Researchers and students from Institute of Ecological Environment and Agrometeorology, CMA National Climate Centre, CAS Institute of Botany attended the presentation.

2014年5月21日，英国国家物理实验室的首席科学家Paul Gray Quincey应邀访问大气成分研究所，并做了题为“英国PM_{2.5}治理”的学术报告，介绍了英国大气污染治理的成果与现状。Quincey博士还与科研人员就我国大气污染形势及治理方法进行了交流和探讨。孙俊英所长主持了报告会。

On 21 May 2014, Mr. Paul Gray Quincey, the chief scientist of UK National Physics Laboratory was invited to CAMS Institute of Atmospheric Composition and presented the report titled "PM_{2.5} Governance in UK", which introduced the outcomes and status of air pollution governance in UK. The presentation was chaired by Dr. Sun Junying, Director of CAMS Institute of Atmospheric Composition.



2014年6月26日，为了执行中加双边合作项目“城市和郊区大气碳气溶胶演化过程的合作研究”，加拿大环境部专家李少萌博士来气科院交流和访问，并做了题为“加拿大油砂矿开采的大气污染物排放”的学术报告。项目中方负责人孙俊英研究员主持了报告会。

On 26 June 2014, Dr. Li Shaomeng from Environment Canada (EC) visited CAMS to implement the CMA-MSC (Meteorological Service of Canada) bilateral cooperative activity “Joint Research on Evolution of Atmospheric Carbon Aerosol in Urban and Rural Areas”. Dr. Li presented the report titled “the Air Pollutants Emission of Oil Sands Mining in Canada”. The CMA focal point of the activity, Dr. Sun Junying, chaired the presentation.



2014年7月3日，加拿大环境部专家张雷鸣博士来气科院进行学术交流和访问。并分别做了题为“环境汞的分析与应用”和“环境大气中不同污染物沉降方法的改进”的2个报告。大气成分研究所张养梅副研究员主持了报告会。

On 3 July 2014, Dr. Zhang Leiming from EC visited CAMS and presented two reports titled “Analysis and Application of Speciated Atmospheric Mercury” and “Method Development Estimating Atmospheric Deposition of Various Pollutants”. Ms. Zhang Yangmei, associate researcher of CAMS Institute of Atmospheric Composition, chaired the presentation.

associate researcher of CAMS Institute of Atmospheric Composition, chaired the presentation.

2014年8月26日，中国气象局人工影响天气中心邀请科罗拉多州立大学（CSU）的Paul J. DeMott博士进行工作交流。DeMott博士介绍了近年气溶胶研究的新动向及催化剂检测的新进展。DeMott博士对人工影响天气中心的暖云室建设给出了建设性意见。人工影响天气中心苏正军博士主持了报告会。

On 26 August 2014, Dr. Paul J. DeMott from US Colorado State University (CSU) was invited by CMA Weather Modification Centre to CAMS. Dr. DeMott introduced the latest progress in aerosol research and catalyst verification. He also provided the Warm Clouds Laboratory of Weather Modification Centre with constructive suggestions. The presentation was chaired by Dr. Su Zhengjun of Weather Modification Centre.





2014年8月28日，美国人工影响天气公司（WMI）主任Bruce Boe先生与人工影响天气中心就人工增雨效果检验评估及雷达资料应用进行了交流讨论。Bruce Boe先生希望有机会就我国的增雨效果检验项目能进一步合作。人工影响天气中心姚展予研究员主持了交流会。

On 28 August 2014, Mr. Bruce Boe, the Director of US Weather Modification Incorporated (WMI) discussed with Weather Modification Centre about precipitation enhancement effect verification and assessment, as

well as radar data application. Mr. Bruce Boe expected potential opportunities of cooperation with project of precipitation enhancement effect verification in China. Dr. Yao Zhanyu, researcher from Weather Modification Centre, presided over the discussion.



2014年10月27—28日，第2届中韩姊妹合作伙伴计划双边研讨会在北京召开。本届研讨会的主题是“回顾双边科研合作进展，商讨双边在亚洲沙尘暴、大气雾-霾污染、东亚季风、灾害天气、人工影响天气和大气探测等领域未来的合作研究以及最新研究成果的交流”。气科院张人禾研究员主持了会议，端义宏院长、韩国气象研究所（NAM）Jae Cheol所长及相关领导专家参加了研讨会。

On 27–28 October 2014, the Second Bilateral Workshop of China-Korea Sister Partners was held in Beijing. The theme of the workshop was reviewing bilateral research progress; discussing bilateral research on Asian sand & dust storm, atmospheric fog-haze pollution, East-Asian monsoons, severe weathers, weather modification and atmospheric sounding; exchange of latest research outcomes. Prof. Zhang Renhe, researcher from CAMS, presided over the workshop and Dr. Duan Yihong, President of CAMS, Mr. Jae Cheol from NAM of Korea, as well as relevant leaders and experts attended the workshop.



2014年11月12—16日，美国著名气溶胶研究科学家、美国科学院院士、德克萨斯A & M大学海洋与大气科学系Robert A. Duce教授受张小曳研究员邀请来气科院进行访问。期间Duce教授做了题为“大气中的营养物（尤其是氮）对海洋的传输”的学术报告。北京大学、清华大学、中科院以及中国气象局相关业务研究单位50余名专家学者及研究生聆听了报告。

On 11–12 November 2014, Prof. Robert A. Duce, renowned US aerosol scientist and Academician of US Academy of Sciences, as well as professor of Oceanic and Atmospheric Colleague of Texas A & M University, was invited by Prof. Zhang Xiaoye to CAMS. Prof. Duce presented the report titled “Atmospheric Transport of Nutrients, Especially Nitrogen, to the Ocean”. Over 50 experts and researchers from Peking University, Qinghua University, Chinese Academy of Sciences and CMA institutions listened to the presentation.



2014年11月27日，在WMO/WWRP处长Paolo M Ruti博士应邀来中国气象局访问期间，气科院承办了WMO-WWRP研究计划研讨会。端义宏院长主持了研讨会。会上有关专家分别介绍了中国气象局在环境气象预报、数值模式、南北极考察与观测、人工影响天气和第3次青藏高原大气科学试验等方面的成果。

On 27 November 2014, during the visit of Dr. Paolo M Ruti, Director of WMO/WWRP to CMA, CAMS hosted the Workshop on WMO/WWRP Research Programs. Dr. Duan Yihong, President of CAMS presided over the workshop. Experts introduced outcomes of the following areas: CMA activities in Atmospheric Watch and Environmental Meteorological Forecasting, the Numerical Forecast Model of CMA, Monitoring and Exploring the Arctic and Antarctic, Weather Modification Activities in China, the Third Tibetan Plateau Atmospheric Scientific Experiment (TIPEX-III), etc.

2014 年出版物

Publications in 2014

作者 Author (rank)	题名 Title	出版物名 / 出版社 Publication name or Publisher	年, 卷 (期号) Year, Volume (Issue)	备注 Notes
Che Huizheng, et al.	Aerosol optical properties retrieved from a prede skyradiometer over an urban site of Beijing, China	Journal of the Meteorological Society of Japan	2014, 92A	SCI
Che Huizheng, et al.	Aerosol optical properties under the condition of heavy haze over an urban site of Beijing, China	Environmental Science and Pollution Research	2014, 22(2)	SCI
Che Huizheng, et al.	Column aerosol optical properties and aerosol radiative forcing during a serious haze-fog month over North China Plain in 2013 based on ground-based sunphotometer measurements	Atmospheric Chemistry and Physics	2014, 14(4)	SCI
Che Huizheng, et al.(2nd)	Column-integrated aerosol optical and physical properties at a regional background atmosphere in North China Plain	Atmospheric Environment	2014, 84(1)	SCI
Che Huizheng, et al.(2nd)	Establishment of integrating sphere calibration method of China aerosol remote sensing network cimel sunphotometer	Particuology	2014, 13(c)	SCI
Che Huizheng, et al.(2nd)	Study of aerosol optical properties based on ground measurements over Sichuan Basin, China	Aerosol and Air Quality Research	2014, 14(1)	SCI
Che Huizheng, et al.(3rd)	Dust aerosol drives upward trend of surface solar radiation during 1980–2009 in the Taklimakan Desert	Atmospheric Science Letters	2014, 15(4)	SCI
Chen Haoming, et al.(2nd)	Simulations of stratus clouds over Eastern China in CAM5: Sensitivity to horizontal resolution	Journal of Climate	2014, 27(18)	SCI
Chen Haoming, et al.(2nd)	Vertical structures and physical properties of the cold-season stratus clouds downstream of the Tibetan Plateau: Differences between daytime and nighttime	Journal of Climate	2014, 27(18)	SCI
Chen Haoming, et al.(3rd)	Topographic effects on spatiotemporal variations of short-duration rainfall events in warm season of central North China	Journal of Geophysical Research	2014, 119(19)	SCI
Ding Minghu, et al.(3rd)	Temporal variations in marine chemical concentrations in coastal areas of eastern Antarctica and associated climatic causes	Quaternary International	2014, 352(1)	
Ding Minghu, et al.(3rd)	Variations in stable hydrogen and oxygen isotopes in atmospheric water vapor in the marine boundary layer across a wide latitude range	Journal of Environmental Sciences	2014, 26(11)	SCI
Fang Shibo, et al.(2nd)	Vegetation coverage changes and their response to meteorological variables from 2000 to 2009 in Naqu	Canadian Journal of Remote Sensing	2014, 40(1)	
Fang Shuangxi, et al.	In situ measurement of atmospheric CO ₂ at the four WMO/ GAW stations in China	Atmospheric Chemistry and Physics	2014, 14(5)	SCI
Gao Wenhua	A study of macrophysical and microphysical properties of warm clouds over the Northern Hemisphere using CloudSat/ CALIPSO data	Journal of Geophysical Research	2014, 119(3)	SCI
Guo Jianping(2nd)	A new statistic approach towards landslide hazard risk assessment	International Journal of Geosciences	2014, 5(1)	
Guo Jianping,et al.	Attribution of maize yield increase in China to climate change and technological advancement between 1980 and 2010	Journal of Meteorological Research	2014, 28(6)	SCIE
Guo Jianping,et al.	Diurnal variation and the influential factors of precipitation from surface and satellite measurements in Tibet	International Journal of Climatology	2014, 34(9)	SCI
Guo Jianping,et al.	Precipitation and air pollution at mountain and plain stations in Northern China: Insights gained from observations and modeling	Journal of Geophysical Research	2014, 119(8)	SCI
Guo Jianping, et al.(2nd)	Satellite observed aerosol-induced variability in warm cloud properties under different meteorological conditions over Eastern China	Atmospheric Environment	2014, 84(2)	SCI

作者 Author (rank)	题名 Title	出版物名/出版社 Publication name or Publisher	年,卷(期号) Year, Volume (Issue)	备注 Notes
Guo Jianping, et al.(2nd)	Scenario analysis on the adaptation of different maize varieties to future climate change in Northeast China	Journal of Meteorological Research	2014, 28(3)	SCIE
Guo Xueliang	A case study of aerosol impacts on summer convective clouds and precipitation over Northern China	Atmospheric Research	2014, 142(2)	SCI
Guo Xueliang, et al.(2nd)	Observation analysis on characteristics of formation, evolution and transition of a long-lasting severe fog and haze episode in North China	Science China: Earth Sciences	2014, 57(4)	SCI
Hu Zhiqun,et al.	Applications of wavelet analysis in differential propagation phase shift data de-noising	Advances in Atmospheric Sciences	2014, 31(4)	SCI
Li Jian,et al.	A method to linearly evaluate rainfall frequency-intensity distribution	Journal of Applied Meteorology and Climatology	2014, 53(4)	SCI
Li Jian,et al.	Characteristics of cold season rainfall over the Yungui Plateau	Journal of Applied Meteorology and Climatology	2014, 53(7)	SCI
Li Lun,et al.	Diurnal variation in the occurrence frequency of the Tibetan Plateau Vortices	Meteorology and Atmospheric Physics	2014, 125(3-4)	SCI
Li Lun,et al.	Effect of the atmospheric heat source on the development and eastward movement of the Tibetan Plateau Vortices	Tellus A	2014, 66	SCI
Liu Ge	A dipole pattern of summer precipitation over mid-high latitude Asia and related snow cover anomalies in the preceding spring	Atmospheric and Oceanic Science Letters	2014, 7(4)	
Liu Ge,et al.	Persistence of snow cover anomalies over the Tibetan Plateau and the implications for forecasting summer precipitation over the Meiyu-Baiu region	Atmospheric and Oceanic Science Letters	2014, 7(2)	
Liu Ge,et al.	The summer snow cover anomaly over the Tibetan Plateau and its association with simultaneous precipitation over the Meiyu-Baiu region	Advances in Atmospheric Sciences	2014, 31(4)	SCI
Liu Ge,et al.(2nd)	Contrasting Eurasian spring and summer climate anomalies associated with western and eastern Eurasian spring snow cover changes	Journal of Geophysical Research	2014, 119(1)	SCI
Liu Liping, et al.(2nd)	Comparison of the observation capability of an X-band phased-array radar with an X-band doppler radar and S-band operational radar	Advances in Atmospheric Sciences	2014, 31(4)	SCI
Liu Liping, et al.(2nd)	Test pattern identification algorithm and its application to CINRAD/SA(B) data	Advances in Atmospheric Sciences	2014, 31(2)	SCI
Liu Lixin,et al.	Background variations of atmospheric CO ₂ and carbon-stable isotopes at Waliguan and Shangdianzi stations in China	Journal of Geophysical Research	2014, 119(9)	SCI
Liu Ying,et al.	Implication of negative entropy flow for local rainfall	Entropy	2014, 15(9)	SCIE
Luo Yali	Initiation and organizational modes of an extreme-rain-producing mesoscale convective system along a Mei-Yu front in East China	Monthly Weather Review	2014, 142(1)	SCI
Luo Yali	The persistent heavy rainfall over Southern China in June 2010: Evolution of synoptic systems and the effects of the Tibetan Plateau heating	Journal of Meteorological Research	2014, 28(4)	SCIE
Luo Yali,et al.(2nd)	Initiation, maintenance, and properties of convection in an extreme rainfall event during SCMREX: Observational analysis	Journal of Geophysical Research	2014, 119(23)	SCI
Luo Yali,et al.(3rd)	Changes of summer precipitation in China: The dominance of frequency and intensity and linkage with changes in moisture and air temperature	Journal of Geophysical Research	2014, 119(10)	SCI
Luo Yali,et al.(3rd)	The atmospheric anomalies associated with the drought over the Yangtze River Basin during spring 2011	Journal of Geophysical Research	2014, 119(10)	SCI
Lü Junmei, et al.(2nd)	The southern annular mode (SAM) in PMIP2 simulations of the last glacial maximum	Advances in Atmospheric Sciences	2014, 31(4)	SCI
Lü Weitao,et al.	Four ways of how downward and upward leaders make connection during the lightning attachment process	ICAE2014(论文集)	2014, 6	

作者 Author (rank)	题名 Title	出版物名/出版社 Publication name or Publisher	年,卷(期号) Year, Volume (Issue)	备注 Notes
Lü Weitao,et al.	Three-dimensional propagation characteristics of leaders in a downward negative lightning flash	ICLP2014(论文集)	2014, 10	
Lü Weitao, et al.(2nd)	Three-dimensional propagation characteristics of the upward connecting leaders in six negative tall-object flashes in Guangzhou	Atmospheric Research	2014, 149(1)	SCI
Ma Jianzhong, et al.(3rd)	Lidar-observed enhancement of aerosols in the upper troposphere and lower stratosphere over the Tibetan Plateau induced by the Nabro volcano eruption	Atmospheric Chemistry and Physics	2014, 14(21)	SCI
Meng Zhaoyang, et al.	Seasonal variation of ammonia and ammonium aerosol at a background station in the Yangtze River Delta Region, China	Aerosol and Air Quality Research	2014, 14(3)	SCI
Ren Fumin	Characteristics of the regional meteorological drought events in Southwest China during 1960—2010	Journal of Meteorological Research	2014, 28(3)	SCIE
Ruan Zheng	Analysis of microphysical properties within the stratiform region using spectra of L-band profile radar	Journal of Meteorological Research	2014, 28(2)	SCIE
Ruan Zheng	Spectrum analysis of wind profiling radar measurements	Journal of Meteorological Research	2014, 28(4)	SCIE
Su Jingzhi,et al.	Abrupt termination of the 2012 Pacific warming and its implication on ENSO prediction	Geophysical Research Letters	2014, 41(24)	SCI
Su Jingzhi,et al.	The initiation and developing mechanisms of central Pacific El Niños	Journal of Climate	2014, 27(12)	SCI
Su Jingzhi, et al.(2nd)	The natural oscillation of two types of ENSO events based on analyses of CMIP5 model control runs	Advances in Atmospheric Sciences	2014, 31(3)	SCI
Wang Donghai, et al.	In-situ measurements of cloud-precipitation microphysics in East Asia monsoon region since 1960	Journal of Meteorological Research	2014, 28(2)	SCIE
Wang Donghai, et al.(3rd)	An orthogonal terrain-following coordinate and its preliminary tests using 2-D idealized advection experiments	Geoscientific Model Development	2014, 7(4)	
Wang Guanghui, et al.(2nd)	Numerical solution for a parabolic obstacle problem with nonsmooth initial data	Numerical Methods for Partial Differential Equations	2014, 30(5)	SCI
Wang Hong,et al.	A multisource observation study of the severe prolonged regional haze episode over eastern China in January 2013	Atmospheric Environment	2014, 48	SCI
Wang Hong,et al.	A study of the meteorological causes of a prolonged and severe haze episode in January 2013 over central-eastern China	Atmospheric Environment	2014, 48	SCI
Wang Hong, et al.(2nd)	The transport and deposition of dust and its impact on phytoplankton growth in the Yellow Sea	Atmospheric Environment	2014, 48	SCI
Wang Peijuan	Operational data fusion framework for building frequent landsat-like imagery	IEEE Transaction on Geoscience and Remote Sensing	2014, 52(11)	SCI
Wang Yafei, et al.(2nd)	Impact of preceding El Niño and the Indian Ocean dipole on the southern China precipitation in early summer	Advances in Meteorology	2014, 450691	
Wang Yafei, et al.(3rd)	Large-scale dynamics, anomalous flows, and teleconnections	Advances in Meteorology	2014, 207413	
Wang Yaqiang	MeteoInfo: GIS software for meteorological data visualization and analysis	Meteorological Applications	2014, 21(2)	SCI
Wang Ying,et al.	Coupling of comprehensive two-dimensional gas chromatography with quadrupole mass spectrometry (GC×GC-qMS): Application to the identification of atmospheric volatile organic compounds	Journal of Chromatography A	2014, 1361(1)	SCI
Wang Yue	Precessional forced extratropical North Pacific mode and associated atmospheric dynamics	Journal of Geophysical Research: Oceans	2014, 119(6)	SCI
Wang Zhili,et al.	Black carbon reduction will weaken the aerosol net cooling effect	Atmospheric Chemistry and Physics	2014, 14(23)	SCI
Wang Zhili,et al.	Improvement of cloud microphysics in the aerosol-climate model BCC_AGCM2.0.1_CUACE/Aero, evaluation against observations, and updated aerosol indirect effect	Journal of Geophysical Research	2014, 119(13)	SCI

作者 Author (rank)	题名 Title	出版物名/出版社 Publication name or Publisher	年,卷(期号) Year, Volume (Issue)	备注 Notes
Wu Bingyi	Dominant patterns of winter arctic surface wind variability	Advances in Polar Sciences	2014, 25(4)	
Xiao Dong,et al.	Millennial-scale phase relationship between North Atlantic deep-level temperature and Qinghai-Tibet Plateau temperature and its evolution since the Last Interglaciation	Chinese Science Bulletin	2014, 59(1)	SCI
Xin Yufei,et al.	Individual variations of winter surface air temperature over Northwest and Northeast China and their respective preceding factors	Atmospheric and Oceanic Science Letters	2014, 7(4)	
Xu Xiangde,et al.	An important mechanism sustaining the atmospheric “water tower” over the Tibetan Plateau	Atmospheric Chemistry and Physics	2014, 14(14)	SCI
Xu Xiaobin, et al.(2nd)	Two-year measurements of surface ozone at Dangxiong, a remote highland site in the Tibetan Plateau	Journl of Environmental Sciences	2014, 26(1)	SCI
Xu Xiaobin, et al.(2nd)	Wintertime peroxyacetyl nitrate (PAN) in the megacity Beijing: The role of photochemical and meteorological processes	Journal of Environmental Sciences	2014, 26(1)	SCI
Xu Xiaobin, et al.(3rd)	Wet deposition of acidifying substances in different regions of China and the rest of East Asia: Modeling with updated NAQPMS	Environmental Pollution	2014, 187(4)	SCI
Yao Bo,et al.	Atmospheric sulfur hexafluoride in-situ measurements at the Shangdianzi regional background station in China	Journal of Environmental Sciences	2014, 26(12)	SCI
Yin Jinfang,et al.	An attempt to improve the microphysical parameterization of the Kessler-type warm cloud conversion process using CloudSat observation	Journal of Meteorological Research	2014, 29(1)	SCIE
Yin Jinfang,et al.	An investigation into the relationship between liquid water content and cloud number concentration in the stratiform clouds over North China	Atmospheric Research	2014, 139(1–2)	SCI
Yu Rucong,et al.	Progress in studies of the precipitation diurnal variation over contiguous China	Journal of Meteorological Research	2014, 28(5)	SCIE
Yu Rucong, et al.(2nd)	Study of different diurnal variations of summer long-duration rainfall between the southern and northern parts of the Huai River	Chinese Journal of Geophysics	2014, 57(2)	SCI
Yuan Naiming, et al.	Century-scale intensity modulation of large-scale variability in long historical temperature records	Journal of Climate	2014, 27(1)	SCI
Yuan Naiming, et al.	Different spatial cross-correlation patterns of temperature records over China: A DCCA study on different time scales	Physica A	2014, 400(1)	SCI
Yuan Naiming, et al.	Extracting climate memory using fractional integrated statistical model: A new perspective on climate prediction	Scientific Reports	2014, 4(1)	SCI
Zhai Panmao,et al.(2nd)	Changes in climate regionalization indices in China during 1961–2010	Advances in Atmospheric Sciences	2014, 31(4)	SCI
Zhang Gen,et al.	Seasonal and diurnal variations of atmospheric peroxyacetyl nitrate	Journal of Environmental Sciences	2014, 26(1)	SCI
Zhang Renhe	Meteorological conditions for the persistent severe fog and haze event over eastern China in January 2013	Science China: Earth Sciences	2014, 57(1)	SCI
Zhang Renhe, et al.(2nd)	Impact of East Asian winter and Australian summer monsoons on the enhanced surface westerlies over the western tropical Pacific Ocean preceding the El Niño onset	Journal of Climate	2014, 27(5)	SCI
Zhang Renhe, et al.(2nd)	Impact of Indian summer monsoon on the South Asian High and its influence on summer rainfall over China	Climate Dynamics	2014, 43(5–6)	SCI
Zhang Renhe, et al.(2nd)	Intercomparison of spring soil moisture among multiple reanalysis datasets over eastern China	Journal of Geophysical Research	2014, 119(1)	SCI
Zhang Shengjun, et al.	Three-dimensional variational data assimilation experiments for a heavy rainfall case in the downstream Yangtze River valley using automatic weather station and global positioning system data in southeastern Tibetan Plateau	Journal of the Meteorological Society of Japan	2014, 92(5)	SCI
Zhang Xiaoye	Asian dust, eolian iron and black carbon—connections to climate changes	Developments in Paleoenvironmental Research	2014, 16	

作者 Author (rank)	题名 Title	出版物名/出版社 Publication name or Publisher	年,卷(期号) Year, Volume (Issue)	备注 Notes
Zhang Yang,et al.	Lightning discharges accompanied by initial breakdown pulses	2014 International Conference on Lightning Protection	2014, 10	
Zhang Yang,et al.	Research on chaotic leader in cloud-to-ground lightning	XV International Conference on Atmospheric Electricity	2014, 6	
Zhang Yangmei, et al.	Chemical composition and mass size distribution of PM ₁ at an elevated site in central east China	Atmospheric Chemistry and Physics	2014, 14(22)	SCI
Zhang Yangmei, et al.(2nd)	Variability, formation and acidity of water-soluble ions in PM _{2.5} in Beijing based on the semi-continuous observations	Atmospheric Research	2014, 145	SCI
Zhang Yijun,et al.	Experiments of artificially triggered lightning and its application in Conghua, Guangdong, China	Atmospheric Research	2014, 135(1)	SCI
Zhang Yijun, et al.(2nd)	Simulation of the electrification of a tropical cyclone using the WRF-ARW model: An idealized case	Journal of Meteorological Research	2014, 28(3)	SCI
Zhao Junfang,et al.(3rd)	Efficiency enhancement of a process-based rainfall-runoff model using a new modified AdaBoost.RT technique Shuang	Applied Soft Computing	2014, 23	SCI
Zheng Xiangdong,et al.(2nd)	Atmospheric pollutants transport tracks revealed from ¹³¹ I, ¹³⁷ Cs, and ¹³⁴ Cs leaked from Fukushima accident and ⁷ Be and ²¹⁰ Pb observed at Guiyang of China	Chinese Journal of Geochemistry	2014, 33(3)	SCI
Zheng Xiangdong, et al.(2nd)	Validation of aura microwave limb sounder water vapor and ozone profiles over the Tibetan Plateau and its adjacent region during boreal summer	Science China: Earth Sciences	2014, 57(1)	SCI
Zheng Xiangdong, et al.(3rd)	Influence of air mass downward transport on the variability of surface ozone at Xianggelila Regional Atmosphere Background Station, Southwest China	Atmospheric Chemistry and Physics	2014, 14(4)	SCI
Zhou Guangsheng, et al.(2nd)	Analysis of the variability of canopy resistance over a desert steppe site in Inner Mongolia, China	Advances in Atmospheric Sciences	2014, 31	SCI
Zhou Guangsheng, et al.(2nd)	Climatic suitability of the potential geographic distribution of <i>Fagus longipetiolata</i> in China	Environmental Earth Sciences	2014, 73(3)	SCI
Zhou Guangsheng,et al.(2nd)	Determination of green aboveground biomass in desert steppe using litter-soil-adjusted vegetation index	European Journal of Remote Sensing	2014, 47	SCI
Zhou Guangsheng, et al.(2nd)	Drivers of lightning- and human-caused fire regimes in the Great Xing	Forest Ecology and Management	2014, 329	SCI
Zhou Guangsheng, et al.(2nd)	Estimating aboveground green biomass in desert steppe using band depth indices	Biosystems Engineering	2014, 127	SCI
Zhou Guangsheng, et al.(2nd)	Impacts of climate change on rice yield in China from 1961–2010 based on provincial data	Journal of Integrative Agriculture	2014, 13(7)	SCI
Zhou Guangsheng, et al.(2nd)	Remote estimation of the fraction of absorbed photosynthetically active radiation for a maize canopy in Northeast China	Journal of Plant Ecology	2014, 3	
Zhou Guangsheng, et al.(3rd)	Composition and structure of <i>Pinus Koraiensis</i> mixed forest respond to spatial climatic changes	PLoS ONE	2014, 9(5)	SCI
Zhou Guangsheng, et al.(3rd)	Estimating canopy characteristics of Inner Mongolia's grasslands from field spectrometry	Remote Sensing	2014, 6(3)	SCI
Zhou Guangsheng, et al.(3rd)	Assessment of the redistribution of soil carbon using a new index—a case study in the Haihe River Basin, North China	Environmental Monitoring Assessment	2014, 186	SCI
Zhou Lingxi, et al.(2nd)	Preliminary study of atmospheric carbon dioxide in a glacial area of the Qilian Mountains, West China	Atmospheric Environment	2014, 99	SCI
Zhou Xiujj, et al.(2nd)	On the relationship between direct and anisotropic diffuse radiation	Infrared Physics & Technology	2014, 65(5)	SCI

作者 Author (rank)	题名 Title	出版物名/出版社 Publication name or Publisher	年,卷(期号) Year, Volume (Issue)	备注 Notes
安兴琴等	利用 FLEXPART 模式反演中国区域 SF6	环境科学学报	2014, 34(5)	
安兴琴等(第2)	上甸子本底站卤代温室气体大气浓度短期波动的个例分析	大气科学学报	2014, 37(4)	
安兴琴等(第2)	不同时刻污染减排对北京市 PM _{2.5} 浓度的影响	中国环境科学	2014, 34(6)	
安兴琴等(第2)	珠江三角洲近地层 CO ₂ 通量模拟分析与评估验证	中国环境科学	2014, 34(8)	
安兴琴等(第3)	基于碳源汇模式系统 Carbon Tracker 的广东省近地层典型 CO ₂ 过程模拟研究	环境科学学报	2014, 34(7)	
安兴琴等(第3)	基于卫星遥感的广东地区对流层二氧化碳时空变化特征	中国环境科学	2014, 34(5)	
车慧正等(第3)	区域污染对本底地区气溶胶光学特性及辐射强迫影响的地基和卫星遥感观测研究	环境科学	2014, 35(7)	
程艳丽等(第3)	气候变化下热浪对人群健康的风险及健康经济损失预估研究进展	中华预防医学杂志	2014, 48(9)	
俄有浩	中国内陆干旱、半干旱区苦咸水分布特征	中国沙漠	2014, 34(2)	
俄有浩等(第3)	CO ₂ 浓度升高对冬小麦叶片特性及蒸散影响研究初报	科学技术与工程	2014, 14(2)	
方双喜等	浙江临安大气本底站 CO 浓度及变化特征	环境科学	2014, 35(7)	
房世波等	1961—2010 年中国主要麦区冬春气象干旱趋势及其可能影响	中国农业科学	2014, 47(9)	
郭建平等(第2)	基于极端气象灾害影响的苹果主产国产量预测	陕西农业科学	2014, 60(3)	
郭建平等(第2)	气候变化下东北水稻冷害时空分布变化	中国生态农业学报	2014, 22(5)	
郭建平等(第3)	SRES B2 气候情景下东北玉米产量变化数值模拟	应用气象学报	2014, 25(3)	
郭学良等(第2)	下垫面对雹云形成发展的影响	气候与环境研究	2014, 19(4)	
郭学良等(第2)	华北积层混合云中冰晶形状、分布与增长过程的飞机探测研究	气象学报	2014, 72(2)	
郭学良等(第3)	探测大气温湿廓线的 35 通道微波辐射计设计原理与特点	气象科技	2014, 42(2)	
韩晋平	北太平洋增暖对我国西北秋雨的影响	应用气象学报	2014, 25(3)	
胡志群等	C 波段偏振雷达几种系统误差标定方法对比分析	高原气象	2014, 33(1)	
霍治国等(第2)	20 种非寄主植物挥发物对褐飞虱拒避与引诱行为的影响	华南农业大学学报	2014, 35(3)	
霍治国等(第2)	海南瓜菜春季干旱风险分析与区划	生态学杂志	2014, 33(9)	
霍治国等(第2)	南方晚稻寒露风风险要素的地理分布特征	生态学杂志	2014, 33(10)	
霍治国等(第2)	中国稻飞虱发生的大气环流指示指标	生态学杂志	2014, 33(4)	
霍治国等(第2)	抽穗扬花期淹涝胁迫对杂交稻的影响	中国农学通报	2014, 30(9)	
霍治国等(第2)	海南冬季主要瓜菜寒害风险区划	中国生态农业学报	2014, 22(10)	
霍治国等(第2)	孕穗期低温对水稻产量的影响及其生理机制	中国水稻科学	2014, 28(3)	
霍治国等(第3)	拔节期淹涝胁迫对水稻形态和产量构成因素的影响	生态学杂志	2014, 33(7)	
李丰等	C 波段多普勒天气雷达地物识别方法	应用气象学报	2014, 25(2)	
李宏宇等(第3)	对流云人工增雨效果检验技术方法及应用	气象科技	2014, 42(6)	
李宏宇等(第3)	基于 BJ-RUC 系统的人影冷云催化潜力识别模式平台设计	热带气象学报	2014, 40(8)	
李英等(第2)	辽东半岛热带气旋暴雨的中尺度结构及复杂地形的影响	高原气象	2014, 33(4)	
李英等(第2)	登陆台湾热带气旋的研究现状	浙江气象	2014, 34(2)	

作者 Author (rank)	题名 Title	出版物名/出版社 Publication name or Publisher	年,卷(期号) Year, Volume (Issue)	备注 Notes
李英等(第3)	热带气旋结构和强度变化研究进展	气象与环境学报	2014, 30(4)	
李英等(第3)	西北太平洋热带气旋运动及其突变的若干统计特征	热带气象学报	2014, 30(1)	
梁钊明等	一次台风变性并入东北冷涡过程的动力诊断分析	大气科学	2014, 38(2)	
梁钊明等	京津冀地区与海风锋相互作用的对流系统的发展预判分析	气象学报	2014, 72(1)	
梁钊明等(第3)	渤海湾海风锋触发雷暴的观测和模拟分析	高原气象	2014, 33(3)	
林永辉等(第2)	华南暖区暴雨中一次飑线的中尺度分析	暴雨灾害	2014, 33(2)	
刘舸等(第2)	中国东部冬季温度异常偶极型模态的一个前兆信号	大气科学	2014, 38(4)	
刘建栋等(第2)	华北冬小麦开花及成熟期变化特征分析	干旱地区农业研究	2014, 32(3)	
刘黎平等	X波段相控阵天气雷达对流过程观测外场试验及初步结果分析	大气科学	2014, 38(6)	
刘黎平等	毫米波云雷达功率谱密度数据的检验和在弱降水滴谱反演中的应用研究	大气科学	2014, 38(2)	
刘黎平等(第2)	基于飞机观测资料的降水粒子发射率因子阈值分析	大气科学学报	2014, 37(4)	
刘黎平等(第2)	影响浙江地区降水估测几个因素的分析	气象	2014, 40(5)	
刘黎平等(第2)	S波段相控阵天气雷达与新一代多普勒天气雷达定量对比方法及其初步应用	气象学报	2014, 72(2)	
刘黎平等(第2)	基于雷达组网拼图的定量降水估测算法业务应用及效果评估	气象学报	2014, 72(4)	
刘黎平等(第2)	利用雷达回波三维拼图资料识别雷暴大风统计研究	气象学报	2014, 72(1)	
刘黎平等(第2)	一次高原涡和西南涡作用下强降水的回波结构和演变分析	气象学报	2014, 72(3)	
刘黎平等(第2)	相控阵雷达扫描方式对回波强度测量的影响	应用气象学报	2014, 25(4)	
刘黎平等(第3)	新一代天气雷达三维组网产品在人工防雹的应用	高原气象	2014, 33(5)	
刘黎平等(第3)	基于模糊逻辑的冰雹天气雷达识别算法	应用气象学报	2014, 25(4)	
刘立新等	本底大气CO ₂ 观测分析过程中QA/QC方法的建立与评估	环境科学	2014, 35(12)	
刘玲等	云南山地太阳总辐射的分布式模拟	气象与环境科学	2014, 30(1)	
刘煜等(第2)	对流层气溶胶的直接气候效应对平流层的影响	应用气象学报	2014, 25(1)	
刘煜等(第3)	沙尘气溶胶的跨亚欧大陆传输对东亚地区大气环境	环境科学学报	2014, 34(12)	
楼小凤等	减弱对流云降水的AgI催化原理的数值模拟研究	气象学报	2014, 72(4)	
吕俊梅等	近百年中国东部夏季降水年代际变化特征及其原因	大气科学	2014, 38(4)	
吕伟涛等(第2)	3种阈值方法在闪电通道图像识别中的应用	应用气象学报	2014, 25(4)	
吕伟涛等(第2)	改进的互功率谱相位法在雷声声源定位中的应用	应用气象学报	2014, 25(2)	
罗亚丽	梅雨锋前线状中尺度对流系统成熟阶段的空气垂直运动分析	热带气象学报	2014, 30(4)	
罗亚丽等(第2)	2010年6月中国南方持续性强降水过程:天气系统演变和青藏高原热力作用的影响	气象学报	2014, 72(3)	

作者 Author (rank)	题名 Title	出版物名/出版社 Publication name or Publisher	年,卷(期号) Year, Volume (Issue)	备注 Notes
马建中等	华北地区上空污染烟羽: IPAC-NC 外场实验飞机航测结果	科学通报	2014, 59(2)	
马玉平等(第3)	气候变化对宁夏固原地区胡麻发育进程和产量的影响	应用生态学报	2014, 25(10)	
牛涛等(第2)	2011年9月中国华西致灾暴雨环流特征及地形强迫效应分析	气象与环境学报	2014, 30(4)	
齐艳军等	次季节-季节预测的应用前景与展望	气象科技进展	2014, 4(3)	
任福民	极端天气气候事件监测与预测研究进展及其应用综述	气象	2014, 40(7)	
任福民等(第3)	广义线性统计降尺度方法模拟日降水量的应用研究	气象学报	2014, 72(1)	
阮征等(第2)	机场风廓线雷达参数选择和安装位置分析	现代雷达	2014, 36(8)	
沈小静等	北京上甸子典型天气个例的大气气溶胶数谱分布特征	气象科技进展	2014, 4(1)	
施晓晖	青藏高原东缘对流云和水汽观测试验简介	气象科技进展	2014, 4(5)	
陶玥等(第3)	山西春季层状云系数值模拟及与飞机探测对比	应用气象学报	2014, 25(1)	
王东海等	1960年以来东亚季风区云-降水微物理的直接观测研究	气象学报	2014, 72(4)	
王东海等(第2)	基于CloudSat资料的青藏高原地区云微物理特征分析	气象	2014, 40(2)	
王东海等(第2)	基于WRF/CALMET的近地面精细化风场的动力模拟试验研究	气象	2014, 40(1)	
王改利等(第2)	基于雷达回波外推和中尺度模式预报的短时降水对比分析	高原气象	2014, 33(3)	
王红艳等	浙江省山区新一代天气雷达波束遮挡分析	高原气象	2014, 33(6)	
王红艳等(第2)	华南一次强飚线过程的三维变分风场反演效果分析	暴雨灾害	2014, 33(4)	
王宏等(第2)	NASA/Goddard长波辐射方案在GRAPES Meso模式中的应用研究	大气科学	2014, 38(3)	
王培娟	气候变暖对华北冬小麦返青前热量条件的影响	麦类作物学报	2014, 34(1)	
王培娟	基于分期播种的气候变暖对东北春玉米生长发育与产量的影响研究	中国农学通报	2014, 30(18)	
王培娟等(第2)	1960—2011年东北地区热量资源时空变化特征	自然资源学报	2014, 29(3)	
王培娟等(第3)	漓江上游山区水源林叶面积指数变化的遥感监测	农业工程学报	2014, 30(2)	
王亚非等(第2)	构建描述两种ENSO类型的新指数	气象学报	2014, 72(3)	
王亚强等(第2)	泰山PM ₁₀ 及其中化学成分变化特征	气候变化研究进展	2014, 10(6)	
魏婷等(第3)	谁为气候变化负责?	环球科学	2014, 11	
邹定荣等	基于DEM的广东山地高分辨率太阳辐射模拟研究	热带气象学报	2014, 30(4)	
武炳义等(第2)	冬季欧亚中高纬度大气低频振荡的传播及其与欧亚遥相关型的关系	大气科学	2014, 38(1)	
辛羽飞	一个区域气候模式对南极2 m气温的模拟及其评估	中国科学: 地球科学	2014, 44(4)	
徐洪雄等	台风韦森特对季风水汽流的“转运”效应及其对北京“7·21”暴雨的影响	大气科学	2014, 38(3)	
徐祥德	特殊大地形背景下塔里木盆地夏季降水过程及其大气水分循环结构	沙漠与绿洲气象	2014, 8(2)	

作者 Author (rank)	题名 Title	出版物名/出版社 Publication name or Publisher	年,卷(期号) Year, Volume (Issue)	备注 Notes
徐祥德等	高原东南缘大气近地层湍能特征与边界层动力、热力结构相关特征	气象	2014, 40(10)	
徐祥德等	青藏高原大气水分循环特征	气象学报	2014, 72(6)	
徐祥德等(第3)	中国东部夏季主要降水型与高原春季热力因子间的关系	气象科学	2014, 34(4)	
徐祥德等(第3)	MM5 和 ETA 相似理论近地层方案对农田下垫面通量模拟比较研究	气象学报	2014, 72(4)	
徐晓斌等(第2)	北京及周边地区 3 个典型站点 NO _x 和 CO 的变化	安全与环境学报	2014, 14(6)	
姚波等	北京上甸子区域大气本底站甲基氯仿在线观测研究	环境科学	2014, 35(7)	
尹金方等	区域中尺度模式云微物理参数化方案特征及其在中国的适用性	地球科学进展	2014, 29(2)	
尹金方等(第2)	单双参数云微物理方案对华南暴雨的模拟对比分析	高原气象	2014, 33(5)	
宇如聪等	中国大陆降水日变化研究进展	气象学报	2014, 72(5)	
宇如聪等(第2)	中国东部夏季持续性降水日变化在淮河北南的差异分析	地球物理学报	2014, 57(3)	
张人禾	1 月中国东部持续性强雾霾天气产生的气象条件分析	中国科学: 地球科学	2014, 44(1)	
张人禾等(第2)	中国冬季多种积雪参数的时空特征及差异性	气候与环境研究	2014, 19(5)	
张人禾等(第2)	中国雨季的一种客观定量划分	气象学报	2014, 72(6)	
张胜军等(第2)	强台风“海葵”(1211) 近海急剧增强的数值研究	热带气象学报	2014, 30(6)	
张小曳	中国不同区域大气气溶胶化学成分浓度、组成与来源特征	气象学报	2014, 72(6)	
张小曳等	对 IPCC 第五次评估报告气溶胶-云对气候变化影响与响应结论的解读	气候变化研究进展	2014, 10(1)	
张阳等(第2)	负地闪 CPT 放电事件的发生规律研究	物理学报	2014, 63(1)	SCI
张阳等(第2)	地闪不规则先导的多尺度熵特征	应用气象学报	2014, 25(3)	
张义军等	强风暴中反极性电荷结构研究进展	应用气象学报	2014, 25(2)	
张义军等(第2)	人工触发闪电连续电流过程与 M 分量特征	应用气象学报	2014, 25(3)	
赵俊芳等(第2)	近 30 年东北春玉米发育期对气候变化的响应	应用气象学报	2014, 25(6)	
赵琳娜	集合数值预报在洪水预报中的应用进展	应用气象学报	2014, 25(6)	
赵琳娜等(第3)	通用线性模型在气象水文集合预报后处理中的应用	大气科学学报	2014, 37(2)	
郑栋等(第2)	上海及周边地区地闪活动特征及海陆差异	气象科技	2014, 42(1)	
郑栋等(第2)	一次雹暴过程的闪电活动特征及其与雹暴结构的关系	热带气象学报	2014, 30(6)	
郑栋等(第2)	基于大气层结和雷暴演变的闪电和降水关系	应用气象学报	2014, 25(1)	
周广胜等(第2)	短花针茅 (<i>Stipa Breviflora</i>) 功能性状对水热协同作用的敏感性和适应性	科学通报	2014, 59(34)	
周广胜等(第2)	干旱指标研究进展	生态学报	2014, 34(5)	
周广胜等(第2)	中国兴安落叶松天然林地理分布及其气候适宜性	生态学杂志	2014, 33(6)	



作者 Author (rank)	题名 Title	出版物名/出版社 Publication name or Publisher	年,卷(期号) Year, Volume (Issue)	备注 Notes
周广胜等(第2)	玉米农田冠层光合参数的多光谱遥感反演	植物生态学报	2014, 38(7)	
周广胜等(第2)	1961—2010年阿拉善左旗气温和地温的变化特征分析	自然资源学报	2014, 29(1)	
周海光	2008年1月26日南京暴雪中尺度风场结构双雷达反演研究	热带气象学报	2014, 30(4)	
周凌晔等	城市排放与输送对北京上甸子站温室气体本底观测的影响分析	气象科技进展	2014, 4(3)	
周凌晔等(第2)	龙凤山本底站大气CO ₂ 数据筛分及浓度特征研究	环境科学	2014, 35(8)	
周毓荃等	高炮火箭和飞机催化扩散规律和作业设计的研究	气象	2014, 40(8)	
周毓荃等(第2)	一次超级单体雹暴观测分析和成雹区识别研究2	大气科学	2014, 38(5)	
周毓荃等(第2)	一次积层混合云降水不同尺度结构的数值模拟	大气科学学报	2014, 37(4)	
周毓荃等(第2)	一次西风槽过程过冷水分布特征观测研究	气象学报	2014, 72(3)	
周毓荃等(第3)	L波段探空判别云区方法的研究	大气科学	2014, 38(2)	
周毓荃等(第3)	一次超级单体雹暴观测分析和成雹区识别研究	大气科学	2014, 38(5)	
祝从文等(第2)	华北水资源年代际变化及其与全球变暖之间的关联	大气科学	2014, 38(5)	
祝从文等(第2)	中国夏季降水异常EOF模态的时间稳定性分析	大气科学	2014, 38(6)	
祝从文等(第2)	2011年春夏季长江中下游旱涝急转可能成因	气象与环境学报	2014, 30(4)	



中国气象科学研究院年报 2014

主办单位：中国气象科学研究院
编辑出版：《中国气象科学研究院年报》编辑部
主 编：端义宏
执行主编：袁凤杰
制作印刷：北京永峰印刷有限责任公司
地 址：北京中关村南大街 46 号，邮编 100081
[http: //qk.cams.cma.gov.cn](http://qk.cams.cma.gov.cn)
Email: kjdt@cams.cma.gov.cn

ANNUAL REPORT OF CAMS 2014

Sponsor: Chinese Academy of Meteorological Sciences
Publication: Annual Report of CAMS Editorial Division
Chief Editor: Duan Yihong
Executive Chief Editor: Yuan Fengjie
Design and Printing: Beijing Yongzheng Printing Ltd. Co.
Address: 46 Zhongguancun Nandajie, Beijing, 100081, China
[http: //qk.cams.cma.gov.cn](http://qk.cams.cma.gov.cn)
Email: kjdt@cams.cma.gov.cn